Western&Graduate&PostdoctoralStudies

Electronic Thesis and Dissertation Repository

4-18-2022 10:00 AM

Development of High Performance Cathodes: From Liquid to Solid-State Batteries

Sixu Deng, *The University of Western Ontario*

Supervisor: Sun, Xueliang, *The University of Western Ontario*
A thesis submitted in partial fulfillment of the requirements for the Doctor of Philosophy degree
in Mechanical and Materials Engineering
© Sixu Deng 2022

Follow this and additional works at: https://ir.lib.uwo.ca/etd

Part of the Materials Science and Engineering Commons, and the Nanoscience and Nanotechnology Commons

Recommended Citation

Abstract

Lithium-ion batteries (LIBs) are critical for the development of electric vehicles (EVs) because of their higher operating voltages compared to other energy storage technologies. However, the development of start-of-the-art LIBs touched the ceiling because of three main challenges: safety risks, limited energy density, and high cost. Accordingly, all-solid-state lithium-ion batteries (ASSLIBs) have recently emerged as promising alternative batteries for next-generation EVs because of their ability to overcome the drawbacks of conventional LIBs. Whether in conventional liquid LIBs or ASSLIBs, cathode materials are crucial in determining the overall performance. Hence, this thesis focuses on understanding the degradation mechanism of cathode interfaces and developing novel interfacial strategies in both liquid LIBs and ASSLIBs.

The first work in this thesis develops a hybrid Li_3PO_4-TiO_2 coating layer by atomic layer deposition (ALD) to improve both interfacial ionic/electronic conductivities and stability for high-voltage $LiNi_{0.5}Mn_{1.5}O_4$ (LNMO) cathode in liquid LIBs.

In the second work, a dual-functional Li_3PO_4 (LPO) modification is designed for Ni-rich layered oxide cathodes, aiming to address both the interfacial side reactions and the microstructural cracks in sulfide-based ASSLIBs.

In the third work, the origin of cathode interface degradation in sulfide-based ASSLIBs is unveiled by the X-ray and electrochemical analyses. Residual lithium compounds on the surface of Ni-rich layered cathodes are proved as the main reason that triggers the oxidation of sulfide solid-state electrolytes (SSEs), therefore inducing severe side reactions at cathode interface and structural degradation of Ni-rich cathodes.

The fourth wok for the first time reports a controllable semi-conductive additive, poly(3,4-ethylenedioxythiophene) (PEDOT), in sulfide-based ASSLIBs, therefore realizing effective electron transfer at the cathode/SSE/additive three-phase interface along with a competitive rate capacity.

To realize fast-charging ASSLIBs, the fifth work investigates the interfacial evolution of Al foil current collector in all-climate environment. At room temperature, side reactions are the main challenge for interfacial stability. At low temperature, the low Li$^+$ and electron transfer kinetics along with side reactions are the key limitations for rate capability. The challenges at both room temperature and low temperature can be addressed by the graphene modification on Al foil.

Keywords

Summary for Lay Audience

Electric Vehicles (EVs), as an ideal solution to address the challenges of global climate change, developed rapidly in the past ten years. The performance of lithium-ion batteries (LIBs), particularly the cathodes in LIBs, is critical for the development of safe, long-range, and fast-charged EVs. However, the start-of-the-art cathodes still face some significant challenges that deteriorate the performance of LIBs, therefore limiting their application in EVs. In conventional liquid-based LIBs, high working voltage of cathode materials leads to severe side reactions with the liquid organic electrolytes. In solid-state batteries (SSBs), the unstable cathode interfaces also bring poor performance. Hence, this thesis develops multiple strategies to address the challenges of cathode interfaces in both liquid LIBs and SSBs as well as investigates the interfacial degradation mechanisms by advanced characterizations.

First of all, a hybrid coating material, Li_3PO_4-TiO_2, is deposited on the surface of high-voltage $LiNi_{0.5}Mn_{1.5}O_4$ (LNMO) cathode by atomic layer deposition. The coating layer avoids the direct contact between LNMO and liquid electrolytes, therefore suppressing the side reactions. Furthermore, the interfacial ionic/electronic conductivities also be enhanced by the hybrid coating layer, resulting in the much improved performance. The second work in this thesis focuses on the cathode interface in sulfide-based SSBs. A dual-functional Li_3PO_4 modification is developed to address both the side reactions with sulfide electrolytes and microstructure evolution of Ni-rich cathodes. As a result, an excellent long-term cycling performance is achieved with an improved rate capability. In the third work, the degradation mechanism of cathode interface in sulfide-based SSBs is clearly unveiled by advanced X-ray characterizations. Residual lithium compounds on the surface of Ni-rich cathodes are the origin that triggering side reactions with sulfide electrolytes, therefore deteriorating the performance of SSBs. The fourth part for the first time develops a semi-conductive poly(3,4-ethylenedioxythiophene) as additive in sulfide SSBs, that realizing an excellent rate performance. The fifth work investigates the effect of Al foil current collector in halide-based SSBs. Side reactions between Al foil and halide electrolyte and limited charge transfer kinetics are two main reasons that limiting the performance of SSBs, which can be addressed by the modification of graphene coating.

Co-Authorship Statement

1.

Title: Manipulation of An Ionic and Electronic Conductive Interface for Highly Stable High-Voltage Cathodes

Authors: Sixu Deng, Biqiong Wang, Yifei Yuan, Xia Li, Qian Sun, Kieran Doyle-Davis, Mohammad Norouzi Banis, Jianneng Liang, Yang Zhao, Junjie Li, Ruying Li, Tsun-Kong Sham, Reza Shahbazian-Yassar, Hao Wang, Mei Cai, Jun Lu, Xueliang Sun

The final version of this paper has been published in *Nano Energy*, 2019, 65, 103988. Sixu Deng carried out all of the experiments and finished the draft of manuscript; Xueliang Sun, Mei Cai, and Hao Wang conceived the overall project; Biqiong Wang and Yang Zhao carried out the ALD process; Yifei Yuan, Reza Shahbazian-Yassar, and Jun Lu helped the TEM testing; Xia Li, Qian Sun, Kieran Doyle-Davis, Jianneng Liang, and Junjie Li performed the physical characterizations and interpreted the results and data analysis; Mohammad Norouzi Banis and Tsun-Kong Sham carried out the synchrotron characterizations; Ruying Li provided access to the equipment. All authors contributed editorial comments on the manuscript.

2.

Title: Dual-functional interfaces for highly stable Ni-rich layered cathodes in sulfide all-solid-state batteries

Authors: Sixu Deng, Xia Li, Zhouhong Ren, Weihan Li, Jing Luo, Jianwen Liang, Jianneng Liang, Mohammad Norouzi Banis, Minsi Li, Yang Zhao, Xiaona Li, Changhong Wang, Yipeng Sun, Qian Sun, Ruying Li, Yongfeng Hu, Huan Huang, Li Zhang, Shigang Lu, Jun Luo, Xueliang Sun

The final version of this paper has been published in *Energy Storage Materials*, 2020, 27, 117. Sixu Deng carried out all of the experiments and finished the draft of manuscript; Xueliang Sun and Shigang Lu conceived the overall project; Xia Li, Weihan Li, Mohammad

Norouzi Banis, Minsi Li, and Yongfeng Hu carried out the synchrotron characterizations; Zhouhong Ren and Jun Luo helped the TEM testing; Jing Luo, Jianwen Liang, Jianneng Liang, Xiaona Li, Changhong Wang, and Qian Sun helped the preparation of electrolytes; Yang Zhao and Yipeng Sun carried out the ALD process; Huan Huang and Li Zhang helped discuss the results; Ruying Li provided access to the equipment. All authors contributed editorial comments on the manuscript.

3.

Title: Insight into cathode surface to boost the performance of solid-state batteries

Authors: Sixu Deng, Qian Sun, Minsi Li, Keegan Adair, Chuang Yu, Junjie Li, Weihan Li, Jiamin Fu, Xia Li, Ruying Li, Yongfeng Hu, Ning Chen, Huan Huang, Li Zhang, Shangqian Zhao, Shigang Lu, Xueliang Sun

The final version of this paper has been published in *Energy Storage Materials*, 2021, 35, 661. Sixu Deng carried out all of the experiments and finished the draft of manuscript; Xueliang Sun and Shigang Lu conceived the overall project; Qian Sun, Keegan Adair, and Xia Li performed the physical characterizations; Chuang Yu helped the preparation of electrolytes; Junjie Li, Weihan Li, Jiamin Fu, Yongfeng Hu, and Ning Chen carried out the synchrotron characterizations; Ruying Li provided access to the equipment. Huan Huang, Li Zhang, and Shangqian Zhao helped discuss the results. All authors contributed editorial comments on the manuscript.

4.

Title: Eliminating the detrimental effects of conductive agents in sulfide-based solid-state batteries

Authors: Sixu Deng, Yipeng Sun, Xia Li, Zhouhong Ren, Jianwen Liang, Kieran Doyle-Davis, Jianneng Liang, Weihan Li, Mohammad Norouzi Banis, Qian Sun, Ruying Li, Yongfeng Hu, Huan Huang, Li Zhang, Shigang Lu, Jun Luo, Xueliang Sun

The final version of this paper has been published in *ACS Energy Letters*, 2020, 5, 1243. Sixu Deng carried out all of the experiments and finished the draft of manuscript; Xueliang

Sun and Shigang Lu conceived the overall project; Yipeng Sun carried out the MLD process; Xia Li, Kieran Doyle-Davis, Jianneng Liang, and Qian Sun performed the physical characterizations; Zhouhong Ren and Jun Luo helped the TEM testing; Jianwen Liang, Huan Huang, and Li Zhang helped discuss the results; Weihan Li, Mohammad Norouzi Banis, and Yongfeng Hu carried out the synchrotron characterizations; Ruying Li provided access to the equipment. All authors contributed editorial comments on the manuscript.

5.

Title: Fast-Charging Halide-Based All-Solid-State Batteries by Manipulation of Current Collector Interface

Authors: Sixu Deng, Ming Jiang, Adwitiya Rao, Xiaoting Lin, Kieran Doyle-Davis, Jianwen Liang, Chuang Yu, Ruying Li, Shangqian Zhao, Li Zhang, Huan Huang, Jiantao Wang, Chandra Veer Singh, Xueliang Sun

The final version of this paper has been published in *Advanced Functional Materials*, 2022, 2200767. Sixu Deng carried out all of the experiments and finished the draft of manuscript; Xueliang Sun conceived the overall project; Ming Jiang, Adwitiya Rao, and Chandra Veer Singh performed the DFT calculation; Xiaoting Lin and Kieran Doyle-Davis performed the physical characterizations; Jianwen Liang and Chuang Yu helped the preparation of electrolytes; Ruying Li provided access to the equipment; Shangqian Zhao, Li Zhang, Huan Huang, and Jiantao Wang helped discuss the results. All authors contributed editorial comments on the manuscript.

Dedication

This thesis is dedicated to my parents, Mr. Qi Deng and Mrs. Yuping Wang

my wife, Xia Li

and my daughter, Ella Yiyang Deng

风檐展书读，古道照颜色

-文天祥《正气歌》

Acknowledgments

This Ph.D. work was accomplished in Professor Xueliang (Andy) Sun's Advanced Materials for Clean Energy Group at Western University (UWO). I want to express my great appreciation to everyone that helped and supported me during my study period at UWO.

First of all, I would like to thank my supervisor, Dr. Xueliang (Andy) Sun, a Professor in the Department of Mechanical and Materials Engineering (MME) at UWO, Canada Research Chair (Tire 1), Fellow of the Canadian Academy of Engineering and Fellow of the Royal Society of Canada. I appreciate Prof. Sun for providing me an opportunity to study in our group as a visiting Ph.D. student and then supporting me to pursue my second Ph.D. degree at UWO. Prof. Sun is a perfect mentor, researcher, and example of me. Prof. Sun always encourages me to think about the key questions in our research fields, gives me guidance on my research directions, and trains me to disseminate my research findings. His passion, diligence, and brilliance in research have greatly inspired me and will encourage me in my future research career. Not only the help for my research, but I would also like to thank Prof. Sun for giving me full support for my scholarship applications during my Ph.D. study. With the help of Prof. Sun, I have been granted several highly competitive scholarships in Canada, including Canada Graduate Scholarships-Doctor, MITACS Accelerate Fellowship, Ontario Graduate Scholarships, and Queen Elizabeth II Graduate Scholarships. Prof. Sun is the person that helps me to build my research philosophy, and I will always see him as the paragon that heartens me better.

I would also like to give my greatest appreciation to Mrs. Ruying (Kathy) Li, Prof. Sun's wife, and our lab manager. Kathy always encourages me when I face challenges in my research. Without her help, I couldn't achieve many achievements during my Ph.D. study. I also wonder to appreciate Kathy's great support for my family. Kathy is not only my teacher but also like my mom that teaches me how to be a good husband and how to be a good father. Thanks Kathy for always staying with my family and me. I will never forget her help when my daughter, Ella, faced a dangerous moment after she was born.

I also like to thank all current and former members of Prof. Sun's group. It is my great honor to work with you together. You are the most brilliant persons that I have never seen before.

Finally, I would like to express my most significant appreciation to my family. My parents, Mr. Qi Deng and Mrs. Yuping Wang, provided me with everything they had without any reservations and hesitations. Without your love and support, I cannot be the present myself. I'm proud of being your son, and I love you forever. I also would like to thank my parents-in-law, Mr. Jiexin Li and Mrs. Xiaoning Jiao, for their great support and understanding. No words can express my love to my wife, Xia Li. Thank you for always trusting me even sometimes I did not trust myself. Your accompaniment, understanding, and support encourage me to be better for our family. Although we face challenges in our life, I believe that we can overcome every difficulty as long as we are together. Final of the final, I would like to thank my daughter, Ella Yiyang Deng. It is you that let me know what I am fighting for. This thesis is a gift for you.

Sixu Deng
January 14, 2022
London, Ontario, Canada

Table of Contents

List of Figures

List of Appendices

Preface

A:

AB: acetylene black

ALD: atomic layer deposition

ASSLIBs: all-solid-state lithium-ion batteries

C:

CEI: cathode electrolyte interphase

CFI: Canada Foundation for Innovation

CLS: Canadian Light Source

CNTs: carbon nanotubes

CRC: Canada Research Chair Program

CV: Cyclic voltammetry

D:

DEC: diethylene carbonate

DFT: density functional theory

DMC: dimethylene carbonate

DOE: Department of Energy

E:

EC: ethylene carbonate

EDOT: 3,4-ethylenedioxythiophene

EDX: energy dispersive spectrometer

EELS: electron energy loss spectroscopy

EIS: electrochemical impedance spectroscopy

EMC: ethylmethyl carbonate

EVs: electric vehicles

F:

FESEM: field emission scanning electron microscopy

FIB: focused ion beam

G:

GHC: graphitic hollow nanocarbon

GITT: galvanostatic intermittent titration technique

GLC: graphene like carbon

GM: General Motors

H:

HAADF-STEM: high-angle annular dark-field scanning trans-mission electron microscopy

HRTEM: high-resolution transmission electron microscopy

HXMA: Hard X-ray Micro Analysis

I:

IDI: Interdisciplinary Development Initiatives

L:

LBCO: Li_3BO_3-Li_2CO_3

LCO: $LiCoO_2$

LCTO: $Li_2CoTi_3O_8$

LFP: $LiFePO_4$

LGPS: $Li_{10}GeP_2S_{12}$

LIBs: lithium-ion batteries

LMO: $LiMn_2O_4$

LNMO: $LiNi_{0.5}Mn_{1.5}O_4$

LNTO: $LiNb_{0.5}Ta_{0.5}O_3$

LPO: Li_3PO_4

LPS: Li_2S-P_2S_5

LPSCl: Li_6PS_5Cl

LPO-TiO: Li_3PO_4-TiO_2

M:

MLD: molecular layer deposition

N:

NBR: nitrile butadiene rubber

NCA: $LiNi_{0.6}Co_{0.15}Al_{0.25}O_2$

NMC: $LiNi_xMn_yCo_{1-x-y}O_2$

NMC70: $LiNi_{0.70}Co_{0.15}Mn_{0.15}O_2$

NMC811: $LiNi_{0.8}Mn_{0.1}Co_{0.1}O_2$

NMP: N-methyl-pyrrolidione

NSERC: Natural Science and Engineering Research Council of Canada

O:

oCVD: oxidative chemical vapor deposition

P:

PBE: Perdew-Burke-Ernzerhof

PC: propylene carbonate

PEDOT: poly(3,4-ethylenedioxythiophene)

PPC: poly(propylene carbonate)

S:

SCL: space-charge layer

SEM: scanning electron microscopy

SGM: Spherical Grating Monochromator

SGPS: School of Graduate and Postdoctoral Studies

SSBs: solid-state batteries

SSEs: solid-state electrolytes

STEM: scanning transmission electron microscopy

SOC: state of charge

SXRMB: Soft X-ray Microcharacterization Beamline

T:

TEM: transmission electron microscopy

TEY: total electron yield mode

TGA: thermal gravimetric analysis

TM: transition metal

ToF-SIMS: time-of-flight secondary-ion mass spectrometry

U:

USABC: U.S. Advanced Battery Consortium

UWO: Western University

V:

VASP: Vienna Ab Initio Simulation Package

vdW: van der Waals

VGCF: vapor-grown carbon fiber

X:

XANES: X-ray absorption near-edge spectroscopy

XRD: X-ray power diffraction

XPS: X-ray photoelectron spectroscopy

Chapter 1

1 Introduction of This Thesis

In the past four years, the author's Ph.D. studies fully focus on lithium-ion cathode materials and the corresponding cathode interfaces. The study in this thesis starts from the liquid-based lithium-ion batteries (LIBs). The objective in this part is to develop the multi-functional coatings to address the challenges of high-voltage spinel cathodes. After finishing the project of liquid LIBs, the author's research moves to all-solid-state lithium-ion batteries (ASSLIBs), including sulfide and halide solid-state electrolytes. Combining with advanced characterizations, the degradation mechanisms of different cathode interfaces are deeply understood. Furthermore, the novel interfacial strategies have been developed, therefore the high-performance ASSLIBs have been achieved in this thesis.

1.1 Thesis objectives

Cathode materials, as the critical component in lithium-ion batteries, play a key role in determining performance. However, the instability of cathode interface is a big obstacle for high performance in both conventional liquid LIBs and ASSLIBs. In this thesis, the authors develop a series of strategies to address the challenges of the cathodes and their interfaces from liquid to solid-state batteries. In the liquid-based LIB, the interfacial stability of high-voltage $LiNi_{0.5}Mn_{1.5}O_4$ (LNMO) is investigated in detail. In the solid-state batteries, the individual strategies are developed for the different interfaces in composite cathodes. The main research objectives are divided into five parts and are shown below.

(1) To stabilize the LNMO interface in carbonate-based liquid electrolytes. A hybrid Li_3PO_4-TiO_2 coating layer is developed as an interfacial material for LNMO via controllable atomic layer deposition (ALD). The lithium-ion and electronic conductivities of coating layer are manipulated by optimizing the ALD processes.

(2) To overcome the incompatible cathode interface and chemo-mechanical degradation of Ni-rich NMC cathodes in sulfide-based SSBs. A hierarchical Li_3PO_4 modification is

developed to not only alleviate the severe side-reactions with sulfide electrolyte at high voltages but also suppress the microstructural cracks of cathodes during cycling.

(3) To investigate the origin of degradation at cathode interface in sulfide-based SSBs. A comprehensive X-ray analysis combined with detailed electrochemical characterizations is adopted to unveil the effects of surface residual lithium compounds on Ni-rich NMC cathode interfaces.

(4) To overcome the challenges of using carbon additives at cathode composites in sulfide-based SSBs. A semi-conductive polymer thin film, poly(3,4-ethylenedioxythiophene) (PEDOT), is constructed by molecular layer deposition (MLD) to realize the superior electrochemical performance with high-rate capacity.

(5) To investigate the effect of current collector in halide-based SSBs. The degradation mechanism between Al foil current collector and composited cathode is studied at both room temperature and low temperature. A modification of Al foil is also developed to enhance the stability and facilitate the charge transfer kinetics at the current collector interface.

1.2   Thesis organizations

This thesis includes nine chapters, including an introduction of this thesis, a literature review, an experimental chapter, five published peer-review papers, and one conclusive chapter. The organization of this thesis is followed by the requirements on "Integrated-Article" form as outlined in the Thesis Regulation Guide by the School of Graduate and Postdoctoral Studies (SGPS) of Western University (UWO). Specifically, this thesis consists of the following parts.

Chapter 1 states the research objectives and how I organize this thesis.

Chapter 2 presents a comprehensive introduction of recent development of high-energy cathodes and their challenges and strategies in both liquid and solid-state batteries. Thesis objectives are also listed in this chapter.

Chapter 3 outlines the experimental methods, including ALD and MLD coatings and surface clean of Ni-rich NMC cathodes. Then, the advanced characterization techniques, such as the spectroscopy/microscopy characterizations and electrochemical testing, are described in detail.

Chapter 4 demonstrates a controllable Li_3PO_4-TiO_2 hybrid interface material as a coating layer for LNMO cathode with the use of ALD. Hybrid Li_3PO_4-TiO_2 coating layer effectively suppresses the polarization as well as facilitates Li-ion migration because of its capability to construct a stable interface to avoid side-reactions and also improve the interfacial ionic and electronic conductivity. Hence, hybrid Li_3PO_4-TiO_2 coated LNMO shows much improved cycling stability and rate capability.

Chapter 5 represents a hierarchical LPO modification for Ni-rich NMC811 cathodes by a two-step ALD process. The results indicate the severe side-reactions with sulfide electrolyte and the microstructural cracks of NMC811 are effectively suppressed by the hierarchical LPO stabilization. As a result, an ultra-long cycling life over 300 cycles is achieved with a low capacity degradation rate of 0.22 mAh g^{-1} at 0.2C.

Chapter 6 investigates the underlying degradation mechanism of cathode interface via X-ray characterizations. The surface impurities, rather than cathode particles themselves, are the main reason that triggering the oxidation of sulfide SSEs, therefore leading to the formation of sulfate species. As a result, the cathode interface is damaged by the severe side-reactions along with the structural evolution of NMC811. In contrast, removal of surface impurities helps to alleviate the oxidation of sulfide SSEs and limits the severe side-reactions, therefore stabilizing the cathode interface.

Chapter 7 develops a controllable p-type semi-conductive polymer PEDOT thin film to realize the application of conductive agents in cathode composites for sulfide-based SSBs. Because of effectively suppressing the severe side-reactions between sulfide electrolyte and CNTs, the modified electrode demonstrates enhanced cycling stability and significantly improved rate capability with a capacity of over 100 mAh g^{-1} at 1C, 10 times higher than that of the bare electrode.

Chapter 8 studies the degradation mechanism at the interface of current collector in halide Li_3InCl_6-based (LIC) SSBs. At 25 ℃, the side reactions between Al foil and LIC lead to the corrosion of Al and decomposition of LIC, resulting in the degradation of cycling stability and poor rate capability. At -10 ℃, in addition to side reactions, the low Li^+/electron transfer kinetics are the main challenge that limit the electrochemical performance. By optimizing the interface of current collector, both the corrosion of Al foil and decomposition of LIC are circumvented with an enhanced Li^+/electron transfer, resulting in an improved electrochemical performance at both room and low temperature.

Chapter 9 summarizes results, conclusions, and contributions of this thesis and gives the perspectives and suggestions for the future development of next-generation high-energy cathodes and their application in high-performance ASSLIBs.

Chapter 2

2   Literature Review

In this chapter, a comprehensive literature review on the recent developments of high-energy cathodes and their interfaces in both liquid and inorganic solid-state batteries are presented.

2.1 Introduction

Over the past decades, the abusive consumption of fossil fuels lead to the global warming and energy shortage. It is imperative to developing alternative clean energies and the corresponding energy storage devices.[1] Rechargeable lithium-ion batteries (LIBs) are considered as one of the most promising energy storage devices because of their outstanding advantages such as high energy density, high safety, and long cycling life.[2] LIBs have been widely used in portable electronic devices and become a key player in the development of electric vehicles (EVs).[3] In the past five years, the global EVs market grows rapidly and reached to USD 246 billion in 2020. This market will continue growing and has the potential to reach to 1318 billion in 2028. The growing demand of EVs market provides an excellent opportunity for the development of LIBs but with three outstanding challenges. (1) The increasing market demand for LIBs will cause resource shortage and rise of cost. (2) The state-of-art LIBs can provide 260 Wh kg^{-1} and 780 Wh L^{-1} of gravimetric and volumetric energy densities, respectively, which is insufficient to meet the requirement of EVs for long-range drive. (3) The use of flammable and toxic liquid electrolytes brings high safety risks of battery fire when operated in high temperatures and voltages.[4-6]

To address these challenges, all-solid-state lithium-ion batteries (ASSLIBs) have recently emerged as promising alternative batteries because of their ability to overcome the drawbacks of conventional LIBs.[7-8] As the key component in ASSLIBs, various solid-state electrolytes (SSEs) have be developed with promising properties. For example, polymer electrolytes exhibit excellent mechanical stability for mass production.[9-11] Oxide electrolytes show outstanding high-voltage compatibility with cathodes.[12-14] Sulfide electrolytes demonstrates high ionic conductivity even surpassing the counterpart liquid electrolytes.[15-19] Recently revived halide electrolytes show favorable compatibility with layered oxide cathode.[20-22] ASSLIBs also attract increasing global research and industrial attention. For example, Toyota has accelerated its research towards ASSLIBs. The US Department of Energy (DOE) have increased their support for

developing ASSLIBs for EVs. Nevertheless, the development of ASSLIBs is at the initial stage and the intrinsic challenges still need to make great efforts to address.
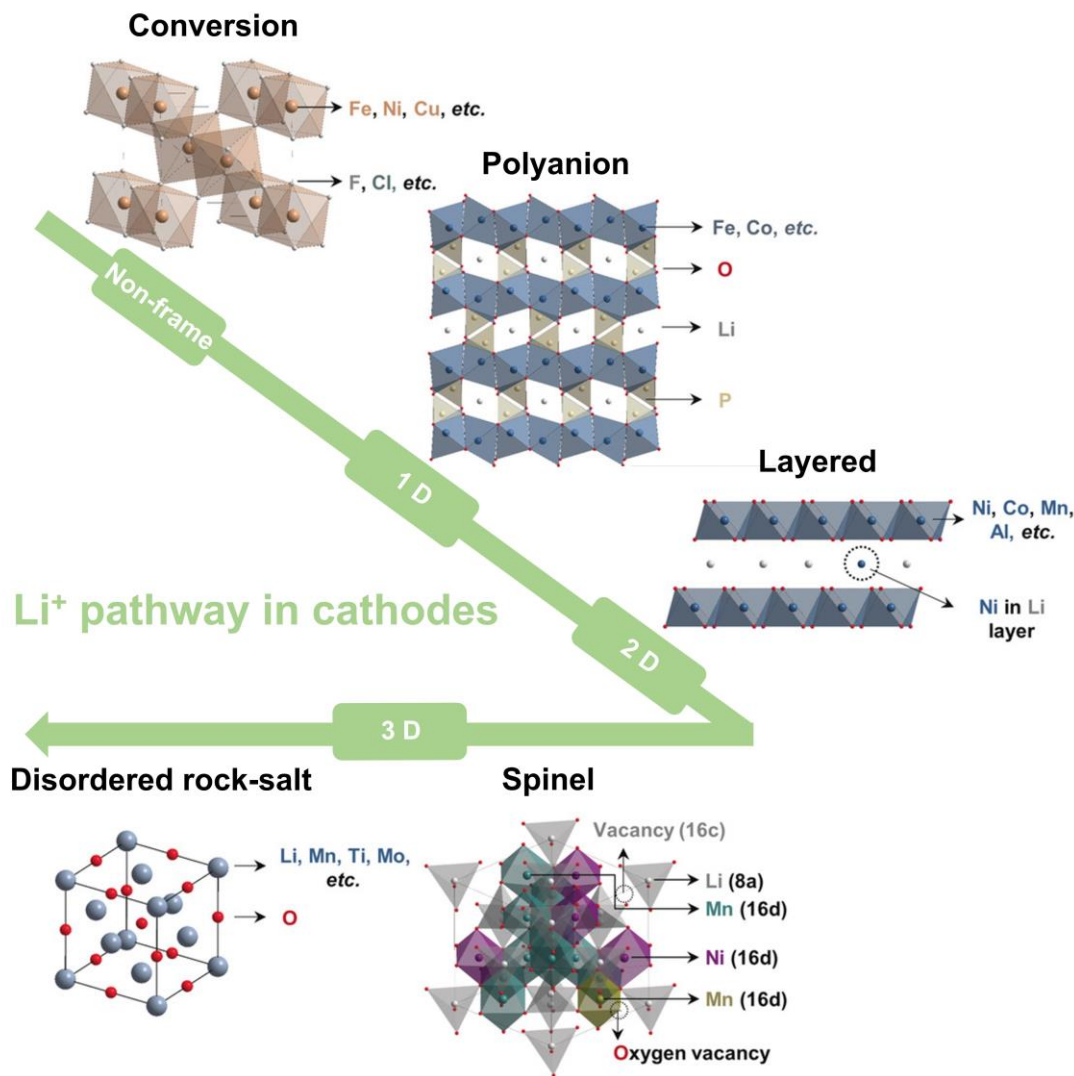
Figure 2.1 Schematic illustration of crystal structure of cathode materials and their Li⁺ pathways.[23]

Not only in conventional liquid LIBs but also in ASSLIBs, cathode materials as the key component determine the overall electrochemical performance. The developed cathode materials in LIBs can be classified into five types based on their crystal structures, including layered, spinel, polyanion, disordered rock-salt, and conversion cathodes (as shown in **Figure 2.1**).[23-28] Among the commercial cathode materials, most of them

have relative low capacities. For example, layered $LiCoO_2$ (LCO) shows the capacity of 140 mAh g^{-1} and $LiMn_2O_4$ (LMO) with a spinel structure can deliver the capacity of 147 mAh g^{-1}.[29-30] Although the capacity of $LiFePO_4$ (LFP) is 170 mAh g^{-1}, low charge-discharge voltages of 3.4 V vs. Li/Li$^+$ limit their energy densities.[31-32] To achieve the higher energy density, developing novel cathode materials with high capacities and voltages is a promising strategy. In the following sections, the high-energy cathodes and their challenges and strategies in both liquid and inorganic solid-state batteries will be discussed in details.

2.2   Introduction of high-energy cathodes

The electrochemical performance of cathode materials is depended on their crystal structure and components. For example, Ni-rich $LiNi_xMn_yCo_{1-x-y}O_2$ (NMC, x $\geq$ 0.8) layered oxide cathodes can offer reversible discharge capacities of over 200 mAh g^{-1}, which are over 1.4 times higher than that of LCO cathodes.[33] The high capacities of Ni-rich NMC cathodes are attributed from the redox of Ni between +2 and +4.[34] Ni-rich NMC cathodes belong to α-NaFeO$_2$-type structure with a hexagonal layered phase (R-3m space group). The Li and O atoms occupy on 3b and 6c sites of the crystal structure, respectively. The transition metal atoms of Ni, Co, and Mn are randomly distributed on 3a sites.[35-36] In the Ni-rich NMC cathodes, the chemical valences of Co and Mn are +3 and +4, respectively. Ni exhibits a mixed valence state of +2 and +3 in NMC cathodes and the numbers of Ni^{3+} keep increasing with the increase of Ni contents. Ni in the Ni-rich NMC cathodes provides main capacity and the redox of Co between +3 and +4 occurs only at the high delithiation state with a high charging cut-off voltages. The chemical valence of Mn remains unchanged at +4, which is beneficial to enhance structural stability of Ni-rich NMC cathode materials.[37-40]

In addition to layered Ni-rich NMC cathodes, the high-voltage $LiNi_{0.5}Mn_{1.5}O_4$ (LNMO) material with spinel structure is also considered as a promising high-energy cathode.[41-43] LNMO cathode is developed by the doping of Ni into LMO cathode. The spinel LNMO cathode have two types of space groups (ordered P4$_3$32 and disordered Fd$\overline{3}$m). In the cubic-phase P4$_3$32 structure, the Li ions are located at the 8a sites, while the O ions

are distributed at the 24e and 8c sites. Mn and Ni ions are located at the 12d and 4b octahedral sites, respectively.[44] In this case, the highly ordered P4$_3$32 structure provides LNMO with a good cationic ordering between Mn^{4+} and Ni^{2+}. For the disordered Fd$\overline{3}$m structure, although Li ions are still located at the 8a sites, O ions are distributed at the 32e sites and Mn and Ni ions are located at the 16d sites with a random distribution.[45-47] The different space groups determine the different electrochemical behaviors. In the disordered Fd$\overline{3}$m LNMO, the redox of Mn between +3 and +4 happens at the voltage of 4 V vs. Li/Li$^+$ with a minor discharge plateau. The major capacity of disordered Fd$\overline{3}$m LNMO is attributed from the redox reaction of Ni ions along with Ni^{2+}/Ni^{3+} at 4.6 V and Ni^{3+}/Ni^{4+} at 4.8 V. In contrast, there is no redox reaction of Mn^{3+}/Mn^{4+} in the ordered P4$_3$32 cathode and the redox reactions of Ni^{2+}/Ni^{3+} and Ni^{3+}/Ni^{4+} are merged into a flat plateau at about 4.7 V.[48-50] Although both the high-capacity Ni-rich NMC layered cathodes and high-voltage LNMO spinel cathodes are considered as the promising cathode candidates to realize the target of high energy density, their outstanding challenges in the liquid and solid-state batteries limit the performance of batteries and need to be addressed.

2.3 Challenges of high-energy cathodes in liquid electrolytes

Developing the high-performance high-energy cathode materials is a key part for the practical application of LIBs. However, there are still many challenges of high-energy cathode materials in the conversional liquid LIBs, such as limited long-term cycling lifetimes, poor rate capability, and safety issues. Although different high-energy cathode materials have different properties because of their specific structures, both the structural instability of cathode materials and the side reactions with liquid electrolytes are considered as two main factors that deteriorate the performance of high-energy cathode materials. In this part, we will summary the challenges of two typical high-energy cathodes, Ni-rich NMC cathodes and LNMO cathodes, in liquid-based LIBs.
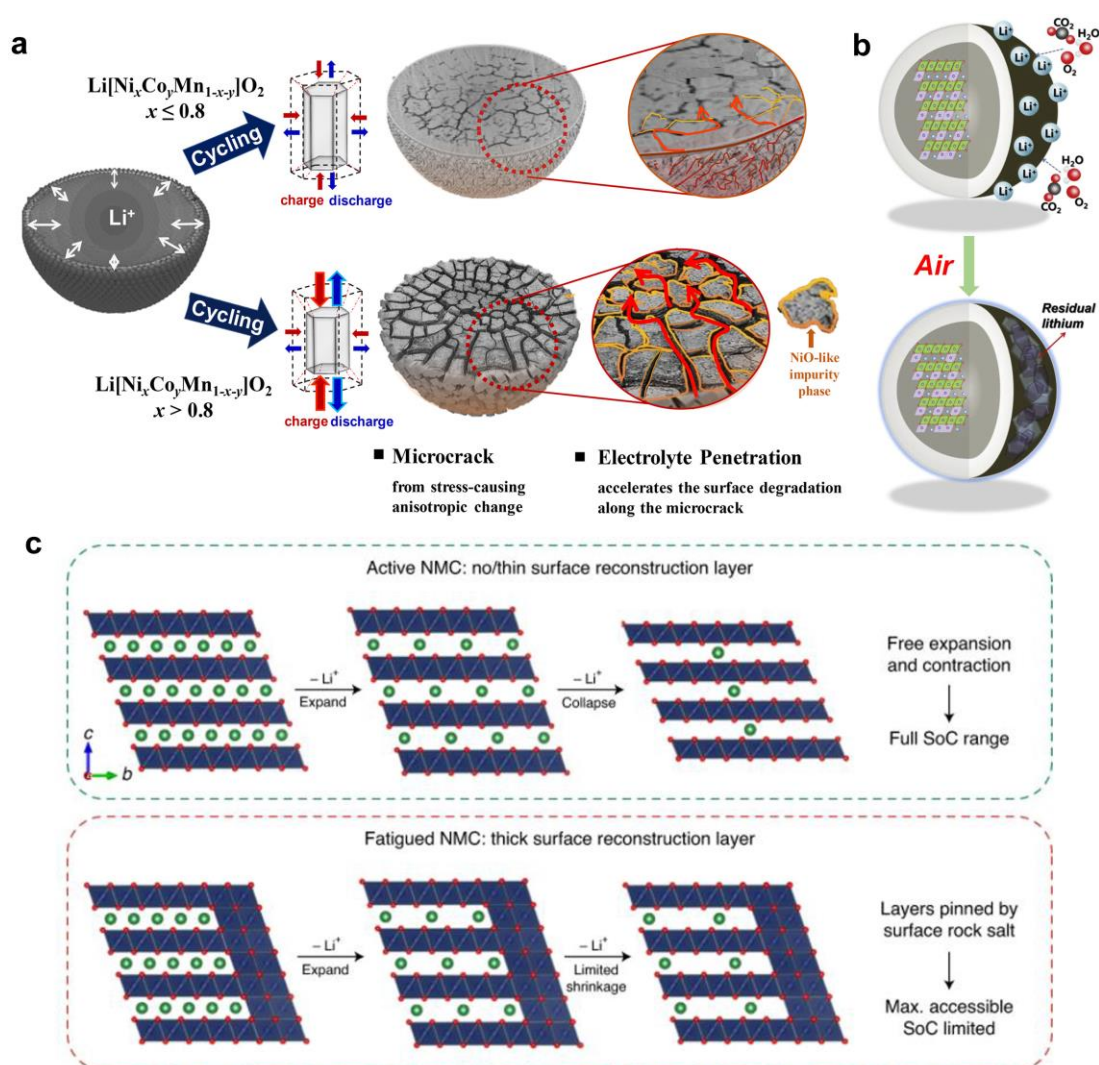
Figure 2.2 Degradation mechanism of cathode in liquid LIBs. (a) Microstructural cracking of Ni rich NMC cathodes,[55] (b) the formation process of LiOH and Li_2CO_3 at Ni-rich cathode surface,[58] and (c) illustrations of the NCM811 structural evolution of the active and fatigued phase during delithiation.[62]

2.3.1 Stress-induced cracking

Microstructural cracking is considered as a major issue that leading to the capacity loss of polycrystalline Ni-rich NMC cathodes for long-term cycling.[51] Because of high tap density, polycrystalline Ni-rich NMC cathodes are widely applied in the conversional liquid-based LIBs. However, polycrystalline Ni-rich NMC cathodes are mechanically

instable during the electrochemical cycling. The anisotropic lattice volume change is the main origin that inducing the microstructural cracking of polycrystalline Ni-rich NMC cathodes.[52-53] Microstructural cracking of Ni-rich NMC cathodes is highly related to the charging voltages. When the extra lithium ions de-intercalate from the layered structure, extra stresses are formed in the Ni-rich NMC particles. Therefore, for most layered cathode materials, high charging cut-off voltage is a challenge that initiating cracks of cathode particles.[54] Furthermore, Ni content is also the key factor of microstructural cracking (as shown in **Figure 2.2a**).[55] With the increasing of Ni content, more severe microstructural cracking happened because of more anisotropic lattice shrinkage during the charging process, although high Ni contents bring the high capacity. The anisotropic volume change of Ni-rich NMC cathodes leads to the phase transition at the end of charging process (over 4.3 V). During the charge/discharge process, non-uniform shrinking and expansion extend from internal structure to the surface, therefore broking the mechanical integrity of cathode particles. Furthermore, the formed structure gap allows liquid electrolyte infiltration into the particle interior, therefore leading to the side reactions extended from the surface to the internal interface of Ni-rich NMC cathodes.[56-57]

2.3.2 Surface phase reconstruction

In addition to the microstructural cracking, the phase reconstruction on the surface of Ni-rich NMC cathodes is another key challenge for the capacity decay. On the one hand, residual lithium on the surface of Ni-rich NMC cathodes tend to react with ambient air, leading to the formation of a interfacial layer consisting of Li_2CO_3 and LiOH (as shown in **Figure 2.2b**).[58] During the charge-discharge cycles, Li_2CO_3 decomposes at the high voltage and generated CO_2, resulting in the safety issues of the battery.[59] In addition, the formed interfacial layer are both ionic and electronic isolation, which block the diffusion of Li^+ and electrons during the charge-discharge process. The formed interfacial layer also increases the PH value of Ni-rich NMC cathodes, leading to the slurry gelation during electrode preparation.[60] On the other hand, the side reactions between liquid electrolytes and Ni-rich NMC cathodes also induce the phase reconstruction on the surface of Ni-rich NMC cathodes. In conventional liquid organic electrolytes, carbonate-

based solvents, such as ethylene carbonate (EC), diethylene carbonate (DEC), propylene carbonate (PC), dimethylene carbonate (DMC), and ethylmethyl carbonate (EMC), with the employment of $LiPF_6$ as Li^+ salt are widely used in LIBs.[61] The stable operational voltage windows of these solvents are less than 4.5 V vs Li/Li^+. Therefore, when these solvents couple with high-energy cathode materials, the high charging cut-off voltage lead to the decomposition of liquid electrolytes, resulting in the formation of thick cathode electrolyte interphase (CEI) composed by the complex organic/inorganic compounds. The formed CEI layer in reverse react with Ni-rich NMC cathodes, leading to the surface phase reconstruction from layer structure to spinel-like phase even the inactive NiO-type rock-salt phase as shown in **Figure 2.2c**.[62]

2.3.3 Transition metal dissolution

In the liquid-based LIBs, transition metal (TM) dissolution is a big challenge particularly in the high-voltage LNMO cathodes.[63] Mn^{3+} are very easy to be formed during the high-temperature synthesis of LNMO cathodes. The formed Mn^{3+} tend to form both Mn^{4+} and Mn^{2+} by the disproportionation reaction during the charge-discharge process. Because of the soluble property, Mn^{2+} tend to dissolve into the liquid electrolyte and then migrating through the separator and depositing on the surface of anode. Mn^{2+} dissolution also facilitate the decomposition of liquid electrolyte, leading to the acceleration of side reactions during cycling. As a result, the structural degradation of LNMO happens at the surface, resulting in the cycling capacity decay of batteries.[64-65] Similarly, the dissolution of TM ions also results in the structural degradation in Ni-rich NMC cathodes. Compared to Co and Mn, Ni ions in Ni-rich NMC cathodes are easier to be dissolved in the liquid electrolytes, further confirming that Ni is extreme instability in layered NMC structure.[66]

2.4   Interfacial strategies for cathodes in liquid electrolytes

As discussed in the last part, layered Ni-rich NMC cathodes undergo the irreversible micro-structural evolution during the charge-discharge cycles. Furthermore, both the Ni-rich NMC cathodes and spinel high-voltage LNMO cathodes face the challenges of side

reactions with electrolytes, surface phase reconstruction, and TM dissolution. All of these issues are highly related to the interface instability with liquid electrolytes, leading to the severely degradation of performance of LIBs, such as the low capacity, poor cycling stability, and inferior rate capability. Accordingly, the strategies that can stabilize both the structure and interface of cathodes are very important for high-performance LIBs.

2.4.1 Novel synthetic control

It is a general comment that increasing the content of Ni in layered NMC cathodes is beneficial for the improvement of specific capacity but deteriorating for the cycling stability. Differently, Co in Ni-rich NMC cathodes contributes to the structural stability and Mn is helpful for the improvement of thermal stability.[67] To maximize the positive effects of Ni, Co, Mn in Ni-rich NMC cathodes, a series of novel structural design is development by the synthetic control. Constructing the core-shell structure is widely used to build a high-capacity core along with a high-stability shell. Such a design is to ensure that the shell has enough Li-ion and electronic conductivity, and the electrochemical active shell provides the high capacity.[68] However, the compatibility between core and shell materials is a big challenge. Compared to the core-shell structure, the concentration-gradient structure is an ideal solution to address the challenge core-shell method facing that.
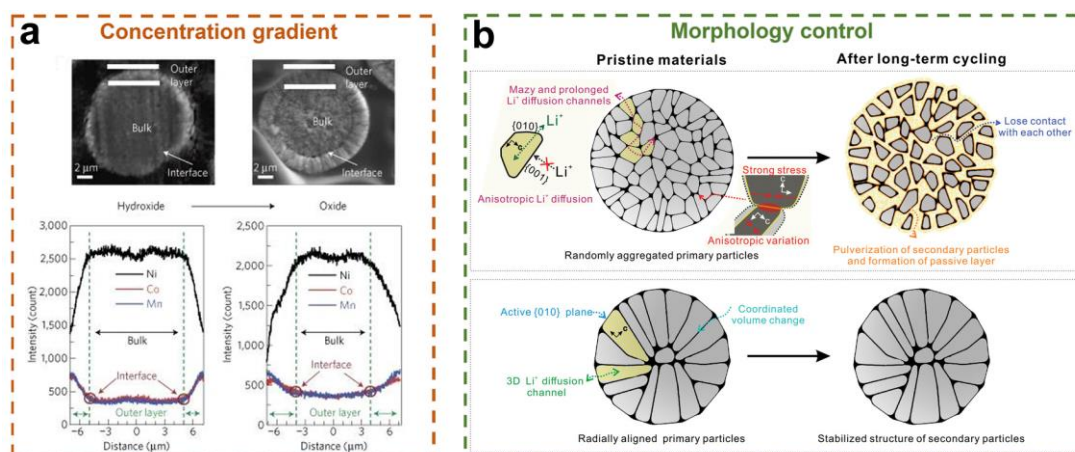
Figure 2.3 (a) SEM photograph and EPMA line scan of precursor hydroxide and the final concentration gradient Ni-rich NMC cathodes,[69] and (b) schematic illustration of the structure and characteristics of commercial NCM and RASC-NCM cathodes.[70]

Sun's group is the pioneer for the development of concentration-gradient strategy. For example, they first developed a Ni-rich NMC cathode with 80% Ni content in the bulk and increased the Co and Mn concentration at the surface.[68] The high Ni content in the bulk provided a high capacity, while high Co and Mn content at the surface enhanced the structural and thermal stabilities. As a result, this Ni-rich NMC cathode showed excellent cycling stability with a capacity retention of 97% after 500 charge-discharge cycles at a high current density of 1C. This work indicated that both the concentration and thickness of Mn and Co at the surface of Ni-rich NMC cathodes are critical for the electrochemical performance. To further improve the performance, Sun's group developed a full concentration-gradient Ni-rich NMC cathode with a gradual decreased Ni concentration from bulk to surface, as shown in **Figure 2.3a**.[69] In contrast, the concentration of Mn increased from the bulk to surface. Such a structure helped Ni-rich NMC cathode achieved an extreme stable cycling performance during the 1000 charge-discharge cycles at the current density of 1C.

In addition to the concentration-gradient structure, the morphology control by manipulating the primary particles is also beneficial for improving the performance of Ni-rich NMC cathodes. One of the biggest challenges in Ni-rich NMC cathodes is the

severe micro-cracks because of the anisotropic volume charge of primary particles with the random orientation. Xu et al. developed a Ni-rich NMC cathode with the radially aligned primary particles (as shown in **Figure 2.3b**).[70] At the surface, the electrochemical active (010) facets are exposed, therefore leading to the improved capability of lithium-ion transfer. Such radial structure also can mitigate the lattice distortion, therefore suppressed the micro-cracks while improved both the cycling stability and rate capability. Compared to the random oriented Ni-rich NMC cathode, the radial oriented one showed a long-term cycling stability with a capacity retention of 95% after 300 charge-discharge cycles and high-rate capacity of over 150 mAh g^{-1} at 5C.

2.4.2 Surface coating

Surface coating has been widely applied in the cathode materials to improve the performance because of its unique properties. Compared to other strategies, application of surface coating is considered as an effective method for providing a stable interface between cathode materials and liquid electrolytes. A series of coating materials have been applied, including metal oxides (Al_2O_3, ZnO, SiO_2, ZrO_2, Y_2O_3), fluorides (BiOF) and metal phosphates (Li_3PO_4, $FePO_4$).[71-77] These coating materials aim to prevent side reactions and dissolution of metal ions to improve performances.
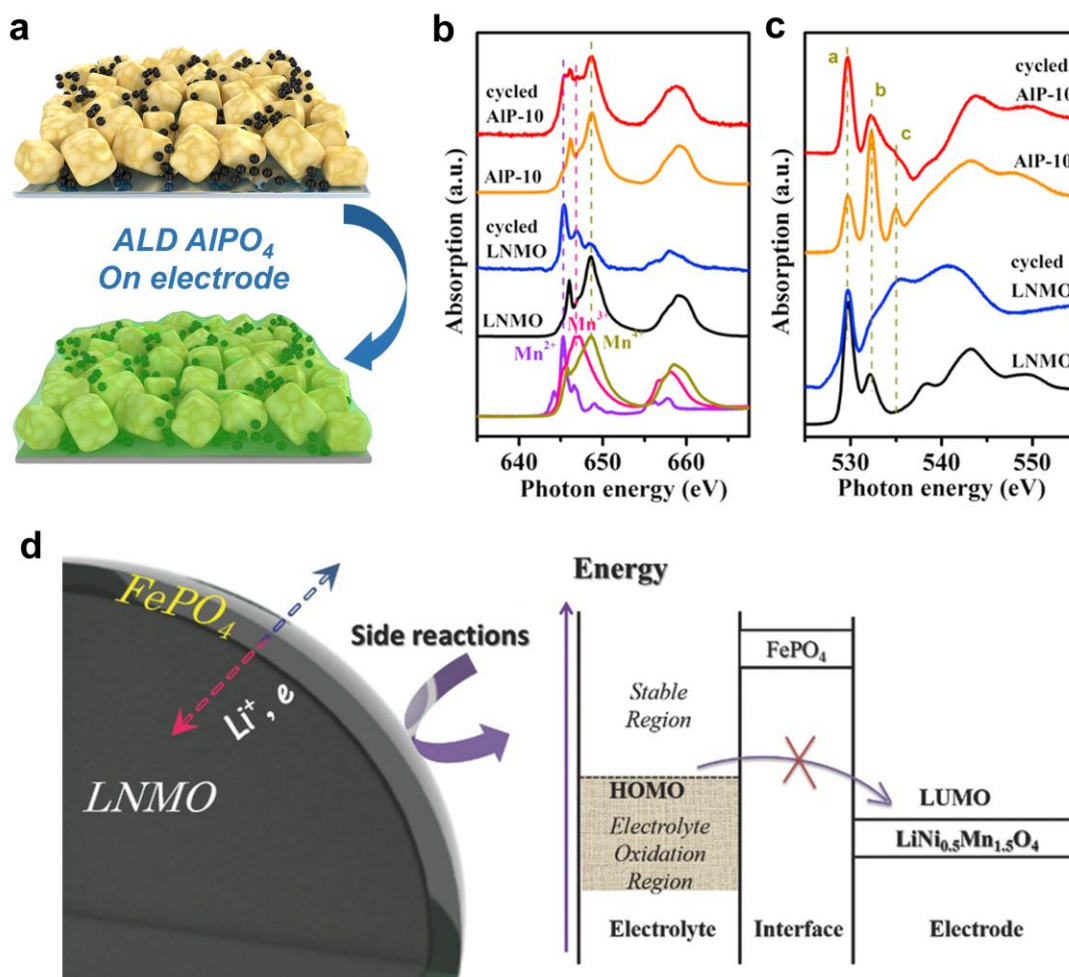
Figure 2.4 (a) Schematic illustration of ALD AlPO$_4$ coating on LNMO electrode, (b) XANES Mn L$_{3,2}$-edges spectra of AlP-10 and LNMO before and after cycling with standard MnO, Mn$_2$O$_3$, MnO$_2$ as references, (c) XANES O K-edges of AlP-10 and LNMO before and after cycling,[78] and (d) schematic illustrations of LNMO-*n* upon cycling and the electrolyte highest occupied molecular orbital (HOMO) and work functions of FePO$_4$ and LNMO cathode [83].

Our group has a long history working on the novel coatings for cathode materials. For example, our group developed an ultrathin AlPO$_4$ coating on high voltage LNMO electrodes via atomic layer deposition (ALD).[78] Unlike other surface modification methods, ALD is a novel coating technique used for the deposition of highly conformal and uniform layers with well controlled thickness.[79-82] Our study demonstrated that 10

ALD-cycles of $AlPO_4$ coating on LNMO has the best long cycling performance. It has been demonstrated that $AlPO_4$ coating layer was shown to effectively suppress dissolution of Mn and maintains the integral structure of LNMO. The ultrathin ALD $AlPO_4$ coating layer acts not only as a barrier layer to separate LNMO and electrolyte, but also transforms into a stable SEI layer during cycling, effectively preventing electrolyte decomposition and protecting LNMO structure during electrochemical reaction (as shown in **Figure 2.4a**). $FePO_4$ coating was also fabricated by ALD on high voltage LNMO cathode. By optimizing the thickness of $FePO_4$ coating, 10 ALD cycles showed the best rate capability while 40 ALD cycles can demonstrated the best cycling stability with a 100% capacity retention after 100 charge-discharge cycles at 0.5C. The ultrathin $FePO_4$ coating layer not only remaining Li^+ in the structure but also suppressed the reduction of Mn^{4+} to Mn^{2+} during the cycling, therefore alleviated the further dissolution of Mn^{2+} into the liquid electrolyte and retained the structural consistency at the surface of LNMO, as shown in **Figure 2.4b-c**.

2.4.3 Tailoring grain boundaries

Although coatings significantly eliminated the side reactions between Ni-rich NMC cathodes and liquid electrolytes, therefore improving the electrochemical performance, the primary particles and their grain boundaries are lack of protection. The structural degradation such as the intragranular and intergranular cracks at the grain boundaries also lead to the performance drop of Ni-rich NMC cathodes. Hence, developing the novel strategies to tailor the grain boundary is very necessary for Ni-rich NMC cathodes to achieve the comprehensive protection against the structural degradation at both the surface and bulk during the charge-discharge cycles.
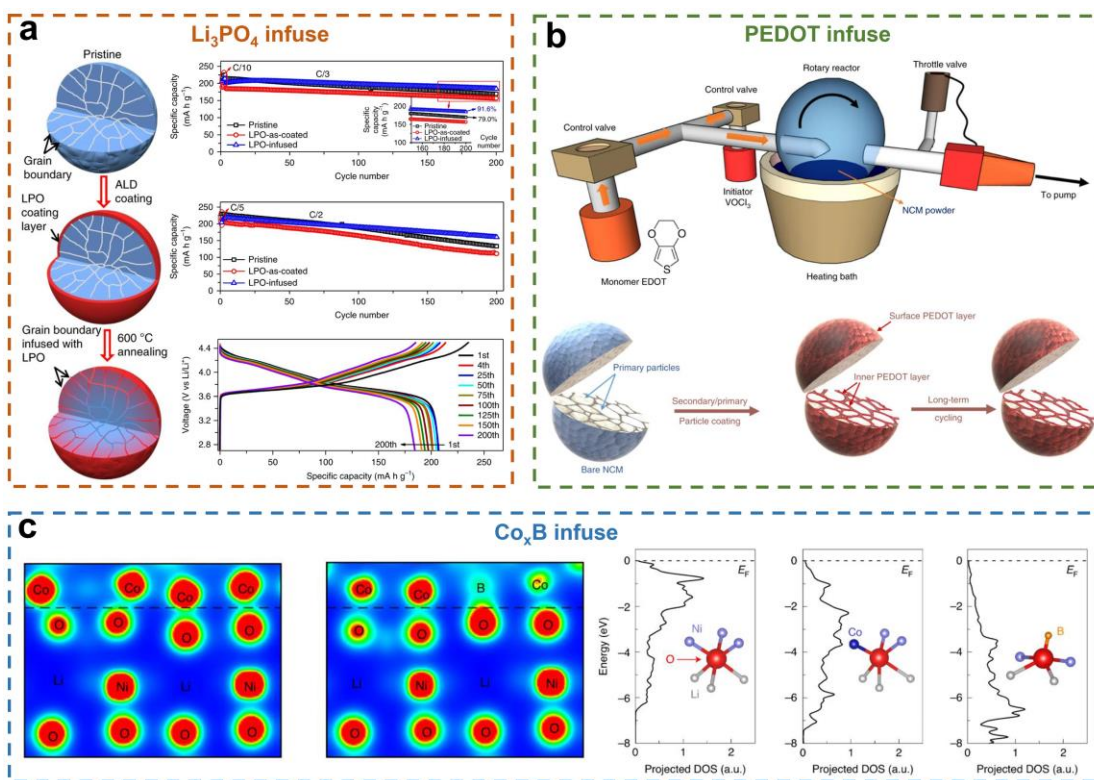
Figure 2.5 Strategies on tailoring grain boundaries of Ni-rich NMC cathodes. (a) Li_3PO_4 infuse,[84] (b) PEDOT infused,[85] and (c) Co_xB infuse.[86]

Zhang et al. developed a modification by infusing Li_3PO_4 solid electrolyte into the grain boundary of Ni-rich NMC cathode (as shown in **Figure 2.5a**).[84] Li_3PO_4 solid electrolyte was first coated on the surface of Ni-rich NMC cathode by advanced ALD and then infused into the grain boundaries by the post-annealing. The infused Li_3PO_4 at the grain boundaries significantly prevent the penetration of liquid electrolyte into the bulk structure of Ni-rich NMC cathode, therefore suppressing the intergranular cracks and formation of inactive rock-salt phase. As a result, the cycling stability is significantly improved with a capacity retention of 92% after 200 cycles. In addition to the inorganic lithium conductor, polymer-based materials with specific properties are also applied to tailor the grain boundaries of Ni-rich NMC cathodes. For example, PEDOT is fabricated by an oxidative chemical vapor deposition (oCVD) as a coating material (as shown in **Figure 2.5b**).[85] PEDOT was not only coated on the surface of secondary particles but also at the grain boundaries of primary particles. Similar as Li_3PO_4, PEDOT is able to

eliminate the side-reactions with liquid electrolyte and suppress the phase transition from the layer to inactive rock-salt. Differently, the novel oCVD method help PEDOT achieve a high electronic conductivity and an improved lithium-ion conductivity, therefore facilitate both the electrons and lithium ions transfer. More importantly, PEDOT is easy to coordinate HF by the formation of O-H-F covalent bonds. Hence, PEDOT is critical to stabilize the cathode electrolyte interface. When PEDOT was coated on the Ni-rich NMC cathode, the long-term cycling stability was significantly improved from 48% to 91% after 200 charge-discharge cycles at the current density of 1C. Recently, Cho et al. developed a metallic compound Co_xB as a complete coating/infusion strategy for Ni-rich NMC cathode (as shown in **Figure 2.5c**).[86] Because of the strong driving force during the chemical reaction at the interface, Co_xB was not only coated on the surface of secondary particles but also infused into the grain boundaries between primary particles. As a result, the modified Ni-rich NMC cathode demonstrated a superior performance with an impressive 95% capacity retention over 500 charge-discharge cycles in pouch cells. Such a complete coating/infuse strategy not only suppressed the microstructural degradation and side reactions but also enhanced the interfacial bonding between Co_xB and Ni-rich NMC cathode, therefore facilitating the performance and expanding the strategy of tailoring grain boundaries.

2.5 Challenges of cathodes in inorganic solid-state electrolytes

Compared to liquid organic electrolytes, inorganic solid-state electrolytes (SSEs) show different electrochemical and interfacial phenomenon. Briefly, there are four key challenges in inorganic solid-state batteries (SSBs): (1) the ionic conductivity of most SSEs is lower than that of liquid electrolytes. Although some sulfide electrolytes can achieve high ionic conductivity, but not stable at high voltage; (2) different from liquid electrolytes, the interfacial compatibility between solid electrolytes and cathodes is usually poor. The interfaces in an inorganic solid-electrolyte battery can be divided into two structures: the electrode-electrolyte interface and the inter-particle interface of SSEs or electrodes. Furthermore, the side-reaction occur with the contact between electrolyte and cathodes, leading to high resistance at the interface; (3) preventing Li dendrite

penetration is still challenging in SSBs, even for ceramic electrolytes with high mechanical strength; (4) the degradation mechanism is still not clear, which needs advanced characterization techniques to give help.

2.5.1 Challenges on microstructures

The electrochemical behaviors of ASSLIBs are very complicated, which are highly related to the properties of microstructures in composite cathode, including cathode materials, solid-state electrolytes (SEs), conductive agents, and binders. In the composite cathode, the movement of electrons and lithium-ions at the multi-phase interfaces are the key to achieve the high performance. Advanced modeling/computation is a very effective method to emulate the complex electrochemical phenomenon in ASSLIBs.
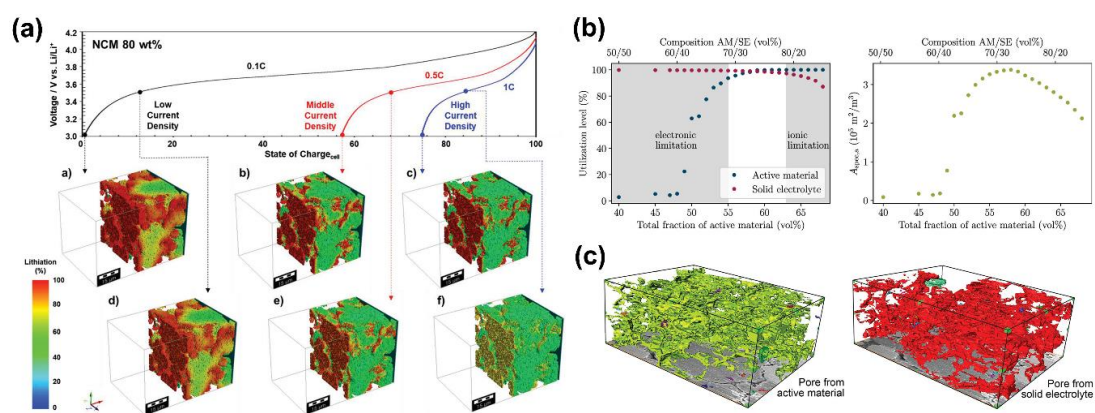
Figure 2.6 Challenges on microstructures in composite cathodes. (a) Lithiation stages during the different discharge voltages under the different current densities,[87] (b) utilization level of cathode material and SE and specific active interface area between the ionic and electronic conduction cluster,[88] and (c) 3D reconstructed rendering images of the decomposed pore structure derived from cathode material and SE.[89]

Lee et al. created a new formation process for a novel digital twin electrode to build the relationship between physical and electrochemical parameters and performance.[87] In the composite cathodes of sulfide based SSB, the electrode parameters, such the ratio of active cathode particles, specific contact area between Ni-rich NMC cathode and sulfide SE, electronic/ionic conductivities, and charge distribution in the composite

cathode, are critical for the performance of SSBs. The operando digital twin-driven experiment enabled visible analysis of state of charge (SOC) in the composite cathode composed by cathode material $LiNi_{0.70}Co_{0.15}Mn_{0.15}O_2$ (NMC70), sulfide SE Li_6PS_5Cl (LPSCl), and binder nitrile butadiene rubber (NBR). The results indicate that the SOC value in composite cathode is inversely proportional to the lithium-ion concentration, as shown in **Figure 2.6a**. After the full discharged, the lithiation state was well distributed and intercalated at the low current density compared to the middle or high current densities. In addition, the composite cathode with 70 wt% of NMC70 had more uniform lithium distribution and lithiation level than those of electrode with 80 wt% of NMC70. Moreover, the NMC70 particles closer to the LPSCl SE layer had sufficient effective electronic conductivity, therefore are more intercalated during the charge-discharge process. More importantly, the simulation results indicate that cathode materials are very hard to be lithiated/delithiated, resulting in the increasing of concentration over-potential because of the insufficient contact with sulfide SE.

Bielefeld et al. studied the effect of macroscopic parameters on electronic conductivity in carbon-free solid-state cathode.[88] The result suggests that cathode materials with small particles can offer higher active surface with SE, therefore are more favorable to form percolating electronic clusters. However, high active surface of cathode material may accelerate the side reactions with SE if the electrochemical stable window of SE is not enough wide to couple with high-energy cathodes, as shown in **Figure 2.6b**. Although high fractions of cathode materials in SSBs are beneficial for enhancing the connection of interfaces of cathode particle and achieving high energy-densities, ionic conductivity is the restriction in the composite cathode and negatively influence cell performance. In addition to the electronic/ionic conductivities, the ratio of pore network in composite cathode is also the critical parameter for the performance of SSBs. Choi et al. for the first time applied quantitative values of a 3D reconstruction structure to track the effect of pore structures in composite cathode.[89] The results show that when the volume ratio of SE and cathode material was similar, cathode material was much easier to form pore than SE because of their poor deformability, as shown in **Figure 2.6c**. Hence, when the high

fractions of cathode materials are applied, the performance of SSB is deteriorated by the pore formation in the composite cathode.

2.5.2 Challenges on materials
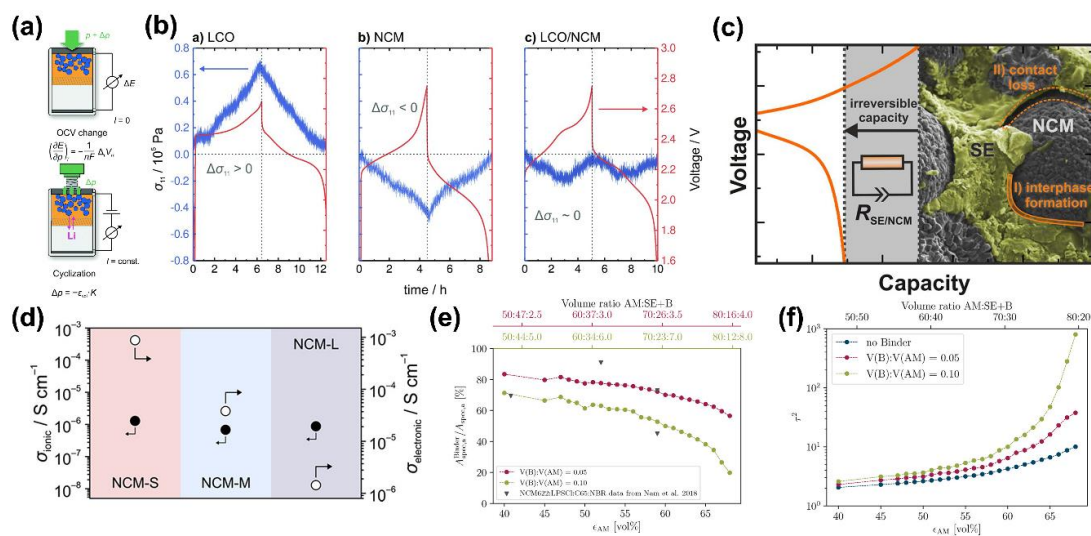
Figure 2.7 Challenges on materials in composite cathodes. (a) Schematic of the different experiments related to volume changes in composite cathode, (b) comparison of the stress response of different cathode materials,[90] (c) interface formation and contact loss between cathode material and SE,[91] (d) mean ionic and electronic partial conductivities of composite cathode using different cathodes with different particle sizes,[92] and influence of binder on (e) relative active interface area and (f) ionic tortuosity factors in composite cathode microstructures.[93]

In an inorganic SSB, the result of mechanical stress induced from cathode materials is different in batteries employing liquid electrolytes. In a liquid-based battery, mechanical stress produces and remains localized in the cathode particles and the stress does not transfer by liquid electrolyte. In contrast, mechanical stress produced from cathode material results in the local volume changes of SE. this stress has non-negligible effect on the performance of SSB. Janek et al. systematically compare the volume changes of different cathode materials occurring in SSBs and analyze their effects on performance.[90] The model cells are designed as shown in **Figure 2.7a**, using Li_3PS_4 and $Li_4Ti_5O_{12}$ as SE and anode, respectively, and coupled with different cathode

materials. The SSB using LCO as cathode shows a volume expansion during charging and then recover during the following discharge process. In contrast, when Ni-rich NMC cathode (here is NMC811) is applied as cathode, SSB exhibits a negative stress response (as shown in **Figure 2.7b**). When LCO and NMC811 were mixed with a 45 : 55 wt%, the composite cathode shows a two-step charge-discharge curve, corresponding to the lithiation/delithiation of LCO and NMC811, respectively. The overall stress response in this composite cathode is a reduced nominal stress. Different from the volume expanded LCO, volume change of Ni-rich NMC cathodes causes contact loss with SE, leading to the increase of interfacial resistance and performance drop. Koerver et al. investigate the cathode microstructure evolution by scanning electron microscopy (SEM), as shown in **Figure 2.7c**.[91] Before cycling, the composite cathode shows a close and intimate contact between the edges of NMC811 cathode and Li_3PS_4 SE. In contrast, NMC811 particles are observed with a severe contact loss with SE after cycling. Such a separation between cathode materials and SE leads to the increasing of dead space and high interfacial resistance, resulting in the electrode fracture and battery degradation.

In addition to the contact issues, particle size of cathode materials is also a critical factor that determining the performance of SSB. Strauss et al. select three types of Ni-rich NMC cathodes (NMC622).[92] The average particle sizes range from approximately 20 to 5 μm. When the as-prepared cathodes operated in liquid electrolyte, the initial capacities are almost same with a capacity of around 200 mAh g^{-1}. Differently, SSBs shows significant capacity drop associated with the increasing of particle size. The capacity of NCM-L (d50 = 15.6 μm) is only 84 mAh g^{-1}. From the results of ionic and electronic partial conductivities, NMC622 with three particle sizes shows similar ionic conductivity around 10^{-6} S cm^{-1}, which is primarily dominated by the SE. In contrast, the particle size of NMC622 has a significantly effect on the electronic conductivity in composite cathode, as shown in **Figure 2.7d**. The electronic conductivity of NCM-S is about 10^{-3} S cm^{-1}, which is three orders of magnitude than that of NCM-L. Hence, the capacity drop of NCM-L is mainly due to the low electronic conductivity.

Binder, as a processing-rooted properties, show a critical influence on ionic transport and active surface area in composite cathode. Bielefeld et al. study the influence of the binder in the effect ionic conductivity/tortuosity in composite cathode (as shown in **Figure 2.7e-f**).[93] On the one hand, ionic conductivity decreases with the increasing of volume ratio of cathode materials in composite cathode. On the other hand, the increasing of volume ratio of binder also causes the decreasing of ionic conductivity. Hence, minimizing the binder amount or suing an ion-conductive binder is critical for the large-scale processing in SSBs.

2.5.3 Challenges on interfaces
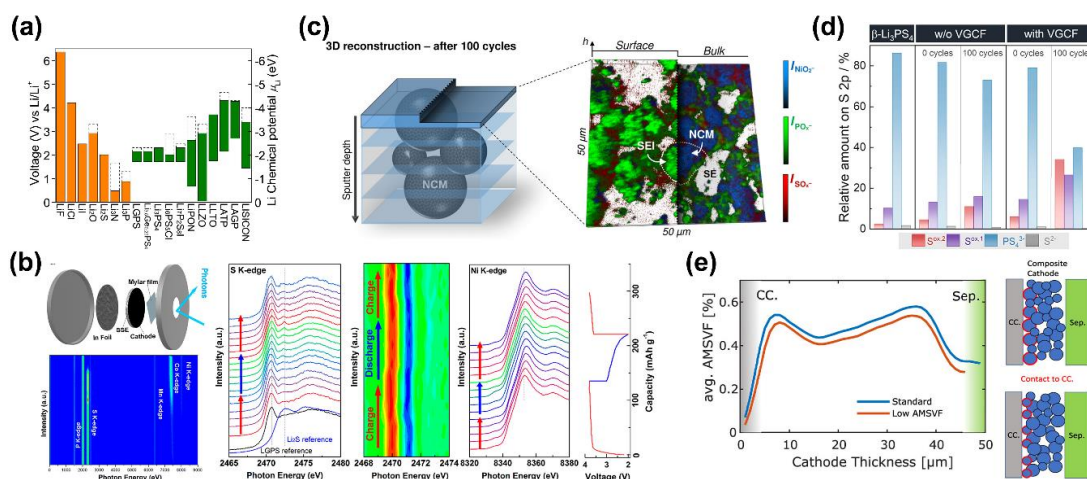
Figure 2.8 Challenges on interfaces in composite cathodes. (a) Electrochemical window of SEs,[94] (b) operando XANES study of SSB with NMC811 cathodes during cycling,[95] (c) three-dimensional reconstruction of the depth profile of the cycled composite cathode,[96] (d) comparison of the relative amounts of the S 2p components for the composite cathodes with and without carbon additives,[99] and (e) averaged layer theoretical active material solid volume fraction in composite cathode.[100]

In an inorganic ASSLIB, there are four interfaces in the composite cathode, including cathode/SE interface, carbon/SE interface, carbon/cathode/interface, and current collector interface. Stability of cathode interfaces is a big challenge for high-performance SSBs, particularly in sulfide-based SEs. Electrochemical stable window of SEs is a key factor

that determining the interfacial stability in SSBs. Mo et al. apply first-principles computation methods to investigate the electrochemical stability of sulfide-based SEs.[94] The results suggest that most of sulfide-based SEs have a limited electrochemical stable window and are easy to be oxidized when couple with high-energy cathodes, as shown in **Figure 2.8a**. For example, $Li_{10}GeP_2S_{12}$ (LGPS) starts to be delithiated and oxidized at 2.14 V vs. Li/Li^+. With increasing voltage to the equilibrium oxidation potential of 2.31 V, the final oxidation by-products are P_2S_5, GeS, and S. Similar as LGPS, most sulfide-based SEs, such as Li_3PS_4, Li_4GeS_4, $Li_7P_3S_{11}$, are easy to be oxidized to form S at 2.0-2.5 V. Although sulfide-based SEs are not thermodynamical stable at high voltages, the kinetic stability is good because that the decomposition reactions formed the stable decomposition interfaces with poor electronic transport.

In addition, the compatibility between high-energy cathodes and sulfide-based SEs is also critical for interfacial stability. In our study, operando X-ray absorption near-edge spectroscopy (XANES) combined with transmission electron microscopy (TEM) and electron energy loss spectroscopy (EELS) is employed to investigate the interfacial behavior between Ni-rich NMC cathode (NMC811) and sulfide-based SE (LGPS) (as shown in **Figure 2.8b**).[95] The results demonstrate a metastable intermediate state of LGPS at high voltage and parasitic reactions with NMC811 during the charge-discharge process, which leads to the surface structural reconstruction of NMC811. The by-product Li_2S is formed during the initial charging process at the SE side. During the following discharge process, the intermediate state cannot fully reverse back. At the same time, the parasitic reactions accelerate the microstructure degradation of NMC811 from the surface to bulk during cycling, leading to the microstructural cracks at the surface of cathode particles, surficial transition metal reduction of cathodes, and phase evolution from the layered to rock-salt structure. The parasitic reactions that occurred at both sulfide SSE and cathode sides are accumulated at the interface gradually and cut off the ionic conductivity, resulting in a large irreversible capacity and fast performance degradation. After long cycling, the interface between cathode and SE continues to degradation. Walther et al. provide a valuable insight into the interphase composition and microstructure evolution at cathode interface by applying time-of-flight secondary-ion

mass spectrometry (ToF-SIMS), as shown in **Figure 2.8c**.[96] When Ni-rich NMC cathode (NMC622) and Li_6PS_5Cl are applied in SSB, phosphates and sulfates are formed in the composite cathode after cycling. The results suggest that oxygen come from the cathode side. On the one hand, oxygen release from the cathode structure is one possible reason. On the other hand, residual lithium compounds, such as Li_2CO_3 and LiOH, on the surface of cathode materials are considered as the possible oxygen sources. As a result, the SSB shows a long-term capacity fading after 100 cycles, indicating the continue degradation of cathode interface.

The instability between Ni-rich cathodes and sulfide SEs leads to several side reactions at this interface. Cation inter-diffusion is observed at cathode/electrolyte interface with the diffusion of transition metals from cathodes and P, S from sulfide SEs. As simulated by Tateyama et al., the mixing of elemental Co and P is energetically preferable to the unmixed states at the cathode/SE interface.[97] In addition, cut-off voltages directly influence the formation of the cathode/SE interface. Janek et al. report that different cut-off charging voltages make NMC811/Li_3PS_4 SSB presenting different cycling performances.[98] A high cut-off voltage, over 4.3 V at charging state, results in a significant interfacial resistance due to the decomposition of sulfide SE, which severely impacts the performance. By using electrochemical impedance spectroscopy (EIS), the research demonstrates that cathode interfacial resistance is partially dependent on the state-of charge of the battery, corroborating the idea of a redox-active CEI layer. The formed interlayer highly increased electrochemical polarization of batteries during the charge-discharge process.

In addition to the interfacial stability between high-energy cathode and sulfide-based SEs, the stability of carbon related interfaces and current collector interface is also important to realizing high performance. For example, Zeier et al. study the influence of carbon as conductive additive on the degradation of a NMC622/Li_3PS_4 composite cathode (as shown in **Figure 2.8d**).[99] The results show that adding carbon increase the electronic conductivity in composite cathode, therefore increasing the utilization of cathode while accelerate the redox-active decomposition reactions. As a result, the SSB show a higher

discharge capacity at the initial charge-discharge cycle than the SSB without carbon. During the following long cycles, SSB with carbon additives show a dramatic capacity fading associated with the decomposition of Li_3PS_4. The formed by-products, such as sulfates/sulfites, phosphates, and polysulfides, are detected by ToF-SIMS. Compared to other interfaces, the current collector interface is always neglected and how the current collector affecting the performance of SSBs still needs to be deep studied. So far, only a simulation work speculated that the limited Li^+ and electronic conductivities between the current collector and composite cathode are the main reasons that causing capacity loss of SSBs especially at high current densities, as shown in **Figure 2.8e**.[100] Furthermore, the reduced contact between cathode layer and current collector is also an important factor that deteriorating the performance of SSBs.

2.6 Strategies of cathodes in inorganic solid-state electrolytes

2.6.1 Coating materials applied at interface

To address the challenges at cathode interfaces in SSBs, coating strategies are considered as the most prevailing method. Various novel coating materials have been developed along with the multi-functions. Because of the severe challenges at cathode interfaces, the following discussed coating strategies mainly focus on sulfide-based SSBs. Solid-solid interface in the composite cathode is a big obstacle for ionic transfer. Therefore, it is very important to make sure the close contact between cathode materials and SEs.
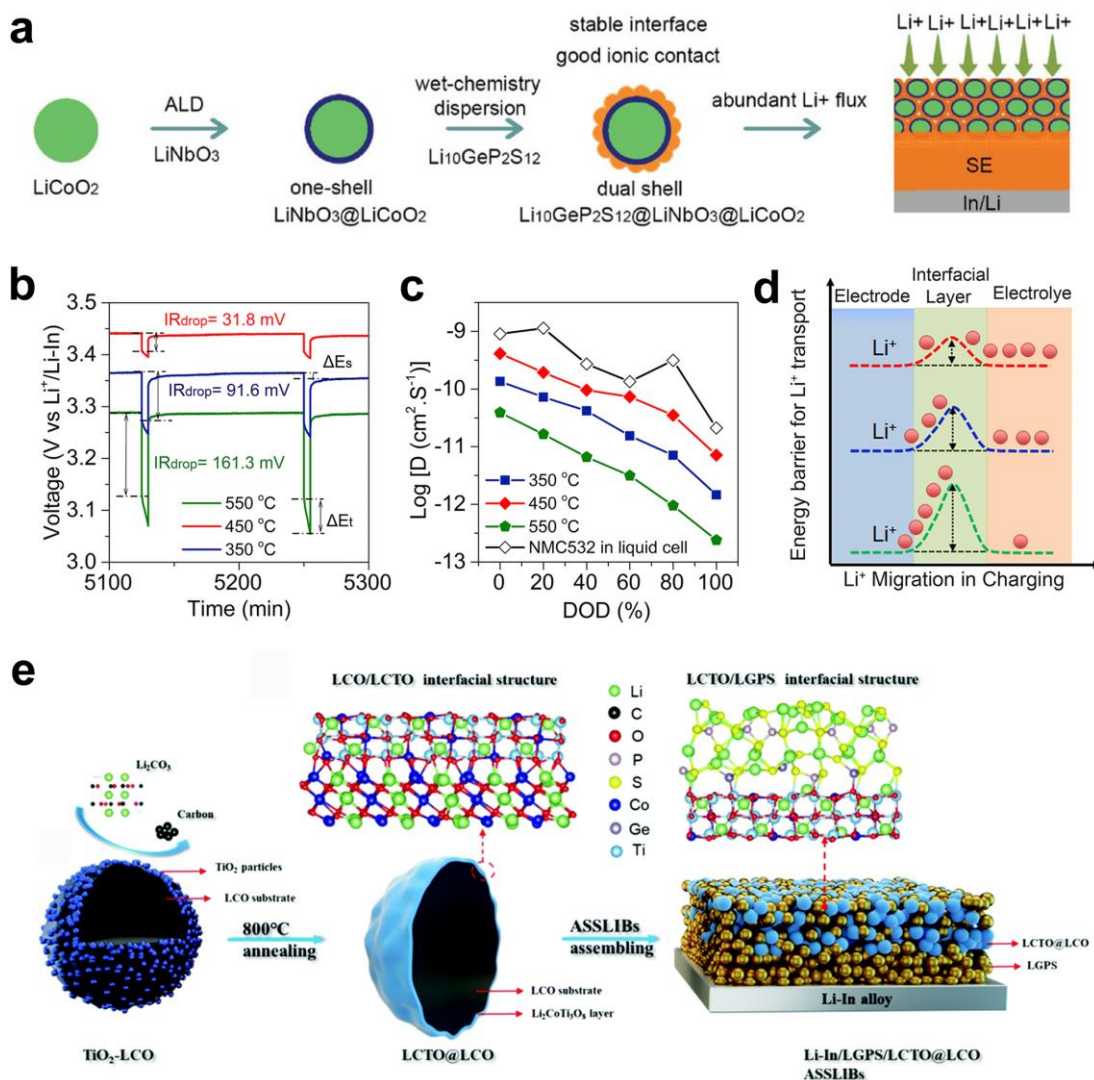
Figure 2.9 Coating strategies for cathode materials in sulfide SSBs. (a) Schematic diagram of ASSLIBs with a dual shell LGPS@LNO@LCO interfacial nanostructure,[102] (b-d) manipulating Li$^+$ transport kinetics of coating layer,[109] and (e) a schematic flowchart to show the in situ formation of the LCTO coating layer on the LCO core.[111]

Applying SE coating on the surface of cathode materials aims to build an intimate contact between cathode materials and SEs. For example, Tatsumisago et al. report a structure of composite cathode, in which LCO particles are closely packed in the composite cathode, while a Li$_2$S-P$_2$S$_5$ (LPS) SE coating occupied the interface around LCO particles.[101]

The post hot-press treatment further enhance the contact between LCO and LPS. As a result, SE-coated LCO shows a much-improved capacity than the cathode without SE coating. Our group develops a dual shell interfacial nanostructure to modify composite cathode.[102] The inner shell constructed by $LiNbO_3$ is devised to suppress the interfacial reactions and lithium-deficient space-charge layer (SCL) between LCO and sulfide-based LGPS SE. The outer shell LGPS coating realized by a universal wet-chemistry dispersion process enables the full utilization and negligible polarization of LCO in sulfide-based SSBs, as shown in **Figure 2.9a**. As a result, the dual shell structured composite cathode shows a high initial specific capacity of 125.8 mAh g^{-1} with an initial Coulombic efficiency of 90.4% at 0.1 C and 87.7 mAh g^{-1} at 1 C. More importantly, charge-discharge curves of the dual shell structured cathode exactly match the counterpart in liquid electrolytes, suggesting the negligible polarization and complete utilization of LCO. Accordingly, coating of a highly conductive SE on cathode particles is a promising technique to form an effective solid-solid interface and ionic transfer in composite cathodes.

It should be noted that although SE-coating can make an intimate contact between cathode materials and SEs, side-reaction at the cathode/SE interface cannot avoid by this strategy. Thereby, other functional coating materials have also been developed to further improve the interfacial stability between cathodes and SEs. Shin et al. develop a Li_2CO_3 coating for LCO via a lithium hydroxide solution method.[103] Li_2CO_3 coated LCO exhibits an enhanced rate capability under all current densities. Particularly, 4 wt% Li_2CO_3 coated LCO exhibits an enhanced discharge capacity of 137.4 mAh g^{-1} at 0.05 C. However, due to the low ionic conductivity of Li_2CO_3, the cycling performance at higher current densities is limited and needs further optimization of coating to obtain homogeneous distribution of Li_2CO_3. ALD, as a novel thin-film fabrication technique, is very suitable for applying in the interfacial modification in SSBs. Because of the ultrathin and conformal feature of ALD thin film, the developed coating can maintain well Li-ion diffusion ability and well protection of cathode from side-reactions at the same time. Lee et al. fabricate ALD coated LCO applied in sulfide-based SSBs.[104] ALD Al_2O_3 layer effectively suppresses side-reaction between LCO and $Li_{3.15}Ge_{0.15}P_{0.85}S_4$ SE, therefore

reducing the formation of unwanted interfacial layer that causing the capacity fade during cycling.

In addition to inactive coating materials as a physical barrier between cathode materials and SEs, advanced ionic conductive coatings are developed in SSBs. These coating materials are proposed to have the following features: (1) good ionic conductivity and (2) well compatibility with both cathode materials and SEs as a buffer layer to avoid side reactions. Lithium metal oxides, such as $LiNbO_3$, $LiAlO_2$, Li_3PO_4, are the most prevailing coating materials for cathodes. For instance, Kanno et al. report a bulk type 5 V-class all solid-state battery, in which $LiNbO_3$ coated LNMO is used as cathode.[105] $LiNbO_3$ coating layer not only suppresses side reactions between LNMO and LGPS SE at high charge-discharge voltage over 4.5 V vs. Li/Li^+ but also provides a pathway for lithium-ion diffusion.

Furthermore, Zhang et al. report a double buffer layer strategy, which a thick and active buffer layer is at the inner of cathode particle and a thin and inactive buffer layer is deposited at the outer layer.[106] During the synthesis process, an Al-rich shell $LiNi_{0.6}Co_{0.15}Al_{0.25}O_2$ (NCA) was first synthesized on the surface of Ni-rich core $LiNi_{0.85}Co_{0.15}O_2$ to form a core-shell structure. Because of similar potential, active NMA shell can significantly suppress interfacial resistance and space-charge effect. Then, a thin and inactive $LiNbO_3$ buffer layer was coated on the surface of core-shell cathode. The thin $LiNbO_3$ layer is beneficial for the lithium-ion diffusion, therefore further suppresses the space-charge effect. As a result, the coated Ni-rich NMC cathode with a double buffer layer shows a high cycling capacity and rate capability. The promising performance indicates that novel double buffer layer strategy is an effective approach to stabilize the cathode interface in sulfide-based SSBs. In addition to $LiNbO_3$ coating, many other ionic conductive coatings have also been investigated in sulfide-based SSBs. Tatsumisago et al. report a Li_3PO_4 thin-film coating by PLD method to fabricate a well-defined cathode/SE interface.[107] Because of its wider electrochemical window and higher thermodynamic stability, Li_3PO_4 coating layer can suppress side reactions between sulfide SE and LCO cathode and the formation of undesirable cathode interfacial layer.

Moreover, amorphous SE thin films Li_4SiO_4, $Li_{3.5}Si_{0.5}P_{0.5}O_4$, Li_3PO_4, $Li_{3.5}Ge_{0.5}P_{0.5}O_4$, and Li_4GeO_4 were also developed via PLD strategy with a KrF excimer laser.[108] The ionic conductivity of $Li_{3.5}Si_{0.5}P_{0.5}O_4$ thin film was reported to 1.6×10^{-6} S cm^{-1} at room temperature, which shows a promising application as coating layer in sulfide SSBs. $Li_{3.5}Si_{0.5}P_{0.5}O_4$ coated LCO shows an obvious decreased interfacial resistance, resulting in the improve capacity and cycling stability. Recently, our group applied a sol-gel method to synthesize $LiNb_{0.5}Ta_{0.5}O_3$ (LNTO) as coating layer and manipulate the interfacial ionic conductivity by tuning post-annealing temperatures.[109] The results indicate that the Ni-rich NMC cathode (NMC532) coated with low Li$^+$-conductive LNTO interfacial layer shows a low Li$^+$ diffusivity of 1.11×10^{-11} cm^2 s^{-1}. In contract, when high Li$^+$-conductive LNTO coated on the surface of NMC532, cathode ionic conductivity increases to 1.36×10^{-10} cm^2 s^{-1} (as shown in **Figure 2.9b-d**). Our results suggest that enhancing the interfacial ionic conductivity of the coating layer can significantly boost lithium-ion transfer at the cathode/SE interface, therefore significantly improving the performance. LNTO coated NMC532 with high ionic conductivity exhibits a high initial discharge capacity of 152 mAh g^{-1} at 0.1 C and 107.5 mAh g^{-1} at 1 C at room temperature.

Considering the complexity of cathode/SE interface, hybrid coatings with muti-functions have also been developed. Jung et al. design a dual composite Li_3BO_3-Li_2CO_3 (LBCO) coated LCO applied in sulfide-based SSBs via a scalable aqueous-solution protocol.[110] During synthesis process, aqueous LBO solution can convert the impurity Li_2CO_3 into LBCO, which has a high ionic conductivity of 6.0 10^{-7} S cm^{-1} at 30 °C. LBCO coated LCO shows the promising discharge capacities of 142 mA h g^{-1} and 94 mA h g^{-1} at 0.2 C and 2 C, respectively. In contrast, the bare LCO only exhibits the discharge capacities of 107 mA h g^{-1} and 18 mA h g^{-1} at the same current densities. The hybrid LBCO coating not only prevents the side reactions occurrence and the formation of by-products Co_3S_4, but also effectively passivates the cathode/SE interface by alternatively forming phosphate-based phases. Wang et al. develop an in-situ functional interface for LCO by a high temperature annealing method.[111] By the chemical reaction between LCO and TiO_2, a highly pure $Li_2CoTi_3O_8$ (LCTO) interfacial layer is formed on the surface of LCO,

as shown in **Figure 2.9e**. Carbon and Li_2CO_3 are acted as critical additives to regulate this reaction. The ultrathin LCTO layer with the thickness of 1.5 nm is formed with a stable 3D network of spinel structures, therefore has a high ionic conductivity of 8.2 10^{-7} S cm^{-1} and relatively low electronic conductivity of 2.5 10^{-8} S cm^{-1}. LCTO layer as a stable interphase shows the excellent thermodynamical and electrochemical stabilities, therefore significantly suppressing the formation of undesirable interface. More importantly, DFT calculations suggest that LCTO exhibits higher interfacial affinity with both LCO cathode and LGPS SE than the LCO/LGPS interface. As a result, LCTO coated LCO cathode shows a significantly improved cycling stability with a 83% capacity retention after 200 cycles at 0.1 C, which is much higher than the bare LCO delivering a 22% capacity retention.

2.6.2 Novel electrode structure fabrication

To overcome the challenges of interface between cathode materials and sulfide-based SEs, many novel electrode structures and fabrication methods have been developed, aiming to build a compact cathode/SE interface and realizing application of SSBs at pouch cell level. In conventional liquid LIB fabrication, a slurry process is adopted to mixing cathode materials, conductive additives, and binders. To realizing the similar electrode process, selection of suitable solutions, optimization of precursors, removing the binders, and constructing free-standing structures are four critical electrode strategies in sulfide-based SSBs.
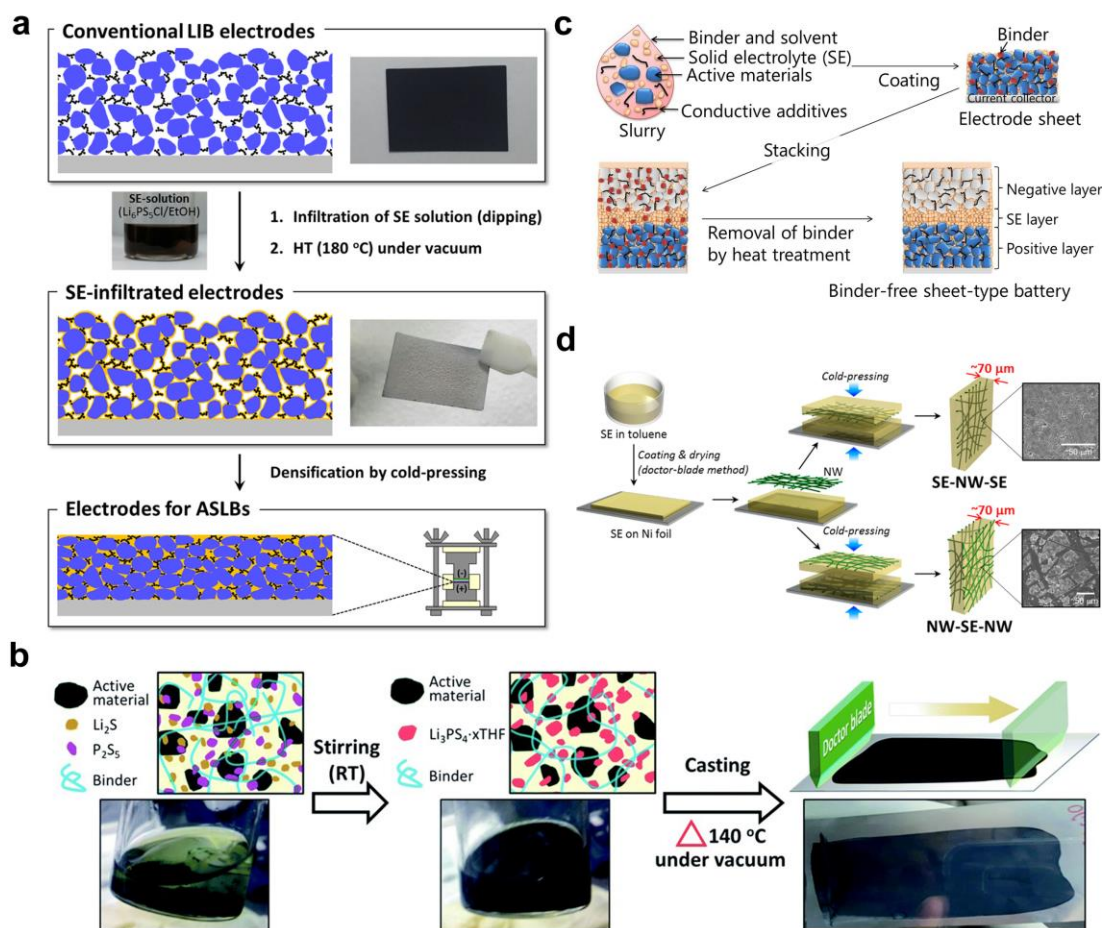
Figure 2.10 Construction of the novel electrode structures. (a) The infiltration of conventional LIB composite electrodes with solution-processable SEs,[118] (b) sheet-type composite electrodes prepared from SE precursors via a single-step wet-chemical route,[119] (c) the fabrication process for binder-free sheet-type SSBs,[120] and (d) the fabrication of bendable sulfide NW-SE films with two different structures.[113]

In most developed sulfide-based solid-state model cells, the fabrication process is in a dry condition, in which cathode materials, SEs, and carbon additives are mixed and pressured to form a think pellet.[112-114] This method is very hard for scale-up. To fabricating large roll-to-roll processable sheet-type electrodes, a wet-process using liquid solvents to dissolve the polymeric binders is a necessary step. However, almost all the sulfide SEs have the severe reactions with polar solvents, which are widely used in the conventional liquid LIBs.[115] Hence, the selection of solvents to fabricating the sheet-type electrodes

in sulfide-based SSBs is a big challenge that limiting to a few candidates. The nonpolar or very less polar aprotic solvents such as toluene and xylene are the few available choices.[116-117] To overcome the above challenges, Jung et al. develop a simple solution process that infiltrate the sulfide SEs into conventional LIB electrodes.[118] The LIB electrodes were prepared by a conventional casting process, in which a slurry composed by LCO cathode, PVDF binder, and NMP solvent is homogeneously spread on the surface of Al foil. Following, the as-prepared LIB electrodes were infiltrated with the EtOH-based LPSCl solution by a dip-coating method, as shown in **Figure 2.10a**. Removing solvents and the cold-pressing processes are two necessary steps to form the final sheet-type electrode. This infiltration process achieved an intimate ionic contact between LCO cathode and LPSCl SE, resulting in a high reversible capacity of 141 mA h g^{-1} at 0.1 C. Furthermore, Jung et al. develop the first single-step fabrication of sheet-type composite cathode for sulfide-based SSB (as shown in **Figure 2.10b**).[119] By using one-pot slurry method, cathode material NMC622 and polymeric binder nitrile-butadiene rubber (NBR) directly mixed with SE precursors (Li_2S and P_2S_5) instead of SEs. This one-pot wet-chemical route offered a significantly improved electrochemical performance for sulfide-based SSBs. The SSB with NMC622 cathode shows a high capacity of 140 mA h g^{-1} at 0.2 C and the enhanced rate capability of over 80 mA h g^{-1} at 1 C.

Although binders are important for fabricating sheet-type SSBs, the increasing of internal resistance from binders deteriorates the electrochemical performance. Hence, developing binder-free sheet-type electrode is critical important. Yamamoto et al. develop a binder-free strategy by removing binder by heat treatment process (as shown in **Figure 2.10c**).[120] By using poly(propylene carbonate) (PPC) as dispersant and binder, ionic conductivity of sulfide SE maintained at the same level as dry process. As a result, the binder-free electrode shows a stable cycling performance with an initial capacity of 149 mA h g^{-1} and 83.9% capacity retention after 175 cycles at 0.17 C. In addition to the sheet-type electrode design, constructing free-standing and stackable electrodes are considered as a promising strategy for high energy and high performance SSBs. Jung et al. report the first free-standing sulfide SE film applied in SSBs (as shown in **Figure 2.10d**).[113] The

fabrication process started with coating the sulfide SE slurry on the Ni foil by using the doctor-blade method. After that, SE-coated Ni foil was cold-pressed onto the nonwoven (NW) substrate. By using pressing process, SE layer transferred from the Ni foil to the NW substrate because of the better adhesion of SE layer to the NW substrate than the Ni foil. The as-prepared free-standing electrode has many outstanding properties, such as a mass loading of ∼5.7 mg cm^{-2} and 70 μm thick. Moreover, the free-standing film shows a good ionic conductivity of 0.20 mS cm^{-1}, which provides sufficient lithium-ion pathways formed in SE materials. As a result, when the free-standing SE film coupled with LCO cathode and $Li_4Ti_5O_{12}$ anode, the SSB shows an excellent rate capability. Even at the ultrahigh current density of 29 C, SSB still delivered a discharge capacity of over 32 mA h g^{-1}.

2.6.3 Manipulation of electronic conductivity
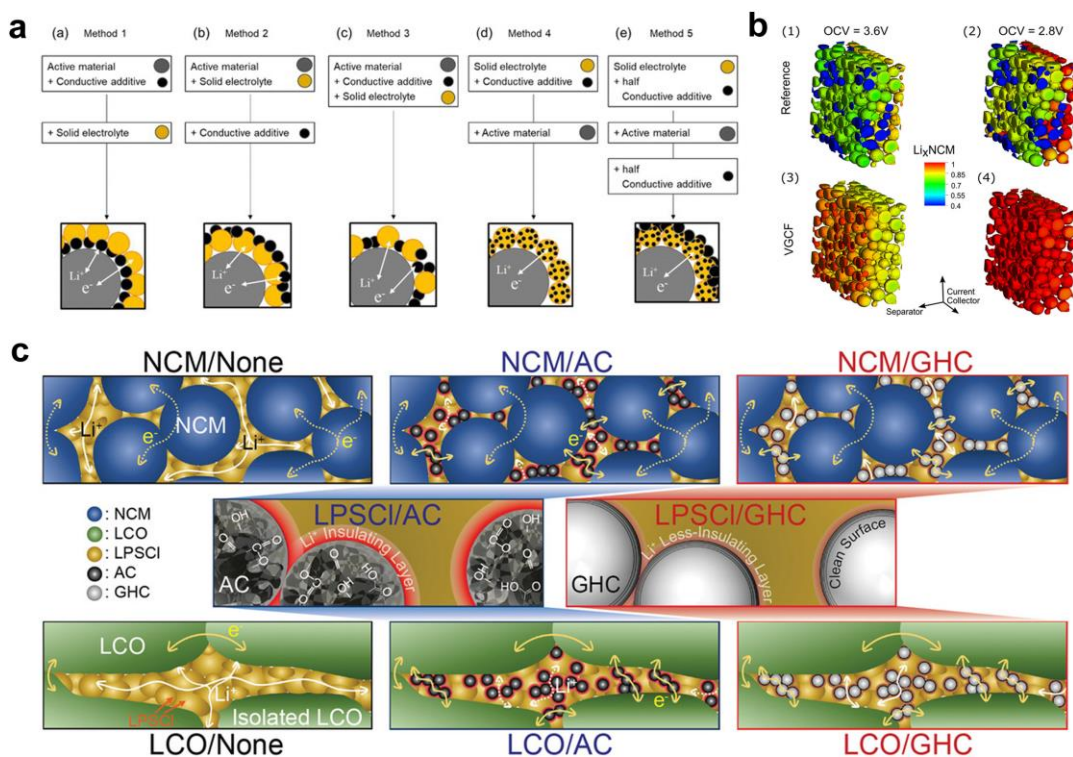
Figure 2.11 Strategies on carbon additives. (a) Protocols for the five different mixing methods along with the anticipated microstructures of the resulting composite cathodes,[121] (b) lithium concentration distribution for the electrode with and without

carbon at different voltages,[122] and (c) three situations that occur on the cathode/SE interface in two representative NCM and LCO cathode systems after long cycles.[123]

Electronic conductivity in composite cathodes is critical for the rate capability in sulfide-based SSBs. Noh et al. investigate the mixing order effect of carbon additives in composite cathodes (as shown in **Figure 2.11a**).[121] Five different orders to mix cathode materials, SEs, and carbon additives are chosen along with the expected microstructures of composite cathodes. First three models bring the improved interfacial conductivities, including inner electronic conductivity/outer ionic conductivity, inner ionic conductivity/outer electronic conductivity, and mixing electronic conductivity. Model 4 pre-mixed the electronic/ionic conductivity and then mixed with cathode materials. Model 5 is an improvement of model 4, which has a pre-mixed electronic/ionic conductivity with an extra electronic conductivity at the outer layer. The electrochemical results indicate that pre-mixed electronic/ionic conductivity lower the interfacial resistance, therefore leading to higher discharge capacity. In contrast, inner ionic conductivity/outer electronic conductivity helps improve the electron pathway between cathode materials, resulting in higher rate capability. When combining two mixing methods, both the highest discharge capacity and best rate capability are achieved.

The morphology and surface area of carbon additives also show the critical influence on the performance of composite cathodes in sulfide-based SSBs (as shown in **Figure 2.11b**).[122] Without the carbon additives in composite cathode, the inhomogeneous distribution of lithium leading to the low electronic conductivity is a major limitation for the utilization of cathode materials. After adding vapor-grown carbon fiber (VGCF) in composite cathode, a homogeneous lithiation of electrode is observed starting from the separator and expending to the current collector. The result suggests that the electronic conductivity is no longer a limiting of poor rate capability in composite cathodes. Compared to other carbon additives with different surface areas and morphologies, the fibrous additives, such as VGCF, tend to form overlapping flexible networks and are uniformly distributed throughout the electrode during the electrode fabrication, therefore are suitable carbon candidates in composite cathodes. Moreover, carbon additives with a

fiber-like morphology result in the less decomposition of sulfide SEs because of their small surface area. In addition to the surface area effect on the decomposition of sulfide SEs, the functional group on carbon is an origin for causing negative effects on interfacial stability. Park et al. design a graphitic hollow nano-carbon (GHC) as carbon additives for the sulfide-based SSBs (as shown in **Figure 2.11c**).[123] The GHC with few surface functional groups significantly suppress the formation of undesired cathode interface and reduce the amount of by-products. More importantly, GHC SSB shows the reduced over-potentials and improved electrochemical performances because of the increasing of electronic conductivity in composite cathode.

2.7 References

(1) Scrosati, B. Challenge of portable power. *Nature* **1995,** *373* (6515), 557-558.

(2) Goodenough, J. B.; Kim, Y. Challenges for rechargeable Li batteries. *Chemistry of materials* **2010,** *22* (3), 587-603.

(3) Choi, J. W.; Aurbach, D. Promise and reality of post-lithium-ion batteries with high energy densities. *Nature Reviews Materials* **2016,** *1* (4), 1-16.

(4) Li, H. Practical evaluation of Li-ion batteries. *Joule* **2019,** *3* (4), 911-914.

(5) Xu, K. Electrolytes and interphases in Li-ion batteries and beyond. *Chemical reviews* **2014,** *114* (23), 11503-11618.

(6) Tarascon, J.-M.; Armand, M. Issues and challenges facing rechargeable lithium batteries. *Materials for sustainable energy: a collection of peer-reviewed research and review articles from Nature Publishing Group* **2011**, 171-179.

(7) Randau, S.; Weber, D. A.; Kötz, O.; Koerver, R.; Braun, P.; Weber, A.; Ivers-Tiffée, E.; Adermann, T.; Kulisch, J.; Zeier, W. G. Benchmarking the performance of all-solid-state lithium batteries. *Nature Energy* **2020,** *5* (3), 259-270.

(8) Liu, L.; Xu, J.; Wang, S.; Wu, F.; Li, H.; Chen, L. Practical evaluation of energy densities for sulfide solid-state batteries. *eTransportation* **2019,** *1*, 100010.

(9) Zhao, Q.; Liu, X.; Stalin, S.; Khan, K.; Archer, L. A. Solid-state polymer electrolytes with in-built fast interfacial transport for secondary lithium batteries. *Nature Energy* **2019,** *4* (5), 365-373.

(10) Zhu, Z.; Hong, M.; Guo, D.; Shi, J.; Tao, Z.; Chen, J. All-solid-state lithium organic battery with composite polymer electrolyte and pillar [5] quinone cathode. *Journal of the American Chemical Society* **2014,** *136* (47), 16461-16464.

(11) Lin, D.; Yuen, P. Y.; Liu, Y.; Liu, W.; Liu, N.; Dauskardt, R. H.; Cui, Y. A silica‐aerogel‐reinforced composite polymer electrolyte with high ionic conductivity and high modulus. *Advanced Materials* **2018,** *30* (32), 1802661.

(12) Duan, H.; Chen, W. P.; Fan, M.; Wang, W. P.; Yu, L.; Tan, S. J.; Chen, X.; Zhang, Q.; Xin, S.; Wan, L. J. Building an Air Stable and Lithium Deposition Regulable Garnet Interface from Moderate‐Temperature Conversion Chemistry. *Angewandte Chemie* **2020,** *132* (29), 12167-12173.

(13) Jiang, Z.; Wang, S.; Chen, X.; Yang, W.; Yao, X.; Hu, X.; Han, Q.; Wang, H. Tape‐Casting Li0. 34La0. 56TiO3 Ceramic Electrolyte Films Permit High Energy Density of Lithium‐Metal Batteries. *Advanced Materials* **2020,** *32* (6), 1906221.

(14) Duan, H.; Zhang, J.; Chen, X.; Zhang, X.-D.; Li, J.-Y.; Huang, L.-B.; Zhang, X.; Shi, J.-L.; Yin, Y.-X.; Zhang, Q. Uniform nucleation of lithium in 3D current collectors via bromide intermediates for stable cycling lithium metal batteries. *Journal of the American Chemical Society* **2018,** *140* (51), 18051-18057.

(15) Kamaya, N.; Homma, K.; Yamakawa, Y.; Hirayama, M.; Kanno, R.; Yonemura, M.; Kamiyama, T.; Kato, Y.; Hama, S.; Kawamoto, K. A lithium superionic conductor. *Nature materials* **2011,** *10* (9), 682-686.

(16) Mizuno, F.; Hayashi, A.; Tadanaga, K.; Tatsumisago, M. New, highly ion‑conductive crystals precipitated from Li2S‑P2S5 glasses. *Advanced Materials* **2005,** *17* (7), 918-921.

(17) Seino, Y.; Ota, T.; Takada, K.; Hayashi, A.; Tatsumisago, M. A sulphide lithium super ion conductor is superior to liquid ion conductors for use in rechargeable batteries. *Energy & Environmental Science* **2014,** *7* (2), 627-631.

(18) Zhao, F.; Liang, J.; Yu, C.; Sun, Q.; Li, X.; Adair, K.; Wang, C.; Zhao, Y.; Zhang, S.; Li, W. A Versatile Sn‑Substituted Argyrodite Sulfide Electrolyte for All‑Solid‑State Li Metal Batteries. *Advanced Energy Materials* **2020,** *10* (9), 1903422.

(19) Jung, W. D.; Kim, J.-S.; Choi, S.; Kim, S.; Jeon, M.; Jung, H.-G.; Chung, K. Y.; Lee, J.-H.; Kim, B.-K.; Lee, J.-H. Superionic halogen-rich Li-argyrodites using in situ nanocrystal nucleation and rapid crystal growth. *Nano letters* **2020,** *20* (4), 2303-2309.

(20) Schlem, R.; Muy, S.; Prinz, N.; Banik, A.; Shao‑Horn, Y.; Zobel, M.; Zeier, W. G. Mechanochemical synthesis: a tool to tune cation site disorder and ionic transport properties of Li3MCl6 (M= Y, Er) superionic conductors. *Advanced Energy Materials* **2020,** *10* (6), 1903719.

(21) Wang, S.; Bai, Q.; Nolan, A. M.; Liu, Y.; Gong, S.; Sun, Q.; Mo, Y. Lithium Chlorides and Bromides as Promising Solid‑State Chemistries for Fast Ion Conductors with Good Electrochemical Stability. *Angewandte Chemie International Edition* **2019,** *58* (24), 8039-8043.

(22) Li, X.; Liang, J.; Luo, J.; Banis, M. N.; Wang, C.; Li, W.; Deng, S.; Yu, C.; Zhao, F.; Hu, Y. Air-stable Li 3 InCl 6 electrolyte with high voltage compatibility for all-solid-state batteries. *Energy & Environmental Science* **2019,** *12* (9), 2665-2671.

(23) Lee, W.; Muhammad, S.; Sergey, C.; Lee, H.; Yoon, J.; Kang, Y. M.; Yoon, W. S. Advances in the cathode materials for lithium rechargeable batteries. *Angewandte Chemie International Edition* **2020,** *59* (7), 2578-2605.

(24) Recham, N.; Chotard, J.-N.; Dupont, L.; Delacourt, C.; Walker, W.; Armand, M.; Tarascon, J.-M. A 3.6 V lithium-based fluorosulphate insertion positive electrode for lithium-ion batteries. *Nature materials* **2010,** *9* (1), 68-74.

(25) Lee, W.; Muhammad, S.; Kim, T.; Kim, H.; Lee, E.; Jeong, M.; Son, S.; Ryou, J. H.; Yoon, W. S. New insight into Ni‑rich layered structure for next‑generation Li rechargeable batteries. *Advanced Energy Materials* **2018,** *8* (4), 1701788.

(26) Rui, X.; Yan, Q.; Skyllas-Kazacos, M.; Lim, T. M. Li3V2 (PO4) 3 cathode materials for lithium-ion batteries: a review. *Journal of Power Sources* **2014,** *258*, 19-38.

(27) Wang, F.; Robert, R.; Chernova, N. A.; Pereira, N.; Omenya, F.; Badway, F.; Hua, X.; Ruotolo, M.; Zhang, R.; Wu, L. Conversion reaction mechanisms in lithium ion batteries: study of the binary metal fluoride electrodes. *Journal of the American Chemical Society* **2011,** *133* (46), 18828-18836.

(28) Kim, Y.; Yoo, J.; Jang, D.; Muhammad, S.; Jeong, M.; Choi, W.; Yoon, W.-S. Further utilization of a Mn redox reaction via control of structural disorder in olivine systems. *Journal of Materials Chemistry A* **2018,** *6* (28), 13743-13750.

(29) Lyu, Y.; Wu, X.; Wang, K.; Feng, Z.; Cheng, T.; Liu, Y.; Wang, M.; Chen, R.; Xu, L.; Zhou, J. An overview on the advances of LiCoO2 cathodes for lithium‑ion batteries. *Advanced Energy Materials* **2021,** *11* (2), 2000982.

(30) Abdollahifar, M.; Lannelongue, P.; Liu, H.-W.; Chen, H.; Liao, C.-H.; Sheu, H.-S.; Lee, J.-F.; Liao, Y.-F.; Wu, N.-L. Room-Temperature Synthesis of LiMn2O4 by Electrochemical Ion Exchange in an Aqueous Medium. *ACS Sustainable Chemistry & Engineering* **2021,** *9* (41), 13717-13725.

(31) Nie, Z.; Liu, Y.; Yang, L.; Li, S.; Pan, F. Construction and application of materials knowledge graph based on author disambiguation: revisiting the evolution of LiFePO4. *Advanced Energy Materials* **2021,** *11* (16), 2003580.

(32) Lin, J.; Sun, Y.-H.; Lin, X. Metal-organic framework-derived LiFePO4 cathode encapsulated in O, F-codoped carbon matrix towards superior lithium storage. *Nano Energy* **2022,** *91*, 106655.

(33) Ryu, H.-H.; Namkoong, B.; Kim, J.-H.; Belharouak, I.; Yoon, C. S.; Sun, Y.-K. Capacity fading mechanisms in ni-rich single-crystal ncm cathodes. *ACS Energy Letters* **2021,** *6* (8), 2726-2734.

(34) Chen, Y.-H.; Zhang, J.; Li, Y.; Zhang, Y.-F.; Huang, S.-P.; Lin, W.; Chen, W.-K. Effects of doping high-valence transition metal (V, Nb and Zr) ions on the structure and electrochemical performance of LIB cathode material LiNi 0.8 Co 0.1 Mn 0.1 O 2. *Physical Chemistry Chemical Physics* **2021,** *23* (19), 11528-11537.

(35) Cui, S.; Wei, Y.; Liu, T.; Deng, W.; Hu, Z.; Su, Y.; Li, H.; Li, M.; Guo, H.; Duan, Y. Optimized temperature effect of li‐ion diffusion with layer distance in Li (NixMnyCoz) O2 cathode materials for high performance Li‐ion battery. *Advanced Energy Materials* **2016,** *6* (4), 1501309.

(36) Xu, C.; Märker, K.; Lee, J.; Mahadevegowda, A.; Reeves, P. J.; Day, S. J.; Groh, M. F.; Emge, S. P.; Ducati, C.; Mehdi, B. L. Bulk fatigue induced by surface reconstruction in layered Ni-rich cathodes for Li-ion batteries. *Nature Materials* **2021,** *20* (1), 84-92.

(37) Dixit, M.; Markovsky, B.; Schipper, F.; Aurbach, D.; Major, D. T. Origin of structural degradation during cycling and low thermal stability of Ni-rich layered transition metal-based electrode materials. *The journal of physical chemistry C* **2017,** *121* (41), 22628-22636.

(38) Li, W.; Asl, H. Y.; Xie, Q.; Manthiram, A. Collapse of LiNi1–x–y Co x Mn y O2 Lattice at Deep Charge Irrespective of Nickel Content in Lithium-Ion Batteries. *Journal of the American chemical society* **2019,** *141* (13), 5097-5101.

(39) Sun, H.-H.; Manthiram, A. Impact of Microcrack Generation and Surface Degradation on a Nickel-Rich Layered Li[Ni0.9Co0.05Mn0.05]O2 Cathode for Lithium-

Ion Batteries. *Chemistry of Materials* **2017,** *29* (19), 8486-8493, DOI: 10.1021/acs.chemmater.7b03268.

(40) Wang, Y.-Y.; Wang, Y.-Y.; Liu, S.; Li, G.-R.; Zhou, Z.; Xu, N.; Wu, M.-T.; Gao, X.-P. Building the Stable Oxygen Framework in High-Ni Layered Oxide Cathode for High-Energy-Density Li-Ion Batteries. *ENERGY & ENVIRONMENTAL MATERIALS n/a* (n/a), DOI: https://doi.org/10.1002/eem2.12242.

(41) Kim, J.-H.; Pieczonka, N. P. W.; Yang, L. Challenges and Approaches for High-Voltage Spinel Lithium-Ion Batteries. *ChemPhysChem* **2014,** *15* (10), 1940-1954, DOI: https://doi.org/10.1002/cphc.201400052.

(42) Xu, X.; Deng, S.; Wang, H.; Liu, J.; Yan, H. Research Progress in Improving the Cycling Stability of High-Voltage LiNi0.5Mn1.5O4 Cathode in Lithium-Ion Battery. *Nano-Micro Letters* **2017,** *9* (2), 22, DOI: 10.1007/s40820-016-0123-3.

(43) Ma, J.; Hu, P.; Cui, G.; Chen, L. Surface and Interface Issues in Spinel LiNi0.5Mn1.5O4: Insights into a Potential Cathode Material for High Energy Density Lithium Ion Batteries. *Chemistry of Materials* **2016,** *28* (11), 3578-3606, DOI: 10.1021/acs.chemmater.6b00948.

(44) Liang, G.; Peterson, V. K.; See, K. W.; Guo, Z.; Pang, W. K. Developing high-voltage spinel LiNi0.5Mn1.5O4 cathodes for high-energy-density lithium-ion batteries: current achievements and future prospects. *Journal of Materials Chemistry A* **2020,** *8* (31), 15373-15398, DOI: 10.1039/D0TA02812F.

(45) Liu, D.; Hamel-Paquet, J.; Trottier, J.; Barray, F.; Gariépy, V.; Hovington, P.; Guerfi, A.; Mauger, A.; Julien, C. M.; Goodenough, J. B.; Zaghib, K. Synthesis of pure phase disordered LiMn1.45Cr0.1Ni0.45O4 by a post-annealing method. *Journal of Power Sources* **2012,** *217*, 400-406, DOI: https://doi.org/10.1016/j.jpowsour.2012.06.063.

(46) Hu, M.; Pang, X.; Zhou, Z. Recent progress in high-voltage lithium ion batteries. *Journal of Power Sources* **2013,** *237*, 229-242, DOI: https://doi.org/10.1016/j.jpowsour.2013.03.024.

(47) Song, J.; Shin, D. W.; Lu, Y.; Amos, C. D.; Manthiram, A.; Goodenough, J. B. Role of Oxygen Vacancies on the Performance of Li[Ni0.5–xMn1.5+x]O4 (x = 0, 0.05, and 0.08) Spinel Cathodes for Lithium-Ion Batteries. *Chemistry of Materials* **2012,** *24* (15), 3101-3109, DOI: 10.1021/cm301825h.

(48) Liang, G.; Didier, C.; Guo, Z.; Pang, W. K.; Peterson, V. K. Understanding Rechargeable Battery Function Using In Operando Neutron Powder Diffraction. *Advanced Materials* **2020,** *32* (18), 1904528, DOI: https://doi.org/10.1002/adma.201904528.

(49) Sheptyakov, D.; Boulet-Roblin, L.; Pomjakushin, V.; Borel, P.; Tessier, C.; Villevieille, C. Stroboscopic neutron diffraction applied to fast time-resolved operando studies on Li-ion batteries (d-LiNi0.5Mn1.5O4vs. graphite). *Journal of Materials Chemistry A* **2020,** *8* (3), 1288-1297, DOI: 10.1039/C9TA11826H.

(50) Liang, G.; Wu, Z.; Didier, C.; Zhang, W.; Cuan, J.; Li, B.; Ko, K.-Y.; Hung, P.-Y.; Lu, C.-Z.; Chen, Y.; Leniec, G.; Kaczmarek, S. M.; Johannessen, B.; Thomsen, L.; Peterson, V. K.; Pang, W. K.; Guo, Z. A Long Cycle-Life High-Voltage Spinel Lithium-Ion Battery Electrode Achieved by Site-Selective Doping. *Angewandte Chemie International Edition* **2020,** *59* (26), 10594-10602, DOI: https://doi.org/10.1002/anie.202001454.

(51) Yan, P.; Zheng, J.; Gu, M.; Xiao, J.; Zhang, J.-G.; Wang, C.-M. Intragranular cracking as a critical barrier for high-voltage usage of layer-structured cathode for lithium-ion batteries. *Nature Communications* **2017,** *8* (1), 14101, DOI: 10.1038/ncomms14101.

(52) Xu, Y.; Hu, E.; Zhang, K.; Wang, X.; Borzenets, V.; Sun, Z.; Pianetta, P.; Yu, X.; Liu, Y.; Yang, X.-Q.; Li, H. In situ Visualization of State-of-Charge Heterogeneity

within a LiCoO2 Particle that Evolves upon Cycling at Different Rates. *ACS Energy Letters* **2017,** *2* (5), 1240-1245, DOI: 10.1021/acsenergylett.7b00263.

(53) Min, K.; Cho, E. Intrinsic origin of intra-granular cracking in Ni-rich layered oxide cathode materials. *Physical Chemistry Chemical Physics* **2018,** *20* (14), 9045-9052, DOI: 10.1039/C7CP06615E.

(54) Ahmed, S.; Pokle, A.; Schweidler, S.; Beyer, A.; Bianchini, M.; Walther, F.; Mazilkin, A.; Hartmann, P.; Brezesinski, T.; Janek, J.; Volz, K. The Role of Intragranular Nanopores in Capacity Fade of Nickel-Rich Layered Li(Ni1–x–yCoxMny)O2 Cathode Materials. *ACS Nano* **2019,** *13* (9), 10694-10704, DOI: 10.1021/acsnano.9b05047.

(55) Ryu, H.-H.; Park, K.-J.; Yoon, C. S.; Sun, Y.-K. Capacity Fading of Ni-Rich Li[NixCoyMn1–x–y]O2 ($0.6 \leqslant x \leqslant 0.95$) Cathodes for High-Energy-Density Lithium-Ion Batteries: Bulk or Surface Degradation? *Chemistry of Materials* **2018,** *30* (3), 1155-1163, DOI: 10.1021/acs.chemmater.7b05269.

(56) Lee, S.-Y.; Park, G.-S.; Jung, C.; Ko, D.-S.; Park, S.-Y.; Kim, H. G.; Hong, S.-H.; Zhu, Y.; Kim, M. Revisiting Primary Particles in Layered Lithium Transition-Metal Oxides and Their Impact on Structural Degradation. *Advanced Science* **2019,** *6* (6), 1800843, DOI: https://doi.org/10.1002/advs.201800843.

(57) Wang, D.; Kou, R.; Ren, Y.; Sun, C.-J.; Zhao, H.; Zhang, M.-J.; Li, Y.; Huq, A.; Ko, J. Y. P.; Pan, F.; Sun, Y.-K.; Yang, Y.; Amine, K.; Bai, J.; Chen, Z.; Wang, F. Synthetic Control of Kinetic Reaction Pathway and Cationic Ordering in High-Ni Layered Oxide Cathodes. *Advanced Materials* **2017,** *29* (39), 1606715, DOI: https://doi.org/10.1002/adma.201606715.

(58) Jo, J. H.; Jo, C.-H.; Yashiro, H.; Kim, S.-J.; Myung, S.-T. Re-heating effect of Ni-rich cathode material on structure and electrochemical properties. *Journal of Power Sources* **2016,** *313*, 1-8, DOI: https://doi.org/10.1016/j.jpowsour.2016.02.015.

(59) Cho, D.-H.; Jo, C.-H.; Cho, W.; Kim, Y.-J.; Yashiro, H.; Sun, Y.-K.; Myung, S.-T. Effect of Residual Lithium Compounds on Layer Ni-Rich Li[Ni0.7Mn0.3]O2. *Journal of The Electrochemical Society* **2014,** *161* (6), A920-A926, DOI: 10.1149/2.042406jes.

(60) Park, J.-H.; Choi, B.; Kang, Y.-S.; Park, S. Y.; Yun, D. J.; Park, I.; Shim, J. H.; Park, J.-H.; Han, H. N.; Park, K. Effect of Residual Lithium Rearrangement on Ni-rich Layered Oxide Cathodes for Lithium-Ion Batteries. *Energy Technology* **2018,** *6* (7), 1361-1369, DOI: https://doi.org/10.1002/ente.201700950.

(61) Li, W.; Dolocan, A.; Oh, P.; Celio, H.; Park, S.; Cho, J.; Manthiram, A. Dynamic behaviour of interphases and its implication on high-energy-density cathode materials in lithium-ion batteries. *Nature Communications* **2017,** *8* (1), 14589, DOI: 10.1038/ncomms14589.

(62) Xu, C.; Märker, K.; Lee, J.; Mahadevegowda, A.; Reeves, P. J.; Day, S. J.; Groh, M. F.; Emge, S. P.; Ducati, C.; Layla Mehdi, B.; Tang, C. C.; Grey, C. P. Bulk fatigue induced by surface reconstruction in layered Ni-rich cathodes for Li-ion batteries. *Nature Materials* **2021,** *20* (1), 84-92, DOI: 10.1038/s41563-020-0767-8.

(63) Liu, T.; Dai, A.; Lu, J.; Yuan, Y.; Xiao, Y.; Yu, L.; Li, M.; Gim, J.; Ma, L.; Liu, J.; Zhan, C.; Li, L.; Zheng, J.; Ren, Y.; Wu, T.; Shahbazian-Yassar, R.; Wen, J.; Pan, F.; Amine, K. Correlation between manganese dissolution and dynamic phase stability in spinel-based lithium-ion battery. *Nature Communications* **2019,** *10* (1), 4721, DOI: 10.1038/s41467-019-12626-3.

(64) Browning, J. F.; Baggetto, L.; Jungjohann, K. L.; Wang, Y.; Tenhaeff, W. E.; Keum, J. K.; Wood, D. L.; Veith, G. M. In Situ Determination of the Liquid/Solid Interface Thickness and Composition for the Li Ion Cathode LiMn1.5Ni0.5O4. *ACS Applied Materials & Interfaces* **2014,** *6* (21), 18569-18576, DOI: 10.1021/am5032055.

(65) Alvarado, J.; Schroeder, M. A.; Zhang, M.; Borodin, O.; Gobrogge, E.; Olguin, M.; Ding, M. S.; Gobet, M.; Greenbaum, S.; Meng, Y. S.; Xu, K. A carbonate-free, sulfone-

based electrolyte for high-voltage Li-ion batteries. *Materials Today* **2018,** *21* (4), 341-353, DOI: https://doi.org/10.1016/j.mattod.2018.02.005.

(66) Ko, D.-S.; Park, J.-H.; Park, S.; Ham, Y. N.; Ahn, S. J.; Park, J.-H.; Han, H. N.; Lee, E.; Jeon, W. S.; Jung, C. Microstructural visualization of compositional changes induced by transition metal dissolution in Ni-rich layered cathode materials by high-resolution particle analysis. *Nano Energy* **2019,** *56*, 434-442, DOI: https://doi.org/10.1016/j.nanoen.2018.11.046.

(67) Xu, G.-L.; Liu, X.; Daali, A.; Amine, R.; Chen, Z.; Amine, K. Challenges and Strategies to Advance High-Energy Nickel-Rich Layered Lithium Transition Metal Oxide Cathodes for Harsh Operation. *Advanced Functional Materials* **2020,** *30* (46), 2004748, DOI: https://doi.org/10.1002/adfm.202004748.

(68) Sun, Y.-K.; Myung, S.-T.; Park, B.-C.; Prakash, J.; Belharouak, I.; Amine, K. High-energy cathode material for long-life and safe lithium batteries. *Nature Materials* **2009,** *8* (4), 320-324, DOI: 10.1038/nmat2418.

(69) Sun, Y.-K.; Chen, Z.; Noh, H.-J.; Lee, D.-J.; Jung, H.-G.; Ren, Y.; Wang, S.; Yoon, C. S.; Myung, S.-T.; Amine, K. Nanostructured high-energy cathode materials for advanced lithium batteries. *Nature Materials* **2012,** *11* (11), 942-947, DOI: 10.1038/nmat3435.

(70) Xu, X.; Huo, H.; Jian, J.; Wang, L.; Zhu, H.; Xu, S.; He, X.; Yin, G.; Du, C.; Sun, X. Radially Oriented Single-Crystal Primary Nanosheets Enable Ultrahigh Rate and Cycling Properties of LiNi0.8Co0.1Mn0.1O2 Cathode Material for Lithium-Ion Batteries. *Advanced Energy Materials* **2019,** *9* (15), 1803963, DOI: https://doi.org/10.1002/aenm.201803963.

(71) Kim, J. W.; Kim, D. H.; Oh, D. Y.; Lee, H.; Kim, J. H.; Lee, J. H.; Jung, Y. S. Surface chemistry of LiNi0.5Mn1.5O4 particles coated by Al2O3 using atomic layer deposition for lithium-ion batteries. *Journal of Power Sources* **2015,** *274*, 1254-1262, DOI: https://doi.org/10.1016/j.jpowsour.2014.10.207.

(72) Arrebola, J. C.; Caballero, A.; Hernán, L.; Morales, J. Re-examining the effect of ZnO on nanosized 5V LiNi0.5Mn1.5O4 spinel: An effective procedure for enhancing its rate capability at room and high temperatures. *Journal of Power Sources* **2010,** *195* (13), 4278-4284, DOI: https://doi.org/10.1016/j.jpowsour.2010.01.004.

(73) Fan, Y.; Wang, J.; Tang, Z.; He, W.; Zhang, J. Effects of the nanostructured SiO2 coating on the performance of LiNi0.5Mn1.5O4 cathode materials for high-voltage Li-ion batteries. *Electrochimica Acta* **2007,** *52* (11), 3870-3875, DOI: https://doi.org/10.1016/j.electacta.2006.10.063.

(74) Wu, H. M.; Belharouak, I.; Abouimrane, A.; Sun, Y. K.; Amine, K. Surface modification of LiNi0.5Mn1.5O4 by ZrP2O7 and ZrO2 for lithium-ion batteries. *Journal of Power Sources* **2010,** *195* (9), 2909-2913, DOI: https://doi.org/10.1016/j.jpowsour.2009.11.029.

(75) Wen, W.; Yang, X.; Wang, X.; Shu, L. G. H. Improved electrochemical performance of the spherical LiNi0.5Mn1.5O4 particles modified by nano-Y2O3 coating. *Journal of Solid State Electrochemistry* **2015,** *19* (4), 1235-1246, DOI: 10.1007/s10008-015-2743-9.

(76) Kang, H.-B.; Myung, S.-T.; Amine, K.; Lee, S.-M.; Sun, Y.-K. Improved electrochemical properties of BiOF-coated 5V spinel Li[Ni0.5Mn1.5]O4 for rechargeable lithium batteries. *Journal of Power Sources* **2010,** *195* (7), 2023-2028, DOI: https://doi.org/10.1016/j.jpowsour.2009.10.068.

(77) Kobayashi, Y.; Miyashiro, H.; Takei, K.; Shigemura, H.; Tabuchi, M.; Kageyama, H.; Iwahori, T. 5 V Class All-Solid-State Composite Lithium Battery with Li[sub 3]PO[sub 4] Coated LiNi[sub 0.5]Mn[sub 1.5]O[sub 4]. *Journal of The Electrochemical Society* **2003,** *150* (12), A1577, DOI: 10.1149/1.1619988.

(78) Deng, S.; Xiao, B.; Wang, B.; Li, X.; Kaliyappan, K.; Zhao, Y.; Lushington, A.; Li, R.; Sham, T.-K.; Wang, H.; Sun, X. New insight into atomic-scale engineering of electrode surface for long-life and safe high voltage lithium ion cathodes. *Nano Energy* **2017,** *38*, 19-27, DOI: https://doi.org/10.1016/j.nanoen.2017.05.007.

(79) Meng, X.; Yang, X.-Q.; Sun, X. Emerging Applications of Atomic Layer Deposition for Lithium-Ion Battery Studies. *Advanced Materials* **2012,** *24* (27), 3589-3615, DOI: https://doi.org/10.1002/adma.201200397.

(80) Marichy, C.; Bechelany, M.; Pinna, N. Atomic Layer Deposition of Nanostructured Materials for Energy and Environmental Applications. *Advanced Materials* **2012,** *24* (8), 1017-1032, DOI: https://doi.org/10.1002/adma.201104129.

(81) Li, X.; Lushington, A.; Sun, Q.; Xiao, W.; Liu, J.; Wang, B.; Ye, Y.; Nie, K.; Hu, Y.; Xiao, Q.; Li, R.; Guo, J.; Sham, T.-K.; Sun, X. Safe and Durable High-Temperature Lithium–Sulfur Batteries via Molecular Layer Deposited Coating. *Nano Letters* **2016,** *16* (6), 3545-3549, DOI: 10.1021/acs.nanolett.6b00577.

(82) Liu, J.; Sun, X. Elegant design of electrode and electrode/electrolyte interface in lithium-ion batteries by atomic layer deposition. *Nanotechnology* **2014,** *26* (2), 024001, DOI: 10.1088/0957-4484/26/2/024001.

(83) Xiao, B.; Liu, J.; Sun, Q.; Wang, B.; Banis, M. N.; Zhao, D.; Wang, Z.; Li, R.; Cui, X.; Sham, T.-K.; Sun, X. Unravelling the Role of Electrochemically Active FePO4 Coating by Atomic Layer Deposition for Increased High-Voltage Stability of LiNi0.5Mn1.5O4 Cathode Material. *Advanced Science* **2015,** *2* (5), 1500022, DOI: https://doi.org/10.1002/advs.201500022.

(84) Yan, P.; Zheng, J.; Liu, J.; Wang, B.; Cheng, X.; Zhang, Y.; Sun, X.; Wang, C.; Zhang, J.-G. Tailoring grain boundary structures and chemistry of Ni-rich layered cathodes for enhanced cycle stability of lithium-ion batteries. *Nature Energy* **2018,** *3* (7), 600-605, DOI: 10.1038/s41560-018-0191-3.

(85) Xu, G.-L.; Liu, Q.; Lau, K. K. S.; Liu, Y.; Liu, X.; Gao, H.; Zhou, X.; Zhuang, M.; Ren, Y.; Li, J.; Shao, M.; Ouyang, M.; Pan, F.; Chen, Z.; Amine, K.; Chen, G. Building ultraconformal protective layers on both secondary and primary particles of layered lithium transition metal oxide cathodes. *Nature Energy* **2019,** *4* (6), 484-494, DOI: 10.1038/s41560-019-0387-1.

(86) Yoon, M.; Dong, Y.; Hwang, J.; Sung, J.; Cha, H.; Ahn, K.; Huang, Y.; Kang, S. J.; Li, J.; Cho, J. Reactive boride infusion stabilizes Ni-rich cathodes for lithium-ion batteries. *Nature Energy* **2021,** *6* (4), 362-371, DOI: 10.1038/s41560-021-00782-0.

(87) Park, J.; Kim, K. T.; Oh, D. Y.; Jin, D.; Kim, D.; Jung, Y. S.; Lee, Y. M. All-Solid-State Batteries: Digital Twin-Driven All-Solid-State Battery: Unraveling the Physical and Electrochemical Behaviors (Adv. Energy Mater. 35/2020). *Advanced Energy Materials* **2020,** *10* (35), 2070145, DOI: https://doi.org/10.1002/aenm.202070145.

(88) Bielefeld, A.; Weber, D. A.; Janek, J. Microstructural Modeling of Composite Cathodes for All-Solid-State Batteries. *The Journal of Physical Chemistry C* **2019,** *123* (3), 1626-1634, DOI: 10.1021/acs.jpcc.8b11043.

(89) Choi, S.; Jeon, M.; Ahn, J.; Jung, W. D.; Choi, S. M.; Kim, J.-S.; Lim, J.; Jang, Y.-J.; Jung, H.-G.; Lee, J.-H.; Sang, B.-I.; Kim, H. Quantitative Analysis of Microstructures and Reaction Interfaces on Composite Cathodes in All-Solid-State Batteries Using a Three-Dimensional Reconstruction Technique. *ACS Applied Materials & Interfaces* **2018,** *10* (28), 23740-23747, DOI: 10.1021/acsami.8b04204.

(90) Koerver, R.; Zhang, W.; de Biasi, L.; Schweidler, S.; Kondrakov, A. O.; Kolling, S.; Brezesinski, T.; Hartmann, P.; Zeier, W. G.; Janek, J. Chemo-mechanical expansion of lithium electrode materials – on the route to mechanically optimized all-solid-state batteries. *Energy & Environmental Science* **2018,** *11* (8), 2142-2158, DOI: 10.1039/C8EE00907D.

(91) Koerver, R.; Aygün, I.; Leichtweiß, T.; Dietrich, C.; Zhang, W.; Binder, J. O.; Hartmann, P.; Zeier, W. G.; Janek, J. Capacity Fade in Solid-State Batteries: Interphase Formation and Chemomechanical Processes in Nickel-Rich Layered Oxide Cathodes and Lithium Thiophosphate Solid Electrolytes. *Chemistry of Materials* **2017,** *29* (13), 5574-5582, DOI: 10.1021/acs.chemmater.7b00931.

(92) Strauss, F.; Bartsch, T.; de Biasi, L.; Kim, A. Y.; Janek, J.; Hartmann, P.; Brezesinski, T. Impact of Cathode Material Particle Size on the Capacity of Bulk-Type

All-Solid-State Batteries. *ACS Energy Letters* **2018,** *3* (4), 992-996, DOI: 10.1021/acsenergylett.8b00275.

(93) Bielefeld, A.; Weber, D. A.; Janek, J. Modeling Effective Ionic Conductivity and Binder Influence in Composite Cathodes for All-Solid-State Batteries. *ACS Applied Materials & Interfaces* **2020,** *12* (11), 12821-12833, DOI: 10.1021/acsami.9b22788.

(94) Zhu, Y.; He, X.; Mo, Y. Origin of Outstanding Stability in the Lithium Solid Electrolyte Materials: Insights from Thermodynamic Analyses Based on First-Principles Calculations. *ACS Applied Materials & Interfaces* **2015,** *7* (42), 23685-23693, DOI: 10.1021/acsami.5b07517.

(95) Li, X.; Ren, Z.; Norouzi Banis, M.; Deng, S.; Zhao, Y.; Sun, Q.; Wang, C.; Yang, X.; Li, W.; Liang, J.; Li, X.; Sun, Y.; Adair, K.; Li, R.; Hu, Y.; Sham, T.-K.; Huang, H.; Zhang, L.; Lu, S.; Luo, J.; Sun, X. Unravelling the Chemistry and Microstructure Evolution of a Cathodic Interface in Sulfide-Based All-Solid-State Li-Ion Batteries. *ACS Energy Letters* **2019,** *4* (10), 2480-2488, DOI: 10.1021/acsenergylett.9b01676.

(96) Walther, F.; Koerver, R.; Fuchs, T.; Ohno, S.; Sann, J.; Rohnke, M.; Zeier, W. G.; Janek, J. Visualization of the Interfacial Decomposition of Composite Cathodes in Argyrodite-Based All-Solid-State Batteries Using Time-of-Flight Secondary-Ion Mass Spectrometry. *Chemistry of Materials* **2019,** *31* (10), 3745-3755, DOI: 10.1021/acs.chemmater.9b00770.

(97) Haruyama, J.; Sodeyama, K.; Tateyama, Y. Cation Mixing Properties toward Co Diffusion at the LiCoO2 Cathode/Sulfide Electrolyte Interface in a Solid-State Battery. *ACS Applied Materials & Interfaces* **2017,** *9* (1), 286-292, DOI: 10.1021/acsami.6b08435.

(98) Koerver, R.; Walther, F.; Aygün, I.; Sann, J.; Dietrich, C.; Zeier, W. G.; Janek, J. Redox-active cathode interphases in solid-state batteries. *Journal of Materials Chemistry A* **2017,** *5* (43), 22750-22760, DOI: 10.1039/C7TA07641J.

(99) Walther, F.; Randau, S.; Schneider, Y.; Sann, J.; Rohnke, M.; Richter, F. H.; Zeier, W. G.; Janek, J. Influence of Carbon Additives on the Decomposition Pathways in Cathodes of Lithium Thiophosphate-Based All-Solid-State Batteries. *Chemistry of Materials* **2020**, *32* (14), 6123-6136, DOI: 10.1021/acs.chemmater.0c01825.

(100) Neumann, A.; Randau, S.; Becker-Steinberger, K.; Danner, T.; Hein, S.; Ning, Z.; Marrow, J.; Richter, F. H.; Janek, J.; Latz, A. Analysis of Interfacial Effects in All-Solid-State Batteries with Thiophosphate Solid Electrolytes. *ACS Applied Materials & Interfaces* **2020**, *12* (8), 9277-9291, DOI: 10.1021/acsami.9b21404.

(101) Sakuda, A.; Hayashi, A.; Ohtomo, T.; Hama, S.; Tatsumisago, M. All-solid-state lithium secondary batteries using LiCoO2 particles with pulsed laser deposition coatings of Li2S–P2S5 solid electrolytes. *Journal of Power Sources* **2011,** *196* (16), 6735-6741, DOI: https://doi.org/10.1016/j.jpowsour.2010.10.103.

(102) Wang, C.; Li, X.; Zhao, Y.; Banis, M. N.; Liang, J.; Li, X.; Sun, Y.; Adair, K. R.; Sun, Q.; Liu, Y.; Zhao, F.; Deng, S.; Lin, X.; Li, R.; Hu, Y.; Sham, T.-K.; Huang, H.; Zhang, L.; Yang, R.; Lu, S.; Sun, X. Manipulating Interfacial Nanostructure to Achieve High-Performance All-Solid-State Lithium-Ion Batteries. *Small Methods* **2019,** *3* (10), 1900261, DOI: https://doi.org/10.1002/smtd.201900261.

(103) Kim, J.; Kim, M.; Noh, S.; Lee, G.; Shin, D. Enhanced electrochemical performance of surface modified LiCoO2 for all-solid-state lithium batteries. *Ceramics International* **2016,** *42* (2, Part A), 2140-2146, DOI: https://doi.org/10.1016/j.ceramint.2015.09.126.

(104) Woo, J. H.; Trevey, J. E.; Cavanagh, A. S.; Choi, Y. S.; Kim, S. C.; George, S. M.; Oh, K. H.; Lee, S.-H. Nanoscale Interface Modification of LiCoO2by Al2O3Atomic Layer Deposition for Solid-State Li Batteries. *Journal of The Electrochemical Society* **2012,** *159* (7), A1120-A1124, DOI: 10.1149/2.085207jes.

(105) Oh, G.; Hirayama, M.; Kwon, O.; Suzuki, K.; Kanno, R. Bulk-Type All Solid-State Batteries with 5 V Class LiNi0.5Mn1.5O4 Cathode and Li10GeP2S12 Solid Electrolyte. *Chemistry of Materials* **2016,** *28* (8), 2634-2640, DOI: 10.1021/acs.chemmater.5b04940.

(106) Li, X.; Liang, M.; Sheng, J.; Song, D.; Zhang, H.; Shi, X.; Zhang, L. Constructing double buffer layers to boost electrochemical performances of NCA cathode for ASSLB. *Energy Storage Materials* **2019,** *18*, 100-106, DOI: https://doi.org/10.1016/j.ensm.2018.10.003.

(107) Chen, K.; Yamamoto, K.; Orikasa, Y.; Uchiyama, T.; Ito, Y.; Yubuchi, S.; Hayashi, A.; Tatsumisago, M.; Nitta, K.; Uruga, T.; Uchimoto, Y. Effect of introducing interlayers into electrode/electrolyte interface in all-solid-state battery using sulfide electrolyte. *Solid State Ionics* **2018,** *327*, 150-156, DOI: https://doi.org/10.1016/j.ssi.2018.10.010.

(108) Ito, Y.; Sakurai, Y.; Yubuchi, S.; Sakuda, A.; Hayashi, A.; Tatsumisago, M. Application of LiCoO2Particles Coated with Lithium Ortho-Oxosalt Thin Films to Sulfide-Type All-Solid-State Lithium Batteries. *Journal of The Electrochemical Society* **2015,** *162* (8), A1610-A1616, DOI: 10.1149/2.0771508jes.

(109) Wang, C.; Liang, J.; Hwang, S.; Li, X.; Zhao, Y.; Adair, K.; Zhao, C.; Li, X.; Deng, S.; Lin, X.; Yang, X.; Li, R.; Huang, H.; Zhang, L.; Lu, S.; Su, D.; Sun, X. Unveiling the critical role of interfacial ionic conductivity in all-solid-state lithium batteries. *Nano Energy* **2020,** *72*, 104686, DOI: https://doi.org/10.1016/j.nanoen.2020.104686.

(110) Jung, S. H.; Oh, K.; Nam, Y. J.; Oh, D. Y.; Brüner, P.; Kang, K.; Jung, Y. S. Li3BO3–Li2CO3: Rationally Designed Buffering Phase for Sulfide All-Solid-State Li-Ion Batteries. *Chemistry of Materials* **2018,** *30* (22), 8190-8200, DOI: 10.1021/acs.chemmater.8b03321.

(111) Wang, C.-W.; Ren, F.-C.; Zhou, Y.; Yan, P.-F.; Zhou, X.-D.; Zhang, S.-J.; Liu, W.; Zhang, W.-D.; Zou, M.-H.; Zeng, L.-Y.; Yao, X.-Y.; Huang, L.; Li, J.-T.; Sun, S.-G. Engineering the interface between LiCoO2 and Li10GeP2S12 solid electrolytes with an

ultrathin Li2CoTi3O8 interlayer to boost the performance of all-solid-state batteries. *Energy & Environmental Science* **2021,** *14* (1), 437-450, DOI: 10.1039/D0EE03212C.

(112) Jung, Y. S.; Oh, D. Y.; Nam, Y. J.; Park, K. H. Issues and Challenges for Bulk-Type All-Solid-State Rechargeable Lithium Batteries using Sulfide Solid Electrolytes. *Israel Journal of Chemistry* **2015,** *55* (5), 472-485, DOI: https://doi.org/10.1002/ijch.201400112.

(113) Nam, Y. J.; Cho, S.-J.; Oh, D. Y.; Lim, J.-M.; Kim, S. Y.; Song, J. H.; Lee, Y.-G.; Lee, S.-Y.; Jung, Y. S. Bendable and Thin Sulfide Solid Electrolyte Film: A New Electrolyte Opportunity for Free-Standing and Stackable High-Energy All-Solid-State Lithium-Ion Batteries. *Nano Letters* **2015,** *15* (5), 3317-3323, DOI: 10.1021/acs.nanolett.5b00538.

(114) Yersak, T. A.; Macpherson, H. A.; Kim, S. C.; Le, V.-D.; Kang, C. S.; Son, S.-B.; Kim, Y.-H.; Trevey, J. E.; Oh, K. H.; Stoldt, C.; Lee, S.-H. Solid State Enabled Reversible Four Electron Storage. *Advanced Energy Materials* **2013,** *3* (1), 120-127, DOI: https://doi.org/10.1002/aenm.201200267.

(115) Oh, D. Y.; Nam, Y. J.; Park, K. H.; Jung, S. H.; Cho, S.-J.; Kim, Y. K.; Lee, Y.-G.; Lee, S.-Y.; Jung, Y. S. Excellent Compatibility of Solvate Ionic Liquids with Sulfide Solid Electrolytes: Toward Favorable Ionic Contacts in Bulk-Type All-Solid-State Lithium-Ion Batteries. *Advanced Energy Materials* **2015,** *5* (22), 1500865, DOI: https://doi.org/10.1002/aenm.201500865.

(116) Inada, T.; Takada, K.; Kajiyama, A.; Kouguchi, M.; Sasaki, H.; Kondo, S.; Watanabe, M.; Murayama, M.; Kanno, R. Fabrications and properties of composite solid-state electrolytes. *Solid State Ionics* **2003,** *158* (3), 275-280, DOI: https://doi.org/10.1016/S0167-2738(02)00889-5.

(117) Ito, S.; Fujiki, S.; Yamada, T.; Aihara, Y.; Park, Y.; Kim, T. Y.; Baek, S.-W.; Lee, J.-M.; Doo, S.; Machida, N. A rocking chair type all-solid-state lithium ion battery adopting Li2O–ZrO2 coated LiNi0.8Co0.15Al0.05O2 and a sulfide based electrolyte.

Journal of Power Sources **2014,** *248*, 943-950, DOI: https://doi.org/10.1016/j.jpowsour.2013.10.005.

(118) Kim, D. H.; Oh, D. Y.; Park, K. H.; Choi, Y. E.; Nam, Y. J.; Lee, H. A.; Lee, S.-M.; Jung, Y. S. Infiltration of Solution-Processable Solid Electrolytes into Conventional Li-Ion-Battery Electrodes for All-Solid-State Li-Ion Batteries. *Nano Letters* **2017,** *17* (5), 3013-3020, DOI: 10.1021/acs.nanolett.7b00330.

(119) Oh, D. Y.; Kim, D. H.; Jung, S. H.; Han, J.-G.; Choi, N.-S.; Jung, Y. S. Single-step wet-chemical fabrication of sheet-type electrodes from solid-electrolyte precursors for all-solid-state lithium-ion batteries. *Journal of Materials Chemistry A* **2017,** *5* (39), 20771-20779, DOI: 10.1039/C7TA06873E.

(120) Yamamoto, M.; Terauchi, Y.; Sakuda, A.; Takahashi, M. Binder-free sheet-type all-solid-state batteries with enhanced rate capabilities and high energy densities. *Scientific Reports* **2018,** *8* (1), 1212, DOI: 10.1038/s41598-018-19398-8.

(121) Noh, S.; Nichols, W. T.; Cho, M.; Shin, D. Importance of mixing protocol for enhanced performance of composite cathodes in all-solid-state batteries using sulfide solid electrolyte. *Journal of Electroceramics* **2018,** *40* (4), 293-299, DOI: 10.1007/s10832-018-0129-y.

(122) Randau, S.; Walther, F.; Neumann, A.; Schneider, Y.; Negi, R. S.; Mogwitz, B.; Sann, J.; Becker-Steinberger, K.; Danner, T.; Hein, S.; Latz, A.; Richter, F. H.; Janek, J. On the Additive Microstructure in Composite Cathodes and Alumina-Coated Carbon Microwires for Improved All-Solid-State Batteries. *Chemistry of Materials* **2021,** *33* (4), 1380-1393, DOI: 10.1021/acs.chemmater.0c04454.

(123) Park, S. W.; Oh, G.; Park, J.-W.; Ha, Y.-C.; Lee, S.-M.; Yoon, S. Y.; Kim, B. G. Graphitic Hollow Nanocarbon as a Promising Conducting Agent for Solid-State Lithium Batteries. *Small* **2019,** *15* (18), 1900235, DOI: https://doi.org/10.1002/smll.201900235.

Chapter 3

3 Experimental Methods and Characterization Techniques

This chapter will introduce two experimental methods for the interfacial modification of high-energy cathodes, as well as the physical and electrochemical characterizations for the as-prepared cathodes/electrodes.

3.1 Experimental methods

3.1.1 Atomic layer deposition coatings

Figure 3.1 Savannah 100 ALD system (Ultratech/Cambridge Nanotech., USA)

In the thesis, we develop Li_3PO_4, TiO_2, and Li_3PO_4-TiO_2 coatings for high-voltage LNMO cathodes and hybrid Li_3PO_4 coating for Ni-rich NMC811 cathodes by ALD method. Li_3PO_4, TiO_2, and Li_3PO_4-TiO_2 were deposited in a Savannah 100 ALD system (Ultratech/Cambridge Nanotech., USA), as shown in **Figure 3.1**. TTIP ($Ti(OCH(CH_3)_2)_4$) and water were used as the precursors for TiO_2, while LiOtBu [$(CH_3)_3COLi$] and TMPO [$(MeO)_3PO$] are used for Li_3PO_4. For Li_3PO_4 coating, the source temperatures for LiOtBu and TMPO were 180 °C and 75 °C, respectively. The deposition temperature for Li_3PO_4 was 250 °C. During one ALD cycle, LiOtBu and TMPO were alternatively introduced into the reaction chamber with a pulse time of 2 s, and the pulsing of each precursor was separated by a 15 s purge with N_2. For TiO_2 coating, the source temperatures for TTIP and water were 80 ºC and room temperature, respectively. The deposition temperature for TiO_2 was 250 °C. During one ALD cycle, TTIP and water were alternatively introduced into the reaction chamber with a pulse time of 2 s, and the pulsing of each precursor was separated by a 15 s purge with N_2. For Li_3PO_4-TiO_2 coating, one ALD cycle consisted of two subcycles of Li_3PO_4 and TiO_2. The overall sequence was the following: $2 \times$ [TTIP (x s pulse/10 s purge) - H_2O (0.5 s pulse/15 s purge)] + [LiOtBu, (2 s pulse/15 s purge) -

TMPO (2 s pulse/15 s purge)]. Li_3PO_4, TiO_2, and Li_3PO_4-TiO_2 materials were coated on both LNMO powders and electrodes, while Li_3PO_4 was only coated on NMC811 powders. In the Li_3PO_4 coated NMC811 samples, the primary LPO coating layer with a thickness of 10 nm was deposited on the surface of NMC811 powders by ALD. For infusion, the LPO-coated cathode powder were further annealed at 600 °C for 2 h. Furthermore, the LPO-annealed powders were subject to another ALD LPO coating with the thickness of 1 nm, 5 nm, or 10 nm.

3.1.2 Molecular layer deposition coating
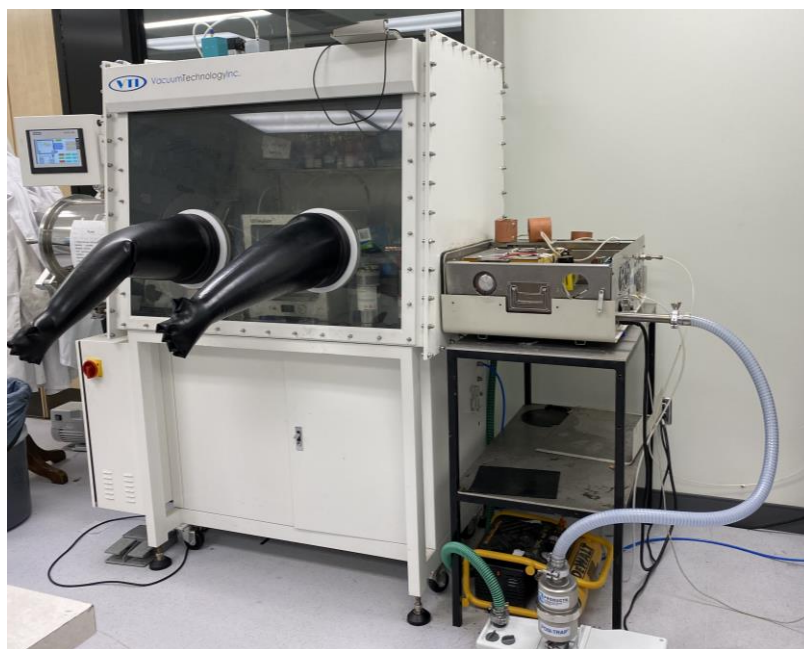
Figure 3.2 Gemstar-8 ALD/MLD system (Arradiance, USA) connected with glove-box for PEDOT coating.

In the thesis, poly(3,4-ethylenedioxythiophene) (PEDOT) coating was developed by MLD in a Gemstar-8 ALD system (Arradiance, USA), which is directly connected to an argon-filed glove box (as shown in **Figure 3.2**). PEDOT was deposited on the surface of carbon nanotubes (CNTs) and NMC811 powders using molybdenum chloride ($MoCl_5$) and 3,4-ethylenedioxythiophene (EDOT) as precursors. The source temperatures for both $MoCl_5$ and EDOT were 80 °C. The deposition temperature for PEDOT was 150 °C.

During one MLD cycle, $MoCl_5$ and EDOT were alternatively introduced into the reaction chamber with a pulse time of 5 s, and the pulsing of each precursor was separated by a 60 s purge with N_2. To investigate to the thickness effect, the PEDOT with 2, 5, 10 nm were coated for both CNTs and NMC811. Because PEDOT coatings are air-sensitive, the coated CNTs and NMC811 were stored in the argon-filed glove box.

3.2 Characterization techniques

3.2.1 Physical characterizations

Figure 3.3 Hitachi S4800 scanning electron microscopy.

The morphologies and structures of electrode materials were observed using a field emission scanning electron microscopy (FESEM, Hitachi S4800), as shown in **Figure 3.3**. The FESEM machine is equipped with an energy dispersive spectrometer (EDX).

Figure 3.4 FEI-Titan Cubed Themis G2 300 scanning transmission electron microscopy.

The requirement of high magnifications for morphologies and structures of electrode materials were observed by transmission electron microscopy (TEM). Three TEM models were applied in the thesis based on different projects. For LNMO cathodes, scanning transmission electron microscopy (STEM) characterization was performed using an aberration-corrected JEOL JEM-ARM 200CF STEM equipped with a 200 keV cold-field emission gun, a HAADF detector and an Oxford X-max 100TLE windowless SDD X-ray detector. In solid-state batteries projects, the morphology and microstructure of cycled cathodes were obtained by focused ion beam (FIB, Helios NanoLab 460HP, FEI)/FESEM (FE-SEM; JEOL JSM-7001F) for a detailed structural analysis. The obtained FIB samples were further investigated by aberration-corrected scanning transmission electron microscopy (STEM, Titan Cubed Themis G2 300) with elemental mapping images (as shown in **Figure 3.4**) and high-resolution transmission electron microscopy (HRTEM, JEOL 2010FEG).

Figure 3.5 Bruker D8 Advance Diffractometer XRD system.

X-ray power diffraction (XRD) measurements were carried out on a Bruker D8 Advance Diffractometer (Cu-Ka source, 40 kV, 40 mA) to study the phase and structure information of the samples (as shown in **Figure 3.5**).

Figure 3.6 TA SDT Q600 thermogravimetric/differential scanning calorimetry analyzer.

For the thermal gravimetric analysis (TGA) testing, the data were acquired using a TA instrument (SDT Q600) as shown in **Figure 3.6**. All testing were in a nitrogen atmosphere at a heating rate of 2 °C min^{-1}.
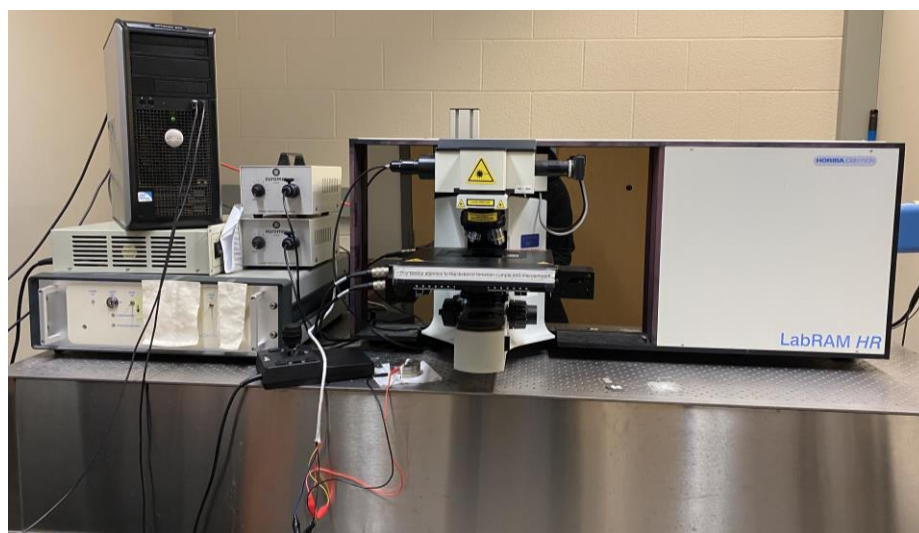
Figure 3.7 HORIBA Scientific LabRAM HR Raman spectrometer system.

Raman scattering spectra were carried out by a HORIBA Scientific LabRAM HR Raman spectrometer system (as shown in **Figure 3.7**).

Figure 3.8 Kratos AXIS Nova (rear) X-ray photoelectron spectrometers at Surface Science Western.

X-ray photoelectron spectroscopy (XPS) testing were measured with a monochromatic Al Kα source (1486.6 eV) in a Kratos AXIS Nova Spectrometer as shown in **Figure 3.8**. The Ar filled glovebox was connected with the XPS machine to avoid the exposure of air. In the time-of-flight (ToF-SIMS) measurements, the action of the primary ion beam bombardment on the sample surface induces the emission of negative secondary ions. Sputtering with a Cs^+ ion beam (3 keV) was used for depth profiling analysis.
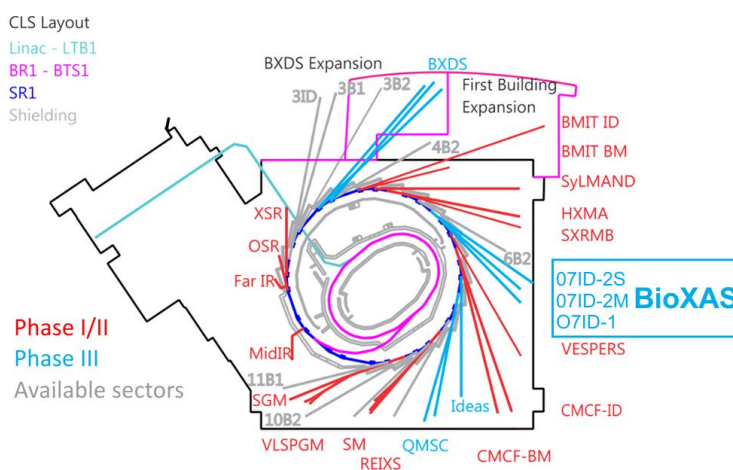
Figure 3.9 Beamlines at Canadian Light Source.

All synchrotron X-ray studies were carried out at the Canadian Light Source (CLS). The beamlines at CLS are shown in **Figure 3.9**. Ti, Mn, and Ni L-edge X-ray absorption near

edge structure (XANES) measurements were conducted on spherical grating monochromator beamline (SGM), while O K-edge XANES spectra were collected in both total electron yield and fluorescence mode at SGM beamline equipped with a 45 mm planar undulator. S, P, Cl, Ni, Co, and Mn K-edge X-ray absorption near edge structure (XANES) spectra were collected in fluorescence mode using Si(111) crystals at Soft X-ray Microcharacterization Beamline (SXRMB). X-ray absorption fine structure (EXAFS) data were collected at Hard X-ray Micro Analysis (HXMA) beamline. Ni K-edge spectra were collected in fluorescence mode using Si(220) crystals. Co and Mn K-edge spectra were also collected in fluorescence mode but using Si(111) crystals.

3.2.2 Electrochemical measurements

Electrochemical testing of liquid coin cells:

Figure 3.10 Photo of glove box for battery assembling.

Electrodes were prepared by slurry casting of cathode material, acetylene black (AB) and polyvinylidene fluoride (PVDF) in N-methyl-pyrrolidione (NMP) on aluminium foil and dried at 80 ^{o}C under vacuum over 12 h. The weight ratio of active materials: AB: PVDF was 80: 10: 10. CR2032 coin cells were assembled in an argon-filled glove-box using lithium metal as the counter electrode and Celgard K2045 as the separator. The photo of glove box for battery assembling is shown in **Figure 3.10**. The electrolyte was composed

of 1 M LiPF$_6$ dissolved in ethylene carbonate (EC)-dimethyl carbonate (DMC) with a volume ratio of 1: 1.
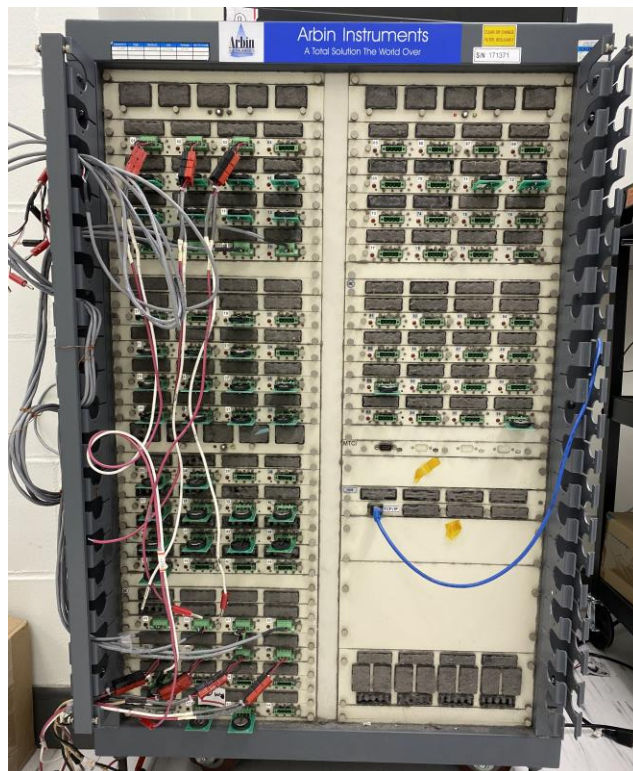
Figure 3.11 Arbin BT2000 system for liquid LIB testing.

Cyclic voltammetry (CV) experiments were studied using a Bio-logic multichannel potentiostat 3/Z (VMP3) with a scanning rate of 0.1 mV s^{-1} and at a potential range of 3.5-5.0 V (vs Li$^+$/Li). Electrochemical impedance spectroscopy (EIS) tests were measured between the frequency range of 0.01 Hz to 100 kHz by versatile multichannel potentiostat 3/Z (VMP3). Charge/discharge tests were carried out on the Arbin BT2000 system with a voltage range of 3.5-5.0 V (as shown in **Figure 3.11**). For GITT measurements, the batteries were charged with 0.2 C for 15 min and rest for 1h.

Electrochemical testing of solid-state model cells:

In solid-state model cells, a sandwiched electrode were fabricated by using cathode material, solid-state electrolyte (SE) and indium/lithium foils (99.99%, Φ10 mm,

thickness 0.1 mm). Firstly, 60 mg SE was pressed at 2 ton with 10 mm diameter to form a pellet. After that, 7 mg cathode power was mixed well with 3 mg SE, and then uniformly spread onto the surface of SE layer and pressed under 3 tons of pressure to form a two-layer pellet. Finally, a piece of indium/lithium foil with the same 10 mm diameter was put onto the other side of the SE layer and pressed at 0.5 tons of pressure. The three-layered pellet was pressed between two stainless-steel rods as current collectors at the both positive and negative sides.

Figure 3.12 LAND CT-2001A system for SSB testing.

The galvanostatic charge-discharge characteristics were tested on a multichannel battery tester (LAND CT-2001A, Wuhan Rambo Testing Equipment Co., Ltd., China), as shown in **Figure 3.12**. CV and EIS were performed on the versatile multichannel potentiostat 3/Z (VMP3), as shown in **Figure 3.13**. EIS was conducted by applying an AC voltage of 10 mV amplitude in the 7000 kHz to 1000 mHz frequency range.

Figure 3.13 Multichannel potentiostat 3/Z (VMP3) system and the oven for temperature testing.

Chapter 4

4 Manipulation of An Ionic and Electronic Conductive Interface for Highly Stable High-Voltage Cathodes*

A stable and conductive interface is one of the decisive factors in manipulating the performance of high voltage $LiNi_{0.5}Mn_{1.5}O_4$ (LNMO) cathode for Li-ion batteries. Herein, a hybrid Li_3PO_4-TiO_2 coating layer is designed as an interfacial material via controllable atomic layer deposition (ALD) on LNMO. The coating acts not just as a physical barrier to prevent the side-reactions between cathode and electrolyte at high voltage, more importantly, the hybrid coating material improves both interfacial ionic and electronic conductivities to build facile Li-ion and electron diffusion pathways for LNMO. The optimized LNMO demonstrates improved rate capability and long-life stability. The capacity retention is 81.2% comparing with 47.4% of bare LNMO at 0.5 C after 300 cycles. Detailed surface structural evolution is studied via X-ray absorption near edge spectroscopy and transmission electron microscopy. This work provides new insights of hybrid interfacial design via ALD and promotes novel electrode architectures for batteries.

4.1   Introduction

The growing demand for high-performance Li-ion batteries has stimulated the exploration of novel electrode materials.[1-3] The development of cathode materials is crucial to Li-ion batteries moving forward, which is currently the major limiting factor of the energy density of full batteries.[4-8] Among the developed cathode materials, spinel structure $LiNi_{0.5}Mn_{1.5}O_4$ (LNMO) is one of the promising candidates due to its high operating voltage, high specific capacity, and natural elemental abundance.[9] However, it should be noted such high voltage operation also brings significant challenges to this cathode material in batteries, such as the irreversible surface phase transition, transition metal dissolution, Jahn-Teller distortion of Mn^{3+}, electrolyte oxidation, etc.[10-12] All of these challenges lead to rapid capacity decay and voltage plateau drop during cycling, resulting in unsatisfy cycling and rate performance.[13, 14]

Considerable efforts have been devoted to overcome these challenges, including surface coating or doping of LNMO, synthesis of novel nanostructure cathode materials, and the investigation of stable high voltage Li-ion electrolyte.[9, 10, 15] Among these developed strategies, coating is an effective method to avoid direct exposure of cathode materials to the electrolyte and therefore prevent the occurrence of side-reactions and the dissolution of transition metals.[16-19] On the other hand, it should be noted that for many developed coating materials, such as metal oxides, phosphates, and fluorides, to ensure the chemical and electrochemical stability at high voltage, they have limited Li^+ ionic and electron conductivity.[20-22] Therefore, introducing these inert coating materials for cathodes as a physical barrier may increase the interfacial resistance of cathodes and therefore reduce the efficiency of transformation from chemical energy to electrical energy of batteries in the electrochemical reaction.[23-25] As a result, despite the improvement of cycling stability of cathode LNMO, inert coating materials will sacrifice capacity, especially at high current densities.

In our previous studies, atomic layer deposited (ALD) $FePO_4$ and $AlPO_4$ were adopted as the coating layer on the modification of LNMO cathodes.[26, 27] Although cycling stability were improved significantly due to the highly stability of phosphates, the

sacrificial initial discharge capacity still hinders the application of these metal phosphates in high voltage LNMO cathodes because of the insufficient interfacial ionic/electronic conductivity. Employing solid-state electrolyte as coating layer by ALD, such as $LiTaO_3$, able to overcome the limited Li-ion conductivity, improving the cycling stability without loss of initial capacity.[28] However, the rate capability still has space to improve by combining with enhanced electronic conductivity.[29] Therefore, the desired interface control strategies for high voltage cathodes are urgent to be developed by designing hybrid coating materials by ALD.

In this work, we propose a novel Li_3PO_4-TiO_2 (LPO-TiO) hybrid coating material via atomic layer deposition (ALD) for LNMO. For the developed hybrid LPO-TiO coating, Li_3PO_4 is considered as a Li-ion solid-state electrolyte with promising ionic conductivity while due to the semi-conductor properties, anatase TiO_2 in the hybrid coating layer has demonstrated an enhanced electronic conductivity compared with single Li_3PO_4.[30] Therefore, the unique hybrid LPO-TiO coating material could not only act as a physical barrier to protect the surface structure of LNMO from side-reactions, but also provide sufficient ionic and electronic conductivity for the cathode material to improve the cycling and rate performance of the batteries. Detailed physical and electrochemical characterizations of the coated LNMO are conducted. Controllable coating strategy, including optimizing coating materials and structure, with the underlying mechanism of coating effect is investigated. Synchrotron-based X-ray absorption near-edge spectroscopy (XANES) and scanning transmission electron microscopy (STEM) are employed to reveal the surface structure revolution of LNMO with the coating layer.

4.2 Experimental section

Preparation of LNMO electrodes: Commercial LNMO powder was purchased from Daejung Energy Materials Co., Ltd., South Korea. Electrodes were prepared by slurry casting of commercial LNMO, acetylene black (AB) and polyvinylidene fluoride (PVDF) in N-methyl-pyrrolidione (NMP) on aluminium foil and dried at 80 $^{\circ}$C under vacuum over 12 h. The weight ratio of active materials: AB: PVDF was 80: 10: 10. The areal mass loading of active materials is 2.29-2.54 mg cm^{-2}.

Preparation of ALD LPO-TiO coated LNMO electrodes: Li_3PO_4, TiO_2, and Li_3PO_4-TiO_2 were deposited in a Savannah 100 ALD system (Ultratech/Cambridge Nanotech., USA) by using TTIP $(Ti(OCH(CH_3)_2)_4)$ and water for TiO_2 cycle and LiOtBu $[(CH_3)_3COLi]$ and TMPO $[(MeO)_3PO]$ for LPO cycle. The deposition of the nanocomposite was carried out at 250 ℃. The chosen temperature was in the overlapped temperature range of the ALD windows of TiO_2 and Li_3PO_4 to achieve ALD growth and prevented precursors from decomposing. Various ALD materials are coating on both LNMO powders and electrodes.

Characterization: The morphologies and structures of LPO-TiO coated LNMO were observed using a field emission scanning electron microscopy (FESEM, Hitachi S4800). STEM characterization was performed using an aberration-corrected JEOL JEM-ARM 200CF STEM equipped with a 200 keV cold-field emission gun, a HAADF detector and an Oxford X-max 100TLE windowless SDD X-ray detector. All synchrotron X-ray studies were carried out at the Canadian Light Source (CLS). X-ray absorption near edge structure (XANES) measurements were conducted on variable line spacing plane grating monochromator and spherical grating monochromator beamlines, respectively. The X-ray photoelectron spectroscopy (XPS) were measured with a monochromatic Al Kα source (1486.6 eV) in a Kratos AXIS Nova Spectrometer.

Electrochemical characterization: CR2032 coin cells were assembled in an argon-filled glove-box using lithium metal as the counter electrode and Celgard K2045 as the separator. The electrolyte was composed of 1 M $LiPF_6$ dissolved in ethylene carbonate (EC)-dimethyl carbonate (DMC) with a volume ratio of 1: 1. Cyclic voltammetry (CV) experiments were studied using a Bio-logic multichannel potentiostat 3/Z (VMP3) with a scanning rate of 0.1 mV s^{-1} and at a potential range of 3.5-5.0 V (vs Li^+/Li). Electrochemical impedance spectroscopy (EIS) tests were measured between the frequency range of 0.01 Hz to 100 kHz by versatile multichannel potentiostat 3/Z (VMP3). Charge/discharge tests were carried out on the Arbin BT2000 system with a voltage range of 3.5-5.0 V. For GITT measurements, the batteries were charged with 0.2 C for 15 min and rest for 1h.

4.3   Results and discussion
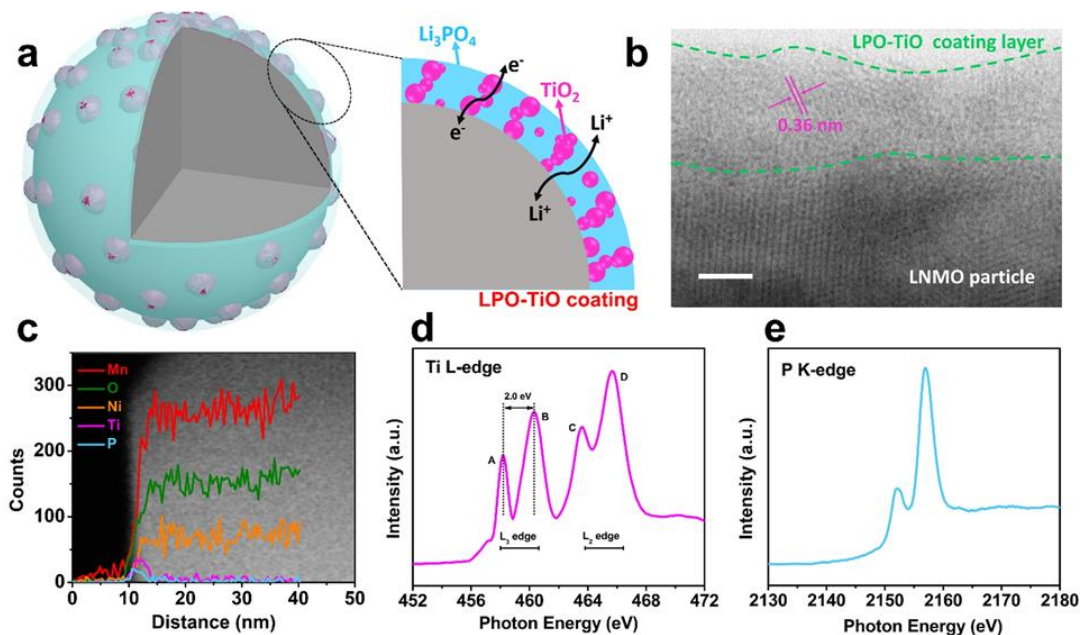
Figure 4.1 Structure scheme and physical characterizations of ALD LPO-TiO coating. (a) Schematic illustration of the detailed structure of hybrid LPO-TiO coated LNMO, (b) STEM image, (c) EDX line-scanned spectrum, (d) Ti L-edge XANES and (e) P K-edge XANES of LPO-TiO coated LNMO. Scale bars, 2 nm (b).

Figure 4.1a describes the proposed schematic figure of ALD LPO-TiO coating on the LNMO cathode particle. As reported in our previous study, the ALD LPO coating layer is in an amorphous state with the ionic conductivity of 1.73×10^{-7} S cm^{-1} at 323 K.[31, 32] ALD crystalline anatase phase TiO_2 nano-particles are dispersed in the LPO layer.[32] The LPO solid-state electrolyte allows for facile Li-ion diffusion, while the semi-conductive TiO_2 nanoparticles form a beneficial electron pathway. STEM and synchrotron XANES are conducted to further demonstrate the proposed ALD LPO-TiO structure. To clearly show the LPO-TiO structure through TEM, 50 cycles of LPO-TiO ALD were applied resulting in a 5 nm coating, while the following electrochemical characterizations were performed using a thinner, more suitable coating thickness. As shown in Figure 4.1b, the ALD LPO-TiO coating presents a clear amorphous layer with a thickness of 5 nm covered on the surface of LNMO particle. Some nanocrystalline

particles of TiO_2 are dispersed in the amorphous LPO matrix layer. The lattice spacing of the plane obtained from the pixel intensity profile of the selected regions is 0.36 nm, which matches the crystal plane (101) of anatase TiO_2.[32] It is clearly seen that the presence of Ti and P signals in EDX line-scanned spectrum (Figure 4.1c), further confirming hybrid LPO-TiO coating on the surface of LNMO particle with a thickness of 5 nm. Ti L-edge and P K-edge XANES spectra are shown in Figure 4.1d and e, which indicate the presence of TiO_2 and PO_4^{3-} composites in the ALD coating layer.[33-35] The feature peaks from A to D in the Ti L-edge spectrum indicate the transition of Ti 2p electrons to unoccupied 3d electronic states. Peak A and B located at 458.2 eV and 460.2 eV, respectively, reflect the L_3-edge transition from $2p_{3/2}$ to $3d_{5/2}$ state, in which the energy gap of 2.0 eV demonstrates the characteristic of anatase structure. Features C and D, located at 463.6 eV and 465.7 eV, belong to L_2-edge transitions from $2p_{1/2}$ to $3d_{3/2}$ states.[36, 37] The presence of both pre-edge and predominant peaks in P K-edge XANES spectrum correspond to phosphates.[38] Other physical characterizations, such as SEM images of bare and coated LNMO, TEM EDX elemental mapping results also demonstrate the presence of Ti and P, further confirming the successful deposition of LPO-TiO coating on LNMO particles via ALD (Supporting Figures S1-S2). Based on the results of physical characterizations, hybrid LPO-TiO ALD coating layer is expected to improve both ionic and electronic conductivity of LNMO cathode.
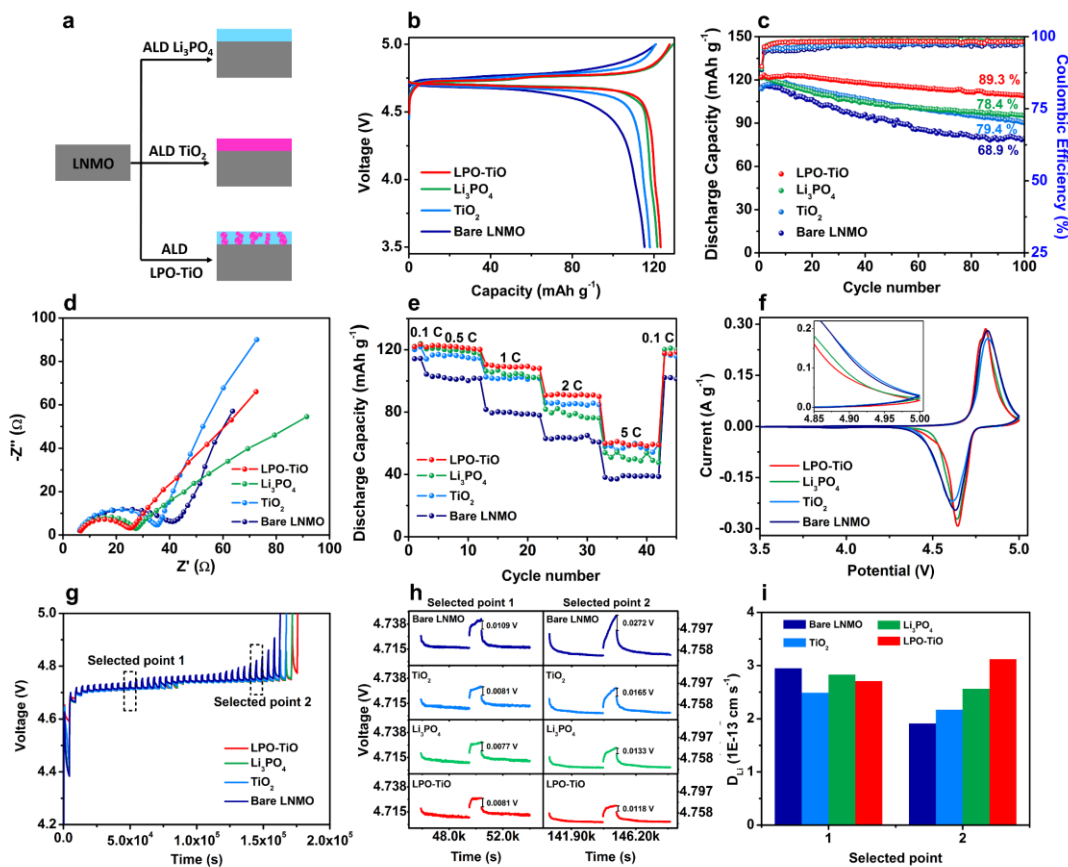
Figure 4.2 Investigation the effect of various ALD coating materials on LNMO cathodes. (a) Schematic figure of various ALD coating on LNMO cathodes. (b-i) Electrochemical characterization of as-prepared LNMO cathodes: (b) Charge/discharge curves at the first cycle, (c) Cyclic performance at 0.5 C, (d) EIS plots after 100 cycles, (e) Rate capability test, (f) CV curves at 0.1 mV s^{-1}, (g) Transient charge voltage profiles, (h) The corresponding polarization plots and (i) Li$^+$ diffusion coefficient obtained by GITT.

Electrochemical characterizations of various coated LNMO cathodes are illustrated in Figure 4.2 and Supporting Figures S4-S6 in order to investigate the effect of coating materials. The thickness effect of hybrid LPO-TiO coating for the performance of LNMO cathodes is firstly optimized (Figure S4) and the 10-ALD cycle coating (around 1 nm) present the best cycling performance. Therefore, LPO-TiO coating layer of 1 nm is chosen for all of the following electrochemical characterizations. In order to investigate

synergistic effect of the LPO-TiO coating for LNMO, comparisons are made between bare LNMO, hybrid LPO-TiO coated, LPO coated, and TiO_2 coated cathodes with the same coating thickness (1 nm), as shown in Figure 4.2a. The first charge-discharge profiles at 0.5 C are shown in Figure 4.2b. Compared to bare LNMO, the LPO-TiO coated cathode shows the maximum discharge capacity with obvious reduced polarization, indicating hybrid LPO-TiO coating layer effectively improves lithium ion diffusion as well as suppressing side-reactions with the electrolyte at high voltage during charge/discharge process. Interestingly, cycling performance at 0.5 C of the four cathodes shows considerable differences between the coatings (Figure 4.2c). Hybrid LPO-TiO coated LNMO presents the best cycling performance where the initial discharge capacity is 121.9 mAh g^{-1} and the retention is over 89.3 % (108.9 mAh g^{-1}) after 100 cycles. On the other hand, the initial capacity of bare LNMO is 115 mAh g^{-1} and the retention after 100 cycles is only 68.9%, illustrating the low cycling stability. The single LPO or TiO_2 coated LNMO cathodes demonstrate similar cycling stability that the capacity retention is about 79% after 100 cycles. In our previous study, inert ALD coating materials, such as metal oxides and metal phosphors, were widely used as the buffer layer, which improved the cycling stability of cathodes.[26, 27] Nevertheless, the initial discharge capacity was lower than the bare electrode due to the reduced ionic and electronic conductivity of these ALD coatings. However, for the LPO-TiO coated LNMO, both the initial discharge capacity and cycling stability are improved comparing with bare LNMO. It indicates this unique coating does not act only as physical buffer layer. More importantly, it provides enhanced ionic and electronic conductivity for the cathode to improve the electrochemical reaction kinetics. Corresponding coulombic efficiency is also shown in Figure 4.2c. The initial coulombic efficiency is around 90% for all four cathodes. After the 1st cycle, the coulombic efficiency of both LPO-TiO and LPO coated LNMO cathodes rises quickly to 98.5% within 10 cycles. However, the TiO_2 coated and bare LNMO cathodes demonstrate a lower coulombic efficiency at the first 40 cycles and then gradually increase to 96-97% in the following cycles. The differences of coulombic efficiency demonstrate the excellent ionic conductivity and electrochemical stability of the LPO coating layer for LNMO cathodes. On the other hand, TiO_2 coating layer with

low ionic conductivity needs longer cycling time to stabilize and re-construct the surface structure to facile Li-ion penetration. For bare LNMO, severe side-reactions with electrolyte lead to the low coulombic efficiency and rapidly decaying cycling capacity.[39, 40] EIS plots of the above four LNMO cathodes after 1, 50, and 100 cycles are shown in Figure S7, S8, and 4.2d, the smallest interfacial resistance of the battery with LPO-TiO coated LNMO cathode further demonstrates the stable and conductive surface of the cathode with the support of hybrid LPO-TiO coating layer during the continued charge/discharge cycling.

Rate performance of the four cathodes is illustrated in Figure 4.2e. The rate capability of cathode material is directly related to the ionic and electronic conductivity at the interface between electrode and electrolyte. Impressively, the LPO-TiO coated LNMO demonstrates significantly improved rate performance than the bare or single LPO/TiO coated cathodes. Even at 2 C and 5 C, the LPO-TiO coated LNMO still delivers the capacity over 90 and 60 mAh g^{-1}, which is over 60% of bare LNMO. The significant improvement of rate performance is contributed by the synergistic effect of Li_3PO_4 and TiO_2, enhancing electronic and ionic conductivity at the same time to build a smooth ion and electron diffusion way between LNMO and electrolyte. CV profiles of the four cathodes are shown in Figure 4.2f. Interestingly, LPO-TiO coated LNMO demonstrates the lowest anodic peak potential (4.80 V) and highest cathodic peak potential (4.64 V) compared to other cathodes, indicating the highest electrochemical reaction activity of battery with lower resistance. Furthermore, as shown in the insert figure, LPO-TiO coated LNMO also demonstrates the lowest current at the cut-off voltage (5 V), which indicates a smaller potential polarization at a high operating voltage of the battery.

Finally, the galvanostatic intermittent titration technique (GITT) is employed to further investigate the origin of improved electrochemical properties of hybrid LPO-TiO coating layer. Transient voltage curves and the corresponding polarization and Li^+ diffusion coefficient are plotted in Figure 4.2g-i. Two charging plateaus can be clear seen in the transient voltage curves of four cathodes, originating from two redox couples of Ni^{2+}/Ni^{3+} and Ni^{3+}/Ni^{4+}, respectively. Hybrid LPO-TO coated LNMO demonstrates the highest

capacity and the lowest charging potential. Two selected points at the different charging plateaus are used to evaluate the polarization and capability of Li^+ diffusion of various LNMO cathodes at different charging stage. Compared to bare LNMO, the increasing of polarization potential is significantly retard in hybrid LPO-TiO coated LNMO, which indicates the side-reactions during charging process can be effectively suppressed by coating layer. Interestingly, bare LNMO exhibits the highest Li^+ diffusion coefficient at the first point, but decrease significantly during the continued charging process. However, the Li^+ diffusion coefficient in hybrid LPO-TiO increase with the deeper of charging, which is opposite comparing with bare and single LPO/TiO_2 coated LNMO. These results demonstrate hybrid LPO-TiO coating layer does not impede the Li^+ transformation within the LNMO particles. More important, it facilitates ionic migration during the charging process because of its capability to construct a stable interface to suppress side-reactions and also improve the ionic and electronic conductivity for the cathode electrode. Based on the obtained electrochemical results, LPO-TiO coating promotes higher cycling capacity and improved stability of LNMO compared to the bare or single LPO/TiO coated LNMO. LPO-TiO coating also demonstrates promising rate performance for LNMO with smaller potential polarization and battery resistance during cycling.
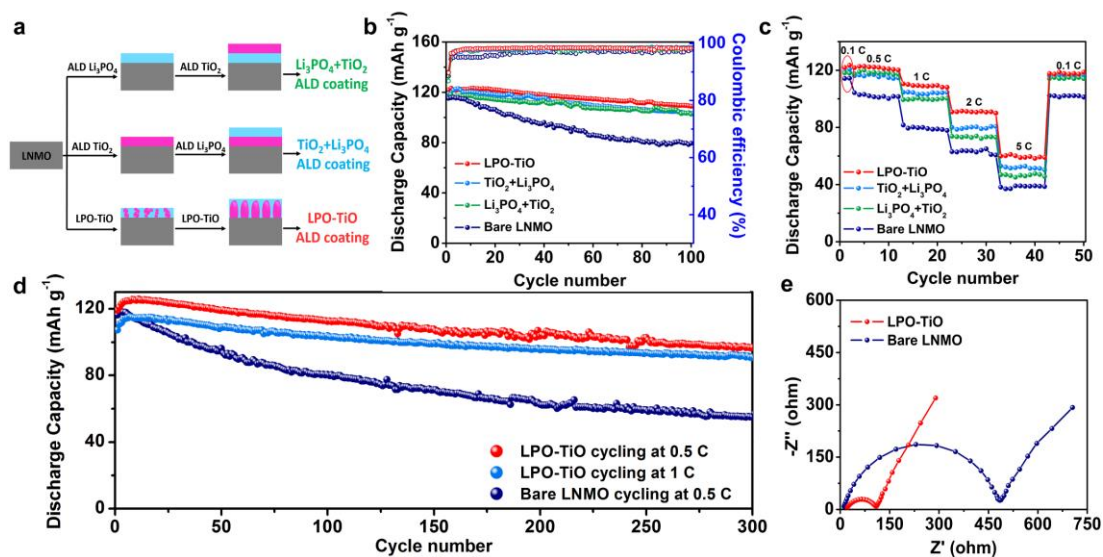
Figure 4.3 Investigation of ALD coating structure effect on LNMO cathodes. (a) Schematic figure of different coating sequences of LPO and TiO during the ALD process. (b-e) Electrochemical characterization of as-prepared LNMO cathodes: (b) Cyclic performance at 0.5 C, (c) Rate capability performance, (d) Long cycling stability of bare and hybrid LPO-TiO coated LNMO, and (e) EIS plots after 300 cycles of bare and hybrid LPO-TiO coated LNMO.

Controllable ALD synthetic process with various LPO/TiO growth sequences is further investigated to demonstrate the unique structural properties of the developed hybrid LPO-TiO coating for LNMO cathodes. As presented in Figure 4.3a, different ALD growth sequences result in alternative coating structures. No matter what ALD sequence is employed, the fundamental design of layer-by-layer LPO + TiO (or TiO + LPO) coating is different from the synchronous growth of hybrid LPO-TiO coating layer. Although depositing with the same thickness of 1 nm, the layer-by-layer structure, which is composed by 0.5 nm LPO coating layer and 0.5 nm TiO coating layer, blocks the Li-ion or electron path-way that cannot provide continuous ionic or electronic conductivity for cathode at the same time. Especially for high-rate cycling performance, the LPO-TiO hybrid structure is proposed to have the edge over the layer-by-layer structure to build an ionic and electronic conductive interface for LNMO. Figure 4.3b describes the cycling performance of LNMO cathodes with as-prepared ALD coatings at 0.5 C. All of the

coated cathodes demonstrate improved cycling stability compared to the bare LNMO because the ionic and electronic conductivity are not the determining factor for the discharge capacity and cycling stability at such low current density. EIS plots of the above four LNMO cathodes after 100 cycles are shown in Figure S9, all modified LNMO cathodes demonstrate reduced interfacial resistance comparing with the bare LNMO cathode, indicating both hybrid and layer-by-layer coating layer are able to suppress the side-reactions with electrolyte. Impressively, the four cathodes demonstrate significant different rate capability as shown in Figure 4.3c. The hybrid LPO-TiO coated LNMO presents the best rate performance that the capacity at 2 C (91.4 mAh g^{-1}) and 5 C (60 mAh g^{-1}) is much higher than the other three cathodes. The performance differences are from the distinct structural mechanisms of the ALD coatings. As aforementioned, the hybrid LPO-TiO coating enables to improve the electronic and ionic conductivity at the same time for LNMO, facilitating the electrochemical reaction transformation at high current density. For layer-by-layer structured LPO + TiO (or TiO + LPO) coating, there is not a continuous Li-ion or electron path-way for LNMO cathode and therefore presenting limited high-rate capacities. Long-cycling performance at different current densities of hybrid LPO-TiO coated LNMO is present in Figure 4.3d. The coated cathode demonstrates a stable and prolonged cycle life at 0.5 C over 300 cycles with the capacity retention of 81.2%. The capacity decay is only 0.075 mAh g^{-1} per cycle. On the contrary, the capacity retention of bare LNMO is only 47.4% after 300 cycles at 0.5 C with capacity decay of 0.204 mAh g^{-1} per cycle, which is 2.72 times worse than the hybrid LPO-TiO coated LNMO. Even at 1 C, the battery with coated LNMO still demonstrates very stable and high cycling capacity, where the capacity retention is 84.7% even higher than that of at 0.5 C. EIS plots of the batteries after 300 cycles are investigated in Figure 4.3e. Interestingly, the hybrid LPO-TiO coated LNMO present a much smaller interfacial resistance than the bare one, confirming the design concept of hybrid LPO-TiO that protect LNMO to minimize unwanted side-reactions on the surface during cycling.
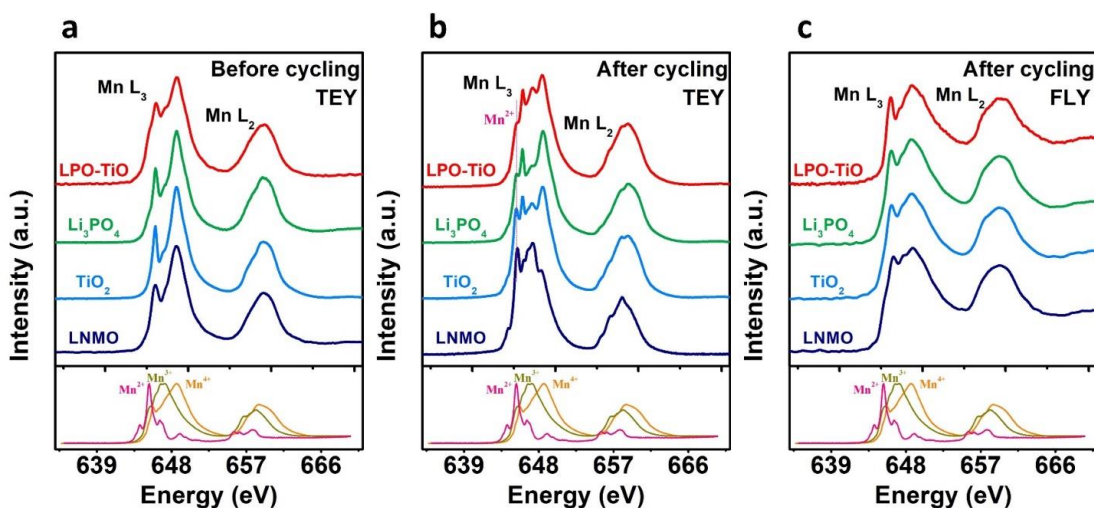
Figure 4.4 Understanding the surface chemical structure evolution of LNMO cathodes before and after the electrochemical reaction. Mn L-edge XANES spectra of bare, TiO$_2$, Li$_3$PO$_4$, and LPO-TiO coated LNMO. (a) Before charge/discharge cycling collected at TEY mode, (b-c) After 100 charge/discharge cycles collected at TEY and FLY mode, respectively.

In order to further unveil the phase transformation mechanism and the change of surface chemical states upon charging/discharging, Mn L-edge XANES of the LNMO cathodes is collected before and after cycling using total electron yield mode (TEY) shown in Figure 4.4. The TEY mode manifests information from the surface region with a depth of around 5 nm.[41, 42] Before cycling, the four as-prepared LNMO cathodes present nearly identical spectra. The spectra consist of well-separated L$_2$ and L$_3$ absorption features, resulting from the 2p core-hole spin-orbital splitting.[43, 44] The predominant peaks at 645.9 eV and 648.6 eV attributing to L$_3$-edge and the broader peak belonging to L$_2$-edge in the spectra can be assigned to Mn^{4+}. The unchanged spectra of the four LNMO cathodes indicate that the Mn species existed in similar chemical environment in the close surface region before and after ALD coating. However, the spectra of cycled cathodes demonstrate significant differences, as shown in Figure 4.4b. The spectrum of the bare LNMO cathode shows two new peaks at 647.2 eV and 645.4 eV that can be assigned to Mn^{3+} and Mn^{2+}, respectively, while the previous predominant Mn^{4+} peaks are nearly disappeared. The formation of Mn^{3+} derives from the Jahn-Teller distortion and

oxidation of electrolyte during charge/discharge processes.[44] The following disproportionation reaction triggers the reduction of Mn from trivalence to bivalence, which takes place at the interface of cathode and electrolyte.[45] Mn^{2+} is easy to dissolve into the electrolyte, and further migrate through the separator then depositing on the surface of anode.[46-48] Meanwhile, transition metals (TMs) can facilitate the decomposition of electrolyte, which accelerate side-reactions during cycling.[26, 49] All of these phase evolution results in the structural degradation of LNMO at the surface and cycling capacity decay of batteries. On the contrary, all three coated LNMO cathodes still maintain the predominant peaks of Mn^{4+} after cycling, although Mn^{3+} peaks still could be found in the spectra of the coated LNMO cathodes after cycling, which indicates that the surface side-reaction of LNMO can be suppressed to some extent but still cannot totally avoid even with the ALD coating materials. Interestingly, the intensity of Mn^{3+} peak in Li_3PO_4 coated LNMO is lower than that of TiO_2 coated LNMO, which demonstrates the electrochemical stability of PO_4^{3-} at high voltage. The intensity ratio of Mn^{2+} to Mn^{4+} is much reduced compared to the bare LNMO, when coating materials are implemented on the surface of LNMO particles. Only a shoulder peak of Mn^{3+} can be found in LPO-TiO coated LNMO cathode, indicating that the hybrid LPO-TiO coating can effectively suppress continued side-reactions with the electrolyte and help to avoid the Mn^{2+} dissolution during cycling. The XPS spectra of Li metals from both bare and LPO-TiO samples are shown in Figure S12. The Mn peak can be detected from the surface of Li metal in bare sample, while no signal of Mn from LPO-TiO sample can be observed after cycling. This result further indicates Mn dissolution and deposition on the surface of Li metal due to lack of the protection of coating layer on the surface of cathodes. The bulk sensitive XANES spectra of LNMO cathodes collecting by florescence yield mode (FLY) are shown in Figure 4.4c. The bulk Mn of bare LNMO after cycling also presents the weak Mn^{3+} peak in the spectrum, indicating electrolyte persistently destroying the inner structure of LNMO particles without any coating protection. On the contrary, all of the FLY spectra of coated cathodes are similar to the spectra before cycling (Figure 4a), indicating the good protection of the LNMO bulk structure by ALD coating.
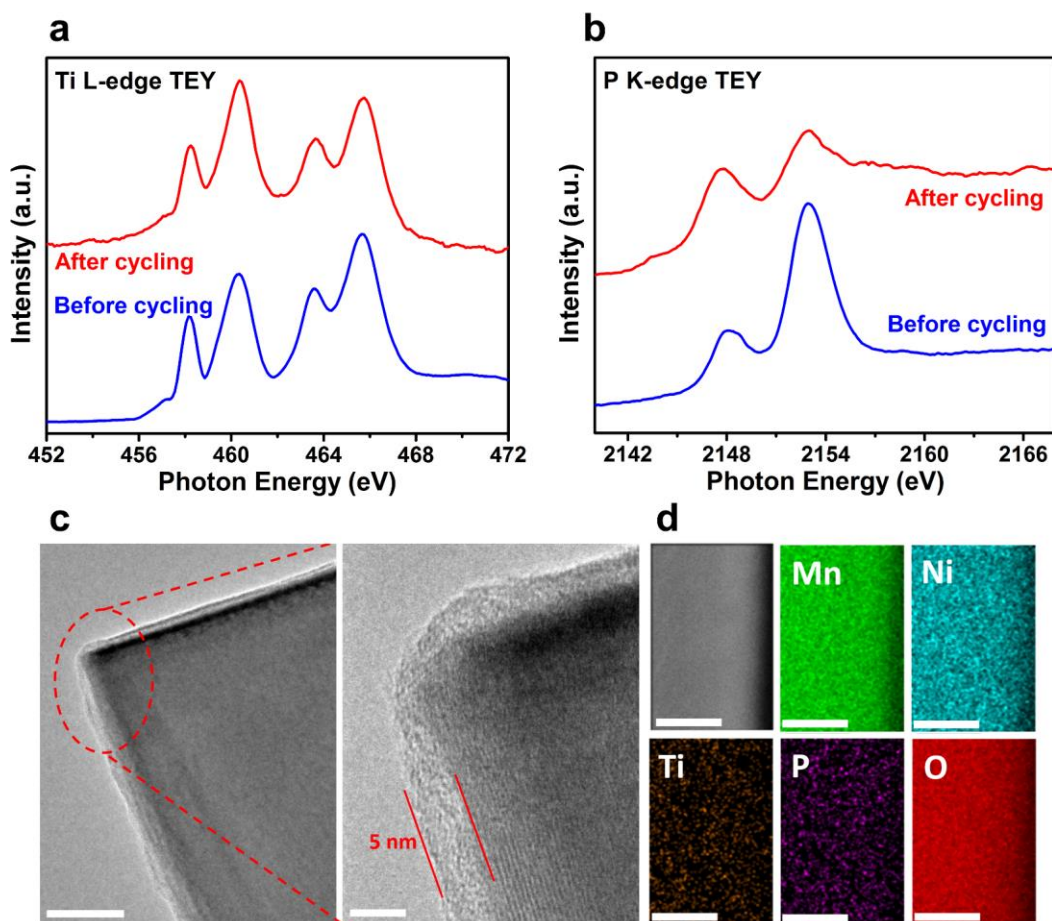
Figure 4.5 Post-characterizations of hybrid LPO-TiO coated LNMO cathode after battery cycling. (a) Ti L-edge and (b) P K-edge XANES spectra of hybrid LPO-TiO coated LNMO before and after charge/discharge cycling, (c) STEM image (scale-bar 40 nm) with selected enlarged region (scale-bar 5 nm) and (d) STEM-HAADF image and the corresponding EDS mapping (scale-bar 25 nm) of hybrid LPO-TiO coated LNMO after charge/discharge cycling.

XANES and STEM characterizations are conducted to further investigate the structure and chemical state stability of hybrid LPO-TiO coating layer during cycling. Figures 4.5a and 4.5b show the Ti L-edge and P K-edge XANES in TEY mode of hybrid LPO-TiO coated LNMO cathode before and after cycling. Impressively, the spectra are nearly identical before and after battery operation, indicating the chemical stability of the coating layer during cycling. (S)TEM and corresponding EDS mapping are shown in

Figure 4.5c and 4.5d. It should be noted that the sample for TEM characterization is using the ALD LPO-TiO coating of 5 nm in thickness, which is the same sample employed in Figure 4.1b. The ALD LPO-TiO hybrid coating layer after battery operation is still conformally coated on the surface of LNMO particle with an approximate thickness of 5 nm, which is consistent with the TEM result of ALD coating layer before cycling (Figure 4.1b). EDX elemental mapping also demonstrates the presence of Ti and P elements on the surface of LNMO particle, further confirming the chemical stability of hybrid LPO-TiO coating layer in high voltage battery operation.

4.4 Conclusion

In conclusion, we demonstrate a controllable LPO-TiO hybrid coating material via ALD for the high voltage LNMO cathode in Li-ion batteries. The novel coating is not only as a simple physical barrier to avoid the side-reactions between cathode and electrolyte at high operating voltage. More importantly, the hybrid LPO-TiO coating layer enables enhanced ionic and electronic conductivity for the cathode that builds a stable solid-state interface between cathode and electrolyte to allow smooth Li-ions and electrons transportation. The initial capacity of the coated LNMO cathode increased from 110 mAh g^{-1} to 122 mAh g^{-1} comparing with bare LNMO, and the cycling capacity retention is over 89.3% after 100 cycles at 0.5 C. Furthermore, the long cycling performance of LNMO cathode for 300 cycles at high current density also presents the significant improvement with the support of LPO-TiO coating. The capacity decay of 0.075 mAh g^{-1} per cycle with 81.2% capacity retention is obtained at 0.5 C, which is only 0.37 times compared to bare LNMO. Even at 1 C, hybrid LPO-TiO coated sample still demonstrates the capacity retention of 84.7%, which is 1.79 times higher than that of bare LNMO at 0.5 C. The excellent electrochemical performance indicates the prolonged cycle life of LNMO cathode with the advanced coating material. TEM and synchrotron XANES characterizations further investigate the evolution of LNMO surfical phase and LPO-TiO coating structure during cycling, which demonstrate that hybrid LPO-TiO coating has sufficient chemical stability to effectively suppress the cathode surface structure degradation and dissolution of transition metals. Compared with traditional inert coating

materials, it is believed that our design of the conductive LPO-TiO hybrid coating by ALD will open up new opportunities for next-generation high energy Li batteries. We hope the revelation of hybrid interfacial design via ALD and other techniques will trigger increased research interests in high-energy batteries and promote novel electrode architectures for energy storage systems.

4.5 Acknowledgements

4.6 References

[1] P.G. Bruce, B. Scrosati, J.M. Tarascon, Angew. Chem. 47 (2008) 2930-2946.

[2] K. Xu, Chem. Rev. 104 (2004) 4303-4418.

[3] P. Yan, J. Zheng, J. Liu, B. Wang, X. Cheng, Y. Zhang, X. Sun, C. Wang, J.-G. Zhang, Nat. Energy 3 (2018) 600-605.

[4] J. Cabana, L. Monconduit, D. Larcher, M.R. Palacin, Adv. Mater. 22 (2010) E170-192.

[5] L. Li, X. Zhang, M. Li, R. Chen, F. Wu, K. Amine, J. Lu, Electrochem. Energy Rev. 1 (2018) 461-482.

[6] R. Schmuch, R. Wagner, G. Hörpel, T. Placke, M. Winter, Nat. Energy 3 (2018) 267-278.

[7] X. Xu, H. Huo, J. Jian, L. Wang, H. Zhu, S. Xu, X. He, G. Yin, C. Du, X. Sun, Adv. Energy Mater. (2019) 1803963.

[8] U.-H. Kim, J.-H. Kim, J.-Y. Hwang, H.-H. Ryu, C.S. Yoon, Y.-K. Sun, Mater. Today 23 (2019) 26-36.

[9] B. Xiao, X. Sun, Adv. Energy Mater. 8 (2018) 1802057.

[10] C. Zhan, T. Wu, J. Lu, K. Amine, Energy Environ. Sci. 11 (2018) 243-257.

[11] M. Hirayama, H. Ido, K. Kim, W. Cho, K. Tamura, J. Mizuki, R. Kanno, J. Am. Chem. Soc. 132 (2010) 15268-15276.

[12] C. Zhan, J. Lu, A. Jeremy Kropf, T. Wu, A. N. Jansen, Y. K. Sun, X. Qiu, K. Amine, Nat. Commun. 4 (2013) 2437.

[13] Y. Ding, Z. P. Cano, A. Yu, J. Lu, Z. Chen, Electrochem. Energy Rev. 2 (2019) 1-28.

[14] U.-H. Kim, H.-H. Ryu, J.-H. Kim, R. Mücke, P. Kaghazchi, C. S. Yoon, Y.-K. Sun, Adv. Energy Mater. 9 (2019) 1803902.

[15] D. Kim, S. Park, O. B. Chae, J. H. Ryu, Y.-U. Kim, R.-Z. Yin, S. M. Oh, J. Electrochem. Soc. 159 (2012) A193-A197.

[16] J. Chong, S. Xun, J. Zhang, X. Song, H. Xie, V. Battaglia, R. Wang, Chem. Eur. J. 20 (2014) 7479-7485.

[17] S. Zhao, B. Sun, K. Yan, J. Zhang, C. Wang, G. Wang, ACS Appl. Mater. Interfaces 10 (2018) 33260-33268.

[18] S. Zhao, K. Yan, P. Munroe, B. Sun, G. Wang, Adv. Energy Mater. 9 (2019) 1803757.

[19] X.-D. Zhang, J.-L. Shi, J.-Y. Liang, Y.-X. Yin, J.-N. Zhang, X.-Q. Yu, Y.-G. Guo, Adv. Mater. 30 (2018) 1801751.

[20] H.-B. Kang, S.-T. Myung, K. Amine, S.-M. Lee, Y.-K. Sun, J. Power Sources 195 (2010) 2023-2028.

[21] J.-H. Cho, J.-H. Park, M.-H. Lee, H.-K. Song, S.-Y. Lee, Energy Environ. Sci. 5 (2012) 7124.

[22] F. Cheng, Y. Xin, Y. Huang, J. Chen, H. Zhou, X. Zhang, J. Power Sources 239 (2013) 181-188.

[23] W.-K. Shin, Y.-S. Lee, D.-W. Kim, J. Mater. Chem. A 2 (2014) 6863-6869.

[24] J.W. Kim, D.H. Kim, D. Y. Oh, H. Lee, J. H. Kim, J. H. Lee, Y. S. Jung, J. Power Sources 274 (2015) 1254-1262.

[25] Q. Wu, X. Zhang, S. Sun, N. Wan, D. Pan, Y. Bai, H. Zhu, Y. S. Hu, S. Dai, Nanoscale 7 (2015) 15609-15617.

[26] S. Deng, B. Xiao, B. Wang, X. Li, K. Kaliyappan, Y. Zhao, A. Lushington, R. Li, T.-K. Sham, H. Wang, X. Sun, Nano Energy 38 (2017) 19-27.

[27] B. Xiao, J. Liu, Q. Sun, B. Wang, M. N. Banis, D. Zhao, Z. Wang, R. Li, X. Cui, T.-K. Sham, X. Sun, Adv. Sci. 2 (2015) 1500022.

[28] X. Li, J. Liu, M. N. Banis, A. Lushington, R. Li, M. Cai, X. Sun, Energy Environ. Sci. 7 (2014) 768-778.

[29] F.-D. Yu, L.-F. Que, C.-Y. Xu, M.-J. Wang, G. Sun, J.-G. Duh, Z.-B. Wang, Nano Energy 59 (2019) 527-536.

[30] H. Liu, C. Chen, C. Du, X. He, G. Yin, B. Song, P. Zuo, X. Cheng, Y. Ma, Y. Gao, J. Mater. Chem. A 3 (2015) 2634-2641.

[31] B. Wang, J. Liu, Q. Sun, R. Li, T.K. Sham, X. Sun, Nanotech. 25 (2014) 504007.

[32] B. Wang, J. Liu, Q. Sun, B. Xiao, R. Li, T.-K. Sham, X. Sun, Adv. Mater. Interfaces 3 (2016) 1600369.

[33] D. Vantelon, A. Hofmann, K. Hanselmann, A. M. Flank 882 (2007) 232-234.

[34] J. Prietzel, A. Dümig, Y. Wu, J. Zhou, W. Klysubun, Geochim. Cosmochim. Acta 108 (2013) 154-171.

[35] B. Kim, M. Gautier, C. Rivard, C. Sanglar, P. Michel, R. Gourdon, Environ. Sci. Tech. 49 (2015) 4903-4910.

[36] A. A. Mosquera, J. L. Endrino, J. M. Albella, J. Anal. Atom. Spectrom. 29 (2014) 736-742.

[37] A. Sharma, M. Varshney, J. Park, T.-K. Ha, K.-H. Chae, H.-J. Shin, RSC Adv. 5 (2015) 21762-21771.

[38] B. Kim, M. Gautier, C. Rivard, C. Sanglar, P. Michel, R. Gourdon, Environ. Sci. Tech. 49 (2015) 4903-4910.

[39] J. M. Tarascon, J. Electrochem. Soc. 138 (1991) 2859.

[40] K. Y. Chung, W.-S. Yoon, K.-B. Kim, X.-Q. Yang, S. M. Oh, J. Electrochem. Soc. 151 (2004) A484-A492.

[41] T. Okumura, T. Fukutsuka, K. Matsumoto, Y. Orikasa, H. Arai, Z. Ogumi, Y. Uchimoto, Dalton T. 40 (2011) 9752-9764.

[42] T. Okumura, M. Shikano, H. Kobayashi, J. Power Sources 244 (2013) 544-547.

[43] F. M. F. de Groot, J. C. Fuggle, B. T. Thole, G. A. Sawatzky, Phys. Rev. B 42 (1990) 5459-5468.

[44] N. P. W. Pieczonka, Z. Liu, P. Lu, K. L. Olson, J. Moote, B. R. Powell, J.-H. Kim, J. Phys. Chem. C 117 (2013) 15947-15957.

[45] C. Zhan, J. Lu, A. Jeremy Kropf, T. Wu, A.N. Jansen, Y.-K. Sun, X. Qiu, K. Amine, Nat. Commun. 4 (2013) 2437.

[46] K. Y. Chung, W.-S. Yoon, H. S. Lee, X.-Q. Yang, J. McBreen, B. H. Deng, X. Q. Wang, M. Yoshio, R. Wang, J. Gui, M. Okada, J. Power Sources 146 (2005) 226-231.

[47] J.-H. Kim, N.P.W. Pieczonka, Z. Li, Y. Wu, S. Harris, B. R. Powell, Electrochim. Acta 90 (2013) 556-562.

[48] P. V. Sushko, K. M. Rosso, J.-G. Zhang, J. Liu, M. L. Sushko, Adv. Funct. Mater. 23 (2013) 5530-5535.

[49] W. Liu, Q. Shi, Q. Qu, T. Gao, G. Zhu, J. Shao, H. Zheng, J. Mater. Chem. A 5 (2017) 145-154.

4.7 Supporting information
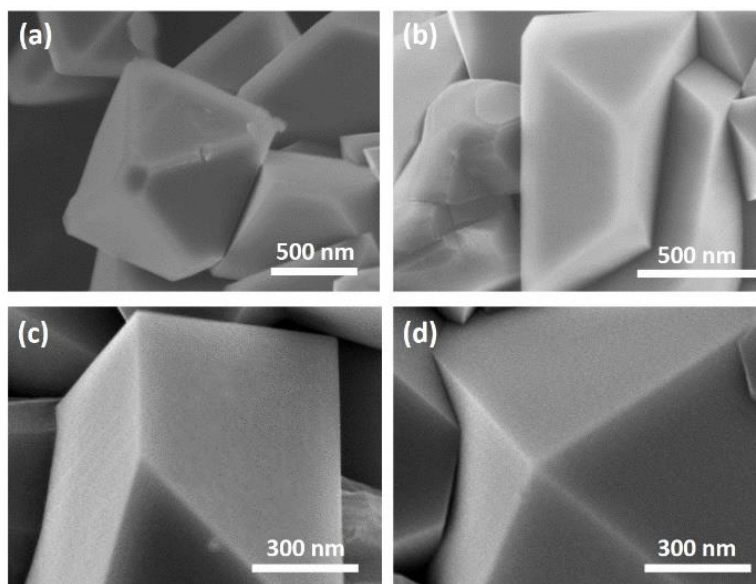
Figure S1. SEM images of (a-b) bare; and (c-d) LPO-TiO coated LNMO.
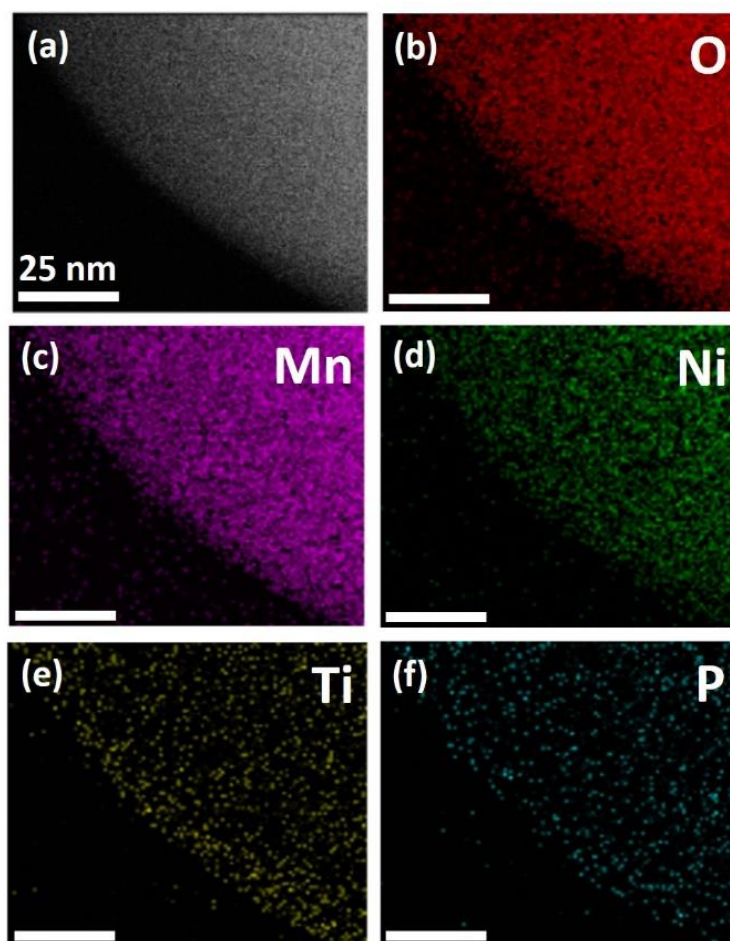
Figure S2. TEM EDS results of LPO-TiO coated LNMO. a) STEM image and (b-f) corresponding EDS elemental mapping. Scale bar, 25 nm.
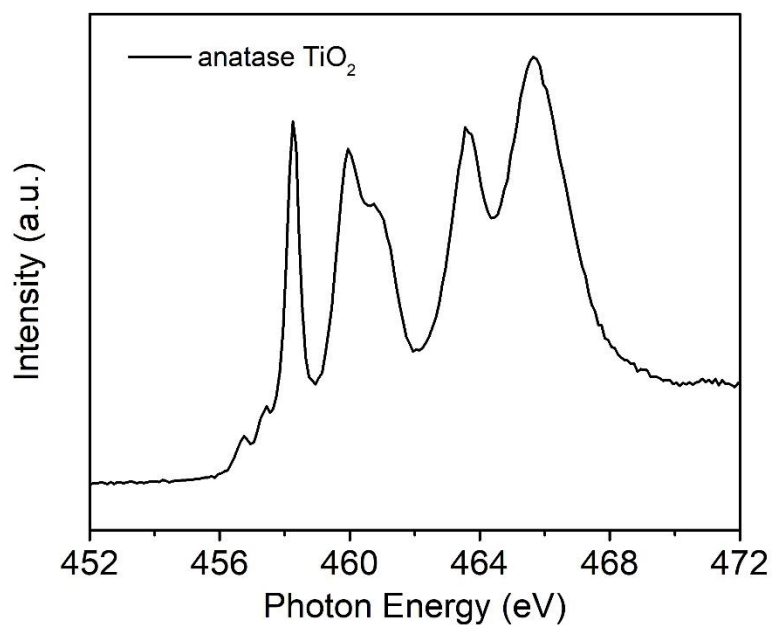
Figure S3. Ti L-edge XANES of anatase TiO_2.
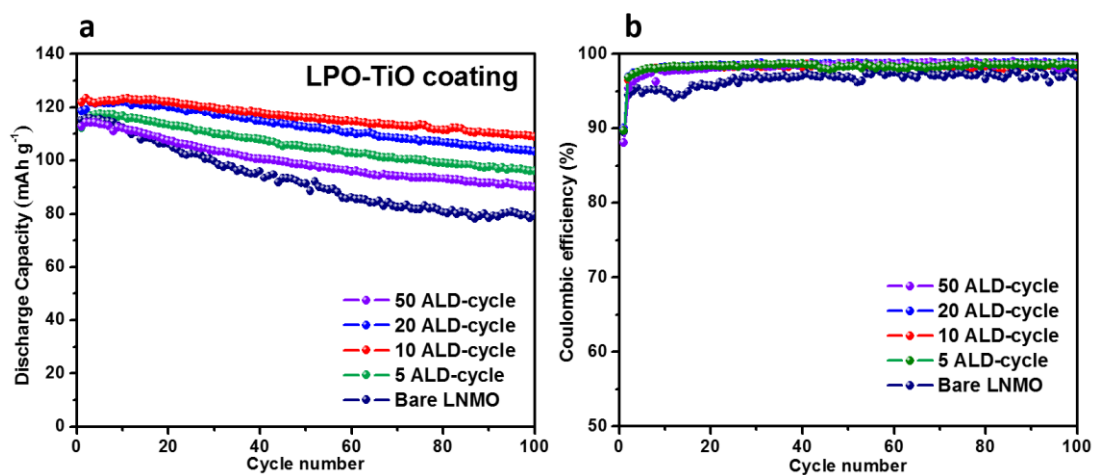
Figure S4. a) Cycling performance and b) coulombic efficiency at 0.5 C of LNMO cathodes with different thicknesses of LPO-TiO coating.
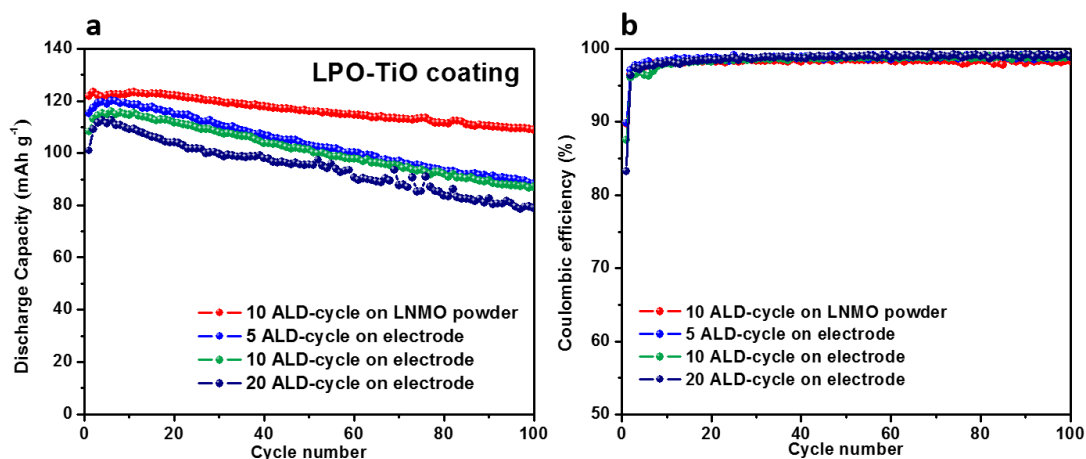
Figure S5. Electrochemical performance comparison of the LNMO cathodes with the LPO-TiO coating on LNMO powder (red) and LNMO electrodes (other colors).
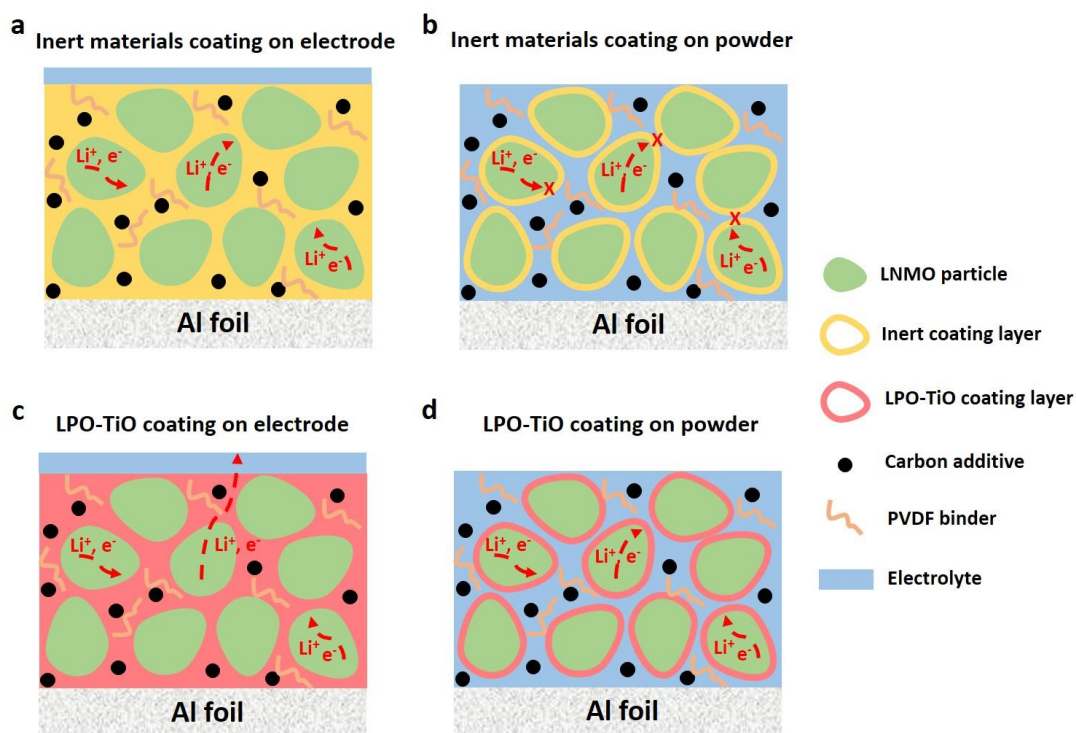
Figure S6. Schematic illustration of different coating materials on LNMO powder and LNMO electrodes.

LPO-TiO coating on cathode powder shows better performance than coating on the electrode. That is because good interfacial ionic and electronic conductivities of LPO-TiO hybrid coating layer facility Li^+ and electron transfer on the surface of cathode particles and increase the contact between cathode particles and electrolyte. On the contrary, the inert materials block the Li^+ and electron transfer if coating on the cathode particles. So the performance is lower than coating on the electrode.
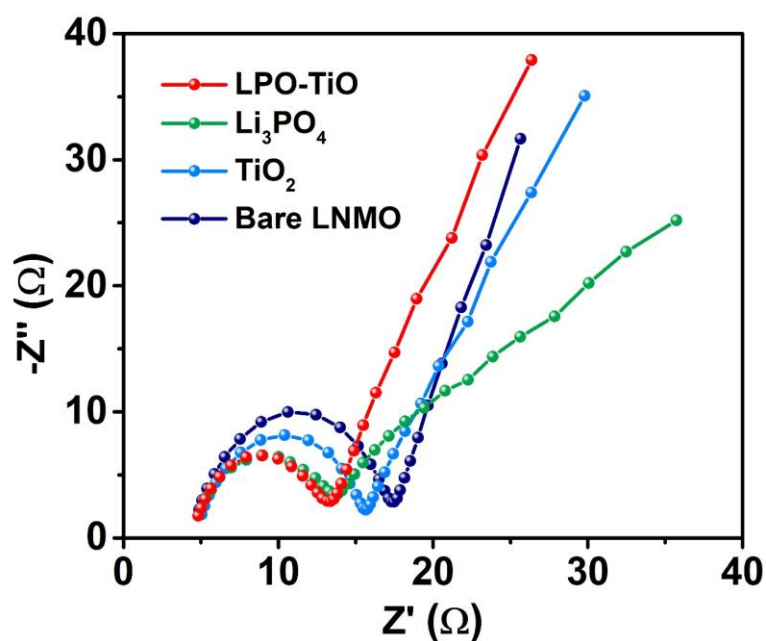
Figure S7. EIS plots of bare and various ALD coating materials on LNMO cathode after 1st cycle.
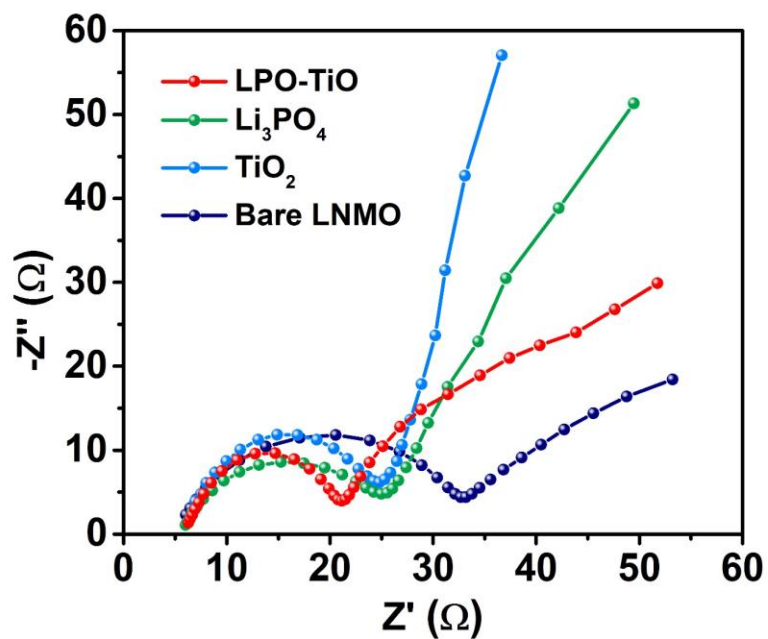
Figure S8. EIS plots of bare and various ALD coating materials on LNMO cathode after 50th cycles.
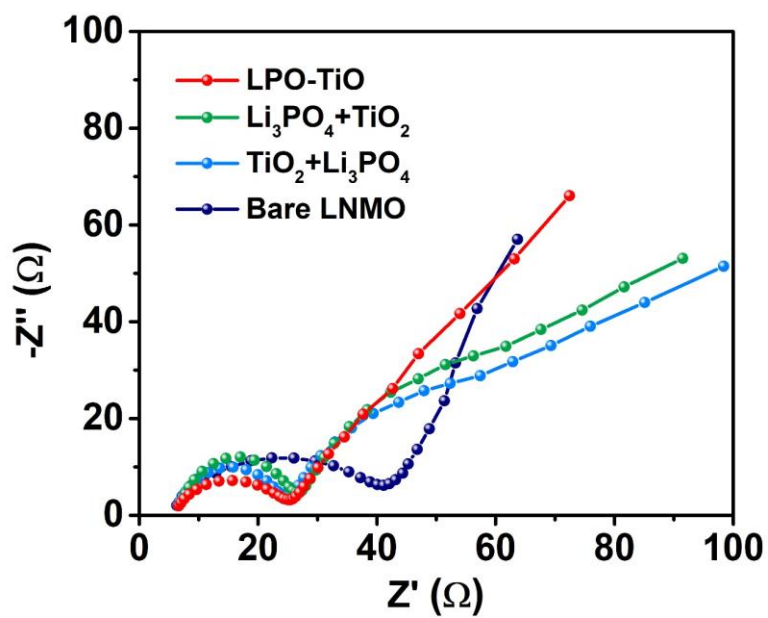
Figure S9. EIS plots of bare and different ALD growth sequences of LPO and TiO on LNMO cathodes after 100th cycles.
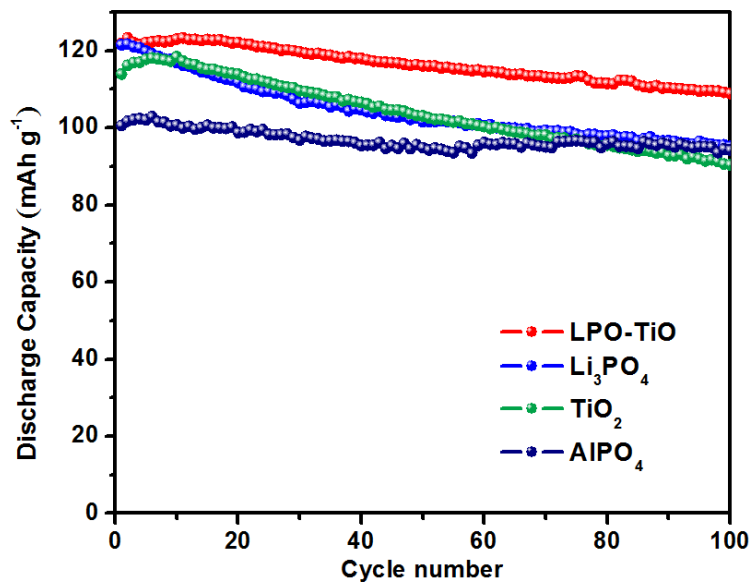
Figure S10. Electrochemical performance comparison of the LNMO cathodes with different coating materials.
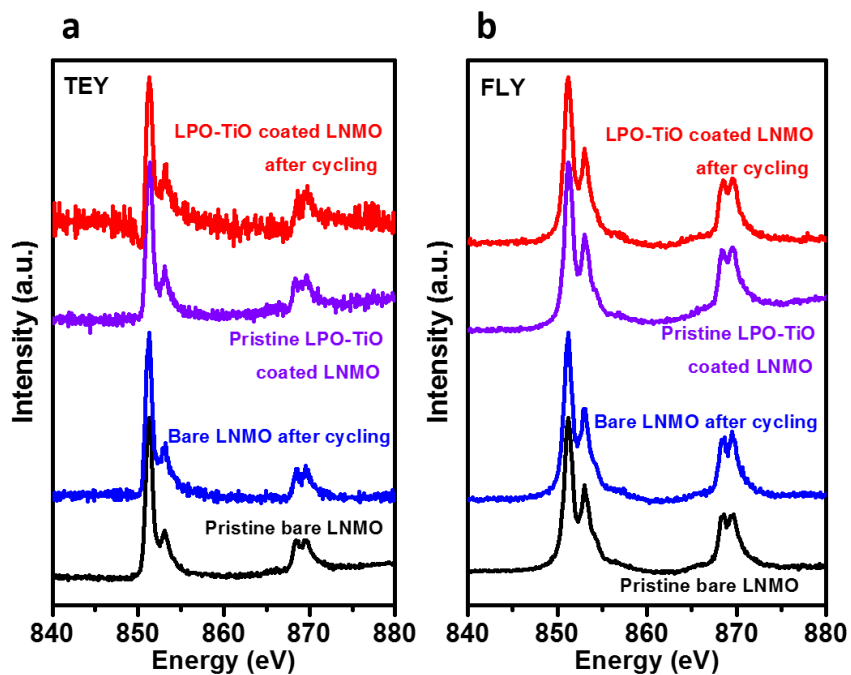
Figure S11. Ni L-edge of a) TEY and b) FLY spectra of bare and LPO-TiO coated LNMO before and after cycling.
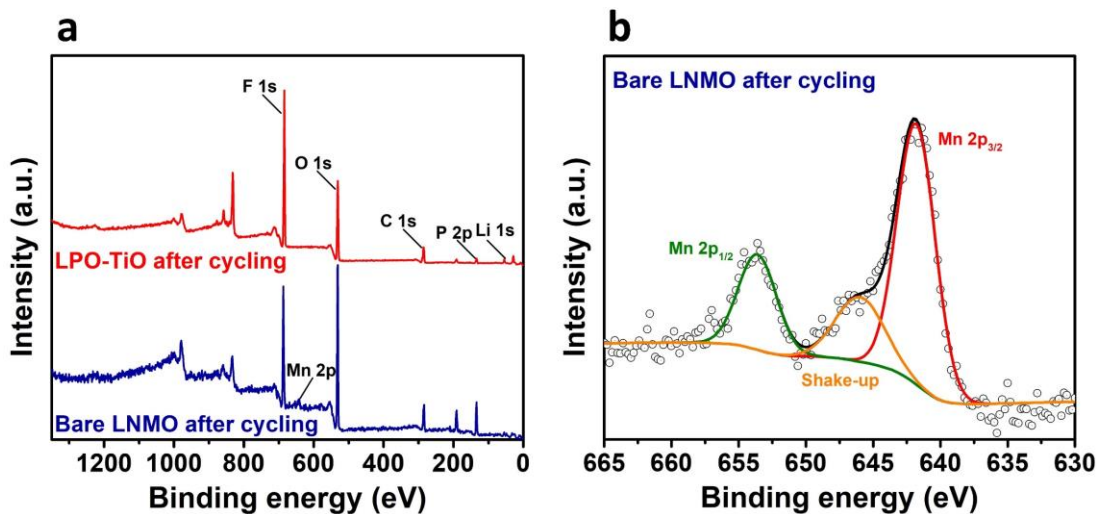
Figure S12. a) The full survey XPS spectra of Li metals in bare and LPO-TiO modified samples after cycling; b) Mn 2p spectrum of Li metal in bare sample after cycling.
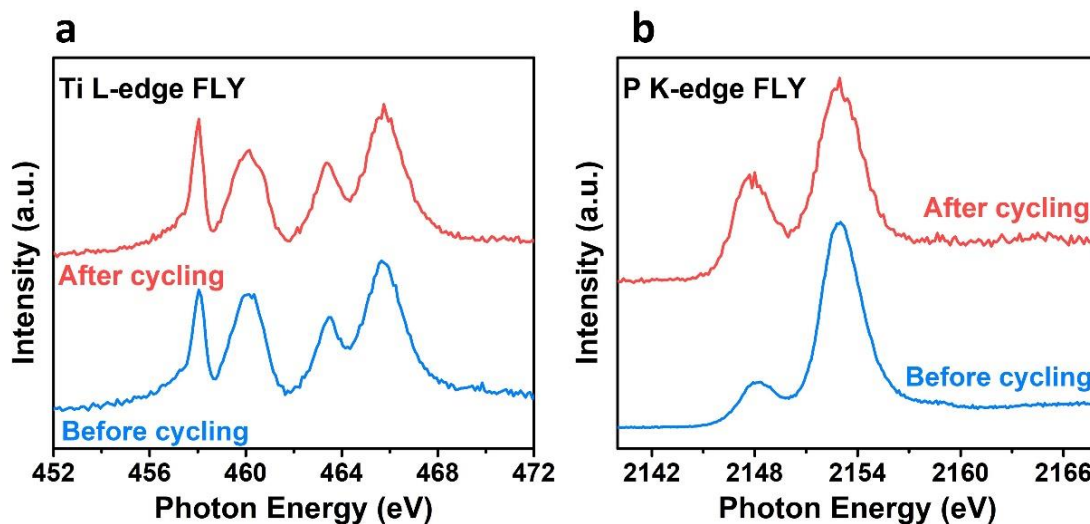
Figure S13. a) Ti L-edge FLY and b) P K-edge FLY spectra of LPO-TiO coated LNMO before and after cycling.

Chapter 5

5   Dual-Functional Interfaces for Highly Stable Ni-Rich Layered Cathodes in Sulfide All-Solid-State Batteries*

All-solid-state lithium-ion batteries (ASSLIBs) are expected as safe and high-performance alternatives to replace the conventional liquid-based lithium-ion batteries. However, the incompatible interface between the most cathode materials and sulfide-based solid electrolytes is still challenging the stable delivery of electrochemical performance for ASSLIBs. Herein, a dual-functional Li_3PO_4 (LPO) modification is designed for Ni-rich layered oxide cathodes in sulfide-based ASSLIBs to realize the high performance. The modified cathode demonstrates a significantly improved initial capacity of 170.6 mAh g^{-1} at 0.1C, better rate capability, and reduced polarization compared to the bare cathode. More importantly, a stable long-term cycling is achieved with a low capacity degradation rate of 0.22 mAh g^{-1} per cycle for 300 cycles at 0.2C. The detailed surface chemical and structural evolutions are studied via X-ray absorption near edge spectroscopy, X-ray photoelectron spectroscopy, and transmission electron microscopy. The results indicate that the LPO modification not only significantly suppresses the side-reactions with sulfide electrolyte but also helps to alleviate the deterioration of the microstructural cracks during the electrochemical reactions. This work provides an ideal and controllable interfacial design for realizing high performance sulfide-based ASSLIBs, which is readily applicable to other solid-state battery systems.

5.1 Introduction

Along with the rapid development of electric vehicles (EVs), the safety concerns and insufficient energy density of conventional lithium-ion batteries with the use of liquid organic electrolytes have become urgent challenges to be solved.[1, 2] All-solid-state lithium-ion batteries (ASSLIBs) are expected to be a promising alternative considering the use of non-flammable inorganic solid electrolytes and the potential boost of energy density due to a simplified battery structure.[3, 4] Among the developed solid-state electrolytes, sulfide-based electrolytes, providing high Li^+ conductivities of 10^{-2}-10^{-4} S cm^{-1} at room temperature, show great promise to replace the commercial liquid electrolytes.[5, 6] However, the application of sulfide-based electrolytes in ASSLIBs still has several outstanding challenges and the cycling performance of the reported batteries decays dramatically with the low initial capacity and Columbic efficiency.[7]

Interfacial incompatibility between cathode materials and sulfide-based electrolytes is the first challenge to the performance of ASSLIBs. The interfacial issues of cathodes mainly derive from the instability of the electrolytes at high voltages, leading to severe side-reactions with cathodes such as the formation of unfavorable cathode electrolyte interface (CEI) and degradation of the surficial structure of cathodes.[8] As a result, the cycling performance decays dramatically with the low initial capacity and Columbic efficiency.[9] As reported in many previous studies, coatings are the most effective strategies to alleviate the side-reactions, such as using $LiNbO_3$, $LiAlO_2$, $Li_4Ti_5O_{12}$, etc.[10-12] Another severe challenge is the integration of high capacity cathodes with outstanding volume change in ASSLIBs. Ni-rich $LiNi_xMn_yCo_{1-x-y}O_2$ (NMC) layered oxide cathodes are capable of delivering high discharge capacity greater than 200 mAh g^{-1}, especially with the high Ni content ($x \geq 0.8$).[13-15] However, due to the anisotropic volume change induced by the unstable Ni^{4+} species in Ni-rich NMC during charging and discharging, Ni-rich NMC in the sulfide-based ASSLIBs still suffers from the severe contact loss between cathode particles and sulfide electrolytes.[16, 17] The irreversible volume change of cathodes leads to the internal microstructural cracks emerge and propagate along the grain boundaries from the bulk to surface,[18, 19] therefore, block

the Li$^+$ diffusion not only inside the secondary particles of cathodes but also at the interface between cathode particles and sulfide electrolytes.[20, 21] As a result, the obvious capacity loss can be detected during the cycling. It is worth noting that although various surficial coating materials have been reported to alleviate side-reactions between sulfide SSEs and cathode materials, very few studies gave effort to the challenge of microstructural cracks and contact loss derived by cathode volume change.

To overcome the two challenges at cathode part in sulfide-based ASSLIBs, in this work, we construct a dual-functional hierarchical Li$_3$PO$_4$ (LPO) modification via atomic layer deposition (ALD) for Ni-rich NMC (LiNi$_{0.8}$Mn$_{0.1}$Co$_{0.1}$O$_2$, in short HLPO@NMC811) cathodes in sulfide-based ASSLIBs. In our previous study, an ALD LPO solid electrolyte was adopted as the interfacial materials to tailor the grain boundaries of Ni-rich NMC cathodes.[22] The infused LPO not only eliminated interfacial reactions with the liquid electrolyte at the grain boundaries, but also alleviated the microstructural cracks and phase evolution from layer to spinel structure, which significantly improved the cycling stability of Ni-rich NMC cathodes in liquid electrolytes. To impart and further advance this developed structure in ASSLIBs, in this research, we first infuse a primary LPO coating layer of 10-nm thick into the inner of NMC811 particles and then deposit a secondary LPO coating layer to shield the NMC811 surface. Detailed electrochemical and material characterizations demonstrate that the dual-functional modification by hierarchical LPO not only effectively alleviates the severe side-reactions with sulfide electrolyte (Li$_{10}$GeP$_2$S$_{12}$, in short LGPS) but also suppresses the microstructural cracks of cathodes during charge/discharge cycling, significantly improves the cycling stability of Ni-rich NMC cathodes in sulfide-based ASSLIBs. Our dual-functional modification design shed lights on simultaneously solving the two key challenges of Ni-rich layered oxide cathodes for sulfide-based ASSLIBs and present promising ultra-long cycle life over 300 cycles of sulfide-based ASSLIBs.

5.2 Experimental section

Preparation of ALD LPO modified NMC811 cathodes: The lithium phosphate (LPO) was deposited on the surface of NMC811 powders using lithium tertbutoxide (LiOtBu)

and trimethyl phosphate (TMPO) as precursors in a Savannah 100 ALD system (Cambridge Nanotech, USA). The source temperatures for LiOtBu and TMPO were 180 °C and 75 °C, respectively. The deposition temperature for LPO was 250 °C. During one ALD cycle, LiOtBu and TMPO were alternatively introduced into the reaction chamber with a pulse time of 2 s, and the pulsing of each precursor was separated by a 15 s purge with N_2. The primary LPO coating layer with a thickness of 10 nm was deposited on the surface of NMC811 powders by ALD. For infusion, the LPO-coated cathode powder were further annealed at 600 °C for 2 h. Furthermore, the LPO-annealed powders were subject to another ALD LPO coating with the thickness of 1 nm, 5 nm, or 10 nm.

Characterizations: X-ray power diffraction (XRD) measurements were carried out on a Bruker D8 Advance Diffractometer (Cu-Ka source, 40 kV, 40 mA). The morphologies of various cathodes were captured using field emission scanning electron microscopy (FESEM, Hitachi S4800) and high-resolution transmission electron microscopy (HRTEM, JEOL 2010FEG). The morphology and microstructure of cycled NMC811 cathodes were obtained by focused ion beam (FIB, Helios NanoLab 460HP, FEI)/FESEM (FE-SEM; JEOL JSM-7001F) for a detailed structural analysis. The obtained FIB samples were further investigated by aberration-corrected scanning transmission electron microscopy (STEM, Titan Cubed Themis G2 300) with elemental mapping images. To avoid contamination of samples, the cycled samples were scratched from the pallet and sealed in a glovebox under Ar. After that, the sealed samples were quickly transferred to the corresponding techniques for further measurements. The X-ray photoelectron spectroscopy (XPS) were measured with a monochromatic Al Kα source (1486.6 eV) in a Kratos AXIS Nova Spectrometer. The Ar filled glovebox was connected with XPS machine to avoid the exposure of air. X-ray absorption near edge structure (XANES) measurements were carried out at the Canadian Light Source (CLS). S, P, Ni, Co, and Mn K-edge XANES were collected using fluorescence yield mode on the soft X-ray microcharacterization beamline (SXRMB). To avoid air exposure, all the samples were covered with Mylar film in glovebox under Ar, and then transferred to the chamber of the corresponding beamline.

Electrochemical Testing: The fabrication of all-solid-state batteries was carried out in an Ar-filled glovebox. Firstly, the electrolyte layer was prepared by pressing 70 mg commercial $Li_{10}GeP_2S_{12}$ (LGPS, 99.95%, MSE supplies, LLC) at 2 ton (~250 MPa) to form a pellet with 10 mm diameter. The cathode composite was then mixed with NMC811 cathodes powder and commercial LGPS powder at a weight ratio of 70:30. 10 mg as-prepared cathode composite was spread on the surface of LGPS electrolyte followed by pressing at 3 ton (~380 MPa). Finally, a piece of In foil (99.99%, Φ 10 mm, thickness 0.1 mm) was put onto the other side of the LGPS pellets with a Cu foil and pressed at 0.5 ton (~65 MPa). The three-layered pellet (cathode composite/LGPS/In anode) was sandwiched between two stainless-steel rods as current collectors for both positive and negative electrodes. No extra pressure was applied on the final tested all-solid-state batteries. The galvanostatic charge/discharge characteristics were tested in a range of 2.7-4.5 V vs. Li/Li^+, at room temperature by using a multichannel battery tester (LAND CT-2001A, Wuhan Rambo Testing Equipment Co., Ltd.). Cyclic voltammograms (CV) were collected on a versatile multichannel potentiostation 3/Z (VMP3) using a scan rate of 0.05 mV s^{-1} between 2.7-4.5 V vs. Li/Li^+. Electrochemical impedance spectroscopy (EIS) was also performed on the versatile multichannel potentiostat 3/Z (VMP3) by applying an AC voltage of 10 mV amplitude in the 7000 kHz to 100 mHz frequency range.

5.3 Results and discussion
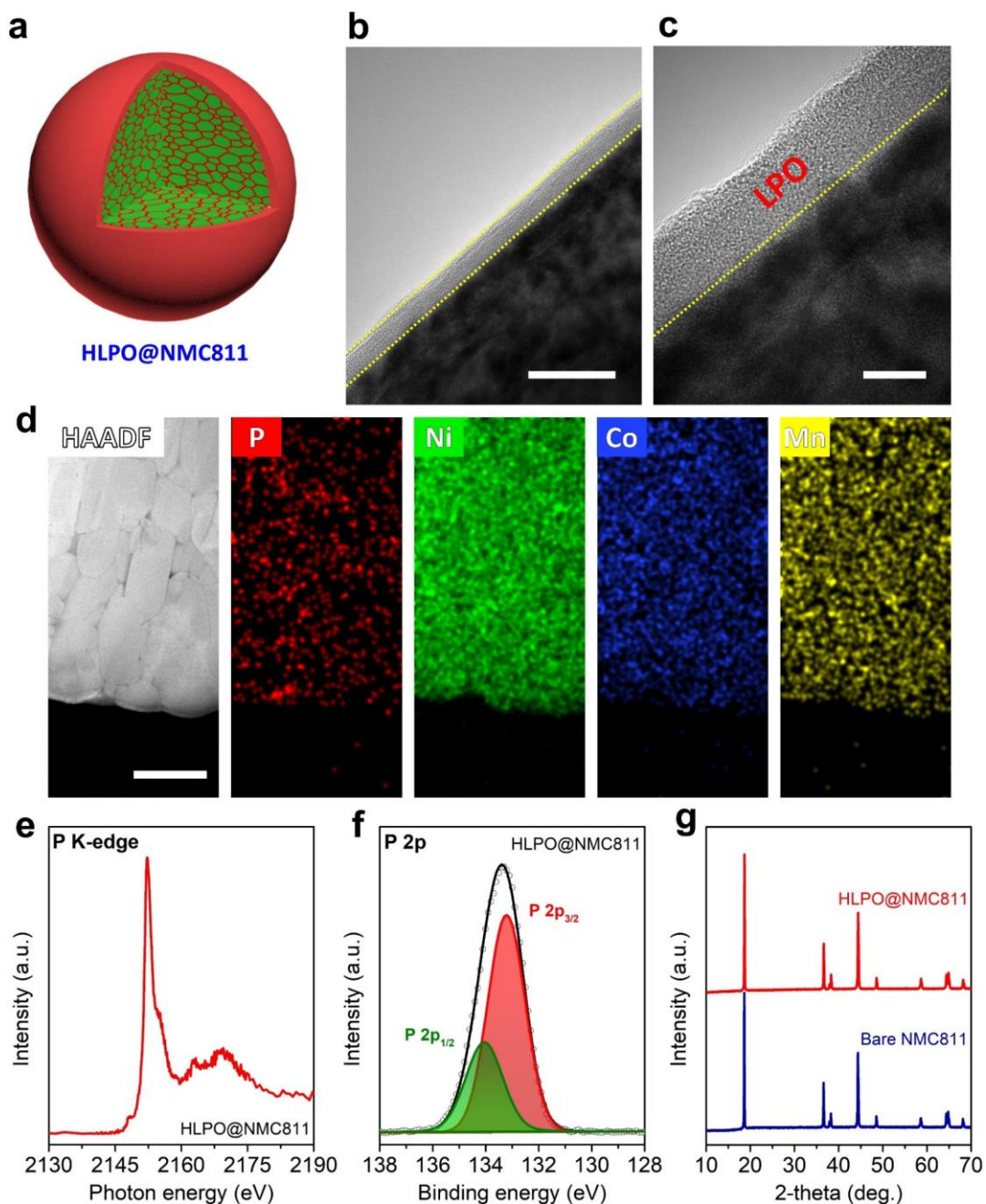
Figure 5.1 Schematic structure and characterizations of HLPO@NMC811 modification. a) Schematic illustration of the detailed structure of HLPO@NMC811, b-c) HR-TEM images of the secondary LPO coating layer on the HLPO@NMC811 surface at different magnifications, d) EDX mappings of the cross-sectional HLPO@NMC811, e-

f) P K-edge XANES and P 2p XPS spectra of HLPO@NMC811, g) XRD patterns of the bare NMC811 and HLPO@NMC811. Scale bars in (b), (c), and (d) are 20 nm, 5 nm, and 500 nm, respectively.

For comparison, four types of NMC811 cathodes with different modification procedures (Figure S1) were prepared, including (i) bare NMC811, (ii) only a primary ALD LPO coating on NMC811 (LPO@NMC811), (iii) infused LPO into NMC811 by subsequent annealing (iLPO@NMC811), and (iv) a secondary ALD LPO coating on top of iLPO@NMC811 for a hierarchical coverage (HLPO@NMC811). Figure 5.1a schematically depicts the ultimate design of HLPO@NMC811. According to the scanning electron microscopy (SEM) and transmission electron microscopy (TEM) analyses, the conformal secondary LPO coating by ALD completely cover the cathode particle with a uniform thickness of 5 nm (Figure 5.1b-c and S2). The energy dispersive X-ray (EDX) elemental mappings of a cross-sectional HLPO@NMC811 particle cut by focused ion beam (FIB) are shown in Figure 5.1d. The enriched P signals across the particle indicate the successful infusion of phosphorus element into the inner of cathode particles by annealing. The P K-edge X-ray absorption near edge structure (XANES) collected by the florescence yield (FLY) mode and P 2p X-ray photoelectron spectroscopy (XPS) analyses of HLPO@NMC811 confirm the chemistry of the LPO components (Figure 5.1e and f). The FLY mode detects a depth up to several microns, obtaining information from the surfaces to the bulk of HLPO@NMC811 (considering the micron-sized scale of NMC811 secondary particles).[23] The P signal can be detected in both P K-edge XANES and P 2p XPS spectra, indicating the LPO exists both on the surface and in the bulk structure of NMC811 particles. X-ray diffraction (XRD) patterns of the bare NMC811 and samples with different modifications show good retention of the NMC811 crystallinity without noticeable impurity phase caused by the ALD or annealing process (Figure 5.1g and S3).
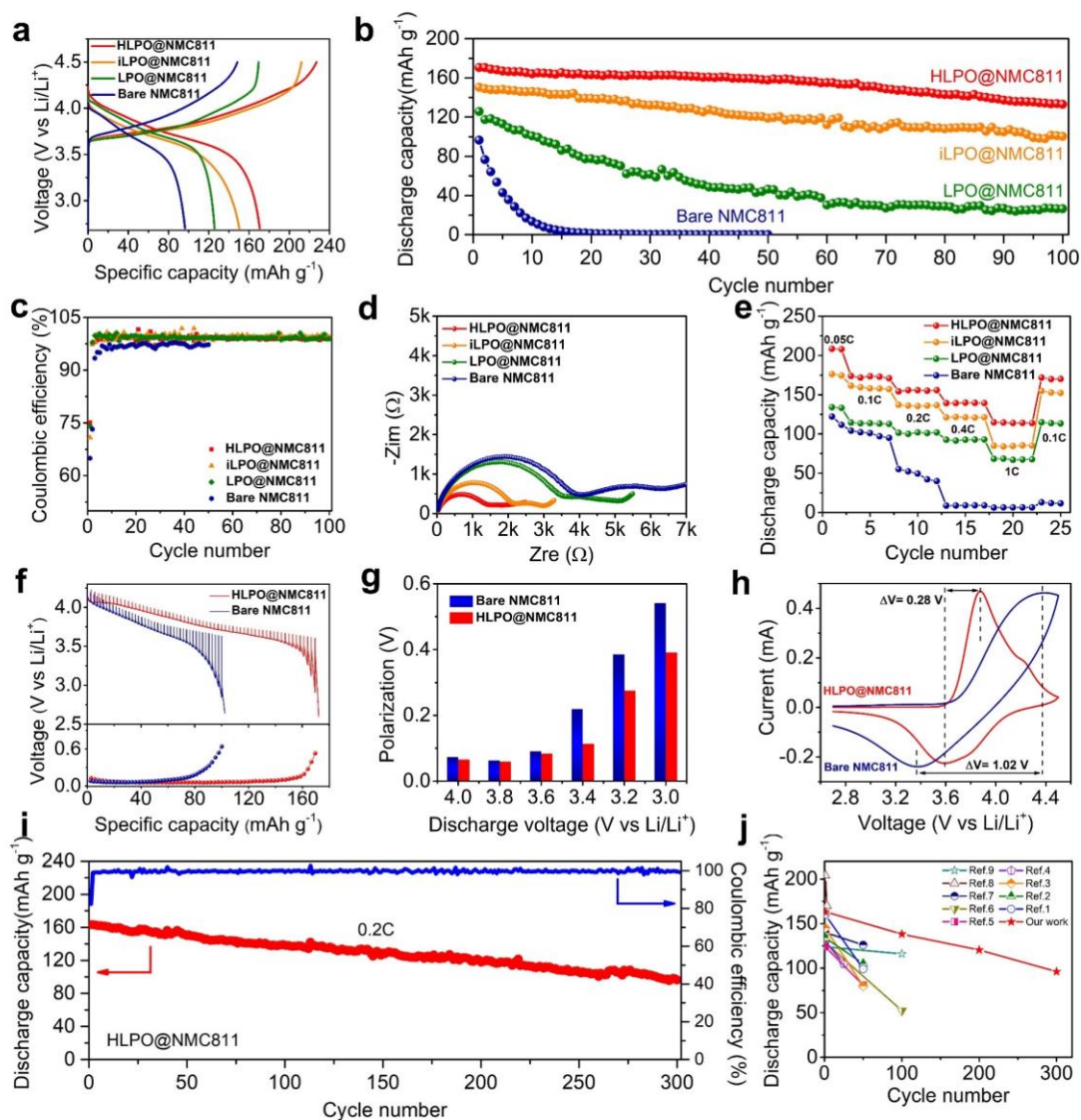
Figure 5.2 Effectiveness of various LPO modifications for ASSLIBs performance. a) Charge/discharge curves of the first cycle, b) cycling stabilities at 0.1C, c) corresponding Coulombic efficiencies, d) EIS plots after 100 cycles, and e) rate capability for the four types of NMC811 cathodes. More details of the optimal HLPO@NMC811 cathode in comparison with the bare NMC811 regarding f) GITT curves during the discharge process (top) and corresponding polarization plots (bottom), g) polarization plots at selected discharge voltages, h) CV profiles at the first cycle. i) Long-term cycling stability of the HLPO@NMC811 cathode at 0.2C. j) Cycling performance of our work and reported Ni-rich NMC cathodes in sulfide-based ASSLIBs.

The bare NMC811, LPO@NMC811, iLPO@NMC811, and HLPO@NMC811 were respectively mixed with the LGPS electrolytes as a composite cathode layer for electrochemical evaluations in ASSLIBs. The detailed fabrication process of the ASSLIBs is described in the experimental section. Figure 5.2a compares the first-cycle charge/discharge curves of these four different ASSLIBs at 0.1C. The initial discharge capacity of the bare cathode is only 96.4 mAh g^{-1} with the severe polarization. Compared to the bare cathode, all LPO modified cathodes exhibit the obviously improved discharge capacities, with the HLPO@NMC811 cathode demonstrating the most significant improvement. The HLPO@NMC811 based ASSLIB achieves a high discharge capacity of 170.6 mAh g^{-1} with the smallest polarization. Upon further cycling at 0.1C, the ASSLIBs with different cathodes show dramatic difference in stability over 100 cycles (Figure 5.2b). The ASSLIB using bare NMC811 is completely failed within 50 cycles. On sharp contrast, the HLPO@NMC811 based ASSLIB maintains a high discharge capacity of 133.0 mAh g^{-1} after 100 cycles, which still far surpasses even the initial discharge capacity of the cells using bare NMC811 and LPO@NMC811. As shown in Figure S4, the optimized thickness of the secondary ALD LPO coating for HLPO@NMC811 is 5 nm. An unoptimized secondary coating could be too thin to prevent side-reactions with the sulfide electrolyte or too thick that in turn limit the ASSLIB performance due to additional internal resistance. In this context, ALD is a unique technique that controls coating precision to the nanoscale.[24] Moreover, the superiority of the HLPO@NMC811 cathode over other NMC811 based cathodes is also consistently exhibited in terms of high Coulombic efficiency and low internal resistance during cycling. The HLPO@NMC811 based ASSLIB possesses a significantly increased initial Coulombic efficiency of 75.1% (versus 64.9% of the bare NMC811 cell) and maintains a high Coulombic efficiency above 99% during the following cycles (Figure 5.2c). As shown in Figure 5.2d, the HLPO@NMC811 based ASSLIB shows the smallest internal resistance after 100 cycles by up to several folds among all the cells, even though the HLPO@NMC811 cathode experienced the greatest depths of charge and discharge.

Interestingly, despite the inferior performance to the HLPO@NMC811 based ASSLIB, the iLPO@NMC811 cathode delivers higher discharge capacity, more stable cycling

performance, and much lower internal resistance than the LPO@NMC811. This suggests that the cracking induced contact loss between cathode particles and the sulfide electrolyte has a more serious influence on the electrochemical performance than the interfacial side-reactions. The electrochemical impedance spectroscopy (EIS) plots show a consistent trend. More specifically, the EIS plots of the ASSLIBs using different NMC811 cathodes show only one semicircle before cycling, which corresponded to the bulk resistance of the solid electrolyte (Figure S5).[20] After cycling, two semicircles emerge in the high and medium frequencies, indicating deteriorative side-reactions and/or loss of contact at the interface between NMC811 and LGPS during cycling. The substantially larger impedance of the LPO@NMC811 cell than that of the iLPO@NMC811 cell again confirms the cracking induced battery degradation. The corresponding equivalent circuit for fitting the EIS plots and the fitted resistance values are shown in Figure S6 and Table S1, respectively.

Under a wide range of current densies from 0.05C to 1C, the ASSLIB using HLPO@NMC811 cathode demonstrates the most outstanding rate capability over other NMC811 based cathodes (Figure 5.2e). Even at 1C, the HLPO@NMC811 cathode still delivered the discharge capacity of about 115 mAh g^{-1}. However, the discharge capacity of the bare cathode dropped to less than 10 mAh g^{-1} at the same current density. Correspondingly, the charge/discharge voltage profiles of the HLPO@NMC811 based ASSLIB exhibit reduced polarization compared to that of the bare NMC811 cell at all current densities (shown in Figure S7). Furthermore, the galvanostatic intermittent titration technique (GITT) curves of the bare NMC811 and HLPO@NCM811 cathodes during the discharge process are given in Figure 5.2f along with the corresponding polarization plots at different voltages in Figure 5.2g. Obviously, HLPO@NCM811 cathode presents smaller polarization potential than that of the bare NMC811 cathode at each voltage, indicating effective stabilization of the cathode throughout the discharging process by the hierarchical LPO modification. Cyclic voltammetry (CV) profiles of the bare and LPO modified cathodes are shown in Figure 5.2h and S8-9. The voltage gap between the redox peaks of the HLPO@NCM811 cathode is significantly smaller than that of the bare NMC811 cathode. Meanwhile, the HLPO@NCM811 cathode shows a

much lower current value at the cut-off charging voltage of 4.5 V than the bare NMC811 cathode, indicating substantially reduced oxidized reaction with sulfide electrolyte. Figure 5.2i shows stable long-term cycling of the HLPO@NCM811 based ASSLIB at 0.2C for 300 cycles. The modified cathode demonstrates a high initial discharge capacity of 163.2 mAh g^{-1} and retains 96.1 mAh g^{-1} after 300 cycles. The average capacity decay is 0.22 mAh g^{-1} per cycle, which is a great improvement for sulfide based ASSLIBs. Figure 5.2j compares the cycling performance between HLPO@NMC811 and the reported Ni-rich NMC in sulfide-based ASSLIBs. The sources of the data are listed in Table S2. It is apparent that the ultra-long cycling stability of the LPO modified cathode overtakes previous results. Overall, the HLPO@NMC811 cathode with hierarchical LPO modification promotes higher specific capacity, improved cycling stability, enhanced rate capability, and reduced voltage polarizations compared to the bare NMC811 cathode, which thanks to the effective suppressions in side-reactions with sulfide electrolyte and internal cracks of NMC811 during the electrochemical cycling.
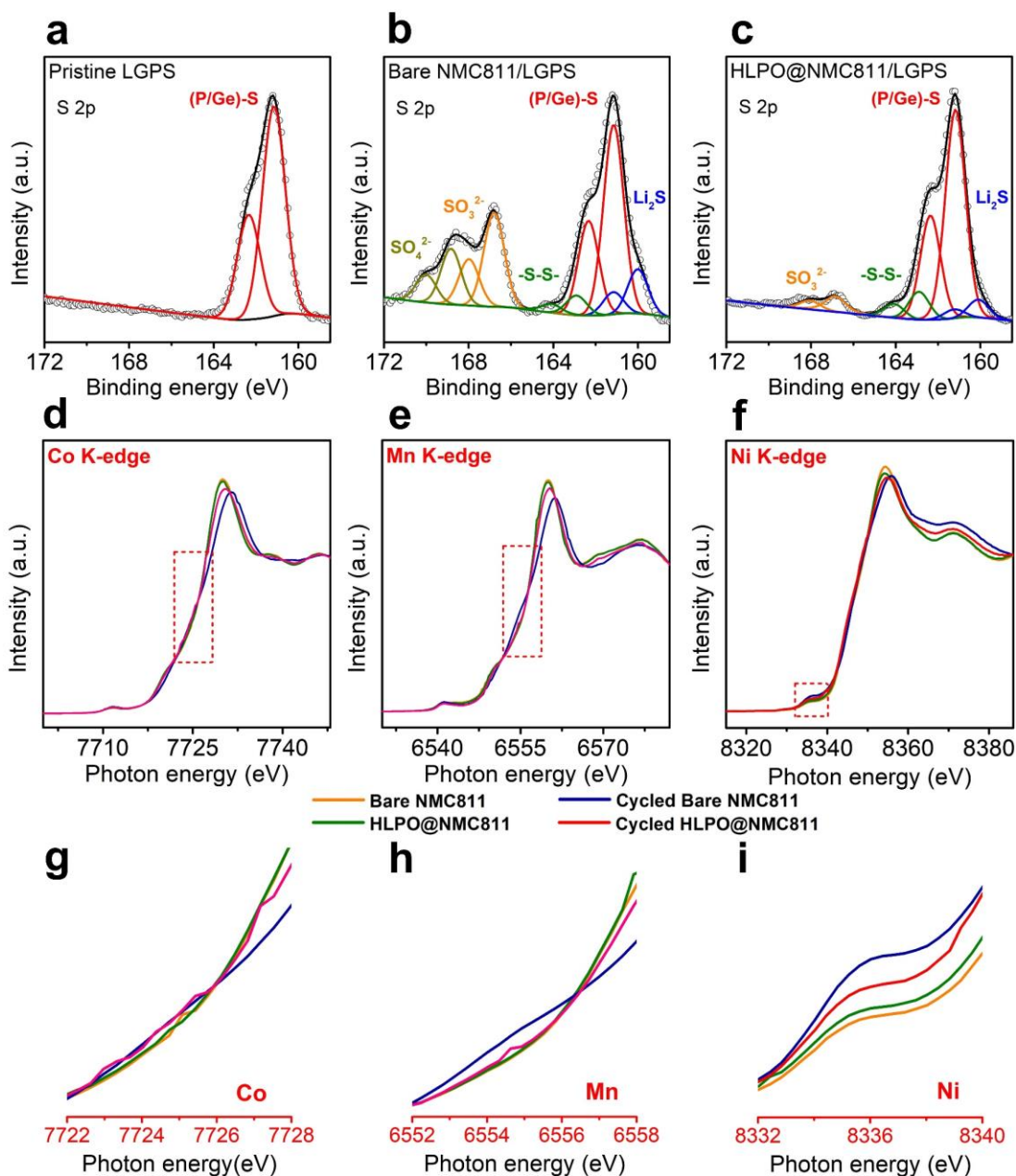
Figure 5.3 Understanding the interfacial chemical evolution during electrochemical reactions. S 2p XPS spectra of the a) pristine LGPS, b) bare NMC811/LGPS electrode after cycling, and c) HLPO@NMC811/LGPS electrode after cycling. d-i) Co, Mn, Ni K-edge XANES spectra of the bare NMC811 and HLPO@NMC811 electrodes before and after cycling: d, g) Co K-edge, e, h) Mn K-edge, f, i) Ni K-edge.

In order to investigate the interfacial chemical evolution as well as the protective role of the LPO modification, XPS and XANES are performed. Figure 5.3b-c and S10 show the XPS results of the LGPS electrolytes collected from the cycled composite electrodes using bare NMC811 and HLPO@NMC811. The XPS spectra of pristine LGPS are provided as references. From S 2p XPS spectra, in addition to the pristine LGPS features at 161.2 eV, the decomposed byproducts of LGPS are observed at 160.1 eV and 162.9 eV from both electrodes because of the inevitable decomposition of LGPS at high voltages,[25] with the bare NMC811 electrode shows higher relative content of Li_2S side product. While the LGPS from both electrodes share common self-decomposition products of Li_2S and -S-S-,[26-28] the dramatically different occurrence of SO_3^{2-} and SO_4^{2-} species indicates different degrees of electrolyte oxidation caused by the cathodes. Presumably, the oxidation of LGPS comes across oxygen participation from the NMC811 structure. Upon increasing depth of charge, the side-reactions between NMC811 and electrolyte become more serious, which lead to the evolution of the layer structure on the cathode particle surface.[29] The structural change is usually accompanied with increase in the effective electron density of oxygen, resulting in the formation of oxygen vacancies.[30-32] The evolution of cathode in turn accelerates the oxidation of electrolyte and the formation of CEI layer, therefore damaging the cycling stability of cathode as shown in Figure 5.2b. The high relative peak intensities of SO_3^{2-} and SO_4^{2-} in Figure 5.3b suggest severe reactions between the unprotected NMC811 and LGPS. Impressively, the SO_4^{2-} signals are essentially absent with only a small amount of SO_3^{2-} when using the HLPO@NMC811, proving effective suppression of side-reactions by the LPO modification. Similar conclusion can be reached from the P 2p and Ge 3d XPS spectra comparisons (Figure S10). After cycling, the characteristic PS_4^{3-} spin-orbit doublet of LGPS is hardly observable on the P 2p spectrum of the bare NMC811 electrode, while the $P_2S_6^{2-}$ peaks (peak B) become stronger. At the same time, three new phosphorus species are found (i.e., C, D, and E), which may be attributed to the -P-S-P- or -Ge-S-P- bonds.[33] As the Ge 3d spectra shown in Figure S10b, the new oxidized species in bare NMC811 electrode are also detected. In great contrast, the evolution of both phosphorus and germanium elements after cycling is effectively suppressed by the hierarchical LPO

modification. The S and P XANES spectra for the bare NMC811 and HLPO@NMC811 electrodes are compared in Figure S11 and show high consistency with the XPS results. Comparing the S K-edge XANES (Figure S11a), the intensity of the peak at 2481.9 eV increases dramatically for the bare NMC811 electrode, confirming the formation of SO_x from the severe side-reactions between NMC811 and LGPS during cycling.[34, 35] On the contrary, the HLPO@NMC811 shows alleviated side-reactions with electrolyte, therefore effectively suppress the formation of SO_x. The S and P XANES spectra of LPO@NMC811 and iLPO@NMC811 are shown in Figure S12 to further demonstrate the different levels of alleviation in the different LPO modification.

The K-edge XANES spectra of transition metals (TMs, including Co, Mn, and Ni) are exhibited in Figure 5.3d-i and S13-14 to understand the structural evolution of the layered NMC811 during cycling. Generally, the oxidation states of TMs in layered cathodes are highly related to the threshold energy position in the K-edge XANES spectra, while the local structural environment between TMs and oxide is determined by the shape of the peaks.[36] Before cycling, both the energy position and the shape of peaks of TMs K-edge XANES spectra of the HLPO@NMC811 cathode show no obvious difference to the bare NMC811 cathode, suggesting the unchanged chemical environments of the TMs upon LPO modification. Interestingly, both Co and Mn K-edge XANES spectra for the cycled bare NMC811 cathode show spectral shape variations without energy shift, indicating changes of local environment of Co and Mn atoms after cycling.[15, 37] In contrast, the shape changes of the spectra for the cycled HLPO@NMC811 cathode are less prominent. Meanwhile, the increased intensity of pre-edge peak for Ni K-edge at 8336.0 eV can be observed in the spectra for both cycled bare NMC811 and HLPO@NMC811 cathodes, indicating local structure distortion of Ni atoms after cycling.[38] However, the HLPO@NMC811 shows much lower level of distortion than the bare NMC811 cathode. Therefore, the obvious shape variations of Co, Mn K-edge spectra and intensity increasing of Ni K-edge spectra after cycling demonstrate that severe side-reactions with LGPS lead to surficial structure evolution of cathode for the cycled bare NMC811, while can be effectively alleviated by the hierarchical LPO modification.
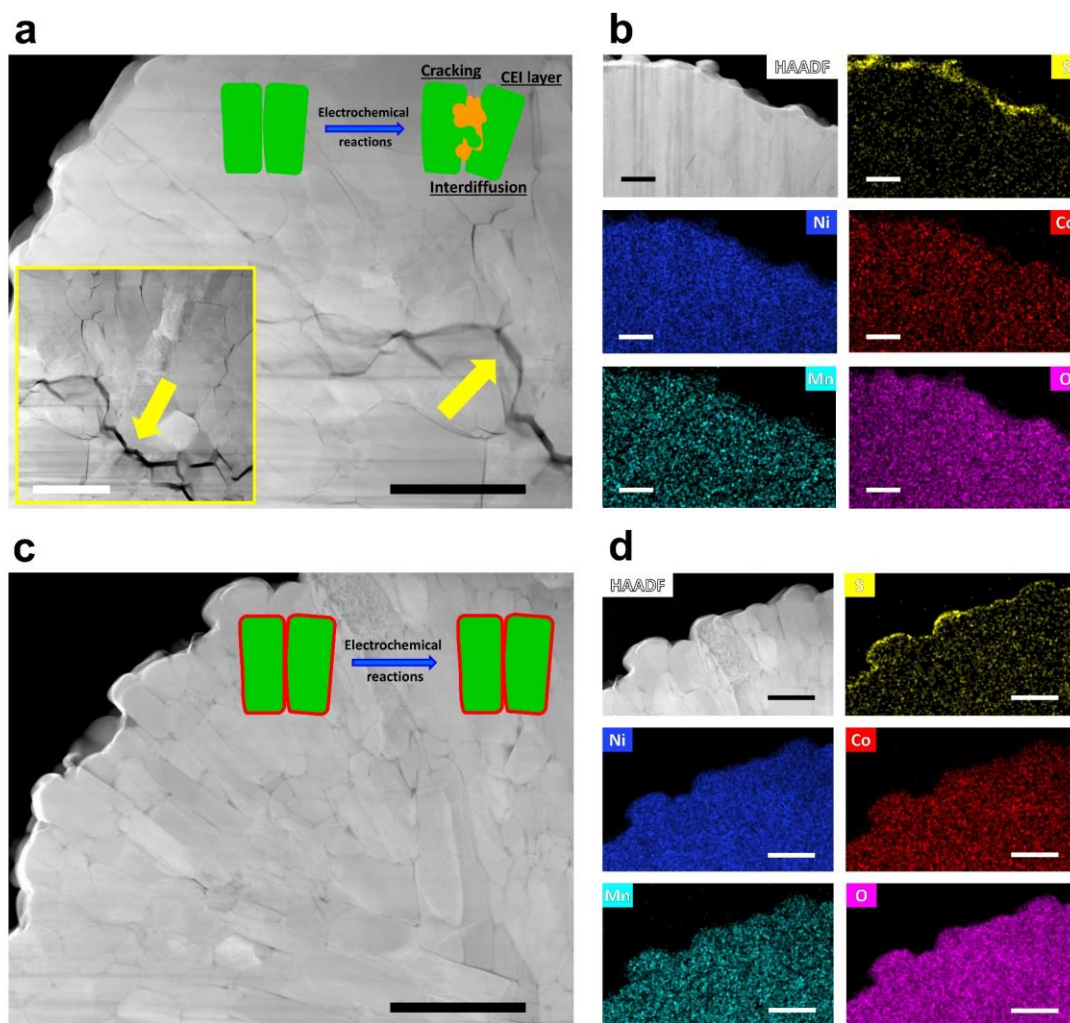
Figure 5.4 Understanding the microstructural evolution of NMC811 during electrochemical reactions. a) Cross-sectional FIB-TEM images of the cycled bare NMC811 particle and b) corresponding EDX mappings. c) Cross-sectional FIB-TEM images of the cycled HLPO@NMC811 particle and corresponding EDX mappings. Scale bars are 1 μm (a and c) and 500 nm (b and d).

The microstructural evolution of Ni-rich NMC cathodes during the electrochemical reactions is another important factor that determines the performance in sulfide-based ASSLIBs. Figure 5.4 compares the cross-sectional TEM images and EDX mappings of the bare NMC811 and HLPO@NMC811 cathode particles after cycling. Obvious microstructural cracks can be observed in the bare NMC811 particle and deteriorate from

central to surface, which can be ascribed to the anisotropic lattice variation induced micro-strain along the grain boundaries of primary cathode particles.[39] As a result, the cracks between primary particles seriously block the lithium ion and electron transfer, therefore isolated primary particles were no longer active in the following cycles, leading to the dramatic performance degradation. On the contrary, the HLPO@NMC811 particle maintains its original microstructure without obvious cracks (Figure 5.4c). As confirmed by the EDX mapping results, despite the uniform distribution of Ni, Mn, Co, and O elements in the bulk of NMC811, the obviously different distributions of S signals are observed for the bare NMC811 and the HLPO@NMC811. The accumulation of sulfur element on the particle surface is much thicker for the bare NMC811 particle than the HLPO@NMC811, indicating the tempting formation of unfavorable CEI layer due to the severe side-reactions with sulfide electrolyte. On the contrary, the LPO modification effectively suppresses the side-reactions between NMC811 and sulfide electrolyte, therefore relieving the formation of CEI layer on the surface of cathode particles.

5.4   Conclusion

In conclusion, we demonstrate a dual-functional ALD LPO modification for Ni-rich NMC layered oxide cathodes for sulfide-based ASSLIBs. The local LPO lithium-ion conductor tailors not only the grain boundaries between the primary cathode particles but also the surface of the secondary particles. Microstructural and interfacial chemical/electrochemical stabilities are simultaneously addressed by the hierarchical design. The optimized HLPO@NMC811 cathode demonstrates significantly improved electrochemical performance with a high initial discharge capacity of 170.6 mAh g^{-1} at 0.1C, good rate capability, small voltage polarization, and encouraging capacity retention of 77.9% after 100 cycles at 0.1C. At a higher current density of 0.2C, a discharge capacity of 96.1 mAh g^{-1} is still maintained after 300 cycles. As confirmed by XPS and synchrotron XANES analyses, the severe side-reactions with LGPS and the surficial structure evolution of the bare NMC811 are effectively suppressed by the hierarchical LPO stabilization. The cross-sectional TEM studies combined with EDX mappings further reveal the microstructural stability of the HLPO@NMC811 cathode and the

minimized interfacial electrolyte decomposition upon cycling, which is distinct from the cracked unprotected NMC811 particle with thick side-products on the surface. Our dual-functional modification design evidently addresses the two main issues of Ni-rich layered oxide cathodes at the same time for sulfide-based ASSLIBs, significantly improving the electrochemical performance, which is a key to the practical application of ASSLIBs in the near future.

5.5 Acknowledgments

5.6 References

[1] H. Li, Joule 3 (2019) 911-914.

[2] F. Lin, D. Nordlund, Y. Li, M.K. Quan, L. Cheng, T.-C. Weng, Y. Liu, H.L. Xin, M.M. Doeff, Nat. Energy 1 (2016) 15004.

[3] A. Manthiram, X. Yu, S. Wang, Nat. Rev. Mater. 2 (2017) 16103.

[4] W. Zhao, J. Yi, P. He, H. Zhou, Electrochem. Energy Rev. (2019) https://doi.org/10.1007/s41918-019-00048-0.

[5] N. Kamaya, K. Homma, Y. Yamakawa, M. Hirayama, R. Kanno, M. Yonemura, T. Kamiyama, Y. Kato, S. Hama, K. Kawamoto, A. Mitsui, Nat. Mater. 10 (2011) 682.

[6] P. Bron, S. Johansson, K. Zick, J. Schmedt auf der Günne, S. Dehnen, B. Roling, J. Am. Chem. Soc. 135 (2013) 15694-15697.

[7] A.M. Nolan, Y. Zhu, X. He, Q. Bai, Y. Mo, Joule 2 (2018) 2016-2046.

[8] W. Zhang, D.A. Weber, H. Weigand, T. Arlt, I. Manke, D. Schröder, R. Koerver, T. Leichtweiss, P. Hartmann, W.G. Zeier, J. Janek, ACS Appl. Mater. Interfaces 9 (2017) 17835-17845.

[9] F. Walther, R. Koerver, T. Fuchs, S. Ohno, J. Sann, M. Rohnke, W.G. Zeier, J. Janek, Chem. Mater. 31 (2019) 3745-3755.

[10] X. Li, M. Liang, J. Sheng, D. Song, H. Zhang, X. Shi, L. Zhang, Energy Storage Mater. 18 (2019) 100-106.

[11] K. Okada, N. Machida, M. Naito, T. Shigematsu, S. Ito, S. Fujiki, M. Nakano, Y. Aihara, Solid State Ionics 255 (2014) 120-127.

[12] Y. Seino, T. Ota, K. Takada, J. Power Sources 196 (2011) 6488-6492.

[13] W. Liu, P. Oh, X. Liu, M.-J. Lee, W. Cho, S. Chae, Y. Kim, J. Cho, Angew. Chem. Int. Edit. 54 (2015) 4440-4457.

[14] H.-H. Ryu, K.-J. Park, C.S. Yoon, Y.-K. Sun, Chem. Mater. 30 (2018) 1155-1163.

[15] S. Guo, B. Yuan, H. Zhao, D. Hua, Y. Shen, C. Sun, T. Chen, W. Sun, J. Wu, B. Zheng, W. Zhang, S. Li, F. Huo, Nano Energy 58 (2019) 673-679.

[16] C.S. Yoon, D.-W. Jun, S.-T. Myung, Y.-K. Sun, ACS Energy Lett. 2 (2017) 1150-1155.

[17] X. Xu, H. Huo, J. Jian, L. Wang, H. Zhu, S. Xu, X. He, G. Yin, C. Du, X. Sun, Adv. Energy Mater. 9 (2019) 1803963.

[18] U.-H. Kim, J.-H. Kim, J.-Y. Hwang, H.-H. Ryu, C.S. Yoon, Y.-K. Sun, Mater. Today 23 (2019) 26-36.

[19] K.-J. Park, H.-G. Jung, L.-Y. Kuo, P. Kaghazchi, C.S. Yoon, Y.-K. Sun, Adv. Energy Mater. 8 (2018) 1801202.

[20] R. Koerver, I. Aygün, T. Leichtweiß, C. Dietrich, W. Zhang, J.O. Binder, P. Hartmann, W.G. Zeier, J. Janek, Chem. Mater. 29 (2017) 5574-5582.

[21] R. Koerver, W. Zhang, L. de Biasi, S. Schweidler, A.O. Kondrakov, S. Kolling, T. Brezesinski, P. Hartmann, W.G. Zeier, J. Janek, Energy Environ. Sci. 11 (2018) 2142-2158.

[22] P. Yan, J. Zheng, J. Liu, B. Wang, X. Cheng, Y. Zhang, X. Sun, C. Wang, J.-G. Zhang, Nat. Energy 3 (2018) 600-605.

[23] A. Erbil, G.S. Cargill Iii, R. Frahm, R.F. Boehme, Phys. Rev. B 37 (1988) 2450-2464.

[24] X. Meng, X.-Q. Yang, X. Sun, Adv. Mater. 24 (2012) 3589-3615.

[25] Y. Zhu, X. He, Y. Mo, ACS Appl. Mater. Interfaces 7 (2015) 23685-23693.

[26] W. Zhang, F.H. Richter, S.P. Culver, T. Leichtweiss, J.G. Lozano, C. Dietrich, P.G. Bruce, W.G. Zeier, J. Janek, ACS Appl. Mater. Interfaces 10 (2018) 22226-22236.

[27] S. Wenzel, S. Randau, T. Leichtweiß, D.A. Weber, J. Sann, W.G. Zeier, J. Janek, Chem. Mater. 28 (2016) 2400-2407.

[28] X. Li, Z. Ren, M. Norouzi Banis, S. Deng, Y. Zhao, Q. Sun, C. Wang, X. Yang, W. Li, J. Liang, X. Li, Y. Sun, K. Adair, R. Li, Y. Hu, T.-K. Sham, H. Huang, L. Zhang, S. Lu, J. Luo, X. Sun, ACS Energy Lett. 4 (2019) 2480-2488.

[29] P. Yan, J. Zheng, J.-G. Zhang, C. Wang, Nano Lett. 17 (2017) 3946-3951.

[30] S. Hwang, W. Chang, S.M. Kim, D. Su, D.H. Kim, J.Y. Lee, K.Y. Chung, E.A. Stach, Chem. Mater. 26 (2014) 1084-1092.

[31] J.D. Steiner, L. Mu, J. Walsh, M.M. Rahman, B. Zydlewski, F.M. Michel, H.L. Xin, D. Nordlund, F. Lin, ACS Appl. Mater. Interfaces 10 (2018) 23842-23850.

[32] C. Tian, D. Nordlund, H.L. Xin, Y. Xu, Y. Liu, D. Sokaras, F. Lin, M.M. Doeff, J. Electrochem. Soc. 165 (2018) A696-A704.

[33] W. Zhang, T. Leichtweiß, S.P. Culver, R. Koerver, D. Das, D.A. Weber, W.G. Zeier, J. Janek, ACS Appl. Mater. Interfaces 9 (2017) 35888-35896.

[34] N. Kornienko, J. Resasco, N. Becknell, C.-M. Jiang, Y.-S. Liu, K. Nie, X. Sun, J. Guo, S.R. Leone, P. Yang, J. Am. Chem. Soc. 137 (2015) 7448-7455.

[35] D.H. Kim, J.H. Kwak, J. Szanyi, S.J. Cho, C.H.F. Peden, J. Phys. Chem. C, 112 (2008) 2981-2987.

[36] X. Yu, Y. Lyu, L. Gu, H. Wu, S.-M. Bak, Y. Zhou, K. Amine, S.N. Ehrlich, H. Li, K.-W. Nam, X.-Q. Yang, Adv. Energy Mater. 4 (2014) 1300950.

[37] E. Hu, X. Yu, R. Lin, X. Bi, J. Lu, S. Bak, K.-W. Nam, H.L. Xin, C. Jaye, D.A. Fischer, K. Amine, X.-Q. Yang, Nat. Energy 3 (2018) 690-698.

[38] P.-Y. Liao, J.-G. Duh, J.-F. Lee, J. Power Sources, 189 (2009) 9-15.

[39] H. Kim, M.G. Kim, H.Y. Jeong, H. Nam, J. Cho, Nano Lett. 15 (2015) 2111-2119.

5.7   Supporting information

A: Bare NMC811

B: LPO@NMC811

C: iLPO@NMC811
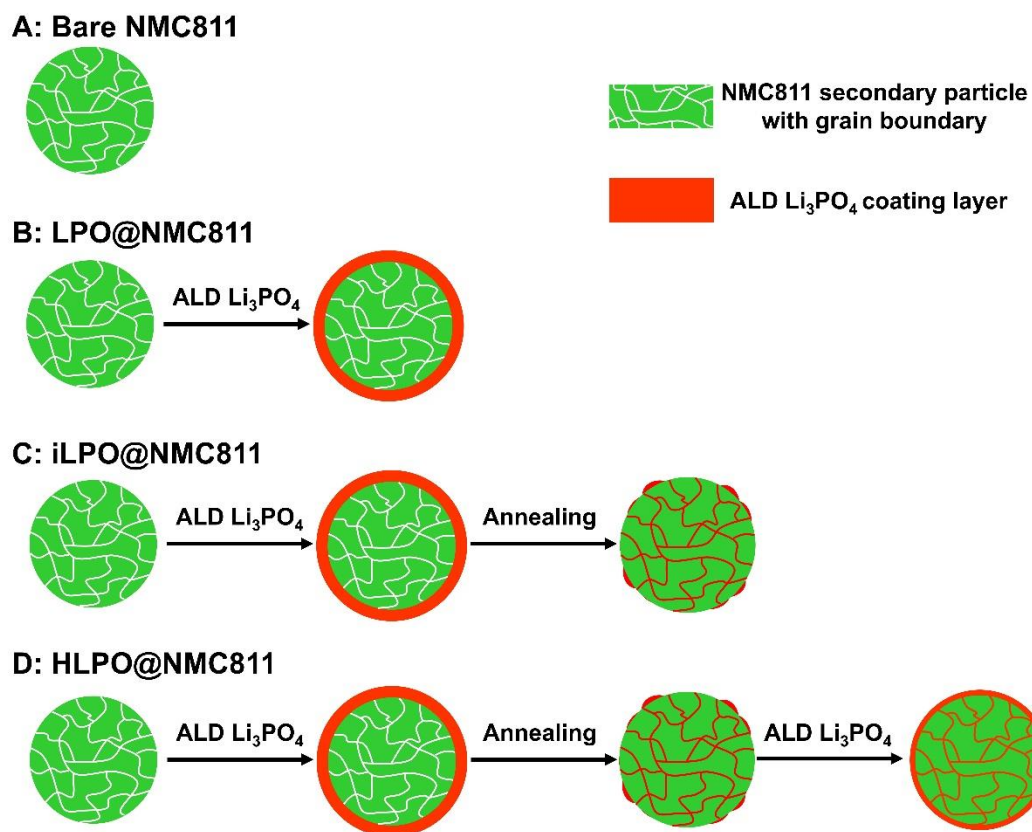
D: HLPO@NMC811

Figure S1. Schematic illustration of four NMC811 cathodes with three different designs of LPO modifications involving ALD coating and/or annealing.
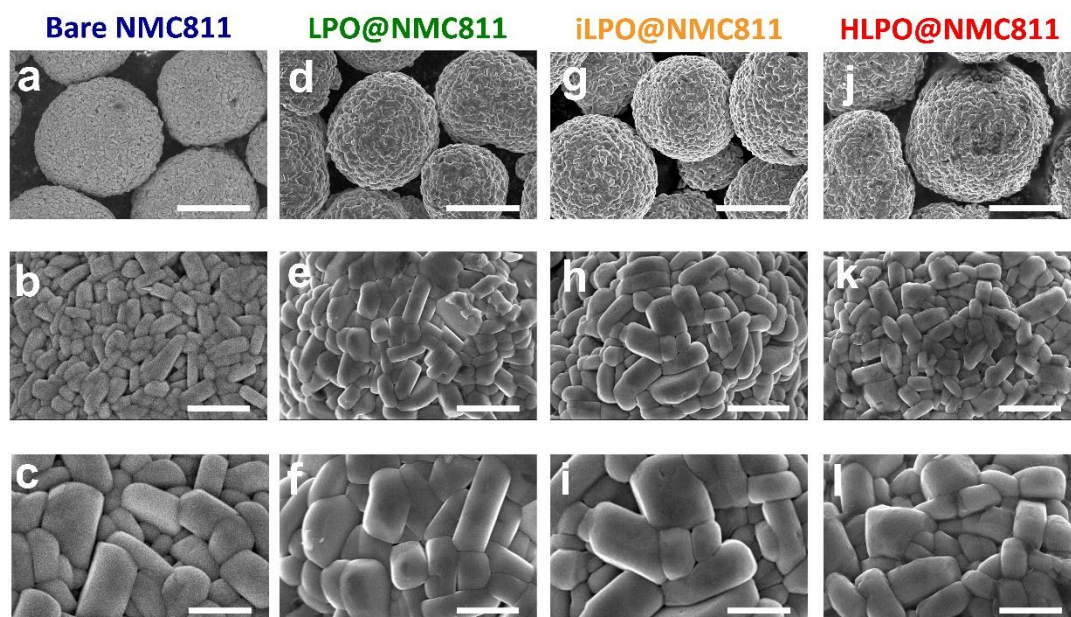
Figure S2. SEM images of the a-c) bare NMC811, d-f) LPO@NMC811, g-i) iLPO@NMC811, j-l) HLPO@NMC811. Scale bars are 5 µm (a, d, g, and j), 1 µm (b, e, h, and k), and 500 nm (c, f, i, and l).
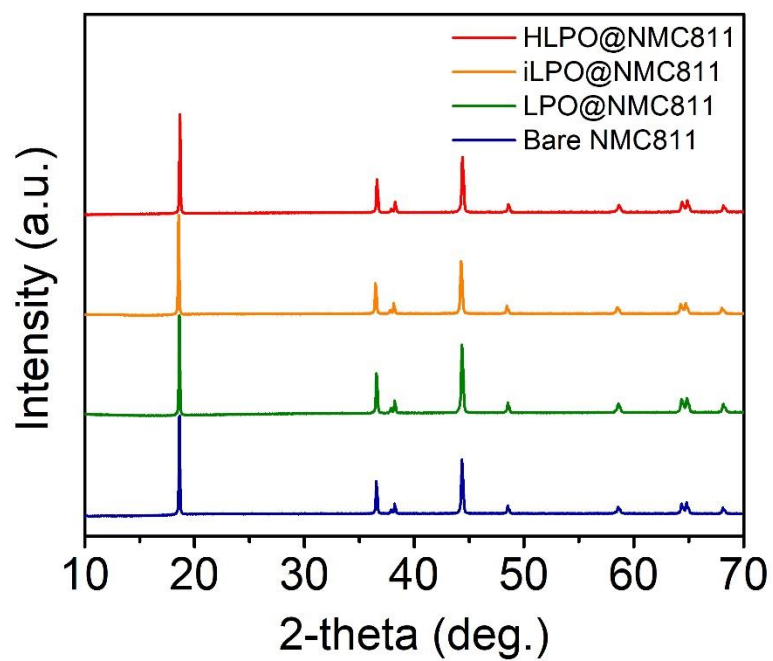
Figure S3. XRD patterns of the bare NMC811 and different LPO modified NMC811 cathodes.
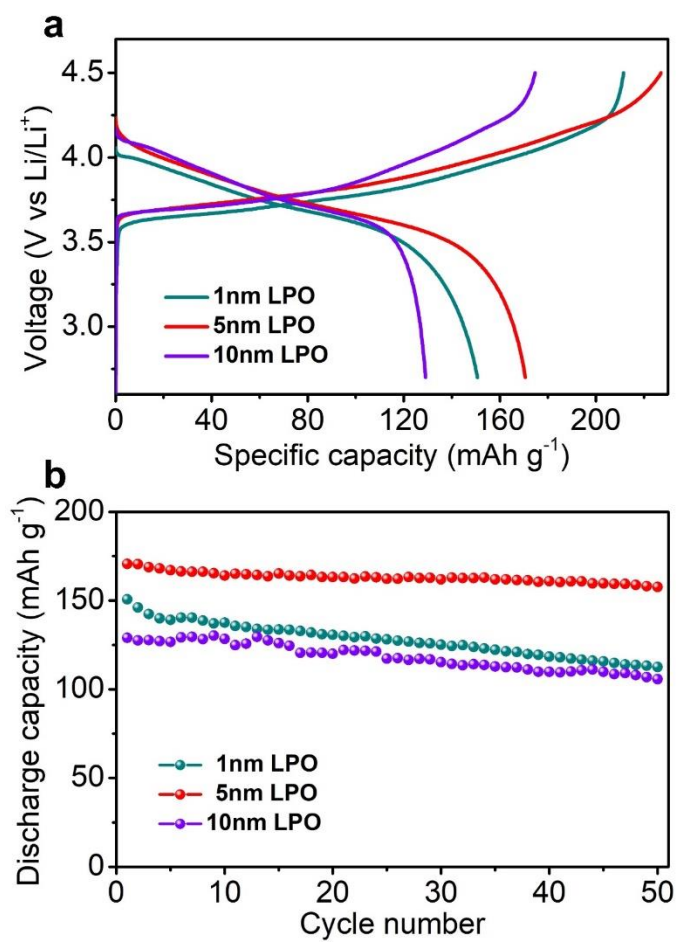
Figure S4. Optimization of the thickness of the surficial LPO coating layer for the HLPO@NMC811 cathodes. a) Charge/discharge curves of the first cycle and b) cycling stability.
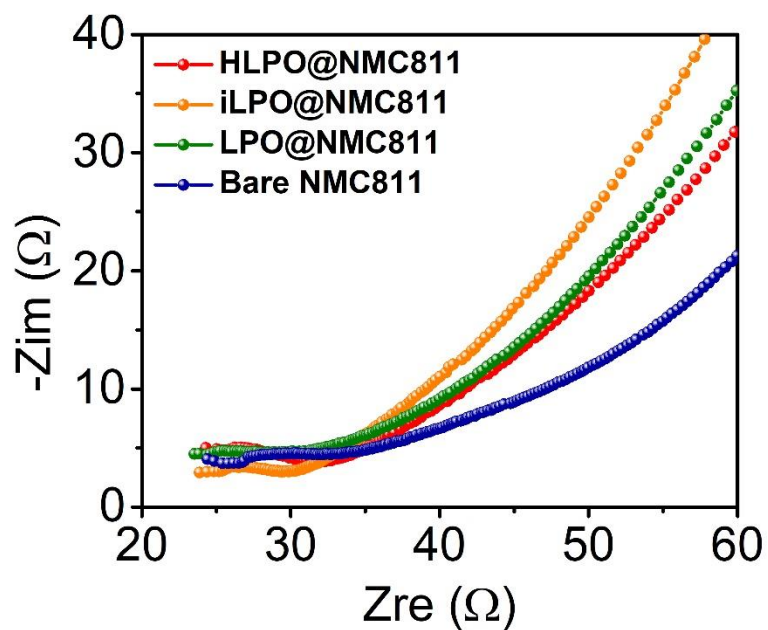
Figure S5. EIS plots of the bare NMC811 and different LPO modified NMC811 cathodes before cycling.
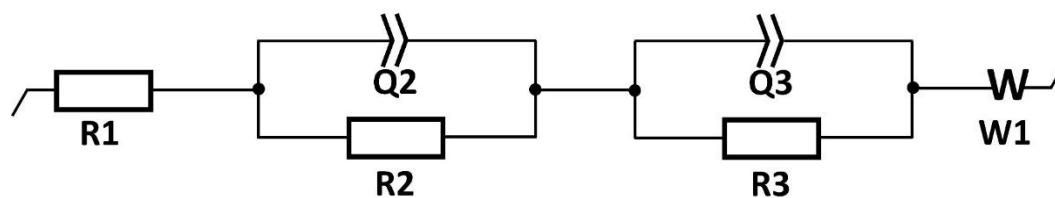
Figure S6. Corresponding equivalent circuit of R1+Q2/R2+Q3/R3+W1 for fitting the EIS plots in Figure 3d.
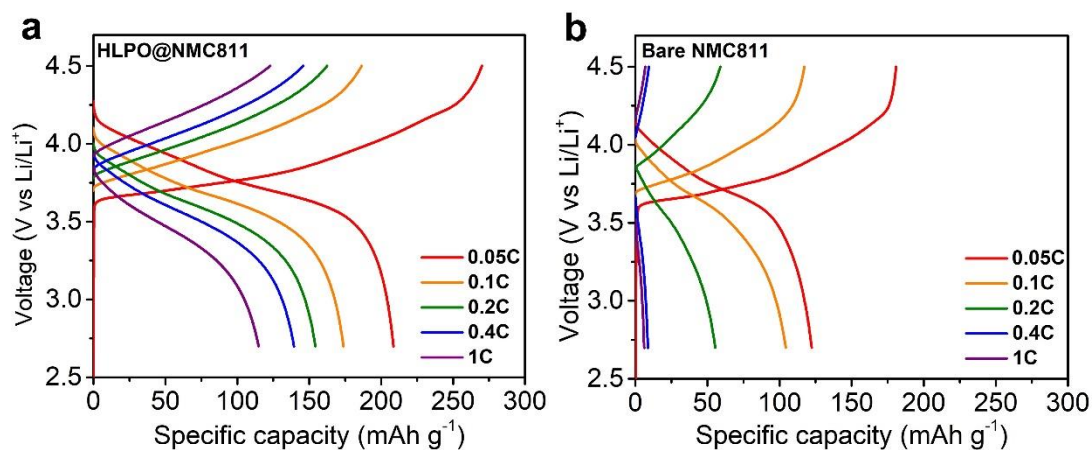
Figure S7. Charge/discharge curves of the a) bare NMC811 and b) HLPO@NMC811 cathodes at various current densities.
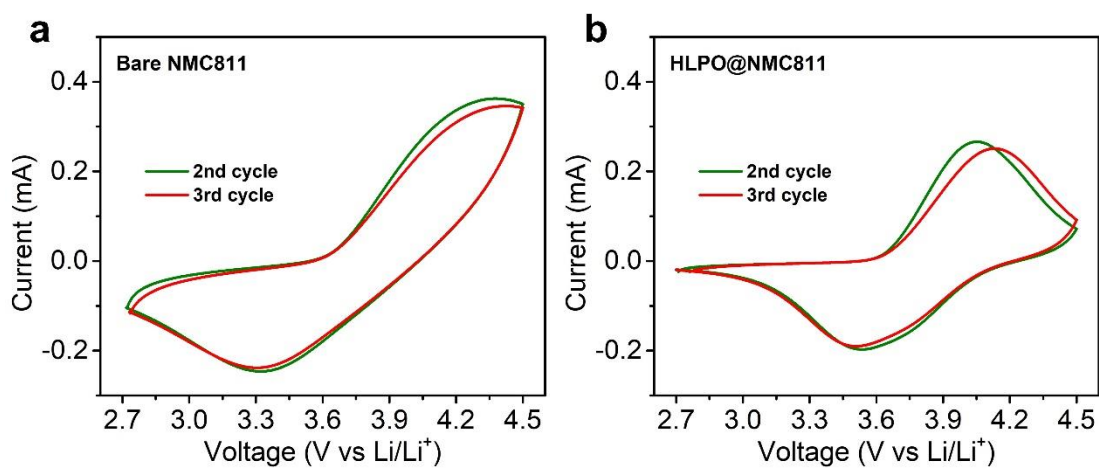
Figure S8. CV profiles of the a) bare NMC811 and b) HLPO@NMC811 cathodes at the second and third cycles.
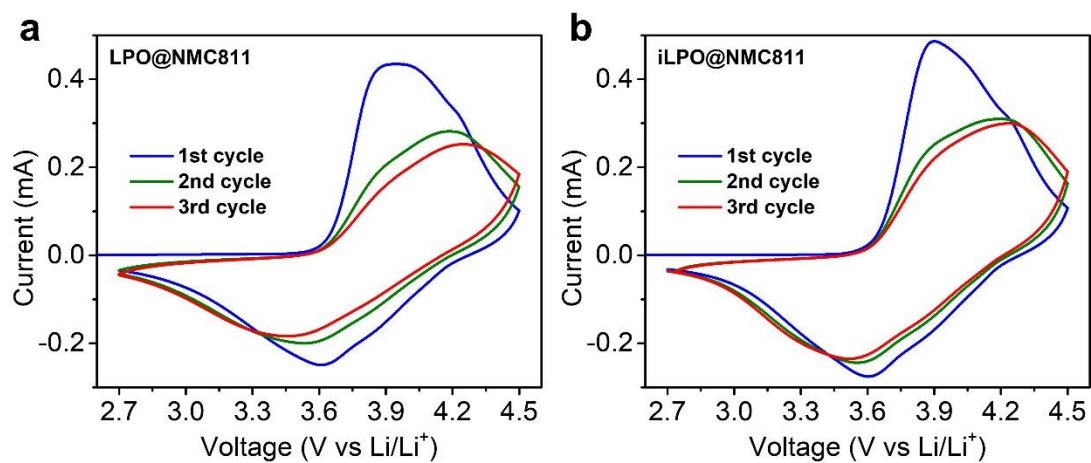
Figure S9. CV profiles of the a) LPO@NMC811 and b) iLPO@NMC811 cathodes at the first three cycles.
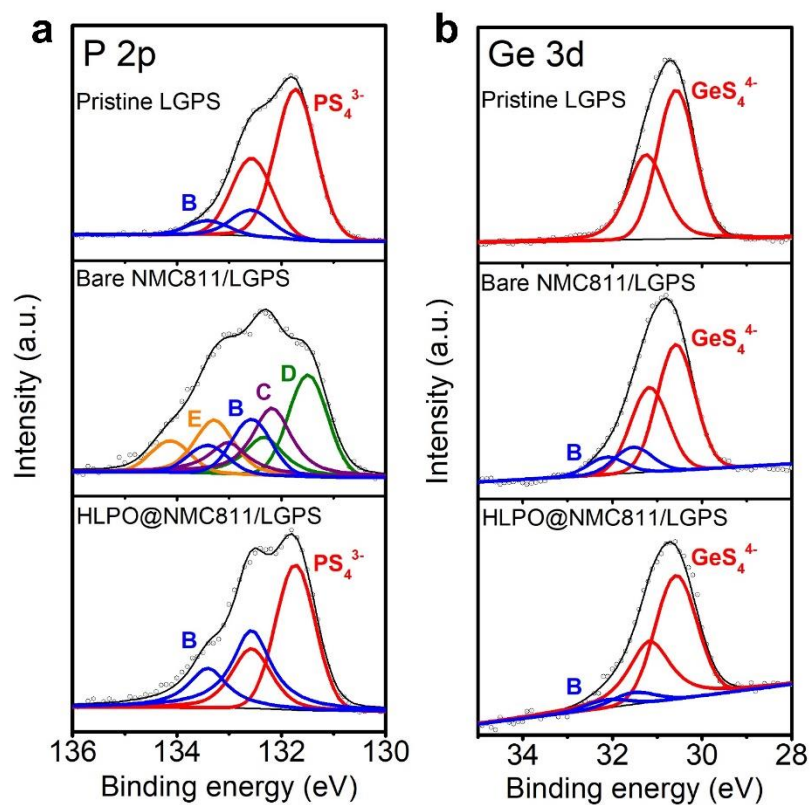
Figure S10. a) P 2p and b) Ge 3d XPS spectra of the pristine LGPS, bare NMC811/LGPS electrode after cycling, and HLPO@NMC811/LGPS electrode after cycling.
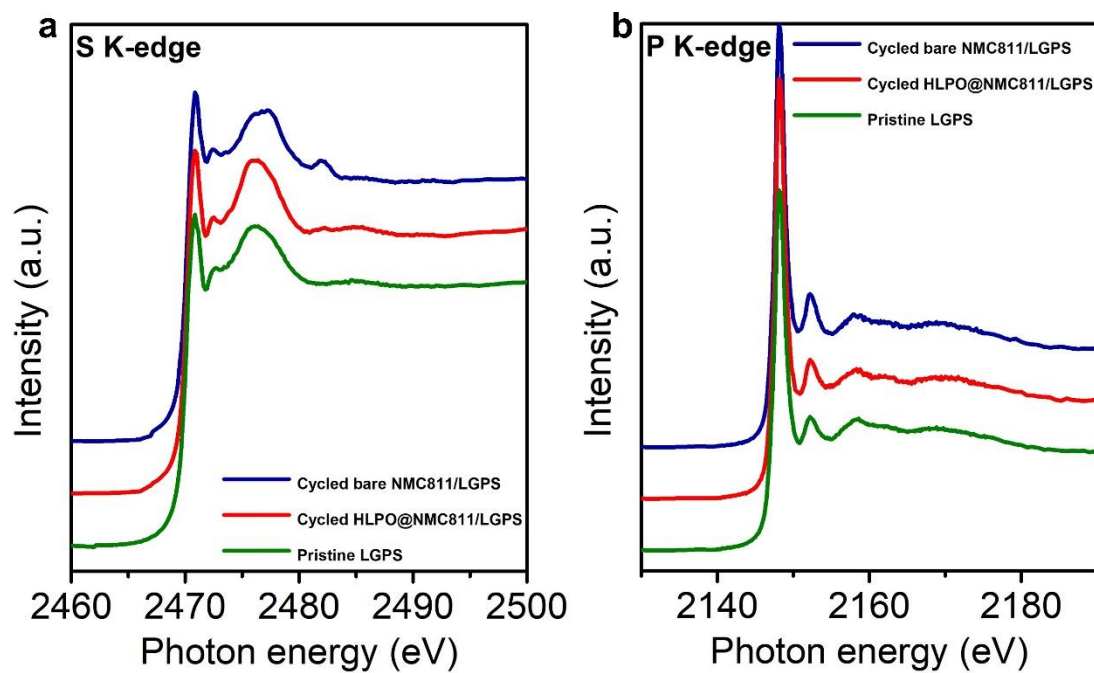
Figure S11. a) S and b) P K-edge XANES spectra of the bare NMC811/LGPS and HLPO@NMC811/LGPS electrodes after cycling as well as the pristine LGPS.
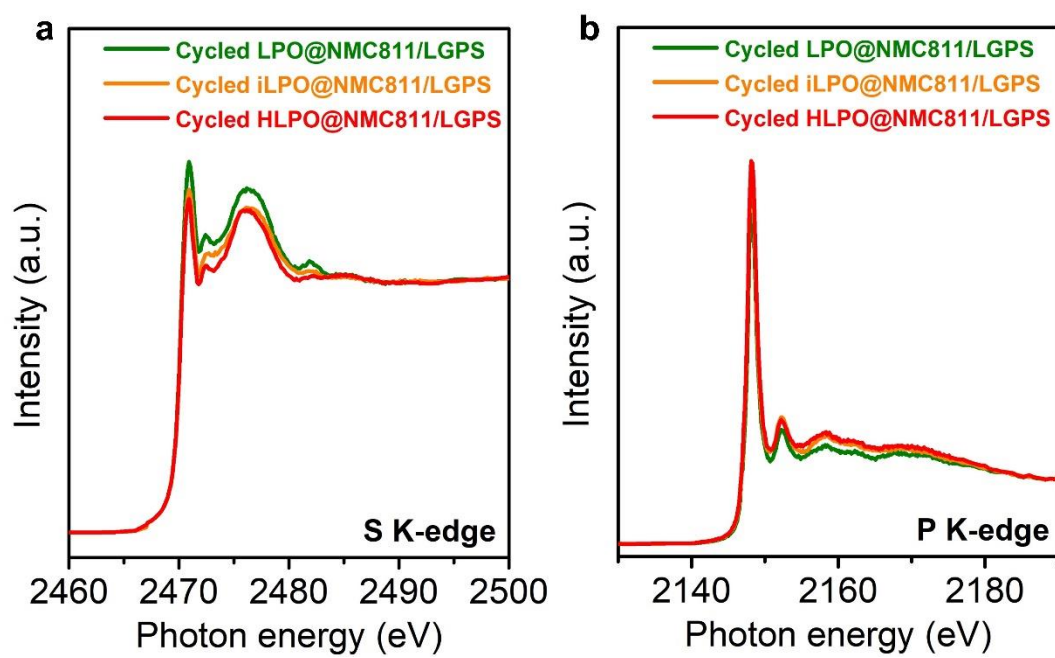
Figure S12. a) S and b) P K-edge XANES spectra of different LPO modified NMC811 cathodes after cycling.
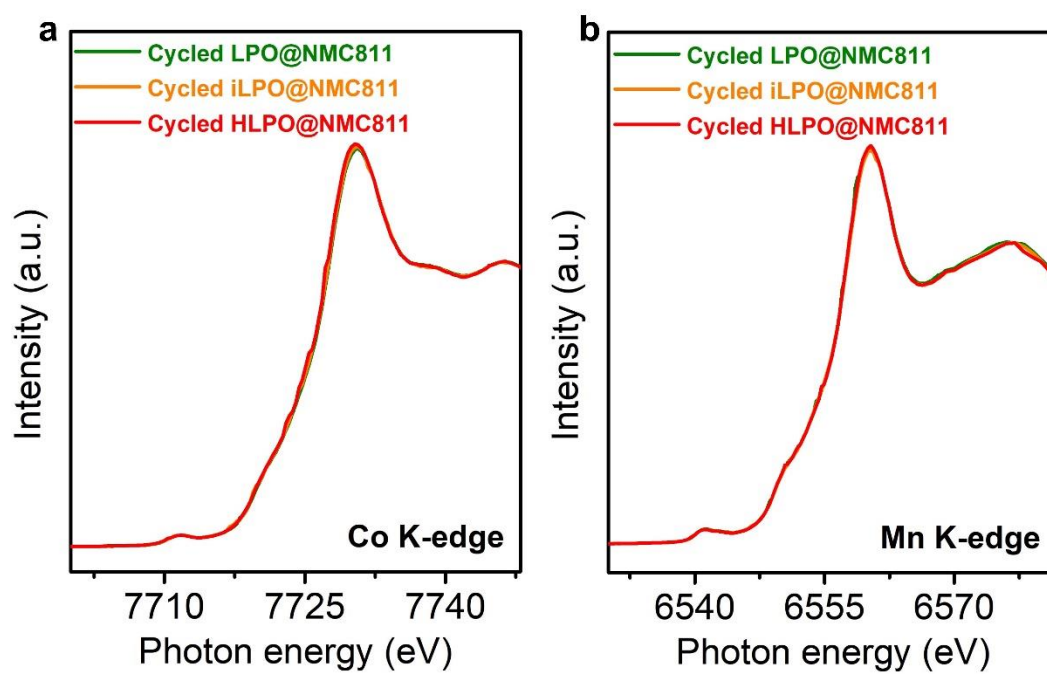
Figure S13. a) Co and b) Mn K-edge XANES spectra of different LPO modified NMC811 cathodes after cycling.
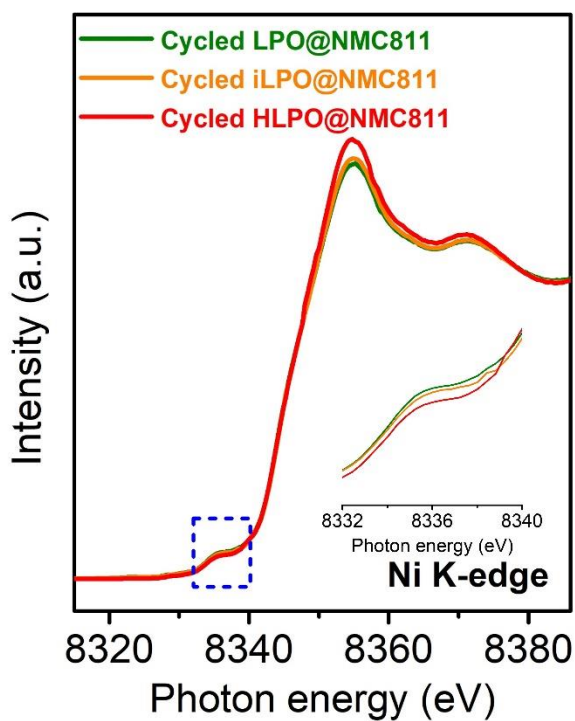
Figure S14. Ni K-edge XANES spectra of different LPO modified NMC811 cathodes after cycling.

Table S1 Resistances obtained from equivalent circuit fitting of EIS experimental data in Figure 3d.

Samples	R1 (Ω)	R2 (Ω)	R3 (Ω)
Bare NMC811	28	3535	2740
LPO@NMC811	31	3146	1825
iLPO@NMC811	29	1913	1079
HLPO@NMC811	24	1305	753

Table S2. Summary of cycling performance in reported Ni-rich layered oxide cathodes in sulfide-based all-solid-state batteries

	Cathode materials	Solid-state electrolytes	Temperature	Voltage range (V)	Current density	Initial capacity/capacity after cycling (mAh g^{-1})	Capacity retention (%)	Charge/discharge cycles
Our work	LiNi$_{0.8}$Mn$_{0.1}$Co$_{0.1}$O$_2$ (NMC811)	Li$_{10}$GeP$_2$S$_{12}$	Room temperature	2.7-4.5	0.2C	163.2/96.1	58.9	300
Ref. [1]	LiNi$_{0.8}$Mn$_{0.1}$Co$_{0.1}$O$_2$ (NMC811)	Li$_{10}$GeP$_2$S$_{12}$	Room temperature	2.6-4.4	0.1C	160/99	61.9	50
Ref. [2]	LiNi$_{0.8}$Mn$_{0.1}$Co$_{0.1}$O$_2$ (NMC811)	Li$_{10}$GeP$_2$S$_{12}$	35 °C	2.1-4.4	0.5C	~134/105	77.9	50
Ref. [3]	LiNi$_{0.8}$Mn$_{0.1}$Co$_{0.1}$O$_2$ (NMC811)	β-Li$_3$PS$_4$	150 °C	2.65-4.35	0.1C	145/~80	~55.2	50
Ref. [4]	LiNi$_{0.8}$Mn$_{0.1}$Co$_{0.1}$O$_2$ (NMC811)	β-Li$_3$PS$_4$	Room temperature	2.6-4.3	0.1C	130/105	80.8	25
Ref. [5]	LiNi$_{0.8}$Mn$_{0.1}$Co$_{0.1}$O$_2$ (NMC811)	β-Li$_3$PS$_4$	Room temperature	2.7-4.3	0.1C	124/81	65.3	50
Ref. [6]	LiNi$_{0.6}$Mn$_{0.2}$Co$_{0.2}$O$_2$ (NMC622)	Li$_6$PS$_5$Cl	Room temperature	2.6-4.3	0.1C	128.9/52.4	40.7	100
Ref. [7]	LiNi$_{0.6}$Mn$_{0.2}$Co$_{0.2}$O$_2$ (NMC622)	β-Li$_3$PS$_4$	60 °C	3.0-4.2	0.05C	140/126	90	50
Ref. [8]	LiNi$_{0.6}$Mn$_{0.2}$Co$_{0.2}$O$_2$ (NMC622)	β-Li$_3$PS$_4$	45 °C	2.9-5.0	0.05C	204/~170	~83.3	3
Ref. [9]	LiNi$_{0.9}$Co$_{0.05}$Mn$_{0.05}$O$_2$	Li$_6$PS$_5$Cl	Room temperature	2.5-4.2	~0.13C	124/116.1	93.6	100
Ref. [10]	LiNi$_{0.8}$Co$_{0.15}$Al$_{0.05}$O$_2$ (NCA)	Li$_{10}$GeP$_2$S$_{12}$	60 °C	2.7-4.3	0.3C	~175/~156.5	89.4	400
Ref. [11]	LiNi$_{0.8}$Co$_{0.15}$Al$_{0.05}$O$_2$ (NCA)	Li$_2$S-P$_2$S$_5$	Room temperature	2.7-4.2	0.1C	N/A	91	100
Ref. [12]	LiNi$_{0.8}$Co$_{0.15}$Al$_{0.05}$O$_2$ (NCA)	Li$_{10}$GeP$_2$S$_{12}$	Room temperature	2.6-4.3	0.1C	123.1/107.2	87.1	30
Ref. [13]	LiNi$_{0.8}$Co$_{0.15}$Al$_{0.05}$O$_2$ (NCA)	Li$_2$S-P$_2$S$_5$	Room temperature	2.5-4.0	0.1C	81.2/73.9	93.1	100

References

[1] X. Li, Z. Ren, M. Norouzi Banis, S. Deng, Y. Zhao, Q. Sun, C. Wang, X. Yang, W. Li, J. Liang, X. Li, Y. Sun, K. Adair, R. Li, Y. Hu, T.-K. Sham, H. Huang, L. Zhang, S. Lu, J. Luo, X. Sun, ACS Energy Lett. 4 (2019) 2480-2488.

[2] X. Li, L. Jin, D. Song, H. Zhang, X. Shi, Z. Wang, L. Zhang, L. Zhu, J. Energy Chem. 40 (2020) 39-45.

[3] T. Yoshinari, R. Koerver, P. Hofmann, Y. Uchimoto, W.G. Zeier, J. Janek, ACS Appl. Mater. Interfaces 11 (2019) 23244-23253.

[4] R. Koerver, F. Walther, I. Aygün, J. Sann, C. Dietrich, W.G. Zeier, J. Janek, J. Mater. Chem. A 5 (2017) 22750-22760.

[5] R. Koerver, I. Aygün, T. Leichtweiß, C. Dietrich, W. Zhang, J.O. Binder, P. Hartmann, W.G. Zeier, J. Janek, Chem. Mater. 29 (2017) 5574-5582.

[6] F. Walther, R. Koerver, T. Fuchs, S. Ohno, J. Sann, M. Rohnke, W.G. Zeier, J. Janek, Chem. Mater. 31 (2019) 3745-3755.

[7] T. Ates, M. Keller, J. Kulisch, T. Adermann, S. Passerini, Energy Storage Mater. 17 (2019) 204-210.

[8] T. Bartsch, F. Strauss, T. Hatsukade, A. Schiele, A.Y. Kim, P. Hartmann, J. Janek, T. Brezesinski, ACS Energy Lett. 3 (2018) 2539-2543.

[9] F. Hippauf, B. Schumm, S. Doerfler, H. Althues, S. Fujiki, T. Shiratsuchi, T. Tsujimura, Y. Aihara, S. Kaskel, Energy Storage Mater. 21 (2019) 390-398.

[10] X. Li, M. Liang, J. Sheng, D. Song, H. Zhang, X. Shi, L. Zhang, Energy Storage Mater. 18 (2019) 100-106.

[11] H. Visbal, Y. Aihara, S. Ito, T. Watanabe, Y. Park, S. Doo, J. Power Sources 314 (2016) 85-92.

[12] J. Yin, X. Yao, G. Peng, J. Yang, Z. Huang, D. Liu, Y. Tao, X. Xu, Solid State Ionics 274 (2015) 8-11.

[13] S. Ito, S. Fujiki, T. Yamada, Y. Aihara, Y. Park, T.Y. Kim, S.-W. Baek, J.-M. Lee, S. Doo, N. Machida, J. Power Sources 248 (2014) 943-950.

Chapter 6

6 Insight into Cathode Surface to Boost the Performance of Solid-State Batteries*

Cathode interface instability is a significant obstacle for the practical application of sulfide-based all-solid-state lithium-ion batteries (ASSLIBs). However, the origin of cathode interface degradation is lack of comprehensive understanding. In this paper, X-ray characterizations combined with electrochemical analysis are adopted to investigate the underlying degradation mechanism at cathode interface. The results indicate that residual lithium compounds on the surface of Ni-rich $LiNi_{0.8}Mn_{0.1}Co_{0.1}O_2$ (NMC811) are the main reason that triggering the oxidation of sulfide solid-state electrolytes (SSEs), therefore inducing severe side-reactions at cathode interface and structural degradation of NMC811. The degradation of the cathode interface can be significantly suppressed when the cathode surface is cleaned. As a result, the surface cleaned NMC811 without coating demonstrates significantly improved electrochemical performance in both $Li_{5.5}PS_{4.5}Cl_{1.5}$ (LPSCl) and $Li_{10}GeP_2S_{12}$ (LGPS) based ASSLIBs, proving the universal application of this strategy.

6.1 Introduction

The use of inflammable solid-state electrolytes (SSEs) makes all-solid-state lithium-ion batteries (ASSLIBs) as promising energy storage devices that can meet the safety requirements of electric vehicles.[1-3] Among the developed SSEs, sulfide-based electrolytes, such as Li_6PS_5Cl (LPSCl) and $Li_{10}GeP_2S_{12}$ (LGPS), have demonstrated high room-temperature lithium-ion conductivities (10^{-2} to 10^{-3} S cm^{-1}), which are comparable with liquid electrolytes.[4-6] Meanwhile, sulfide-based ASSLIBs have great potential to reach competitive energy densities of over 350 Wh kg^{-1} when coupled with high-energy cathodes and lithium metal anodes.[7, 8] Therefore, selection of suitable high-performance cathode materials is critical towards achieving the energy density target. In conventional lithium-ion batteries, Ni-rich layered oxide cathodes, $LiNi_xMn_yCo_{1-x-y}O_2$ (NMC), have become mainstream because of their high specific capacities. For example, a specific capacity of roughly 200 mAh g^{-1} can be reversibly accessed from $LiNi_{0.8}Mn_{0.1}Co_{0.1}O_2$ (NMC811).[9, 10] However, the performance of Ni-rich NMC cathodes in sulfide-based ASSLIBs is still limited by the undesired chemical/electrochemical reactions.

The most significant challenge of Ni-rich NMC cathodes in sulfide-based ASSLIBs is the poor interfacial compatibility. The severe side-reactions between Ni-rich NMC cathodes and sulfide SSEs trigger the oxidative decomposition of sulfide SSEs, in particular at high potentials during charging.[11] As a result, the formation of an unfavorable cathode electrolyte interface (CEI) and degradation of the structure at cathode surface lead to rapid capacity fading, low initial capacity, and poor Columbic efficiency.[12, 13] Although a prevailing coating strategy combined with various coating materials is widely applied for the cathode surface modification in sulfide-based ASSLIBs,[14-19] the underlying degradation mechanism of the cathode interface, especially the origin of the oxidation of sulfide SSEs, is still not clear. The reasonable speculation is that the oxidation of sulfide SSEs is derived from oxygen-containing species in the cathode.[20] On the one hand, oxygen release from the cathode structure at high charge voltage is one possible reason.[21, 22] On the other hand, residual lithium compounds, such as Li_2CO_3

and LiOH, on the surface of Ni-rich NMC cathodes are considered as the possible oxygen sources that result in the reaction with sulfide SSEs.[23] Therefore, two questions arise here: (1) what is the main origin of reaction with sulfide SSEs, cathodes themselves or residual lithium compounds? (2) Is it possible to circumvent the side-reactions by eliminate the origin of oxygen sources?

To answer aforementioned questions, in this study, we adopt the comprehensive electrochemical testing and X-ray characterizations to investigate the underlying degradation mechanism of pristine NMC811 with residual lithium compounds in sulfide-based solid-state batteries (SSBs). The results suggest that the surface impurities of the cathodes, instead of cathode particles themselves, are the main reason that accelerating the oxidation of sulfide SSEs, therefore leading to the structural degradation of NMC811 and fast capacity decay. Promisingly, the removal of the residual lithium compounds effectively alleviates the severe side-reactions between NMC811 and sulfide SSEs, therefore enhancing the interfacial stability and resulting in clearly improved cycling stability with the higher initial capacity and Columbic efficiency in different sulfide-based SSBs with $Li_{5.5}PS_{4.5}Cl_{1.5}$ (LPSCl) and LGPS SSEs. This study reveals the origin of side-reactions of cathode interface in sulfide-based SSE systems, effectively promoting the potential commercialization of high-performance ASSLIBs.

6.2   Experimental section

Preparation of cathodes and sulfide solid-state electrolytes: The commercial $LiNi_{0.8}Mn_{0.1}Co_{0.1}O_2$ (NMC811) and $LiNi_{0.5}Mn_{0.3}Co_{0.2}O_2$ (NMC532) are obtained from China Automotive Battery Research Institute Co., Ltd, China. For the surface modification, both NMC811 and NMC532 powders were heated at 730 ºC for 1 h under the continued O_2 flow, which is followed by the reference.[24] The ALD $LiNbO_x$ coating process was reported in our previous studies.[25] Prior to use, the material was stored in a glovebox under Ar. For sulfide solid-state electrolytes (SSEs), $Li_{5.5}PS_{4.5}Cl_{1.5}$ (LPSCl) is synthesized following our previous study,[6] while $Li_{10}GeP_2S_{12}$ (LGPS, 99.95%) is commercial electrolyte, purchasing from MSE supplies, LLC, United States.

Assembly of the tested batteries and electrochemical testing: In order to investigate the electrochemical performance, the sandwiched model cells were fabricated by using the as-prepared NMC811 cathodes combining with LPSCl or LGPS as SSE layer and indium foil (99.99%, Φ10 mm, thickness 0.1 mm) as anode. The detailed fabrication process is shown as follow. Firstly, 60 mg LPSCl or LGPS was pressed at 2 ton with 10 mm diameter to form a pellet. After that, 7 mg NMC811 power was mixed well with 3 mg LPSCl or LGPS, and then uniformly spread onto the surface of SSE layer and pressed under 3 tons of pressure to form a two-layer pellet. Finally, a piece of indium foil with the same 10 mm diameter was put onto the other side of the SSE layer with a copper foil and pressed at 0.5 tons of pressure. The three-layered pellet was pressed between two stainless-steel rods as current collectors at the both positive and negative sides. When Li compounds were added in the cathode composites, 1 wt%, 5 wt%, and 10 wt% Li_2CO_3 + LiOH were mixed with treated NMC811 and LPSCl to form the cathode layer. The weight ratio of Li_2CO_3: LiOH was 1: 1. The assembly of NMC532 model cells is same as the process of NMC811. All the processes were performed in an argon-filled glove box. The galvanostatic charge-discharge characteristics were tested in the range of 2.1-3.8 V vs. Li^+/Li-In, corresponding to 2.7-4.4 V vs. Li^+/Li by using a multichannel battery tester (LAND CT-2001A, Wuhan Rambo Testing Equipment Co., Ltd., China). Electrochemical impedance spectroscopy (EIS) was performed on the versatile multichannel potentiostat 3/Z (VMP3) by applying an AC voltage of 10 mV amplitude in the 7000 kHz to 1000 mHz frequency range. For galvanostatic intermittent titration technique (GITT) measurements, the cells were charged and discharged with 0.05 C for 10 min and rest for 1h. According to the GITT theoretical analysis, Li^+ diffusion coefficient can be calculated by following equation:

$$D_{Li} = \frac{4}{\pi\tau}\left(\frac{m_B V_m}{M_B S}\right)^2 \left(\frac{\Delta E_s}{\Delta E_\tau}\right)^2 \ (\tau \ll L^2/D) \ (1)$$

Where D is chemical diffusion coefficient; S is interfacial contact area between NMC811 and sulfide SSEs in our case, the specific area of NMC811 is 0.55 m^2 g^{-1}; τ is pulse duration (600 s in our case), ΔEs is the steady-state voltage change; ΔEt is the transient

voltage change; m_B is the mass of the LCO in the cathode composite (7 mg); M_B is the molecular weight of NMC811 (97.28 g. mol^{-1}); V_m is the molar volume of NMC811 (20.33 cm^3 mol^{-1}).[26]

Characterizations: The crystalline structure of the pristine and treated NMC811 were conducted on a Bruker D8 Advance Diffractometer (Cu-Ka source, 40 kV, 40 mA). The morphology and microstructure of the pristine and treated NMC811 were characterized using field emission scanning electron microscopy (FESEM, Hitachi S4800). The LiNbO$_x$ coating layer on the surface of NMC811 was observed by a high-resolution transmission electron microscopy (HRTEM, JEOL 2010F). For the thermal gravimetric analysis (TGA) testing, the data were acquired using a TA instrument (SDT Q600) in a nitrogen atmosphere at a heating rate of 2 °C min^{-1}. X-ray photoelectron spectroscopy (XPS) testing were measured with a monochromatic Al Kα source (1486.6 eV) in a Kratos AXIS Nova Spectrometer. The Ar filled glovebox was connected with the XPS machine to avoid the exposure of air. All synchrotron X-ray studies were carried out at the Canadian Light Source (CLS). X-ray absorption fine structure (EXAFS) data were collected at Hard X-ray Micro Analysis (HXMA) beamline. Ni K-edge spectra were collected in fluorescence mode using Si(220) crystals. Co and Mn K-edge spectra were also collected in fluorescence mode but using Si(111) crystals. S, P, Cl, Ni, Co, and Mn K-edge X-ray absorption near edge structure (XANES) spectra were collected in fluorescence mode using Si(111) crystals at Soft X-ray Microcharacterization Beamline (SXRMB). To avoid air exposure, the samples were firstly covered with Kapton tape for HXMA test and Mylar film for SXRMB test in glovebox under Ar, and then transferred to the corresponding beamlines for further measurements. O K-edge XANES spectra were collected in both total electron yield and fluorescence mode at Spherical Grating Monochrometer (SGM) beamline equipped with a 45 mm planar undulator.

6.3 Results and discussion
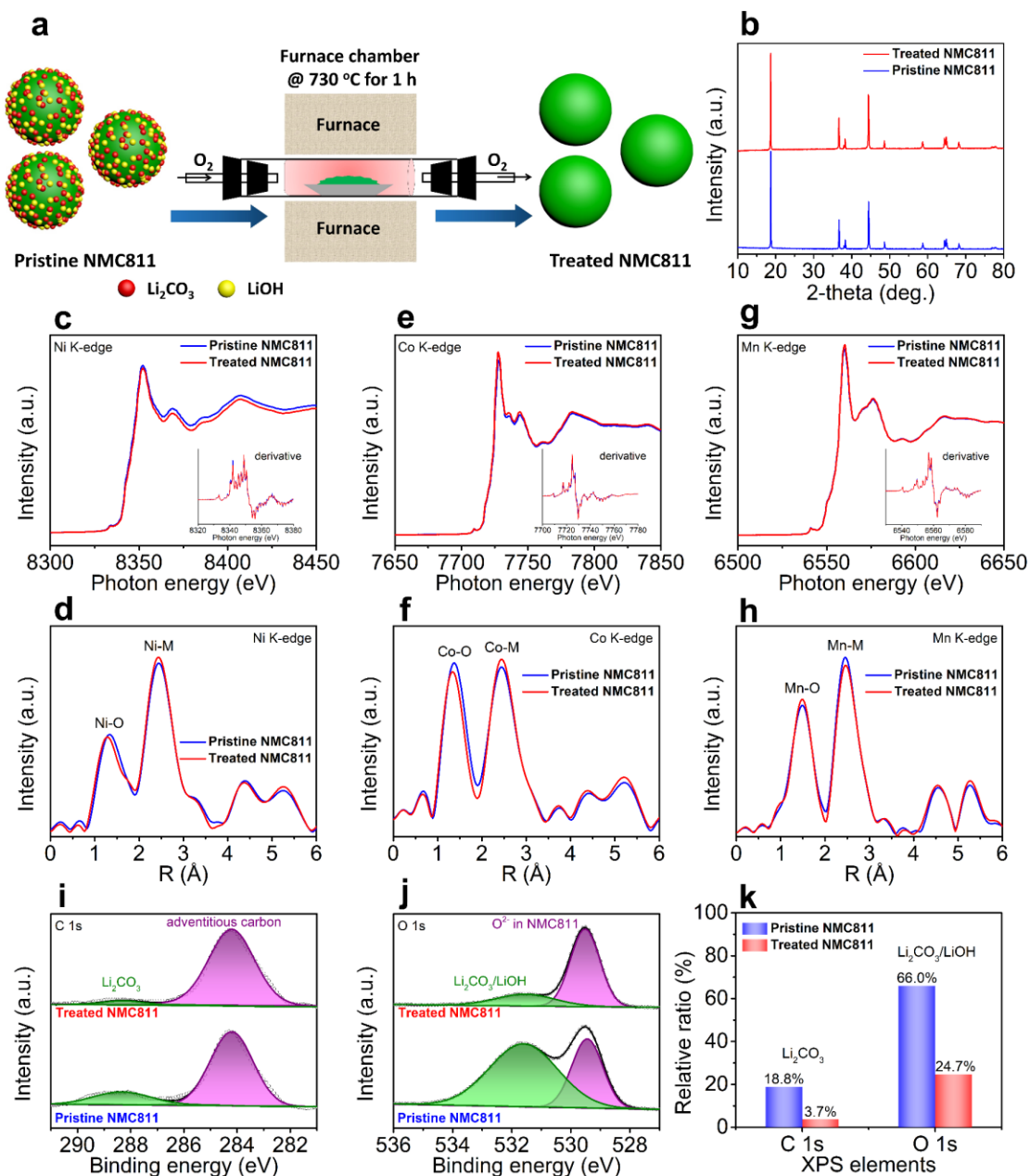
Figure 6.1 Structural and morphological characterizations of the Ni-rich NMC cathode before and after cleaning the surface. (a) Schematic illustration of the surface treatment process for NMC811. (b) XRD patterns of the pristine and treated NMC811. (c-h) Ni, Co, and Mn K-edge XANES and Fourier transformed R space EXAFS spectra: (c-d) Ni K-edge spectra, (e-f) Co K-edge spectra, and (g-h) Mn K-edge spectra. (i-k) XPS

spectra of the pristine and treated NMC811: (i) C 1s, (j) O 1s, and (j) the corresponding relative ratio of $Li_2CO_3/LiOH$ in XPS.

To investigate the effect of impurities on the surface of NMC811 cathode, a high temperature treatment process at 730 $^{\circ}$C for 1 h under continuous O_2 flow is adopted to remove the residual lithium compounds on the surface of NMC811 particles (Figure 6.1a). To identify if changes in the crystal structure of NMC811 occur during the surface modification, X-ray diffraction (XRD) measurements were first conducted for both pristine and treated NMC811. The results show good retention of the NMC811 crystallinity without noticeable impurity phase caused by the surface modification (Figure 6.1b). Furthermore, the bulk structure of NMC811 is investigated by X-ray absorption spectroscopy (XAS), in which both pristine and treated NMC811 show nearly identical features in the Ni, Co, Mn K-edge X-ray absorption near edge structure (XANES) and extended X-ray absorption fine structure (EXAFS) spectra as shown in Figures 6.1c-h, suggesting that no measurable structure evolution of NMC811 resulted from the surface-cleaning procedure.

In addition, the surface-clean effect is also investigated by different characterizations. The C 1s and O 1s X-ray photoelectron spectroscopy (XPS) spectra are displayed in Figures 6.1i and 6.1j, respectively, to analyze the components on the surface of both pristine and treated NMC811. In the C 1s XPS spectra, in addition to the adventitious carbon peak at 284.4 eV from internal calibrator, another carbon peak at 289.3 eV is attributed to Li_2CO_3.[27, 28] After normalizing the peak intensities to the adventitious carbon, the pristine NMC811 shows relatively higher amounts of residual Li_2CO_3 than that of the treated NMC811. O 1s spectra also comprises of two peaks, corresponding to the peak of $Li_2CO_3/LiOH$ at 531.5 eV and the peak of O^{2-} ions in NMC811 at 829.5 eV.[29] The relative ratio of $Li_2CO_3/LiOH$ peaks of both pristine and treated NMC811 is shown in Figure 6.1k. The treated NMC811 shows obvious reduce amounts of residual lithium compounds comparing to the pristine NMC811. Moreover, O K-edge XANES spectra of the pristine and treated NMC811 are demonstrated in Figure S1. The peak at 534 eV is assigned to the oxygen in $Li_2CO_3/LiOH$,[30, 31] which is suppressed in the

treated NMC811 comparing to the pristine NMC811. The morphologies of the pristine and treated NMC811 are characterized using scanning electron microscopy (SEM) as shown in Figure S2. The pristine NMC811 particles show folds on the rough surfaces, while the treated NMC811 particles present very smooth surfaces. From the thermal gravimetric analysis (TGA) profiles (Figure S3), the more obvious weight loss started from 730 °C can be observed in the pristine NMC811. Therefore, combining the comprehensive characterizations, residual lithium compounds on the surface of NMC811 are successfully removed by the surface modification procedure.
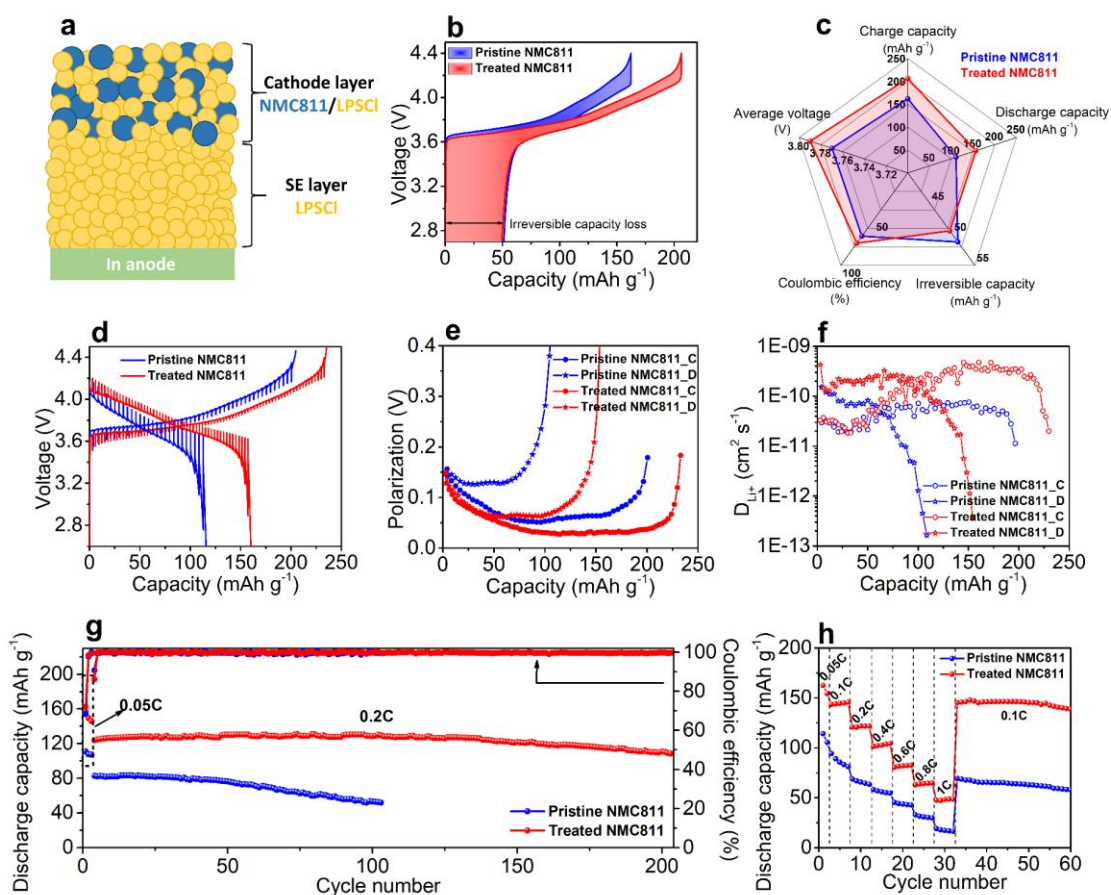
Figure 6.2 Comparison of the electrochemical performance of pristine and treated NMC811 in LPSCl SSBs. (a) Schematic illustration of the designed model cell, (b) charge-discharge curves of the first cycle at 0.05C, (c) the corresponding performance parameters collected from charge-discharge curves, (d) GITT curves during the charge-

discharge process, (e) the corresponding polarization plots and (f) lithium-ion diffusion coefficients, (g) cycling stability, and (h) rate capability.

To investigate the universal effect of the surface impurities on the cathode interface, two promising sulfide SSEs, LPSCl and LGPS, are employed for electrochemical characterizations. LPSCl-based SSBs are first tested and the configuration of the designed model cell is shown in Figure 6.2a. A mixture of NMC811 and LPSCl is used as the cathode combined with LPSCl as the electrolyte layer and indium foil as the anode. Figure 6.2b shows a comparison of the initial charge-discharge curves between the pristine and treated NMC811 at 0.05 C. The initial charge and discharge capacities of the pristine NMC811 are 162.3 and 111.1 mAh g^{-1}, respectively. In contrast, the treated NMC811 presents higher charge and discharge capacities (206.2 and 156.8 mAh g^{-1}, respectively) with reduced irreversible capacity loss. The corresponding differential capacity profiles as a function of voltage indicate reduced polarization during the redox reactions in the treated NMC811 (Figure S4). Furthermore, the treated NMC811 demonstrates higher Coulombic efficiency (76.0% vs. 68.4%) and average discharge voltage (3.79 V vs. 3.77 V) than that of the pristine NMC811 as shown in Figure 6.2c.

To gain further insight into the lithium-ion diffusion kinetics of NMC811 in LPSCl-based SSBs, the galvanostatic intermittent titration technique (GITT) was conducted for both pristine and treated NMC811 during the initial charge-discharge process (Figure 6.2d). The corresponding polarization plots and lithium-ion diffusion coefficients (D_{Li}) are demonstrated in Figures 6.2e and 6.2f, respectively. It is apparent that the treated NMC811 presents higher charge and discharge capacities with greatly reduced polarization potential especially during the discharging process. Meanwhile, the D_{Li} of NMC811 during the charge and discharge processes are also calculated based on the GITT curves by the Equation (1)[26] as follows:

$$D_{Li} = \frac{4}{\pi\tau}\left(\frac{m_B V_m}{M_B S}\right)^2 \left(\frac{\Delta E_s}{\Delta E_\tau}\right)^2 \ (\tau \ll L^2/D) \ (1)$$

During the delithiation process, D_{Li} increases with continued lithium-ion removal from the layered structure until the highest value is achieved, which is followed by a gradual decrease. During the lithiation process, D_{Li} retains a value within the same order of magnitude at the beginning of discharge, and then decreases dramatically by two orders of magnitude at the end of discharge. Considering that the diffusion kinetics is assumed to be the same in the bulk of the NMC811 particles, the difference of the lithium-ion diffusion properties between the pristine and treated NMC811 is determined by the interfacial ionic conductivity. Although maintaining almost the same values at the beginning of charge, the treated NMC811 shows one order of magnitude higher D_{Li} of 10^{-10} cm^2 s^{-1} than that of the pristine NMC 811 (10^{-11} cm^2 s^{-1}) with the deepening of the charge process. During the entire discharge process, D_{Li} of the treated NMC811 is higher than that of the pristine NMC811. Combined with the findings from the charge-discharge and GITT results, the treated NMC811 demonstrates improved electrochemical performance, suggesting that the treated surface of NMC811 is beneficial towards the suppression of side-reactions with LPSCl SSE, therefore helping the NMC811 to obtain higher lithium-ion diffusion kinetics during the initial charge-discharge process.

Cycling stability testing was also conducted to evaluate the effect of the surface impurities of NMC811 during long-term cycling. The treated NMC811 demonstrated an initial discharge capacity of 123.9 mAh g^{-1} with a capacity retention of 87.7% after 200 cycles when the current density switches to 0.2 C (Figure 6.2g). In contrast, the pristine NMC811 delivers a low initial discharge capacity of 82.7 mAh g^{-1} at 0.2 C with a poor capacity retention of 62.9% only after 100 cycles. The electrochemical impedance spectroscopy (EIS) plots of both pristine and treated NMC811 indicate the reduced interfacial resistance after cycling by cleaning the cathode surface (Figure S5). Moreover, to exclude the effect of NMC811 themselves, the different contents of Li compounds were mixed with the treated NMC811 and LPSCl in the cathode composites. The electrochemical performance shown in Figure S6 indicates that the Li compounds as impurities in cathode composites deteriorate the performance of sulfide-based SSBs. The rate capability of the pristine and treated NMC811 also shows considerable differences as shown in Figure 6.2h. The rate capacities of the pristine NMC811 dramatically decay

with an increase of current density. In contrast, the treated NMC811 demonstrates improved rate capacities at each current density. The discharge capacity of the treated NMC811 is still higher than 45 mAh g^{-1} at 1 C, which is over 2.5 times that of the pristine NMC811. The aforementioned electrochemical performance of NMC811 in LPSCl-based SSBs indicates that the cleaned surface helps Ni-rich NMC cathodes to achieve higher discharge capacity, greater cycling stability, and rate capability with enhanced D_{Li} and reduced polarization. Even comparing to the prevailing ALD LiNbO$_x$ coating, the treated NMC811 also demonstrated a comparable long-term cycling stability (Figures S7-8). Furthermore, the effect of surface cleaning is also demonstrated in NMC532 cathodes (Figure S9). The treated NMC532 shows much improved capacity and cycling stability, proving the universality of the surface-cleaning strategy.
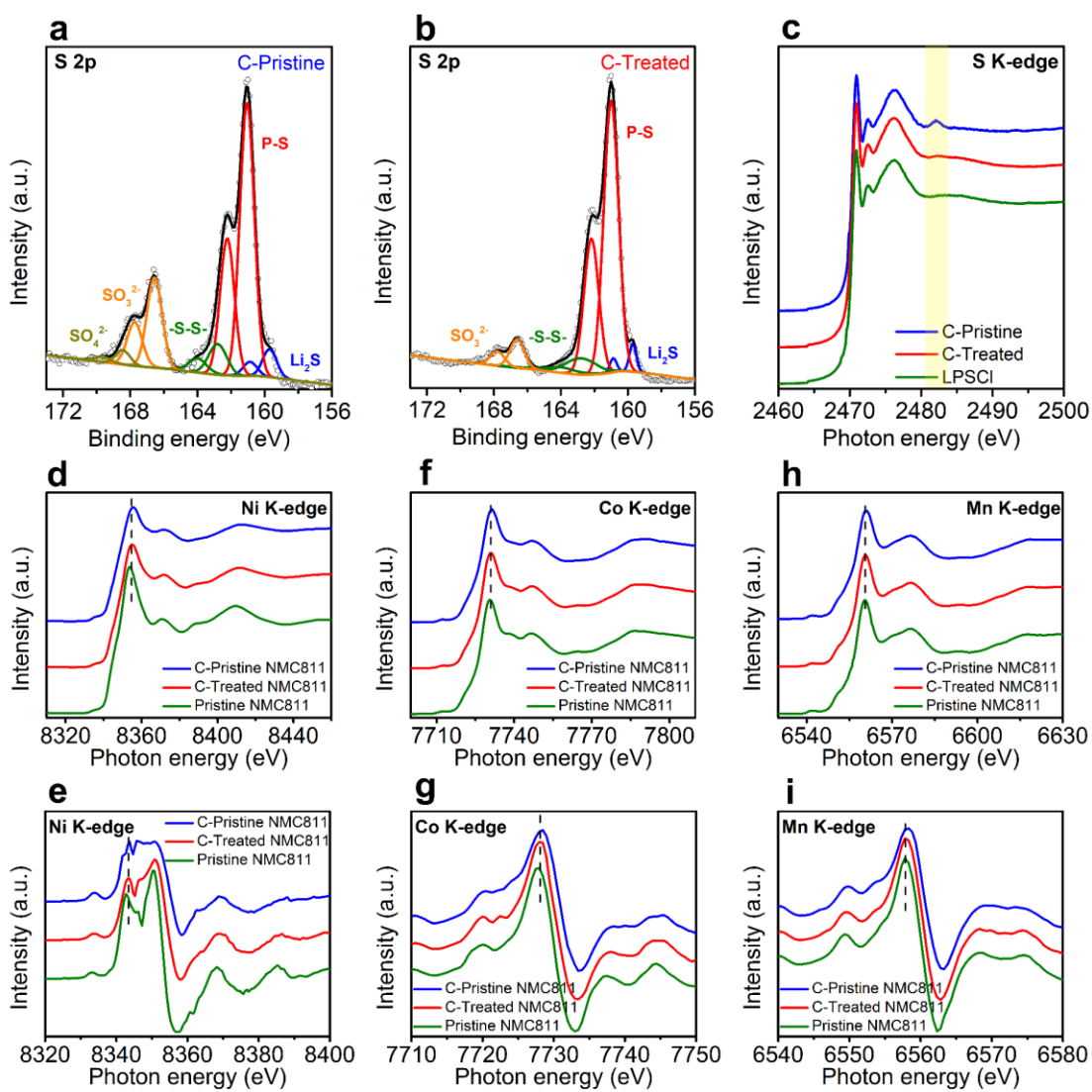
Figure 6.3 Understanding the chemical interactions between NMC811 and LPSCl during electrochemical cycling in LPSCl SSBs. S 2p XPS spectra of the (a) cycled pristine electrode (C-Pristine) and (b) cycled treated electrode (C-Treated), (c) S K-edge XANES spectra of LPSCl in the C-Pristine and C-Treated cells with pristine LPSCl as a reference. (d-i) Ni, Co, and Mn K-edge XANES spectra of the C-Pristine and C-Treated NMC811 with pristine NMC811 as a reference: (d) Ni K-edge and (e) the corresponding first derivative spectra, (f) Co K-edge and (g) the corresponding first derivative spectra, (h) Mn K-edge and (i) the corresponding first derivative spectra.

In order to investigate the interfacial stability between LPSCl and NMC811 with and without surface impurities, XPS and XANES measurements were performed. Figure S10 and Figures 6.3a-b show the S 2p XPS spectra of the LPSCl SSEs collected from the pristine LPSCl, cycled pristine electrode (denoted as C-Pristine), and cycled treated electrode (denoted as C-Treated), respectively. The C-Pristine electrode shows higher relative content of SO_3^{2-} than the C-Treated electrode. Moreover, the further oxidized products of LPSCl, SO_4^{2-}, can be observed in the C-Pristine electrode but are essentially absent in the C-Treated electrode. Figure 6.3c shows the S K-edge XANES spectra of the LPSCl SSEs collected from the C-Pristine and C-Treated with a pristine LPSCl as reference, which are in agreement with the XPS results. A new peak at 2481.9 eV in the C-Pristine electrode increases noticeably compared to that of the pristine LPSCl, indicating the formation of sulfate species as the by-product in LPSCl during cycling.[32, 33] This result is highly consistent with our previous studies on the use of NMC811/LGPS SSBs with and without carbon additives.[17, 34] Our previous studies demonstrated that the formation of sulfate species can be effectively suppressed by surface coating of cathode with either inorganic Li_3PO_4 or PEDOT polymer. Therefore, we proposed that the formed sulfate was derived from the oxygen participation from the NMC811 bulk structure, which could be alleviated by the construction of interfacial layer on the surface of NMC811. Interestingly, in the current study, the sulfate species are significantly suppressed in the C-treated electrode without coating protection. Considering the only difference between the C-Pristine and C-Treated electrodes is the treated surface, the findings suggest that the formation of sulfate is mainly attributed to the oxygen participation from residual lithium compounds on the surface of NMC811. Different from the S XPS results, the oxidation of P is obviously alleviated in the C-Pristine electrode as shown in Figure S11, indicating that the side-reactions between residual lithium compounds and LPSCl mainly lead to the oxidation of S rather than P in LPSCl. Impressively, removing residual lithium compounds from the cathode surface significantly suppresses the oxidation of LPSCl, therefore boosting the electrochemical performance.

The transition metal K-edge XANES spectra (TMs, including Ni, Co, and Mn) are presented in Figures 6.3d-i to better understand the structural evolution of the layered NMC811 during cycling. It should be mentioned that both pristine and treated NMC811 were tested after being fully discharged to 2.7 V vs. Li$^+$/Li. Generally, the oxidation state of the TMs correspond to the threshold energy position of the K-edge XANES peaks, while the shape of the peaks is indicative of the TMs local structural environment.[35-37] The 2 eV peak energy shift for the Ni K-edge can be observed in the spectrum for the C-Pristine electrode (Figure 6.3d), indicating the oxidation of Ni after cycling. In contrast, the C-Treated NMC811 demonstrates less change toward higher energy in the Ni K-edge position after cycling. Consistent with our previous studies, the oxidation of Ni after cycling suggests that a portion of the lithium ions were unable to intercalate back into the layered structure of the NMC811 cathodes because of the formation of a cathode electrolyte interface (CEI) through severe side-reactions between residual lithium compounds and LPSCl.[34] As a result of the changes in the Ni environment, variations in peak shape and position of the Co and Mn K-edge XANES spectra are observed in C-Pristine NMC811, which are identified by the position shift of the first maximum in the derivative of the absorption curves, as shown in Figures 6.3g and 6.3i. In contrast, the changes in the spectral features for the C-Treated NMC811 are less prominent. The shape variations of Co and Mn K-edge spectra indicate the structural evolution of NMC811 during cycling, which is induced from the side-reactions with LPSCl. Moreover, it can be concluded that the suppression of side-reactions aided by the cleaning of the NMC811 surface led to less structural change during cycling.
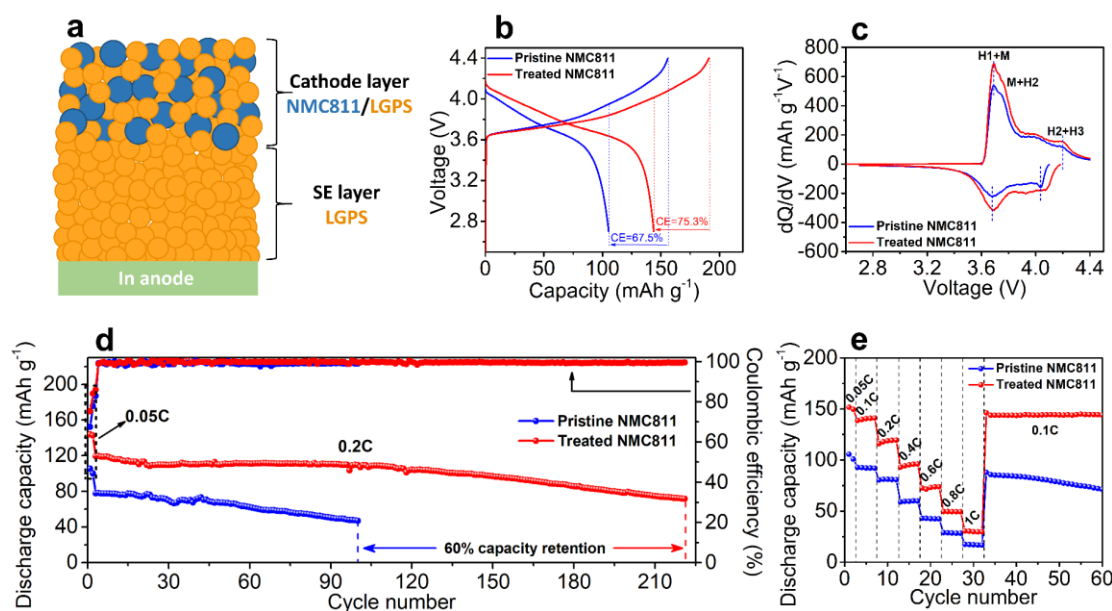
Figure 6.4 Comparison of the electrochemical performance of pristine and treated NMC811 in LGPS SSBs. (a) Schematic illustration of the designed model cell, (b) charge-discharge curves of the first cycle at 0.05C, (c) the corresponding differential capacity profiles, (d) cycling stability, and (e) rate capability.

The electrochemical performance of the pristine and treated NMC811 is also demonstrated in LGPS-based SSBs and the configuration of the designed model is shown in Figure 6.4a. The first charge-discharge profiles of the pristine and treated NMC811 at 0.05 C are demonstrated in Figure 6.4b. The treated NMC811 shows a higher discharge capacity of 143.8 mAh g^{-1} with a Coulombic efficiency of 75.3%. However, the pristine NMC811 only delivered a discharge capacity of 105.3 mAh g^{-1} with a lower Coulombic efficiency of 67.5%. The corresponding differential capacity profiles as a function of voltage are shown in Figure 6.4c to further reveal the different charge-discharge behaviors between the pristine and treated NMC811 in the initial cycle. It is clear that both the pristine and treated NMC811 show three pairs of redox peaks arising from the multiple phase transitions in NMC811 from hexagonal to monoclinic (H1 to M), monoclinic to hexagonal (M to H2), and hexagonal to hexagonal (H2 to H3) during the delithiation-lithiation process.[38, 39] The treated NMC811 demonstrates smaller voltage intervals between the pairs of anodic-cathodic peaks and higher peak intensities than that

of the pristine NMC811, indicating enhanced electrochemical reaction activity with reduced polarization induced by the cleaned surface of NMC811. This conclusion is also confirmed by the GITT results, which demonstrate lower polarization potentials and higher D_{Li} during the initial charge-discharge process in the treated NMC811 as shown in Figure S12.

The long cycling stability of both pristine and treated NMC811 is also demonstrated in Figure 6.4d. The SSBs are first activated with a low current density of 0.05 C for two cycles before switching to a high current density of 0.2 C for long-term cycling. Initial discharge capacities of 143.8 mAh g^{-1} (0.05 C) and 119.4 mAh g^{-1} (0.2 C) are achieved by the treated NMC811, which are much higher than those of the pristine NMC811 with capacities of 105.3 mAh g^{-1} at 0.05 C and 77.9 mAh g^{-1} at 0.2 C, respectively. Furthermore, the treated NMC811 reveals obviously improved cycling stability with 60% capacity retention after 219 cycles, which is much higher than that of the pristine NMC811, which had a 60% capacity retention after only 98 cycles. The EIS results indicate that the increase of the interfacial resistance after cycling in the treated NMC811 is much slower than that of the pristine NMC811 as shown in Figure S13. The rate capability at the different current densities ranging from 0.05 C to 1 C is displayed in Figure 6.4e. The treated NMC811 demonstrates higher rate capacities under each current density compared to the pristine NMC811. Meanwhile, the cycling stability is also enhanced when the current density returns to 0.1 C, which is attributed to the advantages of the cleaned surface of NMC811. The improved electrochemical performance in both LPSCl-based and LGPS-based SSBs show the strong competitiveness when comparing to the reported coating strategies. The sources of the data are listed in Table S1. This result indicates that cleaning the surface of Ni-rich NMC cathodes is a promising strategy to achieve high-performance Ni-rich NMC in sulfide-based SSBs.
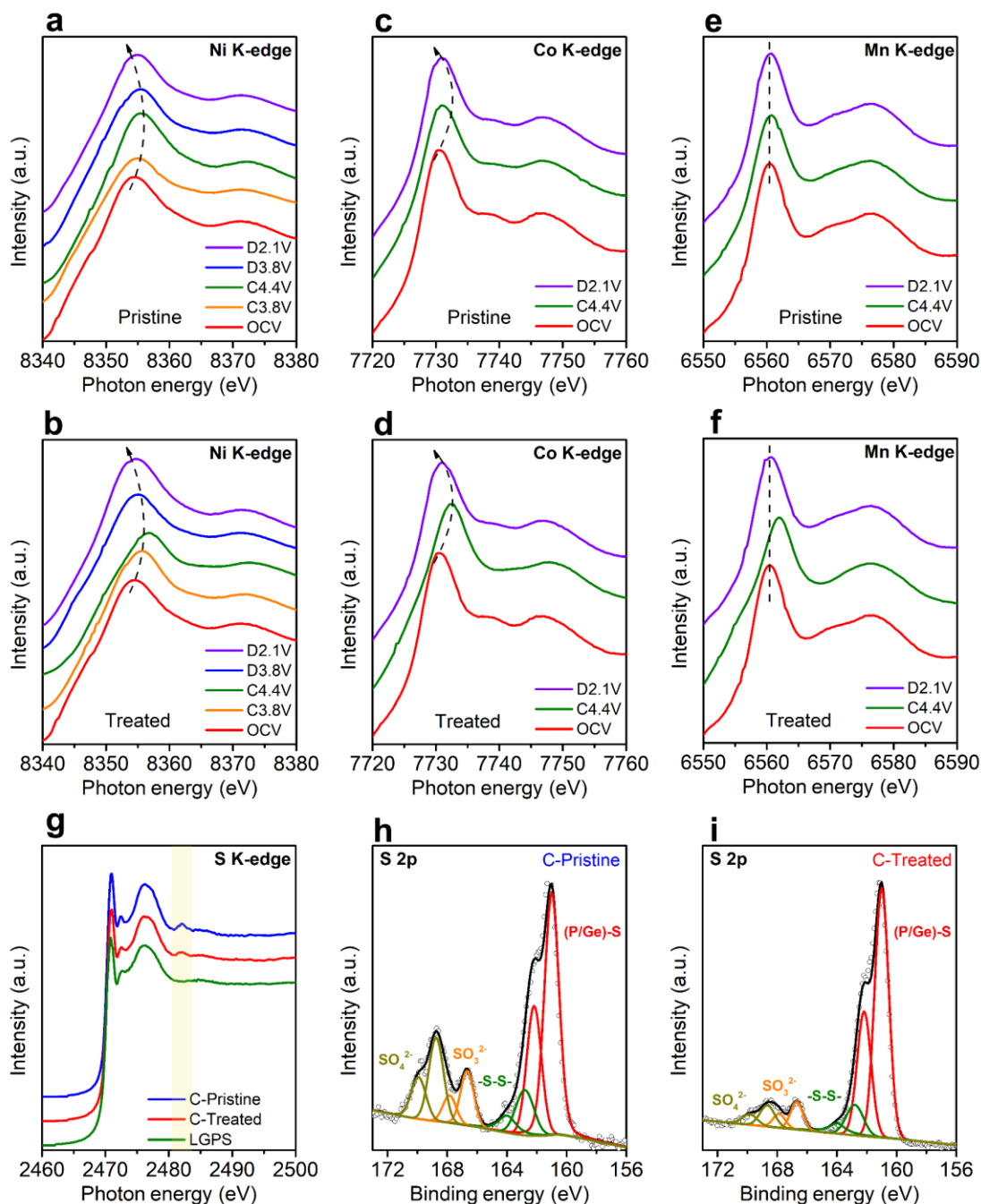
Figure 6.5 Understanding the chemical interactions between NMC811 and LGPS during electrochemical cycling in LGPS SSBs. (a-f) Ni, Co, and Mn K-edge XANES spectra of the pristine and treated NMC811 at the different charge-discharge stages in the initial cycle: (a) Ni K-edge, (c) Co K-edge, and (e) Mn K-edge XANES spectra of the pristine NMC811; (b) Ni K-edge, (d) Co K-edge, and (f) Mn K-edge XANES spectra of

the treated NMC811. (g) S K-edge XANES spectra of LGPS in the cycled pristine electrode (C-Pristine) and cycled treated electrode (C-Treated) cells with pristine LGPS as a reference. S 2p XPS spectra of the (h) C-Pristine and (i) C-Treated.

The cathode interfacial stability was also investigated in LGPS-based SSBs. Both pristine and treated NMC811 were tested at five different charge and discharge states including open-circuit voltage, charging to 3.8 V and 4.4 V, as well as discharging to 3.8 V and 2.1 V, which are denoted as OCV, C3.8V, C4.4V, D3.8V, and D2.1V, respectively. TMs K-edge XANES spectra of both pristine and treated NMC811 are presented in Figures 6.5a-f to evaluate the evolution of NMC811 at different charge-discharge states in the initial cycle. From the Ni K-edge XANES spectra in Figures 6.5a and 6.5b, both pristine and treated NMC811 show a reversible peak shift after a charge-discharge cycle. However, the treated NMC811 demonstrates a shift toward higher energy at the end of the charging state (C4.4V), indicating a deeper charge because of the smaller polarization than that of the pristine NMC811, as demonstrated in the initial charge-discharge curves (Figure 6.4b). Meanwhile, the Co and Mn K-edge XANES spectra also demonstrate reversible peak shifts in both pristine and treated NMC811 during the initial charge-discharge process (Figures S14 and S15). Interestingly, compared to the pristine NMC811, the more obvious energy shift in the Co K-edge XANES spectrum of the treated NMC811 at C4.4V demonstrates that the deeper charging also triggers a Co redox reaction in NMC811 (Figure 6.5c-d).[30] Furthermore, the shape variation in Mn K-edge XANES spectra of the treated NMC811 shown in Figure 6.5f reveals a change in the local environment of Mn atoms because of the more obvious structural evolution during delithiation-lithiation process than that of the pristine NMC811 (Figure 6.5e). In contrast, after long-term cycling, more obvious peak evolution in the TMs K-edge XANES spectra can be observed in the pristine NMC811 compared to that of the treated NMC811 (Figures S16-18), although the SSBs were fully discharged to 2.7 V vs. Li$^+$/Li, indicating the structural evolution of NMC811 is derived from the side-reactions with LGPS.

The corresponding S K-edge XANES spectra of LGPS at different charge and discharge states are presented in Figure S19. There is no noticeable energy shift or new peaks

observed in either pristine or treated electrodes during the initial charge-discharge process. However, as is the case for LPSCl, both the S K-edge XANES and S 2p XPS spectra of LGPS in the pristine electrode reveals an obvious sulfate peak after long-term cycling, which is suppressed in the treated electrode (Figures 6.5g-i and Figure S20). This result indicates that the formation of sulfate generally accumulates with further charge-discharge cycling because of the continued side-reactions between residual lithium compounds and LGPS, which is obviously alleviated by the surface modification. Therefore, removing residual lithium compounds on the surface of Ni-rich NMC significantly suppresses the oxidation of sulfide SSEs, thus alleviating the side-reactions between Ni-rich NMC cathode and sulfide SSEs during electrochemical cycling. In addition to the oxidation of S, the by-products of LGPS also can be observed in the P 2p spectra of both C-Pristine and C-Treated electrodes after the long-term cycling (Figure S21), indicating the decomposition of LGPS at high voltage when coupled with NMC811 cathodes.

6.4 Conclusion

In conclusion, the comprehensive electrochemical analyses and X-ray characterizations are adopted to investigate the origin of cathode interface degradation in sulfide-based ASSLIBs. The electrochemical results indicate that eliminating residual lithium impurities on the surface of NMC811 induces the notably improved electrochemical performance, including higher capacity and Coulombic efficiency, reduced voltage polarization, and enhanced lithium-ion diffusion coefficients in the initial charge-discharge cycle. More importantly, the cleaned surface is beneficial for NMC811 to bolstering the cycling stability and rate capability in two promising sulfide-based SSEs systems (LPSCl and LGPS). The underlying degradation mechanism of cathode interface is investigated by XPS and XANES analyses. The results indicate that residual lithium compounds are the catalyst for accelerating the oxidation of sulfide SSEs. As a result, the formed by-products lead to severe side-reactions between NMC811 and sulfide SSEs, therefore inducing the formation of an undesirable CEI layer and structural degradation of NMC811. In contrast, removal of residual lithium compounds helps to alleviate the

oxidation of sulfide SSEs and limits the severe interfacial side-reactions, therefore boosting the electrochemical performance of NMC811 cathodes. These findings are observed in both LPSCl and LGPS-based ASSLIBs, providing a strong evidence to prove the origin of degradation at cathode interface. Different from the prevailing protection coating methods, which require the addition of a new interfacial layer to suppress the side-reactions, removing the origin of the side-reactions from the pristine materials without introducing new materials into the system is a facile and scalable strategy towards realizing the industrial application of high-performance ASSLIBs.

6.5 Acknowledgments

6.6 References

[1] S. Randau, D.A. Weber, O. Kötz, R. Koerver, P. Braun, A. Weber, E. Ivers-Tiffée, T. Adermann, J. Kulisch, W.G. Zeier, F.H. Richter, J. Janek, Nat. Energy 5 (2020) 259-270.

[2] R. Chen, Q. Li, X. Yu, L. Chen, H. Li, Chem. Rev. 120 (2019) 6820-6877.

[3] H. Li, Joule 3 (2019) 911-914.

[4] H.-J. Deiseroth, S.-T. Kong, H. Eckert, J. Vannahme, C. Reiner, T. Zaiß, M. Schlosser, Angew. Chem. Int. Ed. 47 (2008) 755-758.

[5] Y. Kato, S. Hori, T. Saito, K. Suzuki, M. Hirayama, A. Mitsui, M. Yonemura, H. Iba, R. Kanno, Nat. Energy 1 (2016) 16030.

[6] C. Yu, Y. Li, M. Willans, Y. Zhao, K.R. Adair, F. Zhao, W. Li, S. Deng, J. Liang, M.N. Banis, R. Li, H. Huang, L. Zhang, R. Yang, S. Lu, Y. Huang, X. Sun, Nano Energy 69 (2020) 104396.

[7] X. Li, J. Liang, X. Yang, K.R. Adair, C. Wang, F. Zhao, X. Sun, Energy Environ. Sci. 13 (2020) 1429.

[8] W. Li, E.M. Erickson, A. Manthiram, Nat. Energy. 5 (2020) 26-34.

[9] S.-T. Myung, F. Maglia, K.-J. Park, C.S. Yoon, P. Lamp, S.-J. Kim, Y.-K. Sun, ACS Energy Lett. 2 (2017) 196-223.

[10] T. Li, X.-Z. Yuan, L. Zhang, D. Song, K. Shi, C. Bock, Electrochem. Energy Rev. 3 (2020) 43-80.

[11] Y. Zhu, X. He, Y. Mo, ACS Appl. Mater. Interfaces 7 (2015) 23685-23693.

[12] W. Zhang, D.A. Weber, H. Weigand, T. Arlt, I. Manke, D. Schröder, R. Koerver, T. Leichtweiss, P. Hartmann, W.G. Zeier, ACS Appl. Mater. Interfaces 9 (2017) 17835-17845.

[13] X. Li, Z. Ren, M. Norouzi Banis, S. Deng, Y. Zhao, Q. Sun, C. Wang, X. Yang, W. Li, J. Liang, X. Li, Y. Sun, K. Adair, R. Li, Y. Hu, T.-K. Sham, H. Huang, L. Zhang, S. Lu, J. Luo, X. Sun, ACS Energy Lett. 4 (2019) 2480-2488.

[14] S.P. Culver, R. Koerver, W.G. Zeier, J. Janek, Adv. Energy Mater. 9 (2019) 1900626.

[15] D. Cao, Y. Zhang, A.M. Nolan, X. Sun, C. Liu, J. Sheng, Y. Mo, Y. Wang, H. Zhu, Nano Lett. 20 (2020) 1483.

[16] A.Y. Kim, F. Strauss, T. Bartsch, J.H. Teo, T. Hatsukade, A. Mazilkin, J. Janek, P. Hartmann, T. Brezesinski, Chem. Mater. 31 (2019) 9664-9672.

[17] S. Deng, X. Li, Z. Ren, W. Li, J. Luo, J. Liang, J. Liang, M.N. Banis, M. Li, Y. Zhao, X. Li, C. Wang, Y. Sun, Q. Sun, R. Li, Y. Hu, H. Huang, L. Zhang, S. Lu, J. Luo, X. Sun, Energy Storage Mater. 27 (2020) 117-123.

[18] X. Li, L. Jin, D. Song, H. Zhang, X. Shi, Z. Wang, L. Zhang, L. Zhu, J. Energy Chem. 40 (2020) 39-45.

[19] X. Li, Q. Sun, Z. Wang, D. Song, H. Zhang, X. Shi, C. Li, L. Zhang, L. Zhu, J. Power Sources 456 (2020) 227997.

[20] S.W. Park, G. Oh, J.-W. Park, Y.-C. Ha, S.-M. Lee, S.Y. Yoon, B.G. Kim, Small 15 (2019) 1900235.

[21] T. Bartsch, F. Strauss, T. Hatsukade, A. Schiele, A.Y. Kim, P. Hartmann, J. Janek, T. Brezesinski, ACS Energy Lett. 3 (2018) 2539-2543.

[22] F. Walther, R. Koerver, T. Fuchs, S. Ohno, J. Sann, M. Rohnke, W.G. Zeier, J. Janek, Chem. Mater. 31 (2019) 3745-3755.

[23] H. Visbal, S. Fujiki, Y. Aihara, T. Watanabe, Y. Park, S. Doo, J. Power Sources 269 (2014) 396-402.

[24] H. Liu, Y. Yang, J. Zhang, J. Power Sources, 162 (2006) 644-650.

[25] B. Wang, Y. Zhao, M.N. Banis, Q. Sun, K.R. Adair, R. Li, T.-K. Sham, X. Sun, ACS Appl. Mater. Interfaces 10 (2018) 1654-1661.

[26] J. Zheng, W. Shi, M. Gu, J. Xiao, P. Zuo, C. Wang, J.-G. Zhang, J. Electrochem. Soc. 160 (2013) A2212-A2219.

[27] X. He, X. Xu, L. Wang, C. Du, X. Cheng, P. Zuo, Y. Ma, G. Yin, J. Electrochem. Soc. 166 (2019) A143-A150.

[28] Y. Bi, W. Yang, R. Du, J. Zhou, M. Liu, Y. Liu, D. Wang, J. Power Sources 283 (2015) 211-218.

[29] R. Jung, R. Morasch, P. Karayaylali, K. Phillips, F. Maglia, C. Stinner, Y. Shao-Horn, H.A. Gasteiger, J. Electrochem. Soc. 165 (2018) A132-A141.

[30] C. Tian, D. Nordlund, H.L. Xin, Y. Xu, Y. Liu, D. Sokaras, F. Lin, M.M. Doeff, J. Electrochem. Soc. 165 (2018) A696-A704.

[31] J. Alvarado, C. Wei, D. Nordlund, T. Kroll, D. Sokaras, Y. Tian, Y. Liu, M.M. Doeff, Mater. Today 35 (2020) 87.

[32] M.E. Fleet, X. Liu, S.L. Harmer, H.W. Nesbitt, Can. Mineral. 43 (2005) 1589-1603.

[33] J. Prietzel, A. Botzaki, N. Tyufekchieva, M. Brettholle, J. Thieme, W. Klysubun, Environ. Sci. Tech. 45 (2011) 2878-2886.

[34] S. Deng, Y. Sun, X. Li, Z. Ren, J. Liang, K. Doyle-Davis, J. Liang, W. Li, M. Norouzi Banis, Q. Sun, R. Li, Y. Hu, H. Huang, L. Zhang, S. Lu, J. Luo, X. Sun, ACS Energy Lett. 5 (2020) 1243-1251.

[35] X. Yu, Y. Lyu, L. Gu, H. Wu, S.-M. Bak, Y. Zhou, K. Amine, S.N. Ehrlich, H. Li, K.-W. Nam, X.-Q. Yang, Adv. Energy Mater. 4 (2014) 1300950.

[36] E. Hu, X. Yu, R. Lin, X. Bi, J. Lu, S. Bak, K.-W. Nam, H.L. Xin, C. Jaye, D.A. Fischer, Nat. Energy 3 (2018) 690-698.

[37] P.-Y. Liao, J.-G. Duh, J.-F. Lee, J. Power Sources 189 (2009) 9-15.

[38] U.H. Kim, H.H. Ryu, J.H. Kim, R. Mücke, P. Kaghazchi, C.S. Yoon, Y.K. Sun, Adv. Energy Mater. 9 (2019) 1803902.

[39] X. Xu, H. Huo, J. Jian, L. Wang, H. Zhu, S. Xu, X. He, G. Yin, C. Du, X. Sun, Adv. Energy Mater. 9 (2019) 1803963.

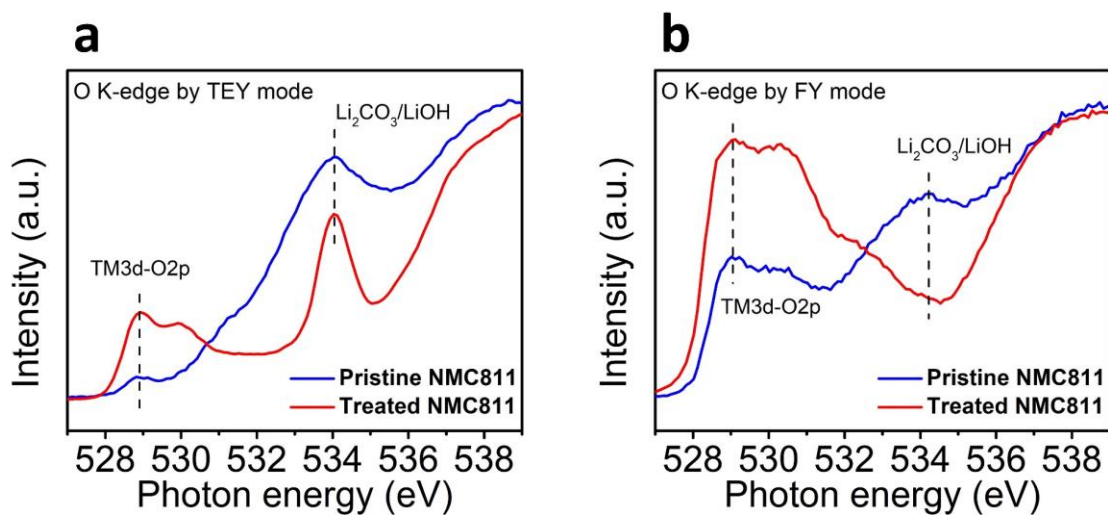## 6.7 Supporting information

Figure S1. O K-edge XANES spectra of the pristine and treated NMC811 in (a) TEY and (b) FY modes, respectively.
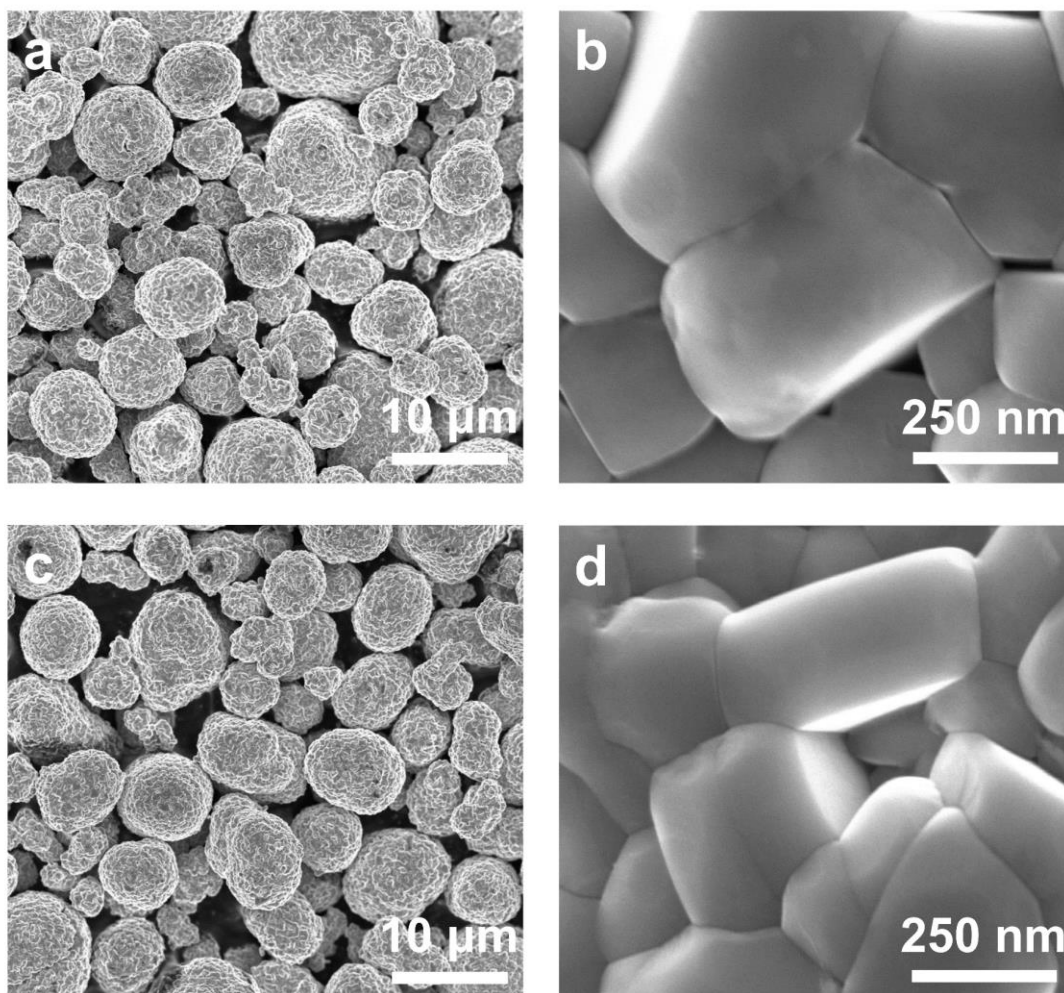
Figure S2. SEM images of the (a-b) pristine and (c-d) treated NMC811.
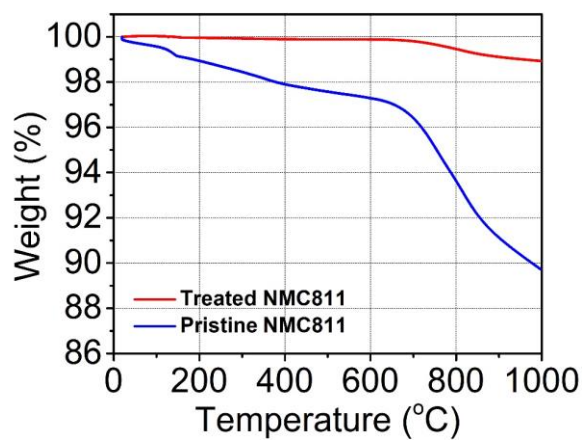
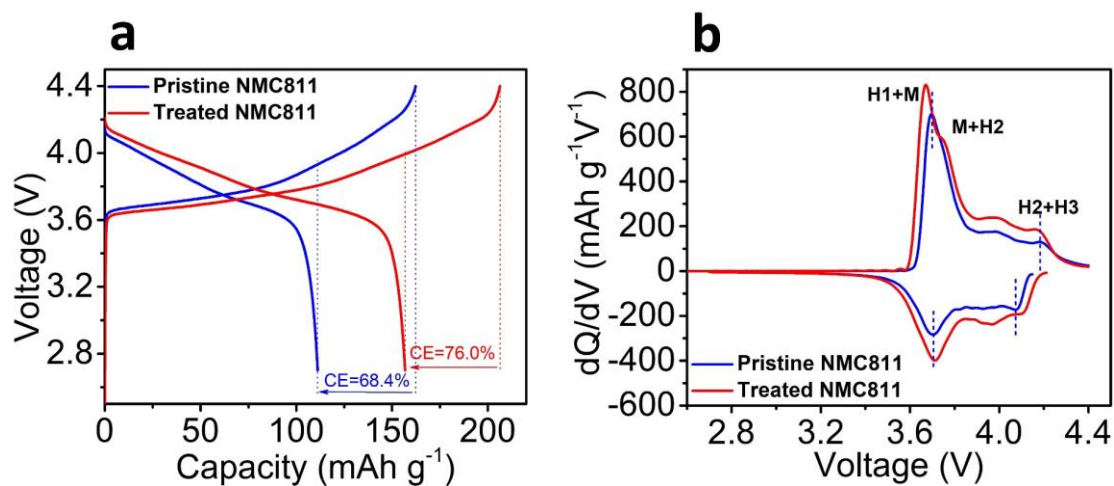Figure S3. TGA profiles of the pristine and treated NMC811.

Figure S4. (a) The initial charge-discharge curves and (b) the corresponding differential capacity profiles of the pristine and treated NMC811 in LPSCl SSBs at 0.05C.
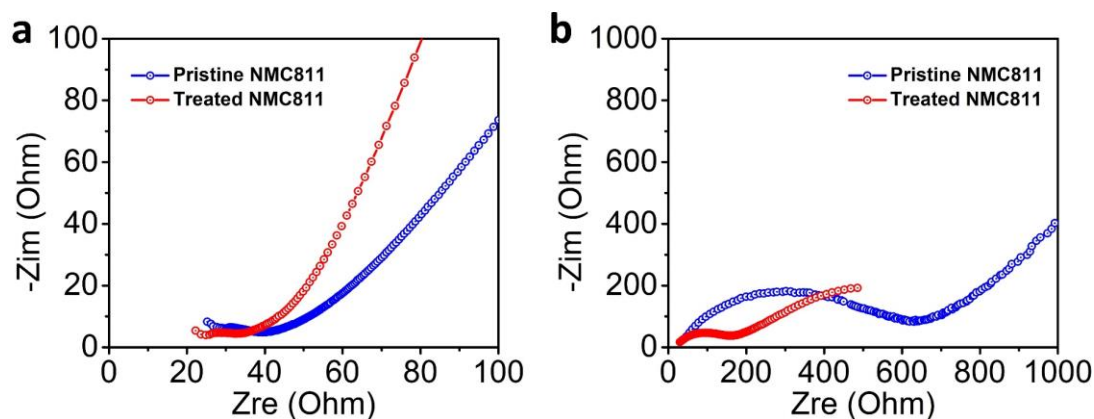
Figure S5. EIS plots of both pristine and treated NMC811 in LPSCl SSBs. (a) Before cycling and (b) after cycling.
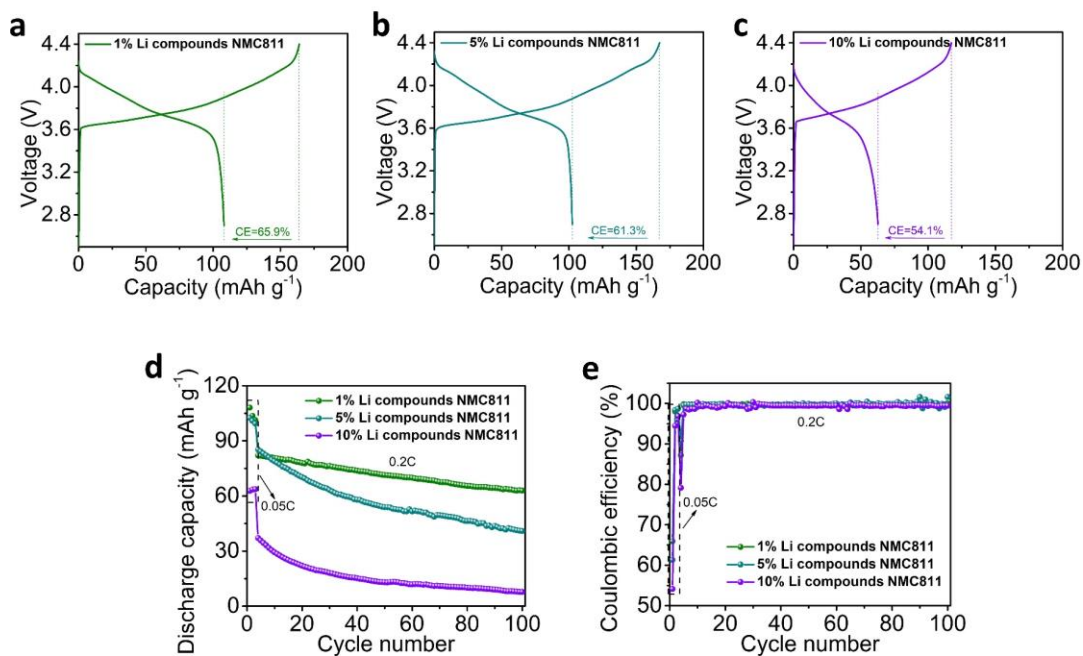

Figure S6. The electrochemical performance of different Li compounds in the treated NMC811 cathode composites in LPSCl-based SSBs. The initial charge-discharge curves of (a) 1 wt%, (b) 5 wt%, and 10 wt% Li compounds, respectively, at 0.05C; (d) cycling stability and (e) the corresponding Coulombic efficiency.
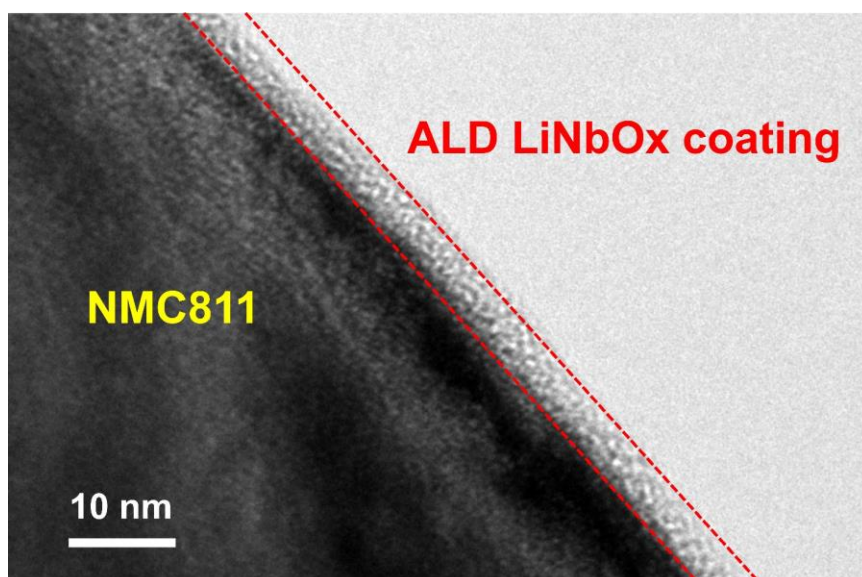
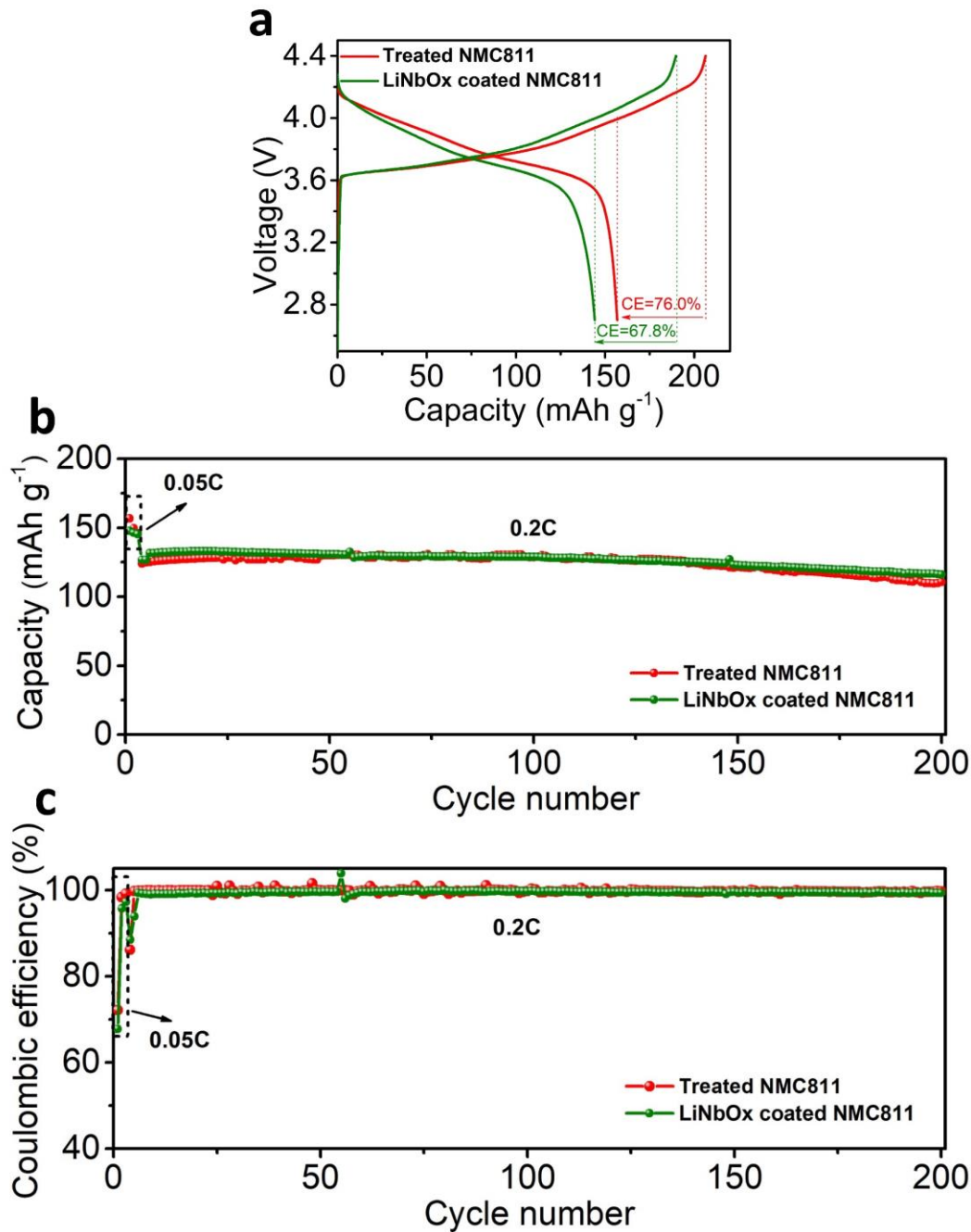Figure S7. TEM image of ALD LiNbO$_x$ coated NMC811.

Figure S8. Electrochemical performance of both treated and LiNbO$_x$ coated NMC811. (a) Charge-discharge curves of the first cycle at 0.05C, (b) cycling stability, and (c) the corresponding Coulombic efficiency.
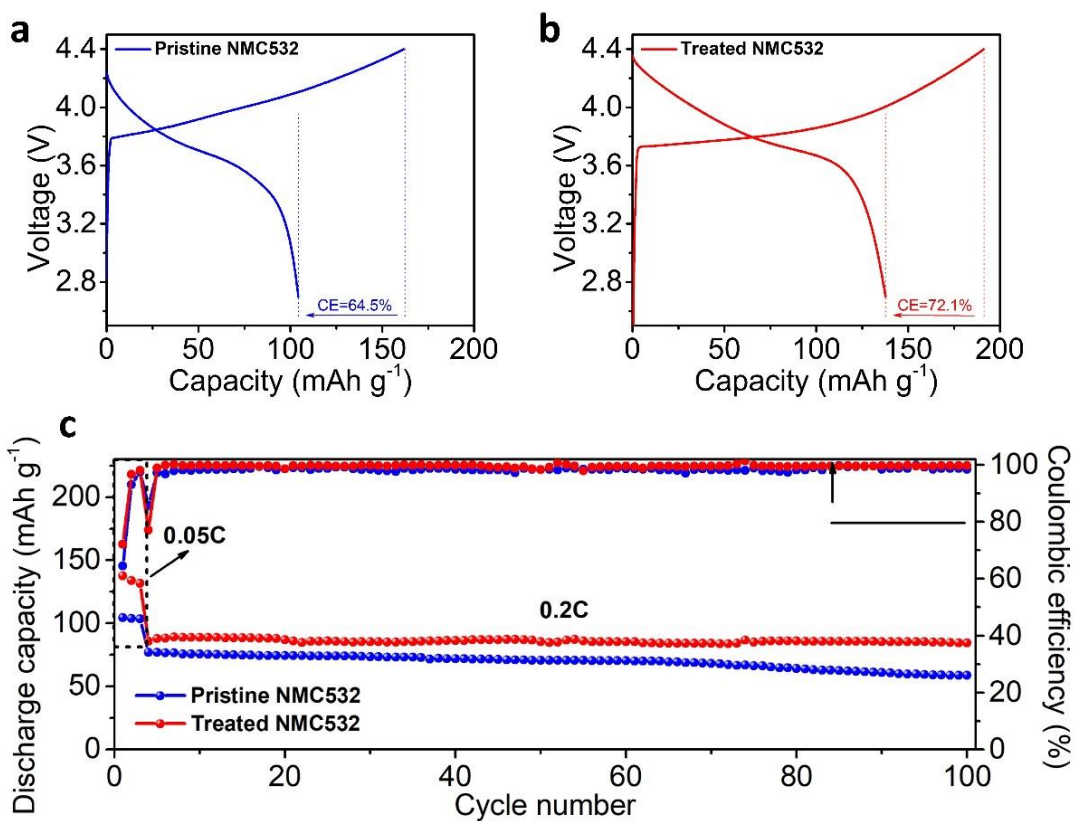
Figure S9. Electrochemical performance of both pristine and treated NMC532. The initial charge-discharge curves of (a) pristine NMC532 and (b) treated NMC532 at 0.05C, (c) cycling stability and the corresponding Coulombic efficiency.
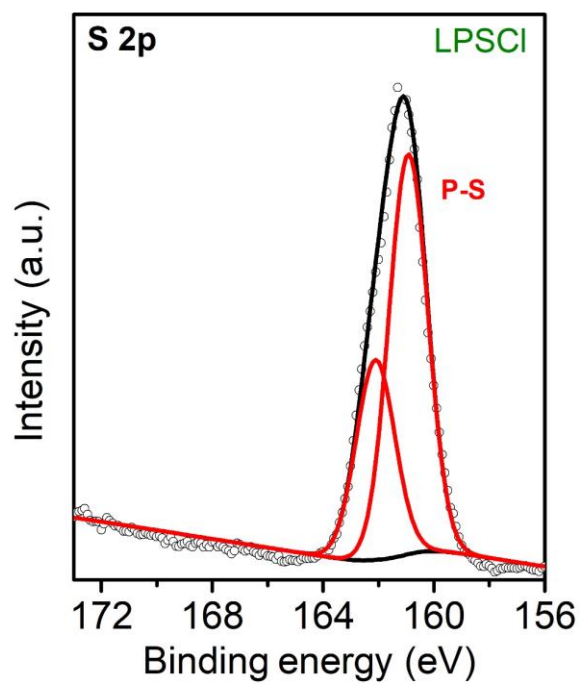
Figure S10. S 2p XPS spectra of pristine LPSCl SSEs.
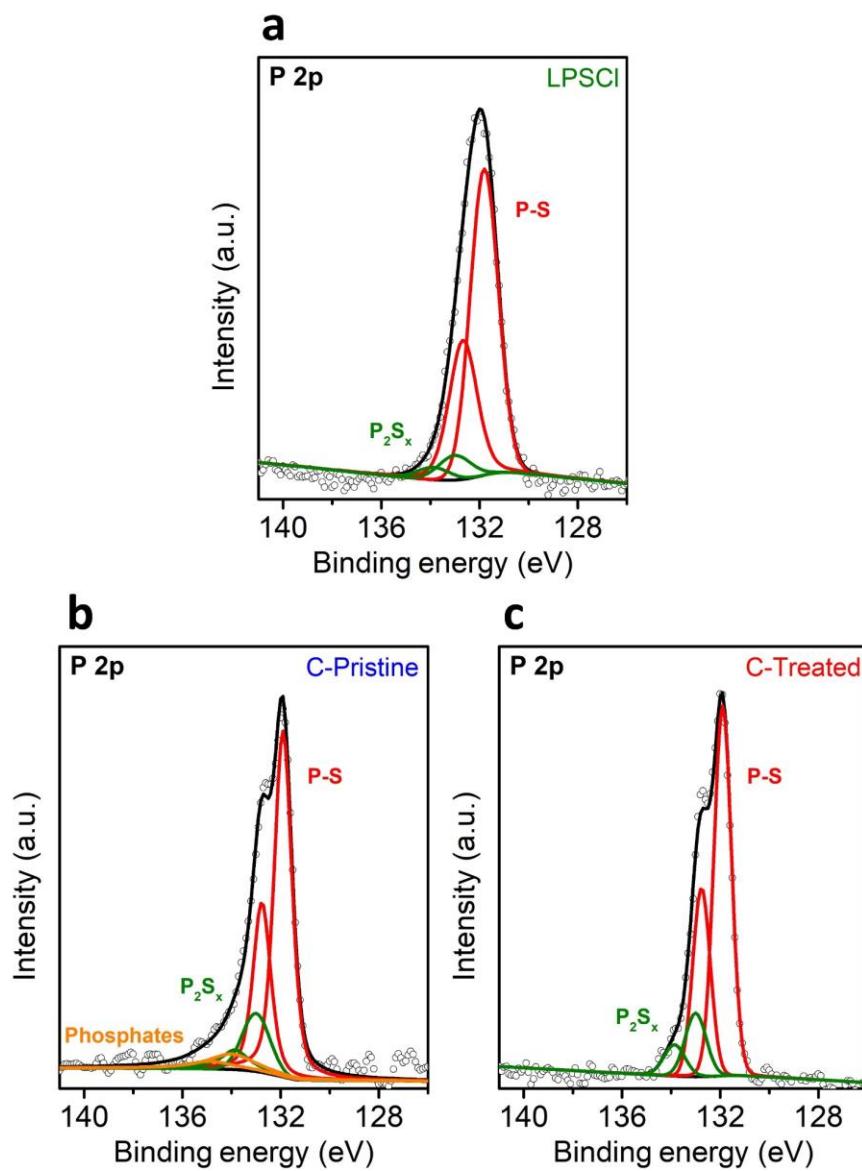
Figure S11. P 2p XPS spectra of (a) pristine LPSCl SSEs, (b) C-Pristine, and (c) C-Treated.
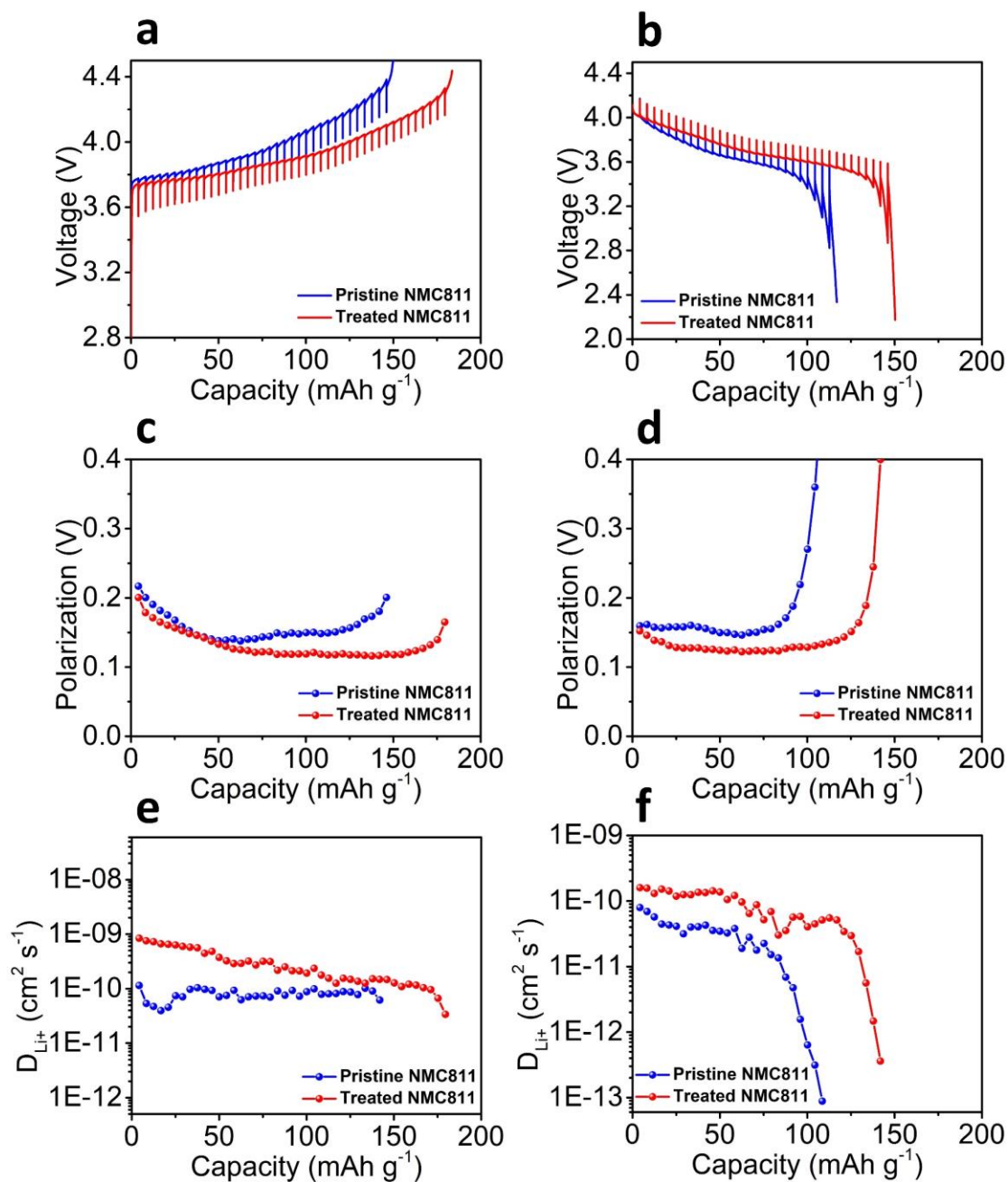
Figure S12. GITT curves of the pristine and treated NMC811 in LGPS SSBs during the (a) charge and (b) discharge processes; the corresponding polarization plots during the (c) charge and (d) discharge processes; and the corresponding lithium ion diffusion coefficients during the (e) charge and (f) discharge processes.
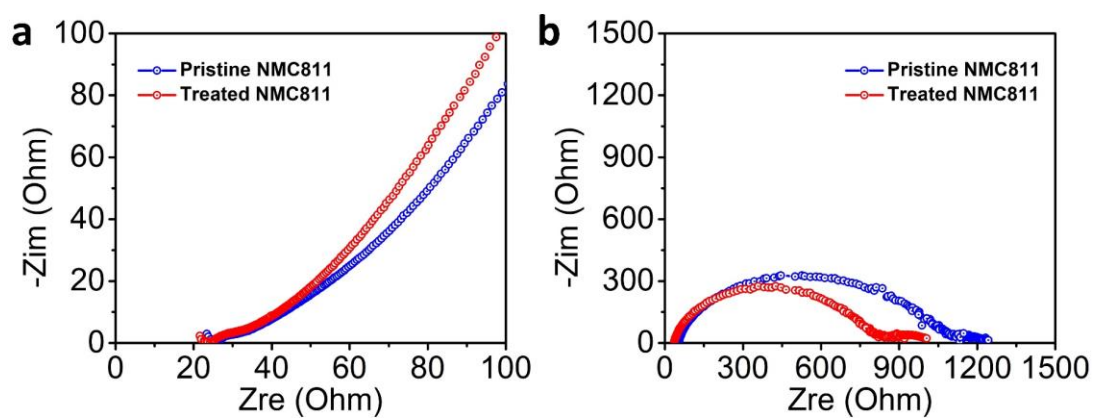
Figure S13. EIS plots of both pristine and treated NMC811 in LGPS SSBs. (a) Before cycling and (b) after cycling.
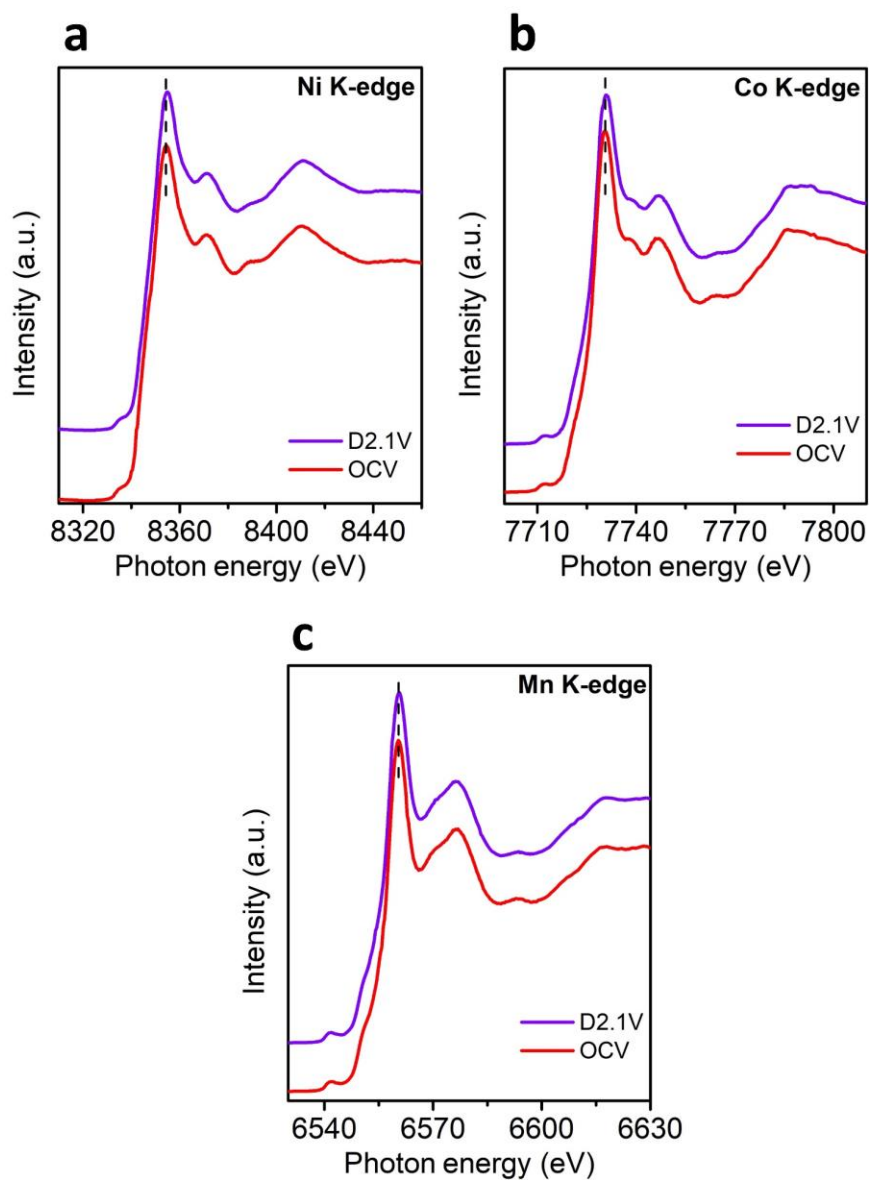
Figure S14. Ni, Co, and Mn K-edge XANES spectra of the pristine NMC811 before and after the initial charge-discharge cycle in LGPS SSBs: (a) Ni K-edge, (b) Co K-edge, and (c) Mn K-edge.
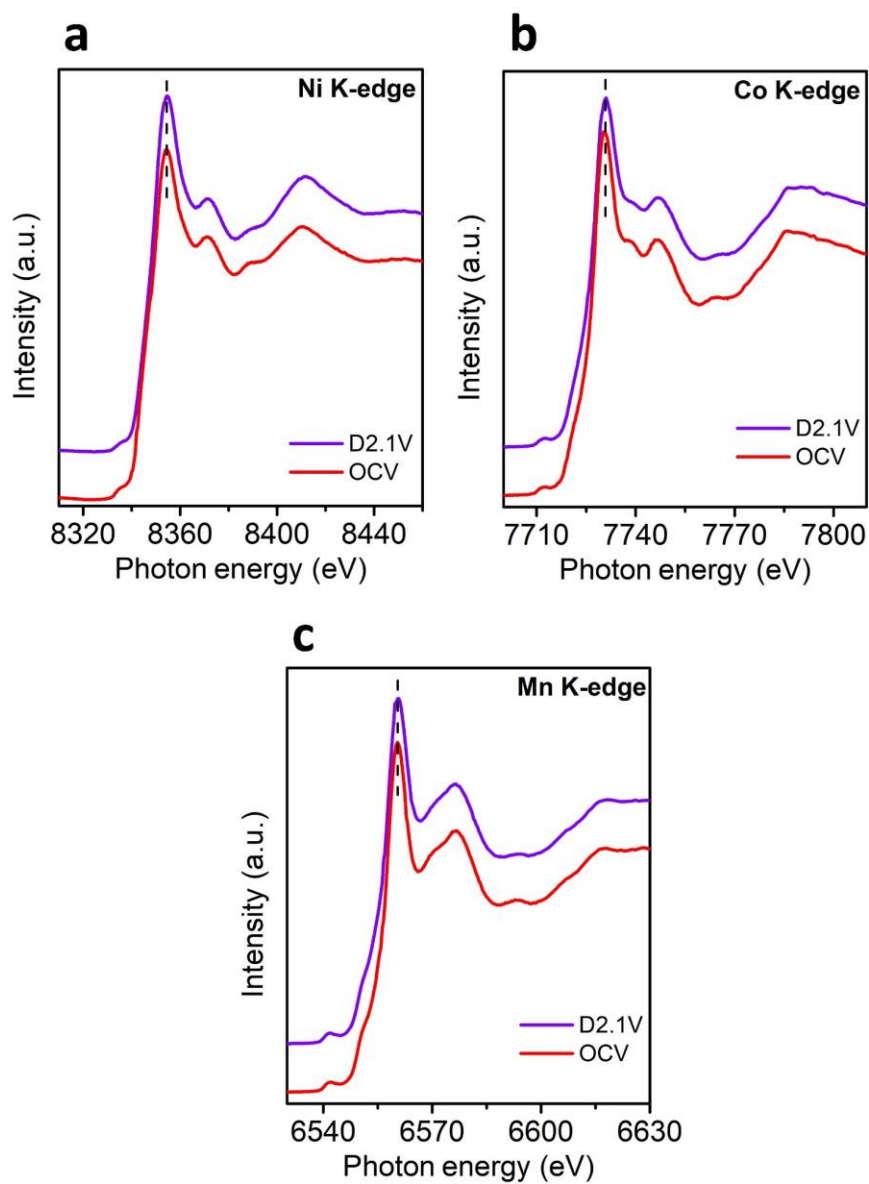
Figure S15. Ni, Co, and Mn K-edge XANES spectra of the treated NMC811 before and after the initial charge-discharge cycle in LGPS SSBs: (a) Ni K-edge, (b) Co K-edge, and (c) Mn K-edge.
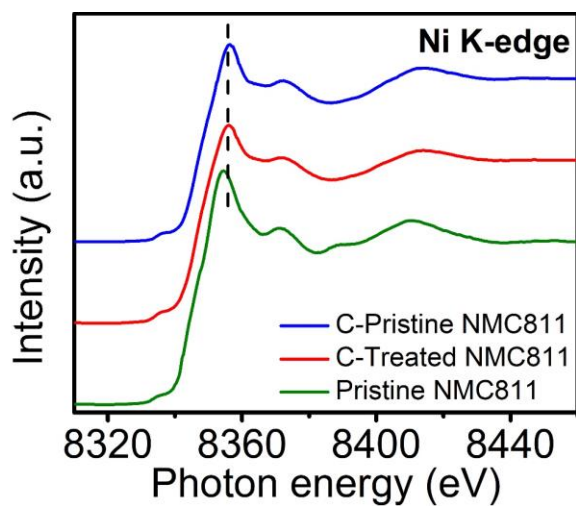
Figure S16. Ni K-edge XANES spectra of the pristine, cycled pristine, and cycled treated NMC811 in LGPS SSBs.
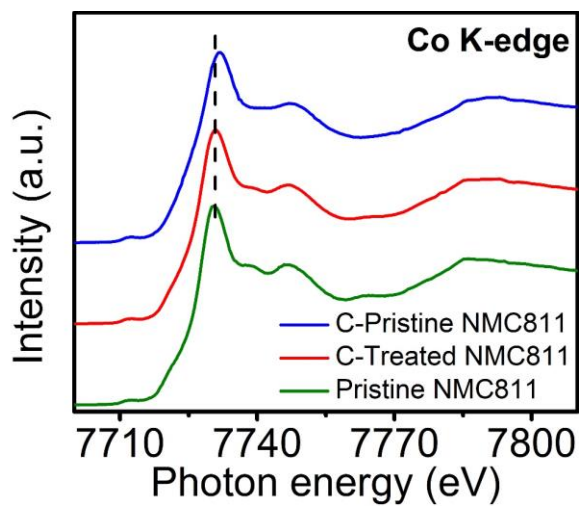
Figure S17. Co K-edge XANES spectra of the pristine, cycled pristine, and cycled treated NMC811 in LGPS SSBs.
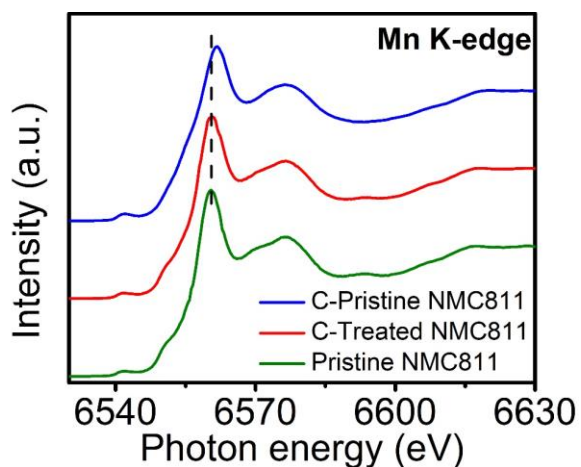
Figure S18. Mn K-edge XANES spectra of the pristine, cycled pristine, and cycled treated NMC811 in LGPS SSBs.

Figure S19. S K-edge XANES spectra of LGPS at the different charge-discharge stages in the initial cycle in the (g) pristine and (h) treated NMC811 cells, respectively.

Figure S20. S 2p XPS spectra of pristine LGPS SSEs.

Figure S21. P 2p XPS spectra of (a) pristine LGPS SSEs, (b) C-Pristine, and (c) C-Treated.

Table S1. Summary of cycling performance in reported NMC811 in both LPSCl and LGPS based SSBs

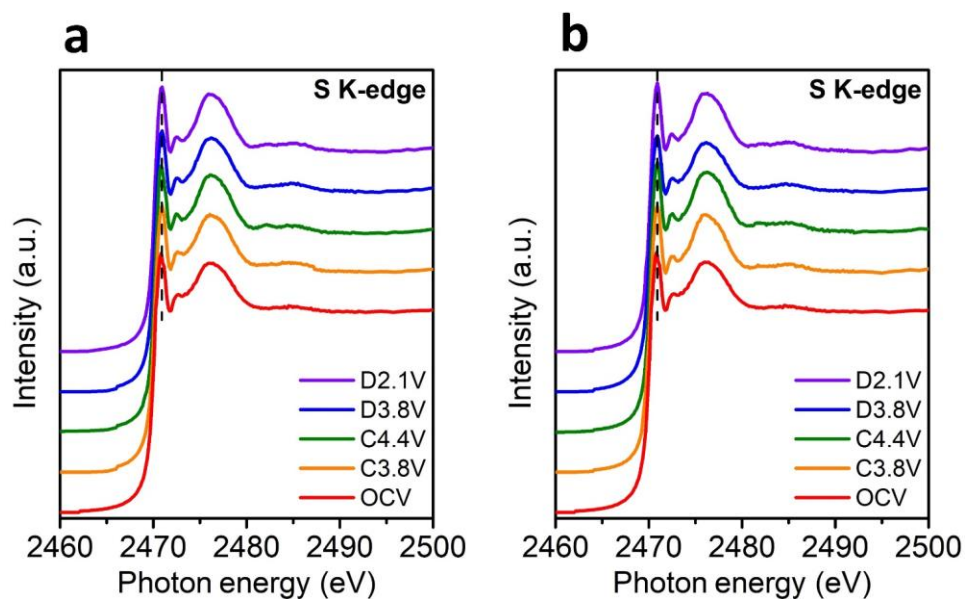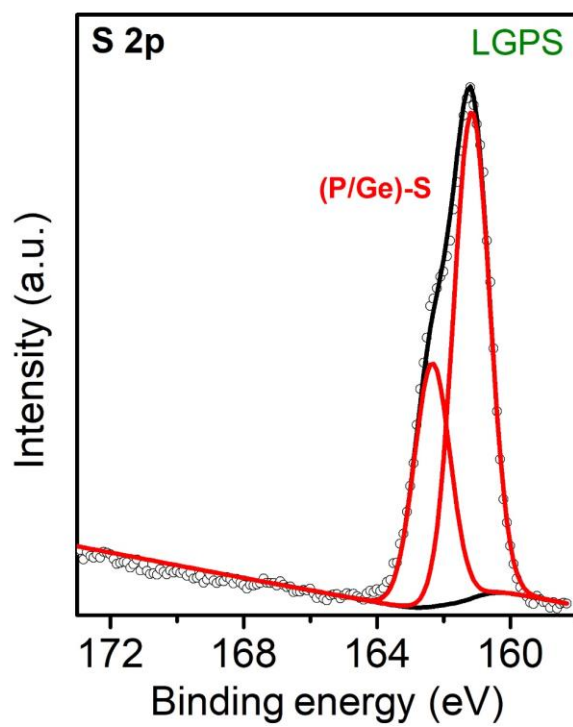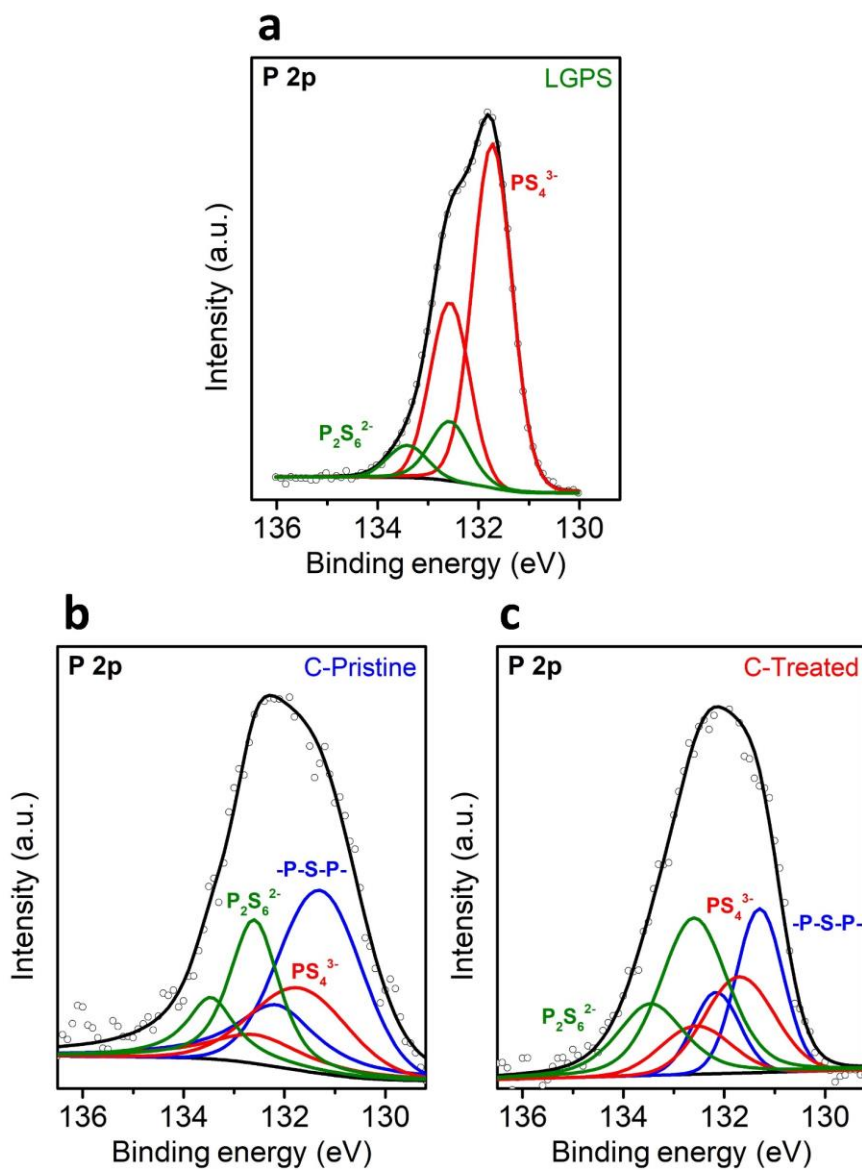|	Cathode materials	Solid-state electrolytes	Temperature	Voltage range (V)	Current density	Initial capacity/capacity after cycling ($mAh\ g^{-1}$)	Capacity retention (%)	Charge/discharge cycles
Our work	$LiNi_{0.8}Mn_{0.1}Co_{0.1}O_2$ (NMC811)	$Li_{5.5}PS_{4.5}Cl_{1.5}$	25 °C	2.7-4.4	0.2C	123.9/108.6	87.7	200
Ref. [1]	NMC811	$Li_{5.7}PS_{4.7}Cl_{1.3}$	25 °C	2.5-4.4	0.15C	140.8/83.4	59.2	100
Ref. [2]	NMC811	Li_6PS_5Cl	25 °C	2.5-4.3	0.1C	~120/115	95.8	20
Our work	NMC811	$Li_{10}GeP_2S_{12}$	25 °C	2.7-4.4	0.2C	119.4/77.7	65.1	200
Ref. [3]	NMC811	$Li_{10}GeP_2S_{12}$	25 °C	2.7-4.5	0.2C	163.2/96.1	58.9	300
Ref. [4]	NMC811	$Li_{10}GeP_2S_{12}$	35 °C	2.7-4.4	0.5C	~134/105	77.9	50
Ref. [5]	NMC811	$Li_{10}GeP_2S_{12}$	35 °C	2.7-4.4	0.3C	~160/128	80	585
Ref. [6]	NMC811	$Li_{10}GeP_2S_{12}$	25 °C	2.6-4.4	0.1C	160/99	61.9	50

References

[1] C. Yu, Y. Li, M. Willans, Y. Zhao, K.R. Adair, F. Zhao, W. Li, S. Deng, J. Liang, M.N. Banis, Nano Energy 69 (2020) 104396.

[2] E.A. Wu, C. Jo, D.H. Tan, M. Zhang, J.-M. Doux, Y.-T. Chen, G. Deysher, Y.S. Meng, J. Electrochem. Soc. 167 (2020) 130516.

[3] S. Deng, X. Li, Z. Ren, W. Li, J. Luo, J. Liang, J. Liang, M.N. Banis, M. Li, Y. Zhao, Energy Storage Mater. 27 (2020) 117-123.

[4] X. Li, L. Jin, D. Song, H. Zhang, X. Shi, Z. Wang, L. Zhang, L. Zhu, J. Energy Chem. 40 (2020) 39-45.

[5] X. Li, Q. Sun, Z. Wang, D. Song, H. Zhang, X. Shi, C. Li, L. Zhang, L. Zhu, J. Power Sources 456 (2020) 227997.

[6] X. Li, Z. Ren, M. Norouzi Banis, S. Deng, Y. Zhao, Q. Sun, C. Wang, X. Yang, W. Li, J. Liang, X. Li, Y. Sun, K. Adair, R. Li, Y. Hu, T.-K. Sham, H. Huang, L. Zhang, S. Lu, J. Luo, X. Sun, ACS Energy Lett. 4 (2019) 2480-2488.

Chapter 7

7 Eliminating the Detrimental Effects of Conductive Agents in Sulfide-Based Solid-State Batteries*

Sulfide-based solid-state electrolytes (SSEs) are considered a key part in the realization of high-performance all solid-state lithiumion batteries (ASSLIBs). However, the incompatibility between conductive additives and sulfide-based SSEs in the cathode composite challenges the stable delivery of high-rate capability. Herein, a poly(3,4-ethylenedioxythiophene) (PEDOT) modification is designed as a semiconductive additive for cathode composites (cathode/SSE/carbon) to realize the high performance. The modified ASSLIB demonstrates a competitive rate capacity of over 100 mAh g−1 at 1C, which is 10 times greater than that of the bare cathode. Detailed surface chemical and structural evolutions at the cathodic interface indicate the PEDOT modification not only significantly suppresses the side reactions but also realizes effective electron transfer at the cathode/SSE/carbon three-phase interface. Introducing a controllable semiconductive additive for the cathode composites in this study offers a promising design to realize the high-rate performance and overcome long-term challenges in the application of conductive additives in sulfide-based ASSLIBs.

7.1 Introduction

All solid-state lithium-ion batteries (ASSLIBs) are considered as a promising candidate for next generation energy storage devices for electric vehicles.[1-2] Compared to conventional liquid lithium-ion batteries, ASSLIBs have excellent safety characteristics by utilizing nonflammable solid-state electrolytes (SSEs) and competitive energy densities by accessing the lithium metal anode and high energy cathode materials.[3] Among the developed SSEs, sulfide-based inorganic electrolytes, such as $Li_{10}GeP_2S_{12}$ (LGPS), Li_6PS_5Cl, $Li_7P_3S_{11}$, and Li_3PS_4, possess high Li^+ conductivities ranging from 10^{-2} to 10^{-4} S cm^{-1}, which have the potential to realize high-performance ASSLIBs with stable cycling and high-rate capacities.[4-6] However, the narrow electrochemical stable window of sulfide-based SSEs challenges the interfacial stability at the both cathode and anode, thus producing dramatically increased interfacial resistance leading to rapid capacity fading.[7-8] In order to solve these issues, interfacial engineering approaches have been widely adopted to avoid direct exposure of the electrode materials to the SSEs and therefore prevent the occurrence of side-reactions.[9-11] As a result, the cycling stability of ASSLIBs has been greatly improved.

On the other hand, in order to further improve the electrochemical performance of the ASSLIBs, specifically the high rate capability, increasing the electronic conductivity in the cathode composites is of crucial importance. In conventional liquid lithium-ion batteries, carbon additives are indispensable to enhance the electronic conductivity of electrodes for high-rate capability. The application of prevailing carbon materials, such as acetylene black (AB), super P, and carbon nanotubes (CNTs), enable the homogeneous current distribution in the cathode layer.[12-14] However, the application of carbon additives in the sulfide-based ASSLIBs faces tremendous obstacles. Carbon additives provide sufficient electronic percolation pathways in the cathode composites, therefore accelerating the decomposition of sulfide SSEs during the charging process.[15] As a result, even with very small amounts of carbon additives, severe decomposition of sulfide SSEs still occurs at the electrolyte/carbon interface and leads to severe side-reactions and the formation of an undesirable interfacial layer between the carbon additives and SSEs.[16-18]

Therefore, the use of carbon additives hinders the electrochemical performance in ASSLIBs instead of showing a positive effect, let alone achieving high-rate capability.

To overcome the challenges of using carbon additives at cathode composites in sulfide-based ASSLIBs, in this study, we present an approach by constructing a semi-conductive polymer thin film for sulfide-based ASSLIBs to realize the superior electrochemical performance with high-rate capacity. A uniform and conformal poly(3,4-ethylenedioxythiophene) (PEDOT) modification was successfully built on both carbon additives (CNTs) and Ni-rich layered cathode of $LiNi_{0.8}Mn_{0.1}Co_{0.1}O_2$ (NMC811) via molecular layer deposition (MLD). The underlying decomposition mechanism of sulfide SSEs (LGPS) associated with CNTs is investigated by various electrochemical tests and characterization techniques, suggesting the high electronic conductivity of CNTs accelerates the decomposition of LGPS and side-reactions in the cathode composites during the electrochemical reactions, therefore leading to the fast capacity degradation especially at high current densities. Promisingly, the PEDOT modification realizes the application of semi-conductive additives to modify conductive additives in the cathode composites, therefore effectively enhancing the interfacial stability between CNTs and LGPS, resulting in the obvious improved rate capability and enhanced cycling stability. This study offers a strategy to address the long-time concern of using conductive additives in sulfide SSEs system, effectively boosting the realization of high-performance ASSLIBs.

7.2   Experimental section

Preparation of PEDOT modified CNTs and NMC811: The poly(3,4-ethylenedioxythiophene) (PEDOT) was deposited on the surface of carbon nanotubes (CNTs) and $LiNi_{0.8}Mn_{0.1}Co_{0.1}O_2$ (NMC811) powders via molecular layer deposition (MLD) using molybdenum chloride ($MoCl_5$) and 3,4-ethylenedioxythiophene (EDOT) as precursors in an Arradiance GEMstar-8 system. The MLD machine was connected with the argon-filled glove box. The source temperatures for both $MoCl_5$ and EDOT were 80 °C. The deposition temperature for PEDOT was 150 °C. During one MLD cycle, $MoCl_5$

and EDOT were alternatively introduced into the reaction chamber with a pulse time of 5 s, and the pulsing of each precursor was separated by a 60 s purge with N_2.

Assembly of the tested batteries and electrochemical testing: To investigate the stability between carbon additives and sulfide electrolytes, the sandwiched model cells were fabricated by using the as-prepared cathode composites combining with commercial $Li_{10}GeP_2S_{12}$ (LGPS, 99.95%, MSE supplies, LLC) as electrolyte layer and indium foil (99.99%, Φ10 mm, thickness 0.1 mm) as anode. The detailed fabrication process is shown as follow. Firstly, 70 mg LGPS was pressed at 2 ton with 10 mm diameter to form a pellet. The cathode composite power (7 mg) was then uniformly spread onto the surface of the LGPS electrolyte and pressed under 3 tons of pressure to form a two-layer pellet. The as-prepared cathode composites include the pristine LGPS (7 mg), bare CNTs mixed with LGPS (1 mg CNTs and 6 mg LGPS), PEDOT protected CNTs mixed with LGPS (1 mg CNTs and 6 mg LGPS), bare CNTs (7 mg), and PEDOT protected CNTs (7 mg). Finally, a piece of indium foil was put onto the other side of the LGPS pellet with a copper foil and pressed at 0.5 tons of pressure. The three-layered pellet was pressed between two stainless-steel rods as current collectors at the both positive and negative sides. The fabrication of all-solid-state batteries is similar to the process for the above model cells. The difference is the cathode layer was fabricated by the mixing of the as-prepared NMC811/LGPS/CNTs composites (10 mg with a weight ratio of 65:30:5). All the processes were performed in an argon-filled glove box. The galvanostatic charge/discharge characteristics were tested in the range of 2.1-3.8 V vs. Li^+/Li-In, corresponding to 2.7-4.4 V vs. Li^+/Li, at room temperature using a multichannel battery tester (LAND CT-2001A, Wuhan Rambo Testing Equipment Co., Ltd.). Linear sweep voltammetry (LSV) was collected on a versatile multichannel potentiostat 3/Z (VMP3) using a scan rate of 0.05 mV s^{-1} for the model cells. Cyclic voltammograms (CV) were collected on a versatile multichannel potentiostat 3/Z (VMP3) using a scan rate of 0.1 mV s^{-1} for the model cells and 0.05 mV s^{-1} for the all-solid-state batteries, respectively. Electrochemical impedance spectroscopy (EIS) was also performed on the versatile multichannel potentiostat 3/Z (VMP3) by applying an AC voltage of 10 mV amplitude in the 7000 kHz to 100 mHz frequency range.

Characterizations: The morphology and microstructure of PEDOT modified CNTs and NMC811 cathodes were characterized using field emission scanning electron microscopy (FESEM, Hitachi S4800) equipped with an energy dispersive spectrometer (EDX), high-resolution transmission electron microscopy (HRTEM, JEOL 2010FEG) and aberration-corrected scanning transmission electron microscopy (STEM, Titan Cubed Themis G2 300) with elemental mapping images. The crystalline structure of as-prepared CNTs and NMC811 cathodes are conducted on a Bruker D8 Advance Diffractometer (Cu-Ka source, 40 kV, 40 mA). X-ray photoelectron spectroscopy (XPS) spectra of the as-prepared samples were measured with a monochromatic Al Kα source (1486.6 eV) in a Kratos AXIS Nova Spectrometer. The Ar filled glovebox was connected with the XPS machine to avoid the exposure of air. Synchrotron-based X-ray absorption near edge structure (XANES) measurements were carried out at the Canadian Light Source (CLS). S, P, Ni, Co, and Mn K-edge spectra were collected by fluorescence mode using Si(111) crystals on the Soft X-ray Microcharacterization Beamline (SXRMB). All of the samples were prepared in a vacuum environment prior to synchrotron measurements. To avoid air exposure, the samples were firstly covered with Mylar film in glovebox under Ar, and then transferred to the corresponding beamline chamber for further measurements.

7.3 Results and discussion
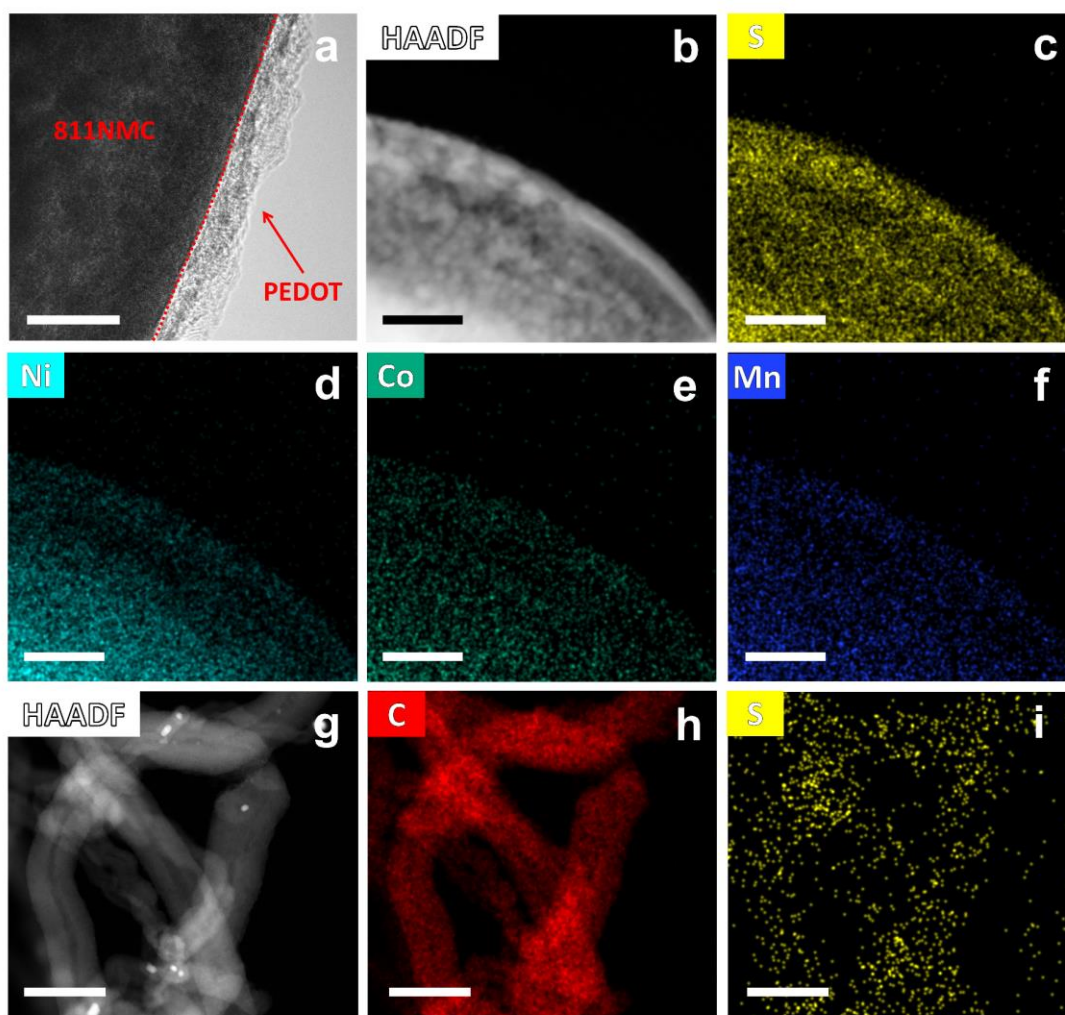
Figure 7.1 Structural and elemental characterizations of PEDOT modification. a) HR-TEM image of PEDOT modification on the surface of NMC811 particles, b-f) EDS mapping of S, Ni, Co, and Mn in PEDOT modified NMC811 by HAADF-STEM, g-i) EDS mapping of C and S in PEDOT modified CNTs by HAADF-STEM. Scale bars in the figures of a) 10 nm, b-f) 20 nm, g-i) 80 nm.

In this study, PEDOT thin film is synthesized via MLD as an interfacial material for both NMC811 and CNTs. To investigate the thickness effect, 2, 5, and 10 nm of PEDOT are deposited on the surface of NMC811 and CNTs, respectively, by controlling the MLD reaction cycles. Figures 7.1 and S1 illustrate the morphology and fine structure of the

PEDOT modified NMC811 and CNTs as confirmed by transmission electron microscopy (TEM) and scanning electron microscopy (SEM) images. The particle size of the commercial NMC811 secondary spheres is around 10 μm (Figure S1a). After 10 cycles of MLD, an amorphous and conformal interfacial layer of PEDOT with the thickness around 5 nm can be observed at the surface of NMC811 as shown in Figure 7.1a. The energy dispersive X-ray spectroscopic (EDX) mappings detected by the high-angle annular dark-field scanning trans-mission electron microscopy (HAADF-STEM) and SEM are shown in Figures 7.1b-f and S2, respectively, demonstrating the uniform distribution of S element with Ni, Co, and Mn among the NMC811 particles, explicitly confirming the successful modification of PEDOT on the surface of NMC811. Meanwhile, C 1s and S 2p X-ray photoelectron spectroscopy (XPS) spectra for the PEDOT modified NMC811 are shown in Figure S3. Typical C 1s XPS spectrum of PEDOT is demonstrated in Figure S3a, including the aromatic C=C bond at 284.2 eV and the C=S bond at 288.1 eV. In the S 2p XPS spectrum shown in Figure S3b, the band between 162.9 and 168.5 eV with doublet peaks is attributed to the sulfur atoms of PEDOT.[19-20] The EDX mappings of PEDOT modified CNTs are demonstrated in Figures 7.1g-i and S4, also confirming the uniform modification of PEDOT on the surface of CNTs. Furthermore, the X-ray diffraction (XRD) is conducted to evaluate the crystal and chemical structure of the bare and PEDOT modified NMC811 and CNTs. As shown from Figures S5-7, XRD patterns of the bare and PEDOT modified NMC811 and CNTs show good retention of the crystallinity without the introduction of a noticeable impurity phase, indicating that the material properties are well maintained throughout the MLD process.
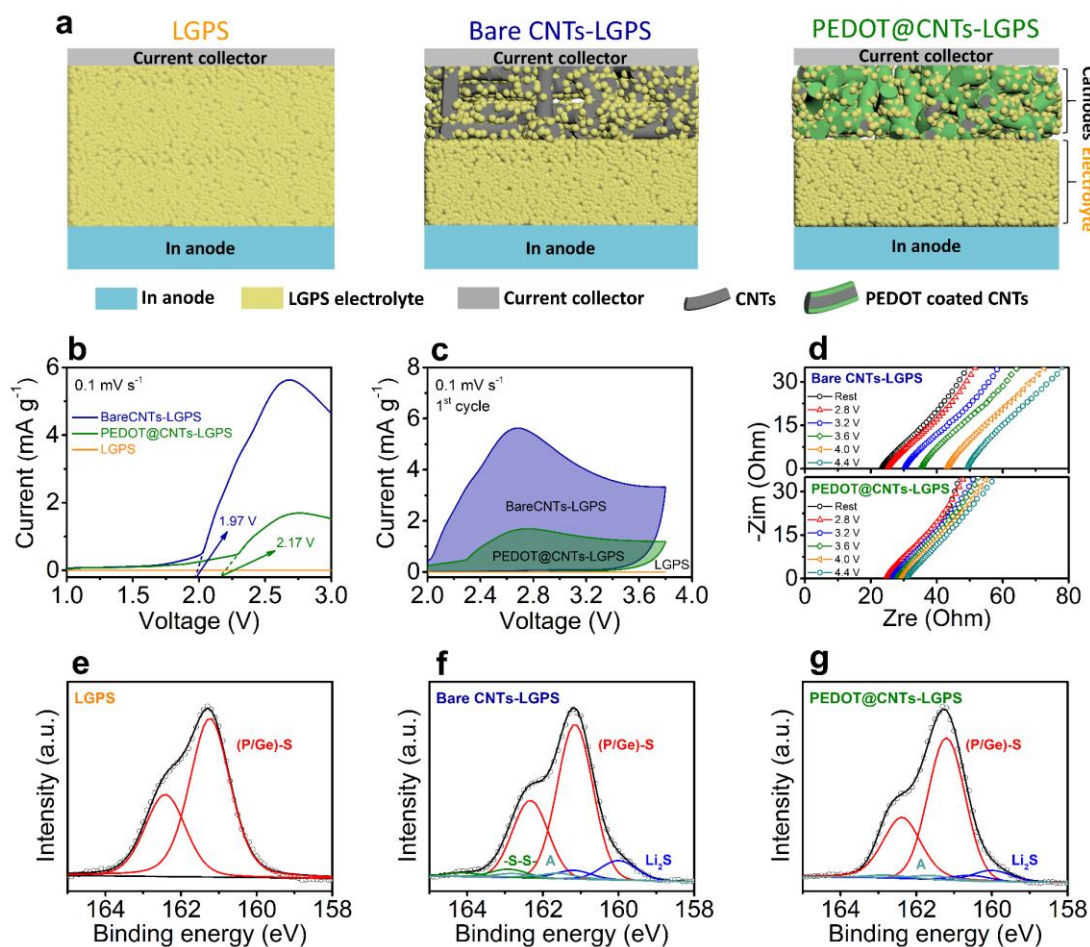
Figure 7.2 Investigation of the stability between CNTs and LGPS during electrochemical reactions. a) Schematic illustration of the designed model cells, b-c) CV profiles at 0.1 mV s⁻¹ during the first cycle, d) EIS spectra at various constant voltages, and e-g) S 2p XPS spectra after CV test in the different cathode composites.

To investigate effect of PEDOT modification on the stability between carbon additives and sulfide SSEs and, five different model cells are designed as shown in Figures 7.2a and S11a. Indium foil and LGPS are employed as the anode and electrolyte layer, respectively. For the cathode layer, (i) the pristine LGPS, (ii) bare CNTs mixed with LGPS, (iii) PEDOT modified CNTs mixed with LGPS, (iv) bare CNTs, and (v) PEDOT modified CNTs (denoted as LGPS, Bare CNTs-LGPS, PEDOT@CNTs-LGPS, Bare CNTs, and PEDOT@CNTs, respectively) are employed for the following characterizations. The chemical stability between CNTs and LGPS is first studied by

electrochemical impedance spectroscopy (EIS) as shown in Figure S8. After several hours' rest (no electrochemical operation), the EIS plots of both (ii) Bare CNTs-LGPS and (iii) PEDOT@CNTs-LGPS cells remain almost the same, indicating the high chemical stability between CNTs and LGPS. The electrochemical stability between CNTs and LGPS is then investigated as follows. Linear sweep voltammetry (LSV) test is first conducted to investigate the thickness effect of PEDOT coating. The onset potential shown in Figure S9 is delayed with the increased thickness of PEDOT coating, indicating the thicker PEDOT coating is more effective to alleviate the decomposition of LGPS. From the cyclic voltammogram (CV) profiles of the first cycle shown in Figures 7.2b and c, there is no appreciable peak in the (i) LGPS cell, indicating the good electrochemical stability during the voltage range of 1.0-3.8 V vs. Li^+/Li-In (1.6-4.4 V vs. Li^+/Li). However, the obvious onset potential of 1.97 V can be observed in the (ii) Bare CNTs-LGPS cell, which is much lower than the onset potential of 2.17 V in the (iii) PEDOT@CNTs-LGPS cell. Meanwhile, the intense anodic peaks can be detected in the (ii) Bare CNTs-LGPS cell with the peak current of 5.63 mA g^{-1}, which is 3.3 times higher than that of the (iii) PEDOT@CNTs-LGPS cell. Although the anodic peaks decrease significantly during the following CV cycles as shown in Figure S10, the intensities of the peak current in the (ii) Bare CNTs-LGPS cell are still much higher than that of the (iii) PEDOT@CNTs-LGPS cell. The above results indicate that the decomposition of LGPS in the (ii) Bare CNTs-LGPS cell is more severe than in the (iii) PEDOT@CNTs-LGPS cell.

The above CV results indicate the decomposition of LGPS may arise in the cathode composites (the interface between CNTs and LGPS particles) and/or the interface between the cathode layer and electrolyte layer. In order to investigate the extent of the electrochemical reactions at these two interfaces, both the (iv) Bare CNTs and (v) PEDOT@CNTs model cells are designed and shown in Figure S11a. Since there are only CNTs in the cathode layer, it means that the possible electrochemical reactions can be only detected at the interface between cathode layer and electrolyte layer. As shown in Figures S11b-c, the obviously reduced intensity of anodic peaks in the first CV cycle can be observed in both (iv) Bare CNTs and (v) PEDOT@CNTs cells. The peak current is

only 0.054 mA g^{-1} in the (iv) Bare CNTs cells. Comparing with the peak current in the (ii) Bare CNTs-LGPS and (iv) Bare CNTs cells, the decomposition of sulfide SSEs mainly occur in the cathode composites with the directly contact between CNTs and LGPS particles rather than at the interface between cathode layer and electrolyte layer.

EIS plots of the (i) pristine LGPS, (ii) Bare CNTs-LGPS, and (iii) PEDOT@CNTs-LGPS cells tested at various constant voltages are shown in Figures 7.2d and S12. The cells are held at the certain voltage for two hours and then tested by the EIS. The obviously increased resistance can be observed in the (ii) Bare CNTs-LGPS cell with the increase of the voltages. On the contrary, the resistance growth can be effectively suppressed by the PEDOT modification. To further evaluate the effect of PEDOT on the interfacial stability between carbon additives and sulfide SSEs, the CV tested cathode samples were characterized by XPS. From the S 2p XPS spectra as shown in Figure 7.2e and Figure S13, there is no distinctive peak in the (i) pristine LGPS cell after CV testing. However, the peaks, corresponding to the decomposition products of LGPS, can be detected in the (ii) Bare CNTs-LGPS cathode (Figure 7.2f) with the formation of Li$_2$S, -S-S-, and germanium sulfides or polysulfide species (peak A),[8, 21] indicating the bare CNTs accelerate the decomposition of LGPS during the electrochemical process. On the contrary, the decomposition of sulfide electrolyte in the (iii) PEDOT@CNTs-LGPS cathode can be effectively alleviated as shown in Figure 7.2g, demonstrating PEDOT modification is able to retard the electrochemical reactions between CNTs and LGPS.
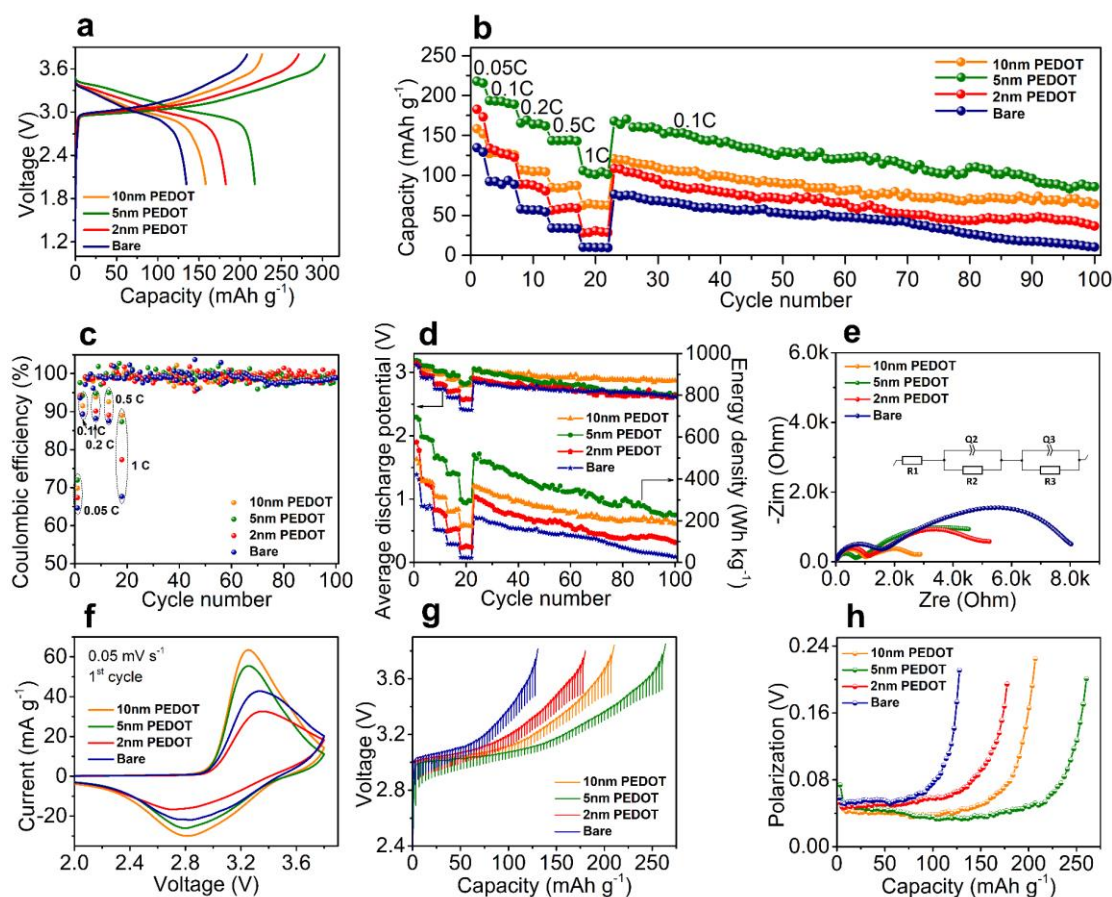
Figure 7.3 Effects of PEDOT modification on the electrochemical performance. a) Charge/discharge curves of the first cycle at 0.05C, b) rate and cyclic stability, c) Coulombic efficiency, d) average discharge voltage and energy density of cathodes, e) EIS spectra after 100 cycles, f) CV profiles at the first cycle, g) GITT curve during the charge process, h) the corresponding polarization plots.

Electrochemical characterizations of the ASSLIBs, in which the cathode layer is composed of the as-prepared NMC811/CNTs/LGPS composites combining with LGPS and indium foil as electrolyte layer and anode, respectively, are illustrated in Figure 7.3 to investigate the effect of PEDOT modification on performance. Both NMC811 and CNTs are coated by PEDOT with the thickness of 2, 5, and 10 nm. The first charge/discharge profiles of the bare and PEDOT modified cathodes at 0.05C are shown in Figure 7.3a. Compared to the bare cathode, the 5 nm PEDOT modified cathode shows the maximum discharge capacity with an obviously reduced polarization. Interestingly,

the rate and cycling performances of the four cathodes show considerable differences (Figure 7.3b). The rate capacities of the bare cathode dramatically decay with the increase in current density. The discharge capacities drop to lower than 10 mAh g^{-1} when the current density increases to 1C. On the contrary, the PEDOT modified cathodes demonstrate much improved rate capacities at each current density. Even at 1C, 5 nm PEDOT modified cathode still delivers a discharge capacity of over 100 mAh g^{-1}, which is over 10 times that of the bare cathode. 5 nm PEDOT modified cathode also demonstrates much improved cycling stability during the following cycles with the capacity retention of 51.1% after cycling when the current density returns to 0.1C. However, the capacity retention of the bare cathode is only 13.6%, illustrating its poor cycling performance. The charge/discharge profiles of the bare and PEDOT modified cathodes at the 100 cycle also demonstrate the reduced polarization by PEDOT modification (Figure S14). The corresponding Coulombic efficiencies of the bare and PEDOT modified cathodes are shown in Figure 7.3c. Interestingly, the initial Coulombic efficiencies at each current density show the obvious differences in the four cathodes. Especially at 1C, the bare cathode demonstrates the lowest initial Coulombic efficiencies of 67.7%. However, the initial Coulombic efficiencies in 5nm and 10 nm PEDOT modified cathodes are much improved and demonstrate 87.3% and 89.0%, respectively. Furthermore, the PEDOT modified cathodes also show improved average discharge voltages thus obtain the higher energy density than that of the bare cathode (Figure 7.3d). As shown in Figure 7.3e and Table S1, the 5nm PEDOT modified cathode shows the smallest internal resistance after 100 cycles among all the cells, demonstrating that the PEDOT modification effectively suppress the side-reactions at the three-phase interface in the cathode composites. Meanwhile, optimizing the thickness of PEDOT layer is also very important to get the best electrochemical performance. Thicker PEDOT layer enable the less side-reactions but limiting the capacity due to the lower conductivity.

CV profiles of the four cathodes are observed in Figure 7.3f. Interestingly, PEDOT modified cathodes demonstrate reduced redox potential gaps and higher peak intensities compared to the bare cathode with increasing thickness in the PEDOT interfacial layer, indicating the enhanced electrochemical reaction activity of batteries with lower

resistance by PEDOT modification. PEDOT modified cathodes also demonstrate lower currents at the cut-off voltage (3.8 V vs. Li^+/Li-In), which indicates a smaller potential polarization at high operating voltage. Furthermore, the galvanostatic intermittent titration technique (GITT) curves of the bare and PEDOT modified cathodes during the charge process are given in Figure 7.3g along with the corresponding polarization plots in Figure 7.3h. Obviously, the 5nm PEDOT modified cathode presents the smallest polarization potential with the highest capacity during the whole charging process, indicating effective stabilization of the cathodic interface throughout the charging process by PEDOT modification. The CV and GITT results indicate that PEDOT modification effectively reduce the interfacial resistance at the cathode/SSE/carbon interface in cathode composites during the electrochemical reactions. The effect of various coating strategies is also investigated in this study. The rate and cycling stability of different interfacial materials on the NMC811 cathode and CNTs are shown in Figure S15. The results indicate the PEDOT modification on both NMC811 and CNTs demonstrates the best rate and cycling capacities.
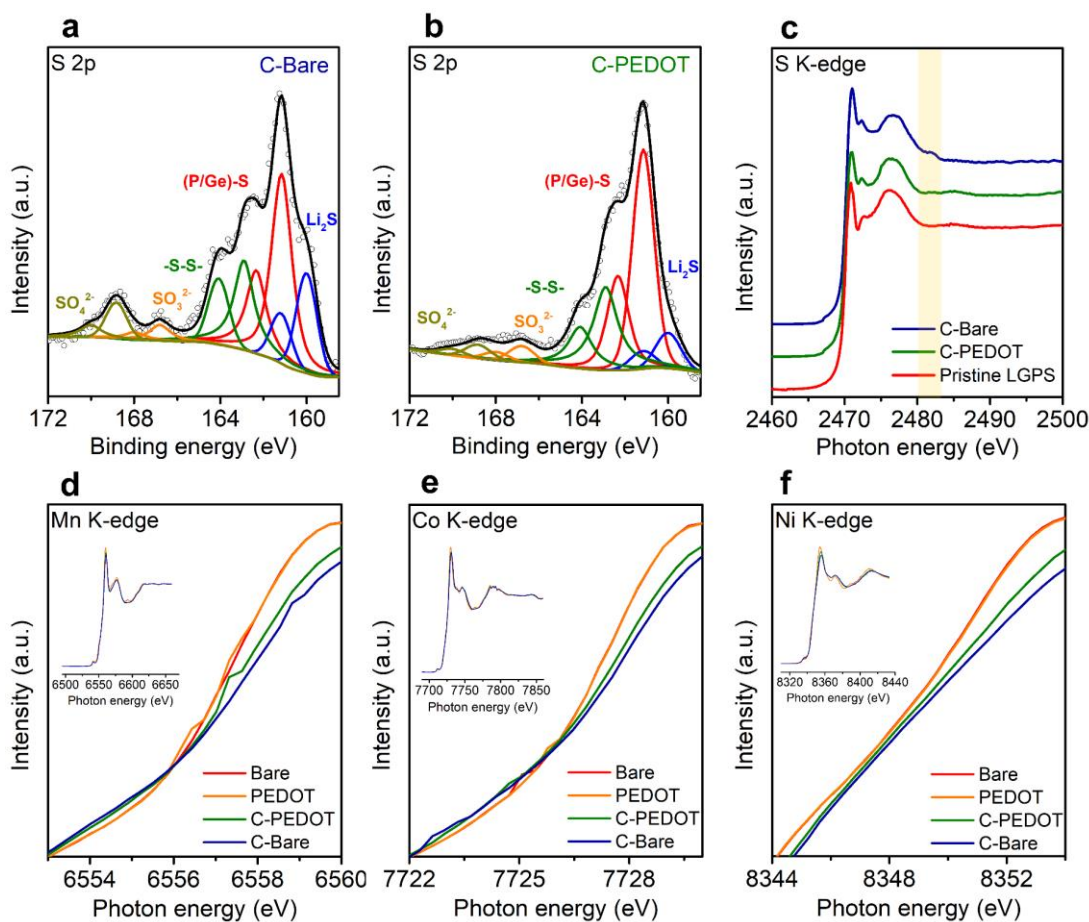
Figure 7.4 Understanding the interfacial chemical evolution during electrochemical reaction. S 2p XPS spectra of the a) cycled bare electrode (C-Bare) and b) cycled PEDOT modified electrode (C-PEDOT), c) S K-edge XANES spectra of the C-Bare and C-PEDOT electrodes with the pristine LGPS as reference, d-f) Mn, Co, Ni K-edge XANES spectra of the bare, PEDOT, C-Bare, and C-PEDOT electrodes: d) Mn K-edge, e) Co K-edge, and f) Ni K-edge.

To investigate the interfacial chemical evolution as well as the protective role of the PEDOT modification, XPS and X-ray absorption near edge structure (XANES) measurements are performed. Figure 7.4a and b show the S 2p XPS spectra of the LGPS electrolytes collected from the cycled bare electrode (denoted as C-Bare) and cycled PEDOT modified electrode (denoted as C-PEDOT). The decomposition products of LGPS are observed at 160.1 eV and 162.9 eV corresponding to the Li_2S and -S-S-,

respectively.[22] While the side-reactions between NMC811 and LGPS induce the further oxidation of LGPS and the formation of SO_3^{2-} and SO_4^{2-} species at 166.8 eV and 168.8 eV, respectively.[23-24] The C-Bare electrode shows higher relative content of Li_2S and -S-S- decomposition products than the C-PEDOT electrode, indicating different degrees of electrolyte decomposition caused by the bare CNTs and PEDOT modified CNTs. Meanwhile, the high relative peak intensities of SO_3^{2-} and SO_4^{2-} in C-Bare electrode suggest the presence of severe side-reactions between the unprotected NMC811 and LGPS.[25-26] Impressively, both the SO_3^{2-} and SO_4^{2-} signals are suppressed when using the C-PEDOT electrode, proving the effective suppression of side-reactions by the PEDOT modification. The S and P K-edge XANES spectra of the C-Bare and C-PEDOT electrodes are compared in Figure 7.4c and S16 and are in agreement with the XPS results. In the S K-edge XANES, the peak intensity of the C-Bare electrode at 2481.9 eV increases noticeably more than that of the C-PEDOT electrode, indicating the formation of SO_x from the severe side-reactions between NMC811 and LGPS during cycling.[27] However, the C-PEDOT electrode demonstrates the alleviated side-reactions with sulfide SSEs, therefore effectively suppress the formation of SO_x.

The K-edge XANES spectra of transition metals (TMs, including Co, Mn, and Ni) are present in Figures 7.4d-f to understand the structural evolution of the layered NMC811 during cycling. Generally, the local structural environment of the TMs and surrounding oxide corresponds to the shape of the K-edge XANES peaks, while the threshold energy position is indicative of the TM oxidation state.[28-30] Before cycling, there is no obvious difference in both the edge energy and the shape of the peaks in the K-edge XANES spectra between the bare and PEDOT modified electrodes, suggesting the PEDOT modification did not change the chemical environments of the TMs. However, both Mn and Co K-edge XANES spectra of the C-Bare electrode show spectral shape variations after cycling, indicating the changes of local environment of Mn and Co atoms. On the contrary, the shape changes of the spectra for the C-PEDOT are less prominent. Meanwhile, the obvious entire rigid edge shift towards higher energy for the Ni K-edge can be observed in the spectra for the C-Bare electrode, indicating the oxidation of Ni even though the XANES spectrum was tested after being fully discharged to 2.1 V vs.

Li^+/Li-In. On the contrary, the C-PEDOT electrode shows less change in the Ni K-edge energy position after cycling. The oxidation of Ni after cycling suggests that a portion of the lithium ions were unable to intercalate back into the layered structure of the NMC811 cathodes even at full discharge, due to the formation of cathode electrolyte interface (CEI) through severe side-reactions with the sulfide electrolyte. This is further demonstrated in the XRD patterns as shown in Figure S17. The (110) peak in the C-Bare electrode shifts to higher scattering after cycling comparing to the C-PEDOT electrode, meaning that the incomplete lithiation after cycling leads to a decrease in the interplanar spacing in the C-Bare electrode. Therefore, the obvious shape variations of Mn, Co K-edge XANES spectra and energy shift of Ni K-edge XANES spectra after cycling combining with the XRD results demonstrate that severe side-reactions between NMC811 and LGPS lead to the surficial structure evolution of cathode for the C-Bare electrode, while can be effectively alleviated by the PEDOT modification. As a result, the cracks on the surface of NMC811 are also suppressed by the PEDOT protection as shown in Figure S18 and 19.
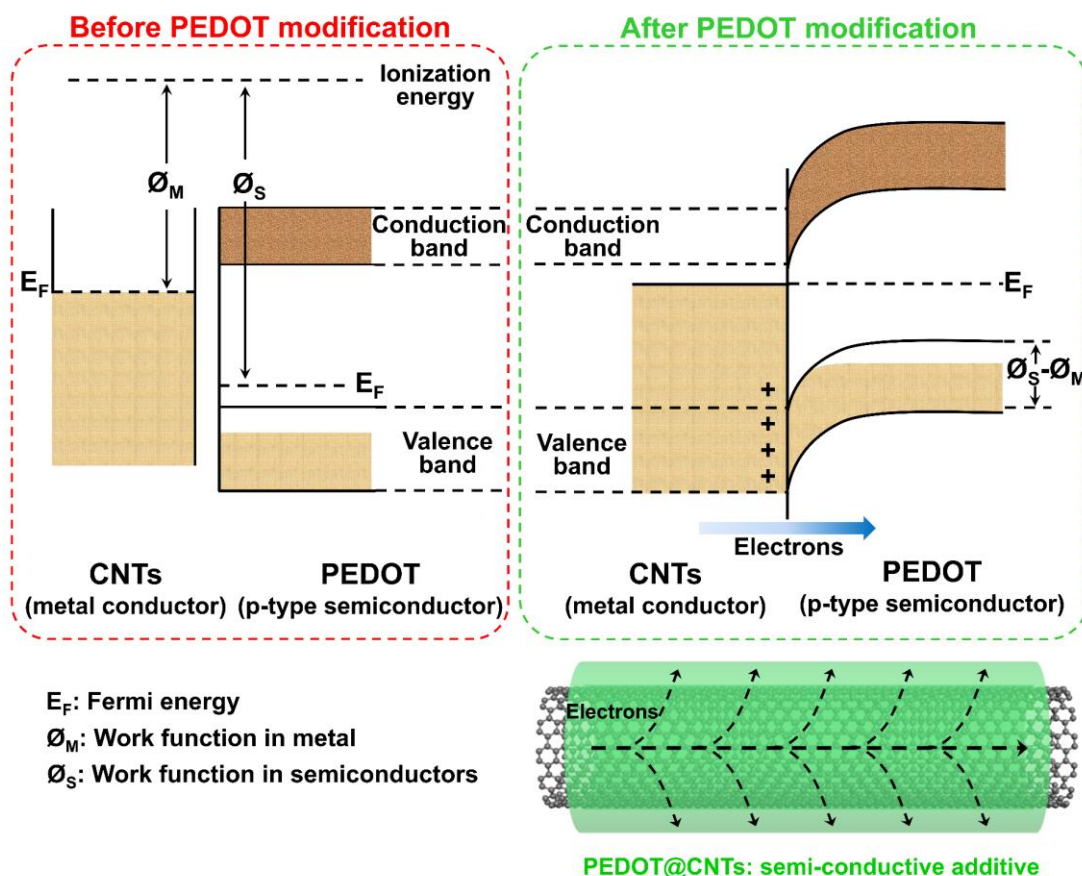
Figure 7.5 Schematic illustration of the role of PEDOT modification.

Based on the electrochemical testing and characterization results, the role of PEDOT modification is demonstrated in Figure 7.5. Electrons act as the charge carrier in the CNTs as a metallic conductor, while PEDOT is a p-type semiconductor, meaning the charge carriers are holes.[31-33] PEDOT thin film is deposited on the surface of CNTs by MLD, forming a metal/p-type semiconductor contact interface. As shown in Figure 7.5, the Fermi energy (E_F) of CNTs is higher than that of the PEDOT since the work function ($\emptyset_M$) of CNTs is lower than that of the PEDOT ($\emptyset_S$).[34-38] In order to maintain the equilibrium of E_F after contact, electrons have to flow from CNTs into PEDOT until the Fermi energies are finally equalized. As a result, the holes in the PEDOT are filled by the electrons, causing decreased PEDOT thin film conductivity. Therefore, the conductivity of the modified CNTs is also decreased. Through this process, the semi-conductive additives are achieved from the conductive additives of CNTs by PEDOT modification.

The conductivity of the semi-conductive additives is manipulated by the different thicknesses of PEDOT layer. During the charge/discharge process, the bare CNTs with excellent electronic conductivity accelerate the decomposition of sulfide SSEs, leading to the severe side-reactions between cathode particles and sulfide SSEs in the cathode composites, therefore damaging the performance of ASSLIBs especially the high-rate capability. On the contrary, the PEDOT modification with the optimized thickness provides a strategy by adopting semi-conductive additive in the cathode composites, which effectively alleviates the decomposition of sulfide SSEs and the side-reactions with cathode particles.

7.4 Conclusion

In conclusion, we develop a strategy to significantly improve the electrochemical performance of sulfide-based ASSLIBs by building a controllable polymer PEDOT thin film as a semi-conductive additive in the cathode composites. This interfacial engineering approach breaks through the limitations of conductive agents applied in the sulfide-based ASSLIBs. The PEDOT modification not only effectively alleviates the decomposition of sulfide SSEs induced by carbon additives in the cathode but also significantly suppresses the side-reactions between cathode materials and sulfide SSEs during the charge/discharge process. As a result, the developed ASSLIBs demonstrate notably improved electrochemical performance, including higher initial discharge capacity, enhanced cycling stability, improved average discharge potential, as well as reduced voltage polarization. More importantly, the successful application of semi-conductive additives in the cathode composites bolsters the rate capability significantly with a capacity of over 100 mAh g^{-1} at 1C, 10 times that of the bare electrode. As confirmed by XPS and synchrotron XANES analyses, the decomposition of sulfide SSEs and severe interfacial side-reactions in the cathode composites are effectively suppressed by the PEDOT modification. The above results demonstrate that PEDOT modification realizes the use of semi-conductive additives which enhance the interfacial stability. This work provides an effective approach to modify conductive additives by semi-conductive

additives in sulfide-based ASSLIBs and will attract more efforts regarding the development of fast-charged cathodes in the ASSLIBs.

7.5 Acknowledgements

7.6 References

(1) Gao, Z.; Sun, H.; Fu, L.; Ye, F.; Zhang, Y.; Luo, W.; Huang, Y. Promises, Challenges, and Recent Progress of Inorganic Solid-State Electrolytes for All-Solid-State Lithium Batteries. Advanced Materials 2018, 30 (17), 1705702.

(2) Manthiram, A.; Yu, X.; Wang, S. Lithium Battery Chemistries Enabled by Solid-State Electrolytes. Nature Reviews Materials 2017, 2 (4), 16103.

(3) Li, H. Practical Evaluation of Li-Ion Batteries. Joule 2019, 3 (4), 911-914.

(4) Kamaya, N.; Homma, K.; Yamakawa, Y.; Hirayama, M.; Kanno, R.; Yonemura, M.; Kamiyama, T.; Kato, Y.; Hama, S.; Kawamoto, K.; Mitsui, A. A Lithium Superionic Conductor. Nature Materials 2011, 10 (9), 682-686.

(5) Zhu, Y.; He, X.; Mo, Y. Origin of Outstanding Stability in the Lithium Solid Electrolyte Materials: Insights from Thermodynamic Analyses Based on First-Principles Calculations. ACS Applied Materials & Interfaces 2015, 7 (42), 23685-23693.

(6) Richards, W. D.; Miara, L. J.; Wang, Y.; Kim, J. C.; Ceder, G. Interface Stability in Solid-State Batteries. Chemistry of Materials 2016, 28 (1), 266-273.

(7) Tan, D. H. S.; Wu, E. A.; Nguyen, H.; Chen, Z.; Marple, M. A. T.; Doux, J.-M.; Wang, X.; Yang, H.; Banerjee, A.; Meng, Y. S. Elucidating Reversible Electrochemical Redox of Li6PS5Cl Solid Electrolyte. ACS Energy Letters 2019, 4 (10), 2418-2427.

(8) Dewald, G. F.; Ohno, S.; Kraft, M. A.; Koerver, R.; Till, P.; Vargas-Barbosa, N. M.; Janek, J.; Zeier, W. G. Experimental Assessment of the Practical Oxidative Stability of Lithium Thiophosphate Solid Electrolytes. Chemistry of Materials 2019, 31 (20), 8328-8337.

(9) Culver, S. P.; Koerver, R.; Zeier, W. G.; Janek, J. On the Functionality of Coatings for Cathode Active Materials in Thiophosphate-Based All-Solid-State Batteries. Advanced Energy Materials 2019, 9 (24), 1900626.

(10) Liang, J.; Li, X.; Zhao, Y.; Goncharova, L. V.; Li, W.; Adair, K. R.; Banis, M. N.; Hu, Y.; Sham, T.-K.; Huang, H.; Zhang, L.; Zhao, S.; Lu, S.; Li, R.; Sun, X. An Air-Stable and Dendrite-Free Li Anode for Highly Stable All-Solid-State Sulfide-Based Li Batteries. Advanced Energy Materials 2019, 9 (38), 1902125.

(11) Cao, D.; Zhang, Y.; Nolan, A. M.; Sun, X.; Liu, C.; Sheng, J.; Mo, Y.; Wang, Y.; Zhu, H. Stable Thiophosphate-Based All-Solid-State Lithium Batteries through Conformally Interfacial Nanocoating. Nano Letters 2020, 20 (3), 1483-1490.

(12) Zheng, H.; Yang, R.; Liu, G.; Song, X.; Battaglia, V. S. Cooperation between Active Material, Polymeric Binder and Conductive Carbon Additive in Lithium Ion Battery Cathode. The Journal of Physical Chemistry C 2012, 116 (7), 4875-4882.

(13) Guoping, W.; Qingtang, Z.; Zuolong, Y.; MeiZheng, Q. The Effect of Different Kinds of Nano-Carbon Conductive Additives in Lithium Ion Batteries on the Resistance and Electrochemical Behavior of the LiCoO2 Composite Cathodes. Solid State Ionics 2008, 179 (7), 263-268.

(14) Palomares, V.; Goñi, A.; Muro, I. G. d.; de Meatza, I.; Bengoechea, M.; Cantero, I.; Rojo, T. Conductive Additive Content Balance in Li-Ion Battery Cathodes: Commercial Carbon Blacks vs. In Situ Carbon from LiFePO4/C Composites. Journal of Power Sources 2010, 195 (22), 7661-7668.

(15) Park, S. W.; Oh, G.; Park, J.-W.; Ha, Y.-C.; Lee, S.-M.; Yoon, S. Y.; Kim, B. G. Graphitic Hollow Nanocarbon as a Promising Conducting Agent for Solid-State Lithium Batteries. Small 2019, 15 (18), 1900235.

(16) Oh, G.; Hirayama, M.; Kwon, O.; Suzuki, K.; Kanno, R. Bulk-Type All Solid-State Batteries with 5 V Class LiNi0.5Mn1.5O4 Cathode and Li10GeP2S12 Solid Electrolyte. Chemistry of Materials 2016, 28 (8), 2634-2640.

(17) Zhang, W.; Leichtweiß, T.; Culver, S. P.; Koerver, R.; Das, D.; Weber, D. A.; Zeier, W. G.; Janek, J. The Detrimental Effects of Carbon Additives in Li10GeP2S12-Based Solid-State Batteries. ACS Applied Materials & Interfaces 2017, 9 (41), 35888-35896.

(18) Yoon, K.; Kim, J.-J.; Seong, W. M.; Lee, M. H.; Kang, K. Investigation on the Interface between Li10GeP2S12 Electrolyte and Carbon Conductive Agents in All-Solid-State Lithium Battery. Scientific Reports 2018, 8 (1), 8066.

(19) Atanasov, S. E.; Losego, M. D.; Gong, B.; Sachet, E.; Maria, J.-P.; Williams, P. S.; Parsons, G. N. Highly Conductive and Conformal Poly(3,4-ethylenedioxythiophene) (PEDOT) Thin Films via Oxidative Molecular Layer Deposition. Chemistry of Materials 2014, 26 (11), 3471-3478.

(20) Du, F.-P.; Cao, N.-N.; Zhang, Y.-F.; Fu, P.; Wu, Y.-G.; Lin, Z.-D.; Shi, R.; Amini, A.; Cheng, C. PEDOT:PSS/Graphene Quantum Dots Films with Enhanced Thermoelectric Properties via Strong Interfacial Interaction and Phase Separation. Scientific Reports 2018, 8 (1), 6441.

(21) Koerver, R.; Walther, F.; Aygün, I.; Sann, J.; Dietrich, C.; Zeier, W. G.; Janek, J. Redox-Active Cathode Interphases in Solid-State Batteries. Journal of Materials Chemistry A 2017, 5 (43), 22750-22760.

(22) Li, X.; Ren, Z.; Norouzi Banis, M.; Deng, S.; Zhao, Y.; Sun, Q.; Wang, C.; Yang, X.; Li, W.; Liang, J.; Li, X.; Sun, Y.; Adair, K.; Li, R.; Hu, Y.; Sham, T.-K.; Huang, H.; Zhang, L.; Lu, S.; Luo, J.; Sun, X. Unravelling the Chemistry and Microstructure Evolution of a Cathodic Interface in Sulfide-Based All-Solid-State Li-Ion Batteries. ACS Energy Letters 2019, 4 (10), 2480-2488.

(23) Zhang, W.; Richter, F. H.; Culver, S. P.; Leichtweiss, T.; Lozano, J. G.; Dietrich, C.; Bruce, P. G.; Zeier, W. G.; Janek, J. Degradation Mechanisms at the Li10GeP2S12/LiCoO2 Cathode Interface in an All-Solid-State Lithium-Ion Battery. ACS Applied Materials & Interfaces 2018, 10 (26), 22226-22236.

(24) Wenzel, S.; Randau, S.; Leichtweiß, T.; Weber, D. A.; Sann, J.; Zeier, W. G.; Janek, J. Direct Observation of the Interfacial Instability of the Fast Ionic Conductor Li10GeP2S12 at the Lithium Metal Anode. Chemistry of Materials 2016, 28 (7), 2400-2407.

(25) Hwang, S.; Chang, W.; Kim, S. M.; Su, D.; Kim, D. H.; Lee, J. Y.; Chung, K. Y.; Stach, E. A. Investigation of Changes in the Surface Structure of LixNi0.8Co0.15Al0.05O2 Cathode Materials Induced by the Initial Charge. Chemistry of Materials 2014, 26 (2), 1084-1092.

(26) Walther, F.; Koerver, R.; Fuchs, T.; Ohno, S.; Sann, J.; Rohnke, M.; Zeier, W. G.; Janek, J. Visualization of the Interfacial Decomposition of Composite Cathodes in Argyrodite-Based All-Solid-State Batteries Using Time-of-Flight Secondary-Ion Mass Spectrometry. Chemistry of Materials 2019, 31 (10), 3745-3755.

(27) Kornienko, N.; Resasco, J.; Becknell, N.; Jiang, C.-M.; Liu, Y.-S.; Nie, K.; Sun, X.; Guo, J.; Leone, S. R.; Yang, P. Operando Spectroscopic Analysis of an Amorphous

Cobalt Sulfide Hydrogen Evolution Electrocatalyst. Journal of the American Chemical Society 2015, 137 (23), 7448-7455.

(28) Yu, X.; Lyu, Y.; Gu, L.; Wu, H.; Bak, S.-M.; Zhou, Y.; Amine, K.; Ehrlich, S. N.; Li, H.; Nam, K.-W.; Yang, X.-Q. Understanding the Rate Capability of High-Energy-Density Li-Rich Layered Li1.2Ni0.15Co0.1Mn0.55O2 Cathode Materials. Advanced Energy Materials 2014, 4 (5), 1300950.

(29) Hu, E.; Yu, X.; Lin, R.; Bi, X.; Lu, J.; Bak, S.; Nam, K.-W.; Xin, H. L.; Jaye, C.; Fischer, D. A.; Amine, K.; Yang, X.-Q. Evolution of Redox Couples in Li- and Mn-rich Cathode Materials and Mitigation of Voltage Fade by Reducing Oxygen Release. Nature Energy 2018, 3 (8), 690-698.

(30) Liao, P.-Y.; Duh, J.-G.; Lee, J.-F. Valence Change and Local Structure during Cycling of Layer-Structured Cathode Materials. Journal of Power Sources 2009, 189 (1), 9-15.

(31) Ebbesen, T. W.; Lezec, H. J.; Hiura, H.; Bennett, J. W.; Ghaemi, H. F.; Thio, T. Electrical Conductivity of Individual Carbon Nanotubes. Nature 1996, 382 (6586), 54-56.

(32) Landi, B. J.; Ganter, M. J.; Cress, C. D.; DiLeo, R. A.; Raffaelle, R. P. Carbon Nanotubes for Lithium Ion Batteries. Energy & Environmental Science 2009, 2 (6), 638-654.

(33) Yao, H.; Fan, Z.; Cheng, H.; Guan, X.; Wang, C.; Sun, K.; Ouyang, J. Recent Development of Thermoelectric Polymers and Composites. Macromolecular Rapid Communications 2018, 39 (6), 1700727.

(34) Xue, M.; Xie, J.; Li, W.; Yang, C.; Ai, Y.; Wang, F.; Ou, J.; Yao, J. Dependence of Electron Work Function of Al-Mg Alloys on Surface Structures and Relative Humidity. Physica B: Condensed Matter 2011, 406 (22), 4240-4244.

(35) Lövenich, W. PEDOT-Properties and Applications. Polymer Science Series C 2014, 56 (1), 135-143.

(36) Lee, T.-W.; Chung, Y. Control of the Surface Composition of a Conducting-Polymer Complex Film to Tune the Work Function. Advanced Functional Materials 2008, 18 (15), 2246-2252.

(37) Liu, P.; Sun, Q.; Zhu, F.; Liu, K.; Jiang, K.; Liu, L.; Li, Q.; Fan, S. Measuring the Work Function of Carbon Nanotubes with Thermionic Method. Nano Letters 2008, 8 (2), 647-651.

(38) Liu, P.; Wei, Y.; Jiang, K.; Sun, Q.; Zhang, X.; Fan, S.; Zhang, S.; Ning, C.; Deng, J. Thermionic Emission and Work Function of Multiwalled Carbon Nanotube Yarns. Physical Review B 2006, 73 (23), 235412.

7.7 Supporting information
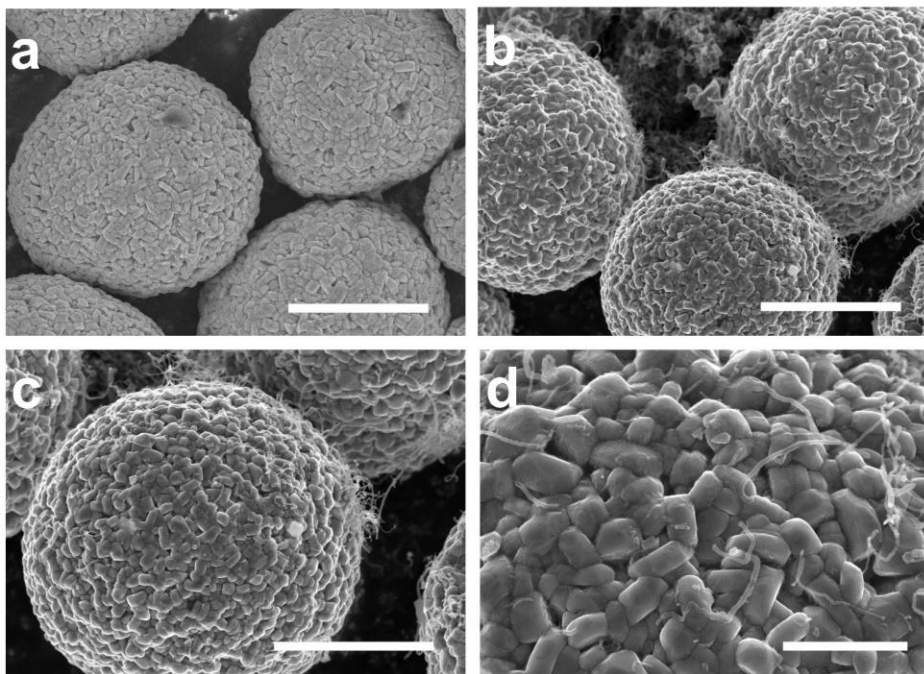
Figure S1. SEM images of a) bare NMC811; b-d) PEDOT modified NMC811/CNTs composites. Scale bars in the figures of a-c) 5 μm, and d) 1 μm.
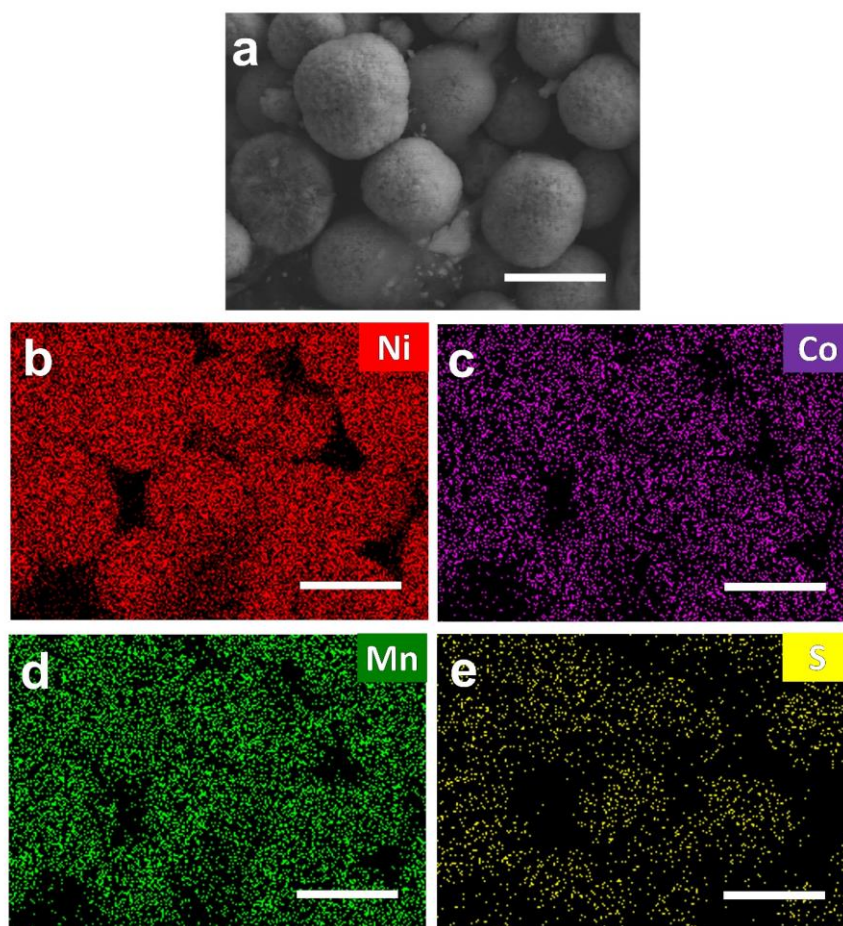
Figure S2. SEM-EDX mappings of PEDOT modified NMC811 cathode particles. b) Ni, c) Co, d) Mn, and e) S. Scale bars in the figures of 10 µm.
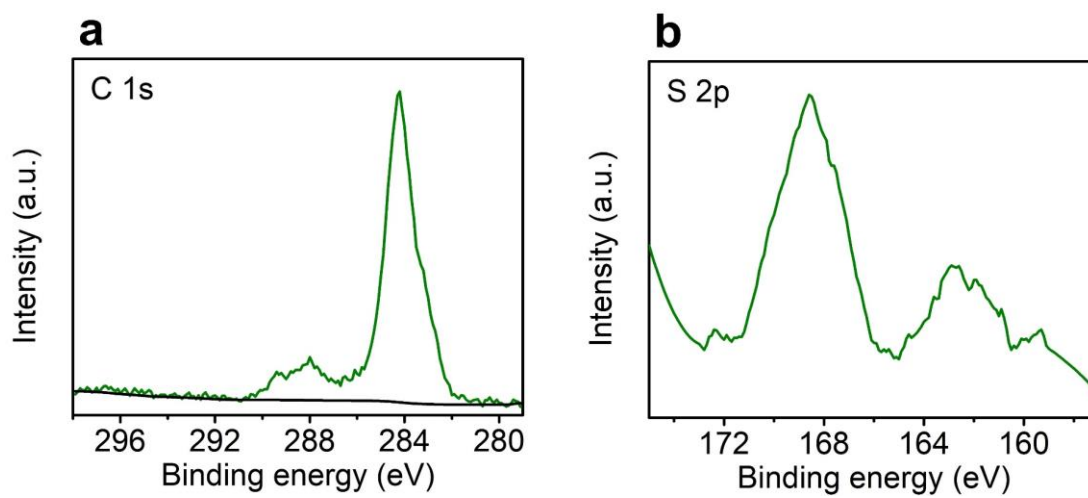
Figure S3. a) C 1s and b) S 2p XPS spectra of PEDOT modified NMC811.
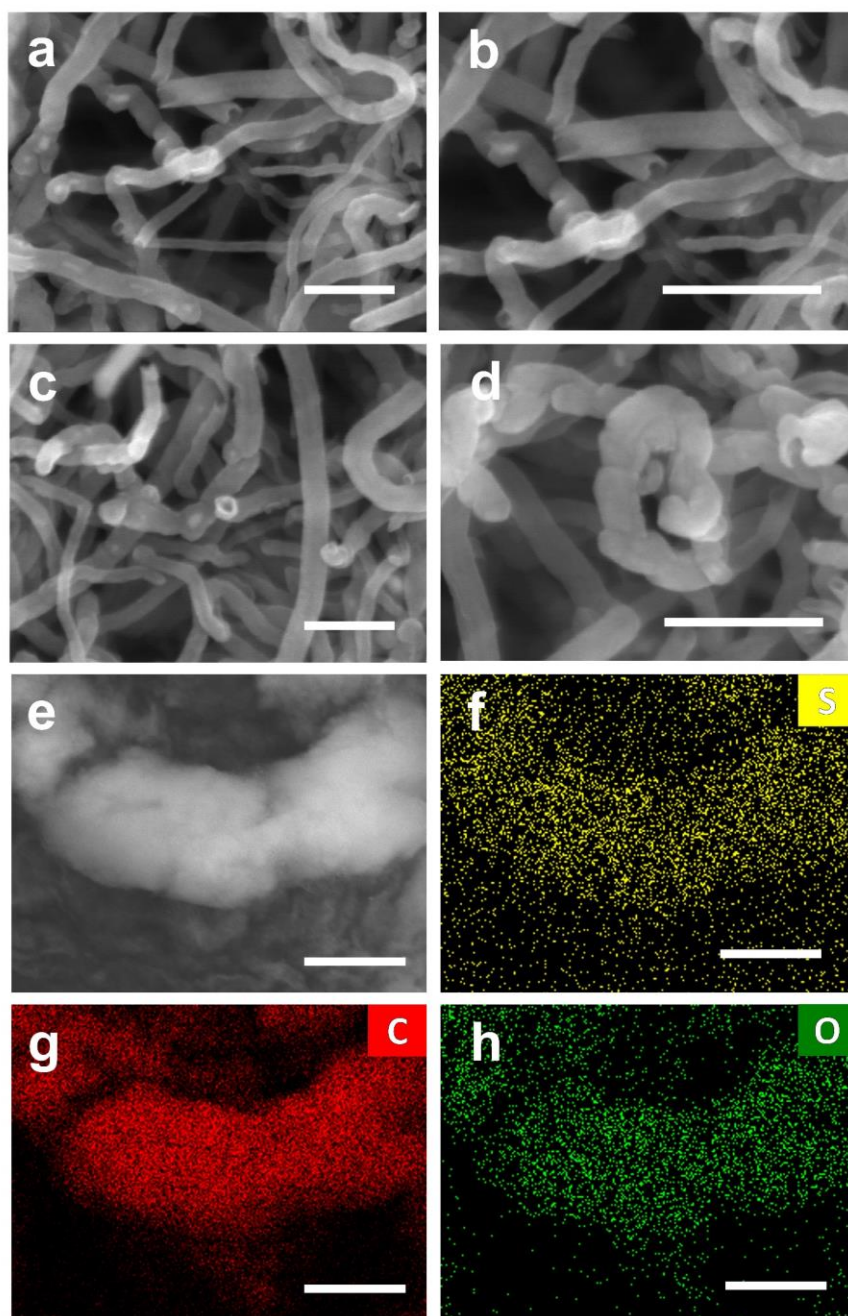
Figure S4. SEM images of a-b) bare CNTs; c-d) PEDOT modified CNTs; e-h) EDX mappings of PEDOT modified CNTs: f) S, g) C, and h) O. Scale bars in the figures of a and c) 150 nm, b and d) 200 nm, e-h) 15 µm.
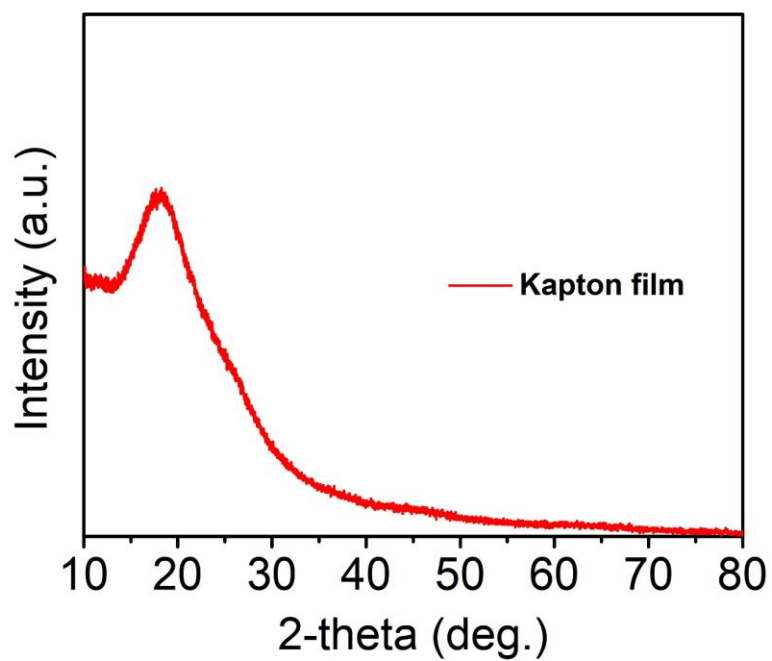
Figure S5. XRD pattern of Kapton film.
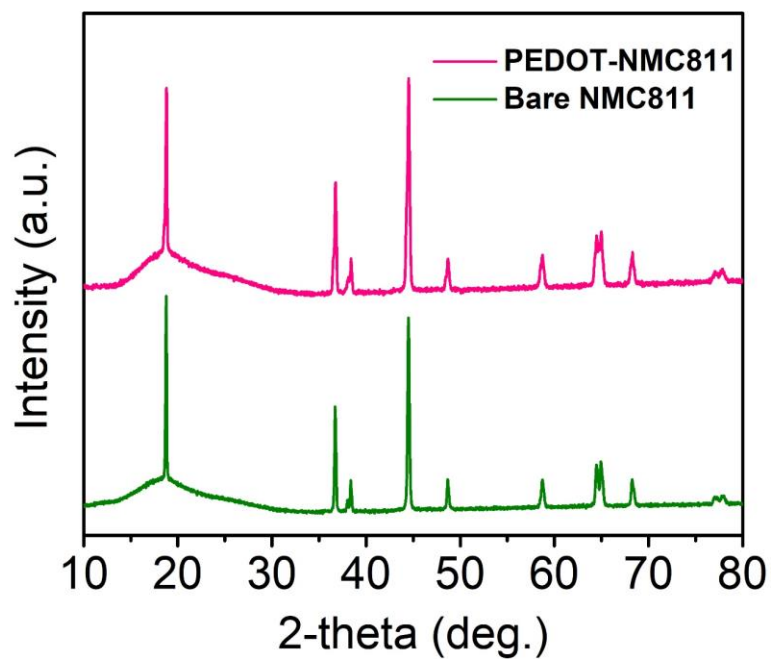
Figure S6. XRD patterns of the bare NMC811 and PEDOT modified NMC811.
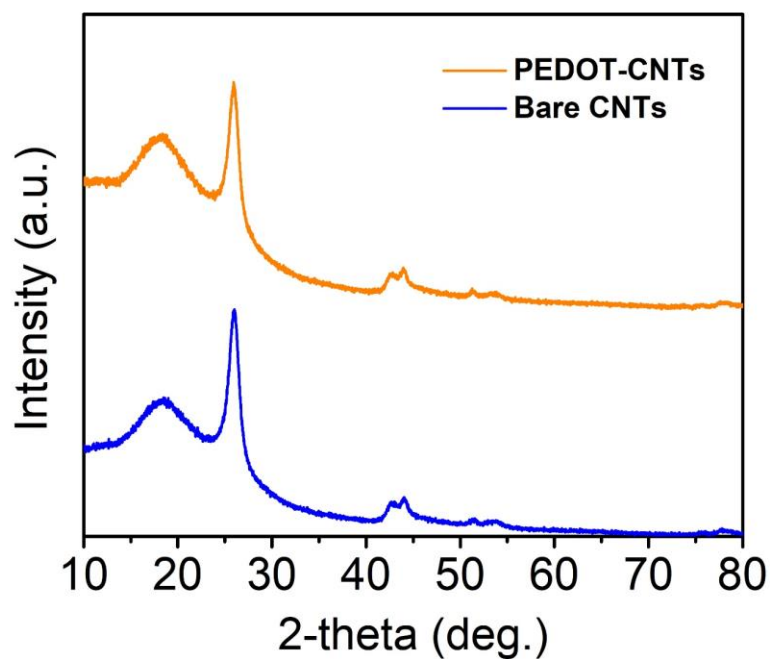
Figure S7. XRD patterns of the bare CNTs and PEDOT modified CNTs.
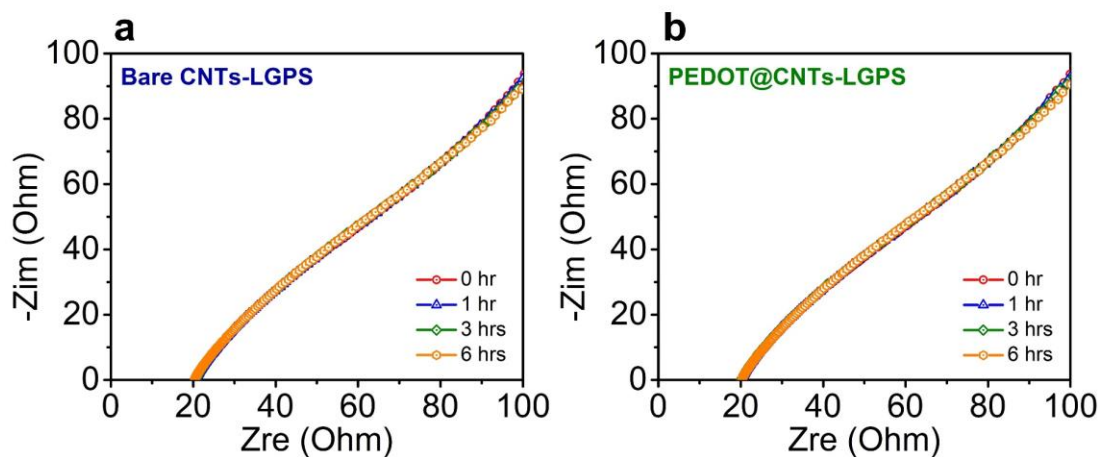
Figure S8. EIS plots of the Bare CNTs-LGPS and PEDOT@CNTs-LGPS cells assembled as shown in Figure 2a measured at a various resting time.
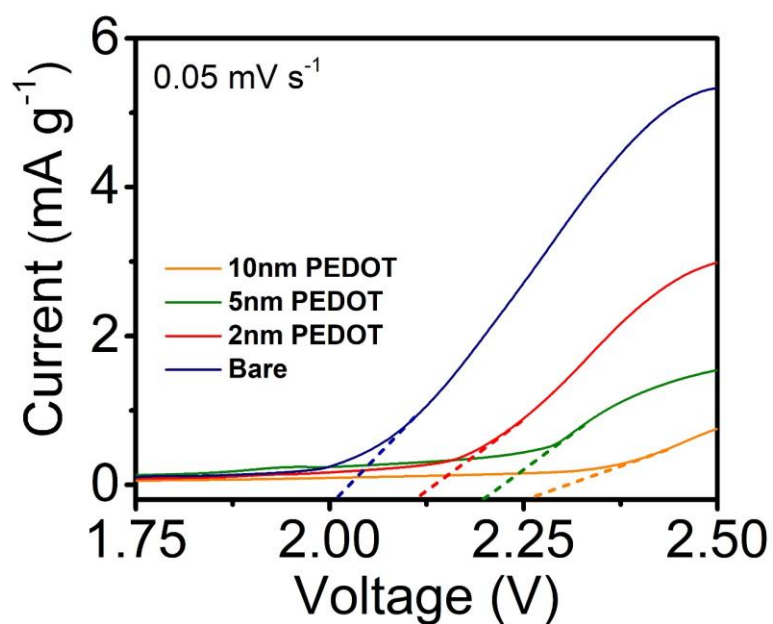
Figure S9. LSV profiles of the bare and different thickness PEDOT coated CNTs at 0.05 mV s^{-1}.
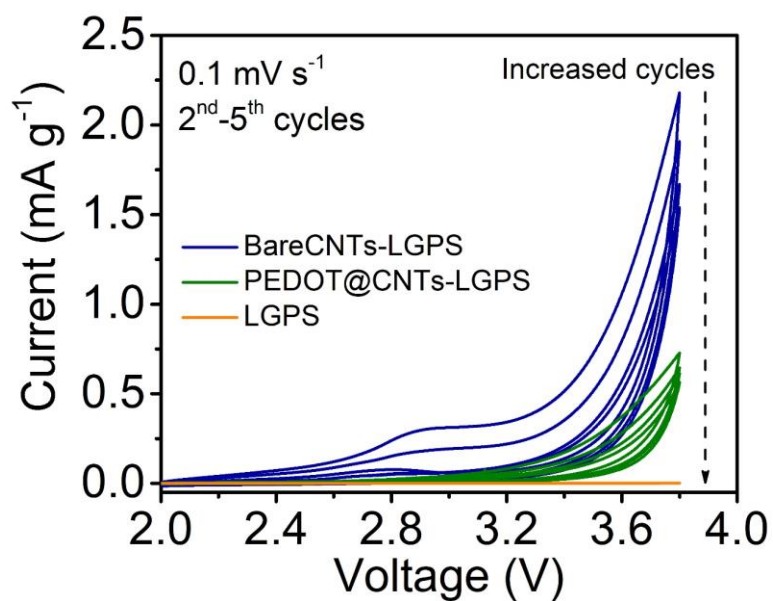
Figure S10. CV profiles of the different cathode composites as shown in Figure 2a during 2nd to 5th cycles.
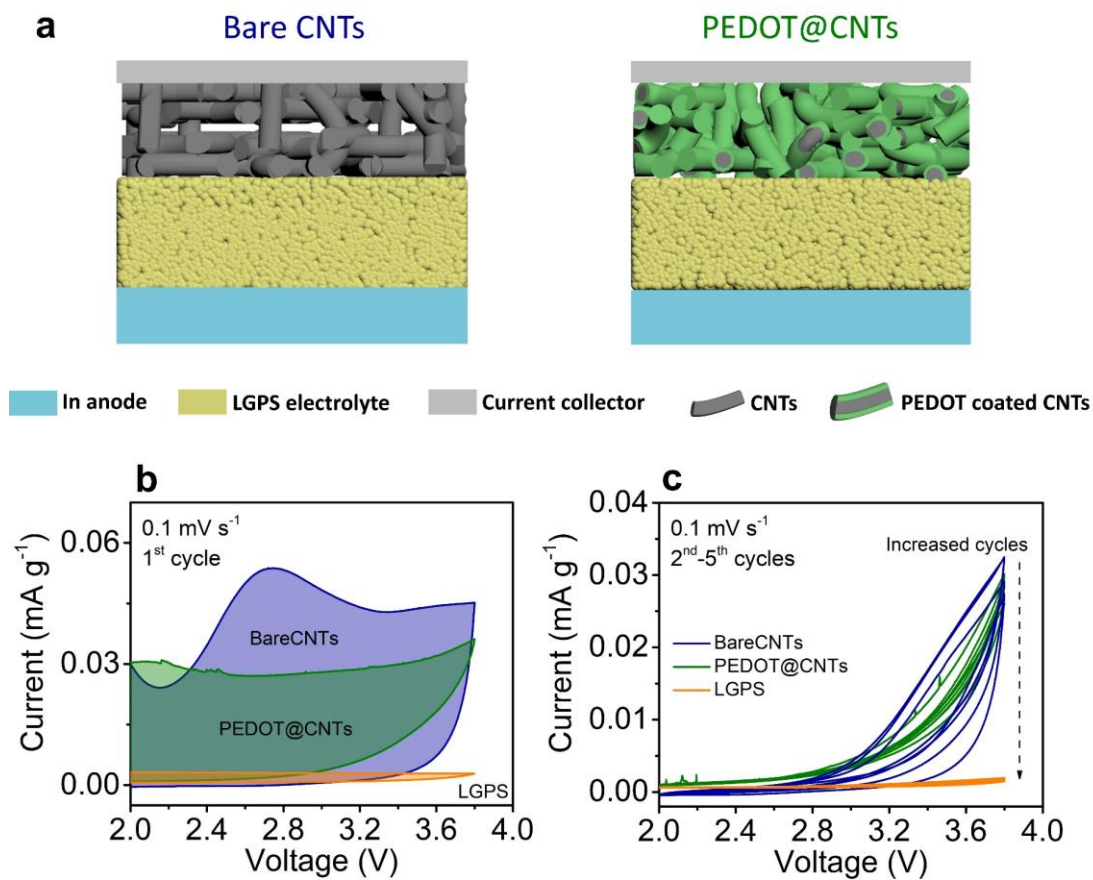
Figure S11. a) Schematic illustration of the designed model cells, b-c) CV profiles of the different cathode composites at 0.1 mV s^{-1} during 5 cycles.
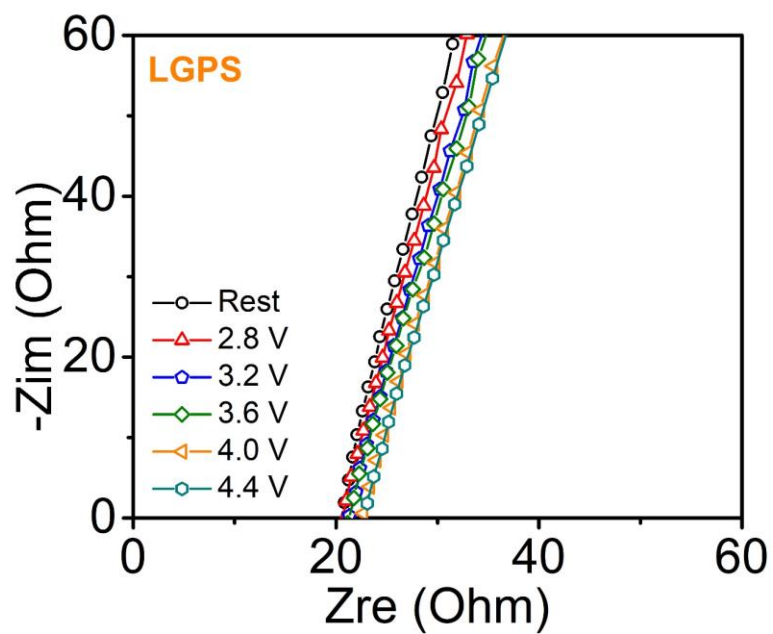
Figure S12. EIS spectra of the pristine LGPS at various constant voltages.
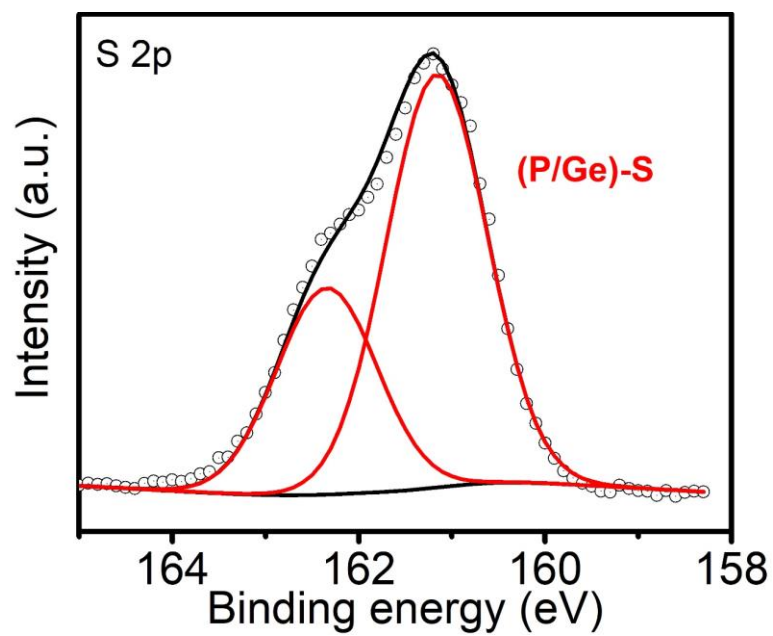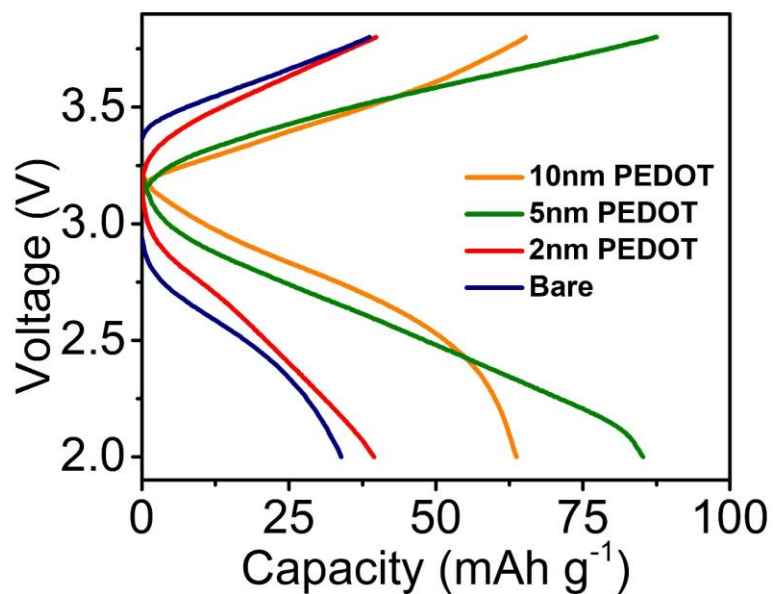

Figure S13. S 2p spectrum of the pristine LGPS.

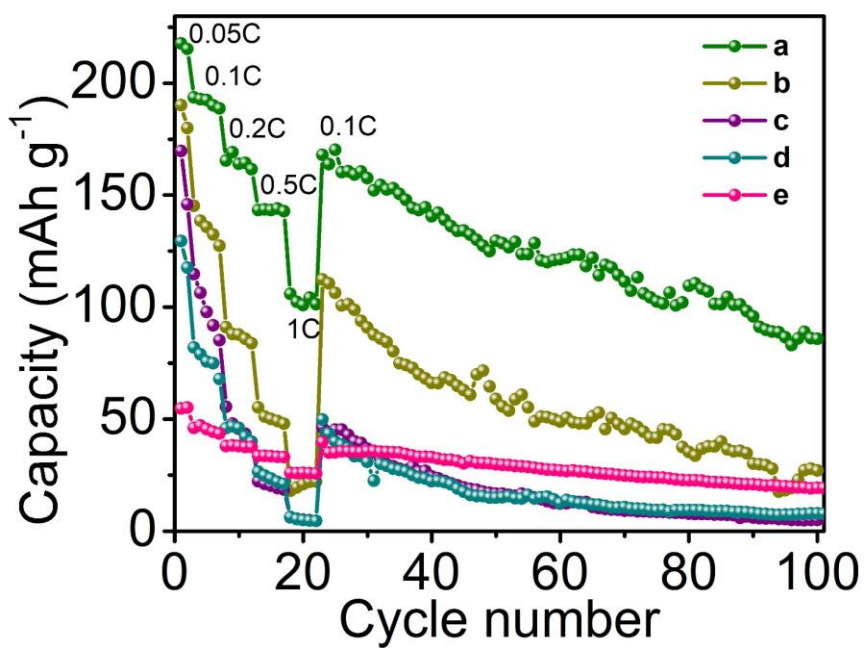Figure S14. Charge/discharge curves of the 100 cycle at 0.05C.

Figure S15. The rate and cycling stability of various coating strategies: a) PEDOT coating on both NMC811 and CNTs, b) LiNbO$_x$ coating on NMC811 and PEDOT

coating on CNTs, c) PEDOT coating on CNTs with bare NMC811, d) PEDOT coating on NMC811 with bare CNTs, e) PEDOT coating on NMC811 without CNTs.
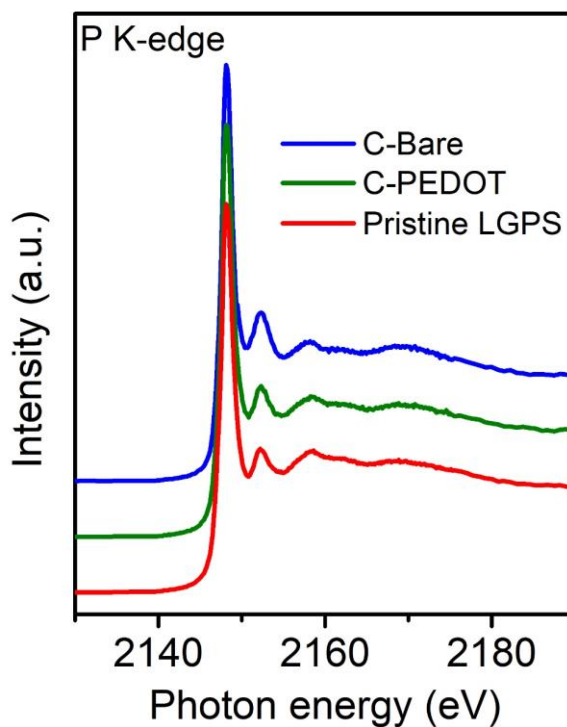

Figure S16. P K-edge XANES spectra of the pristine LGPS, cycled bare electrode (C-Bare), and cycled PEDOT modified electrode (C-PEDOT).
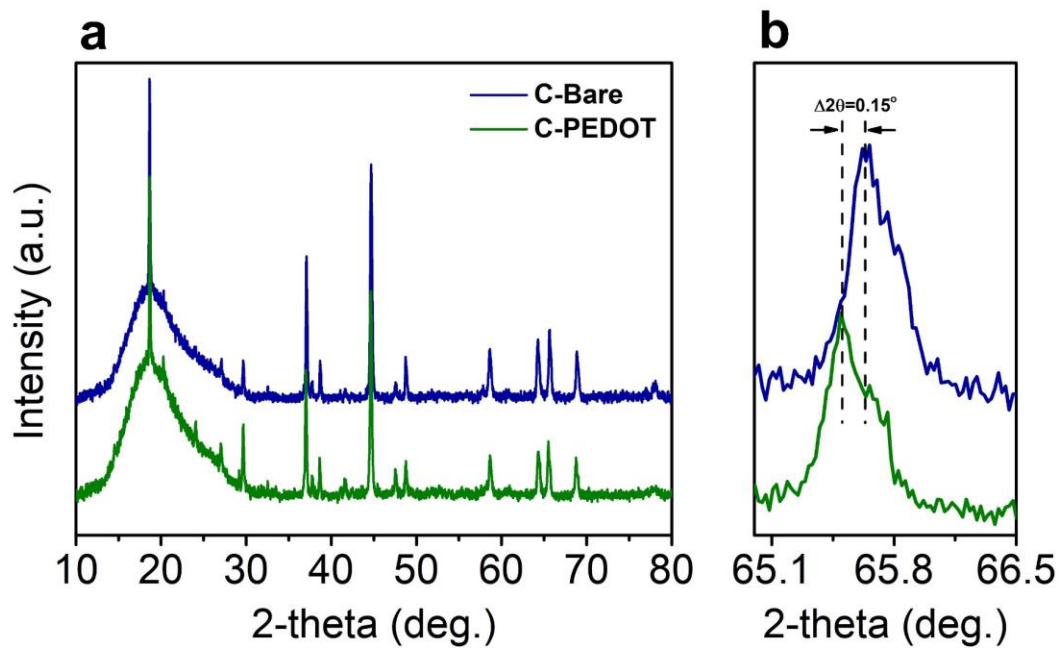
Figure S17. a) XRD patterns and b) the zoom-in patterns of the cycled bare electrode (C-Bare) and cycled PEDOT modified electrode (C-PEDOT).
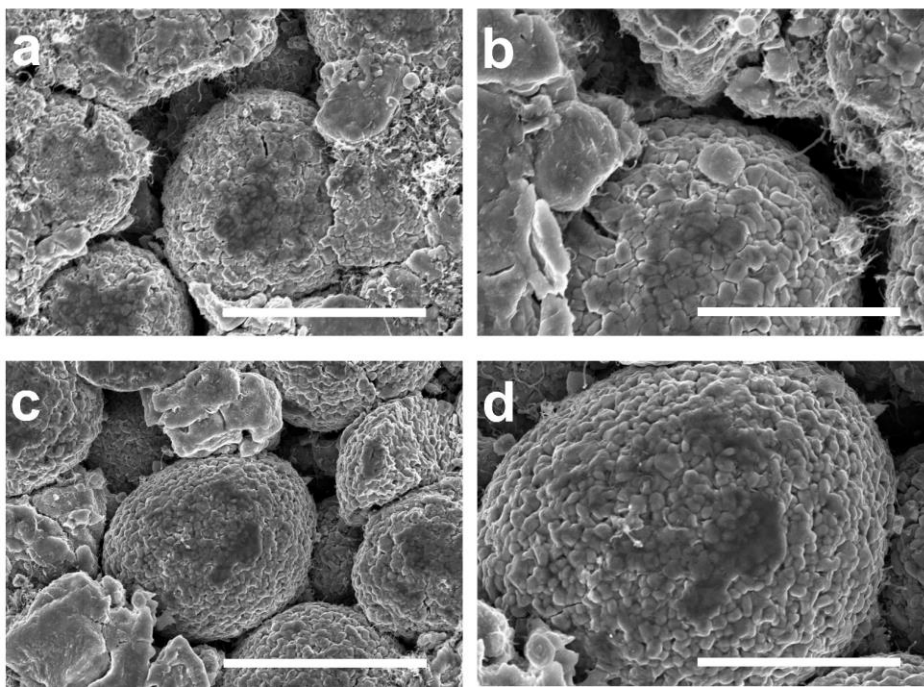
Figure S18. SEM images of a-b) cycled bare electrode; c-d) cycled PEDOT modified electrode. Scale bars in the figures of a and c) 10 µm, b and d) 5 µm.
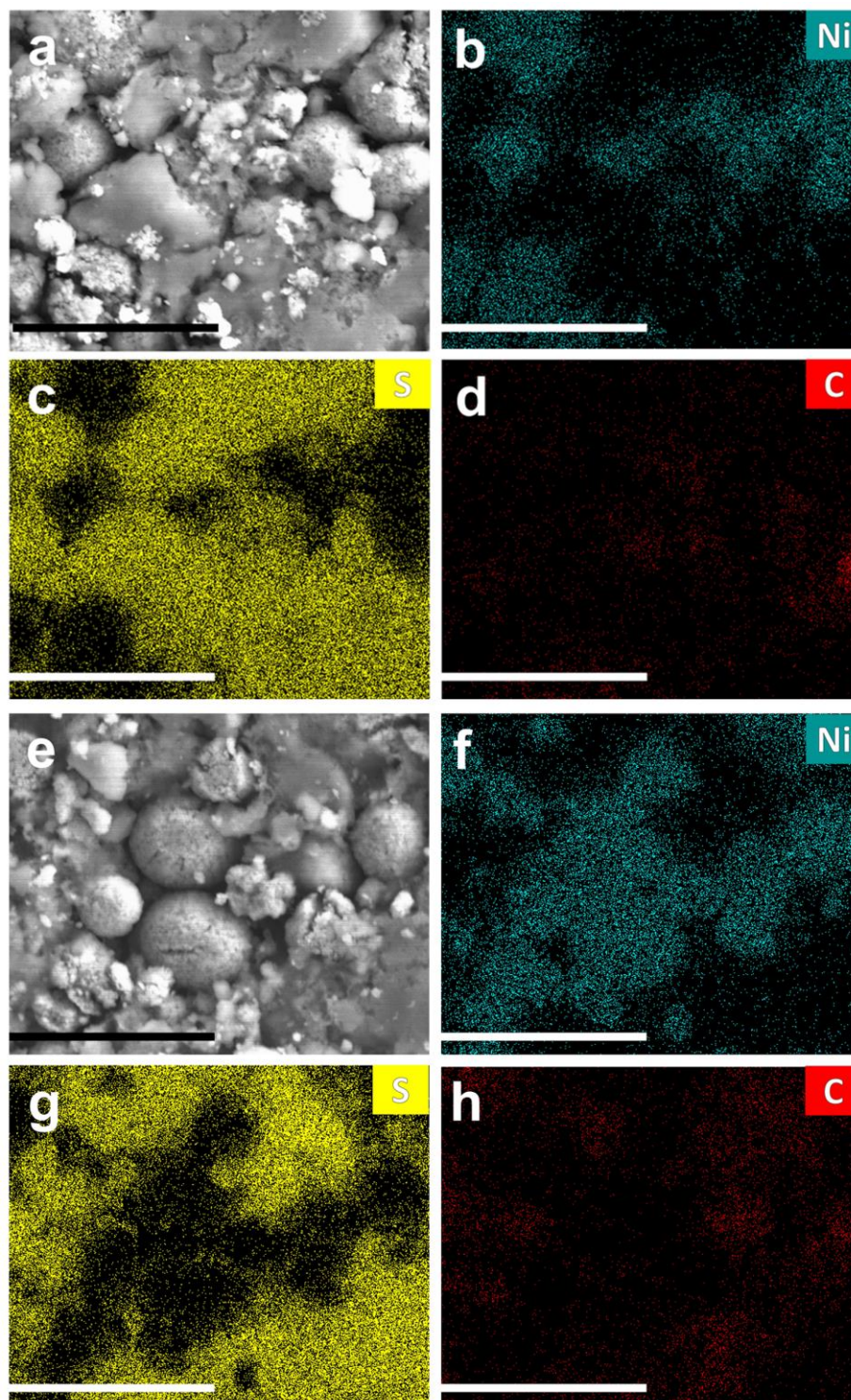
Figure S19. SEM-EDX mappings of the cycled a-d) bare and e-h) PEDOT modified electrodes. b and f) Ni, c and g) S, d and h) C. Scale bars in the figures of 20 µm.

Table S1 Resistances obtained from equivalent circuit fitting of EIS experimental data in Figure 3e.

Samples	R1 (Ω)	R2 (Ω)	R3 (Ω)
Bare	36	1336	8506
2 nm PEDOT	29	987	5140
5 nm PEDOT	26	575	7705
10 nm PEDOT	40	856	2202

Chapter 8

8 Fast-Charging Halide-Based All-Solid-State Batteries by Manipulation of Current Collector Interface*

Poor rate capability is a significant obstacle for the practical application of inorganic all-solid-state lithium-ion batteries (ASSLIBs). The charge transfer kinetics at the interface of current collector is crucial for high-rate capacity, but is typically neglected. In this paper, the interfacial evolution between Al foil current collector and composite cathode is studied in the $LiCoO_2/Li_3InCl_6$ (LCO/LIC) ASSLIBs at both 25 $^{\circ}$C and -10 $^{\circ}$C. The results indicate that, at 25 $^{\circ}$C, the side reactions between Al foil and LIC is the main challenge for the interfacial stability of current collector. The design of a graphene like carbon (GLC) coating for the modification of Al avoids the side reactions at the interface of current collector, resulting in improved cycling stability and high-rate capacity. GLC Al ASSLIB exhibits a high initial capacity of 102.9 mAh g^{-1} with a capacity retention of 89.1% after 150 cycles at 1C. A high-rate capacity of 69 mAh g^{-1} is also achieved at 5C. At -10 $^{\circ}$C, the low Li$^+$ and electron transfer kinetics along with the side reactions is the key limitation for the rate capability. Thanks to the GLC coating, the improved electrochemical performance is achieved with the enhanced charge transfer kinetics at the interface of current collector.

8.1 Introduction

Inorganic all-solid-state lithium-ion batteries (ASSLIBs) have advanced rapidly in recent years because of their intrinsic safety and continually improving ionic conductivity and interfacial stability.[1] For example, the high ionic conductivity of sulfide-based solid-state electrolytes (SSEs) has even surpassed those of conventional liquid electrolytes.[2] Halide-based SSEs, such as Li_3InCl_6 (LIC) and $Li_{2.633}Er_{0.633}Zr_{0.367}Cl_6$, with a wide electrochemical stable window realized along with a stable cathode interface, even without protective coatings.[3] As a result, the cycling stability of inorganic ASSLIBs has been significantly improved in recent literatures.[4] The long-term cycling performance of over 850 cycles has been achieved with a high capacity retention of 91.5%.[5] However, the high-rate capability of inorganic ASSLIBs still falls far below the requirements for the practical application of ASSLIBs in electric vehicles. From a U.S. Advanced Battery Consortium (USABC) report, fast-charging is defined as 40% capacity retention at current density of 4C.[6] Unfortunately, state-of-the-art inorganic ASSLIBs can only operate at very low current densities, such as 0.1C and 0.2C.

The main challenge of fast-charging inorganic ASSLIBs is the limited Li^+ and electronic conductivities at both the internal and external interfaces of composite cathode. At the internal interface of composite cathode, on the one hand, the volume change of cathode materials led to reduced contact between cathode materials and SSEs, resulting in reduced Li^+ transfer at the cathode/SSE interface.[7] To enhance the Li^+ transfer kinetics, various in-situ SSE coating strategies for the surface modification of cathode materials were developed by solution-based methods.[8] On the other hand, the application of carbon additives in composite cathode to enhance the charge transfer kinetics faced tremendous obstacles. The high electronic conductivity of carbon additives accelerated the decomposition of SSEs, resulting in the formation of an undesirable interfacial layer in the composite cathode.[9] Although a strategy of applying semi-conductive additive obtained the improved rate capacity in our previous study,[10] the charge transfer kinetics still need further improvement at the internal interface of composite cathode. At the external interface of the composite cathode, the interface of current collector is of crucial

importance but is left neglected. Only a simulation work speculated that both the Li$^+$ and electronic conductivities are restricted at the interface of current collector.[11] Accordingly, understanding of the degradation mechanism and design of rational strategy at the interface of current collector is critical for the high-rate performance of ASSLIBs.

In this study, we comprehensively investigate the interfacial evolution between Al foil and composite cathode during the electrochemical reactions in halide-based LIC ASSLIBs. Detailed electrochemical and X-ray characterizations combined with density functional theory (DFT) calculations and microscopy results indicate that the side reactions between Al foil and LIC SSE lead to the corrosion of Al foil and decomposition of LIC, resulting in the degradation of cycling stability and poor rate capability. Promisingly, a graphene like carbon (GLC) coating modified Al foil avoids the direct contact between Al foil and LIC, therefore circumventing the side reactions at the interface of current collector. As a result, the GLC Al ASSLIB demonstrates obviously improved rate capability and enhanced cycling stability. Impressively, a discharge capacity of 69 mAh g^{-1} is achieved at the current density of 5C in the LiCoO$_2$ (LCO) based ASSLIBs, which shows great potential for the application of fast-charging ASSLIBs. Promisingly, the GLC Al ASSLIB also shows much improved electrochemical performance at low temperature (-10 ^{o}C), indicating that GLC modification not only avoids the side reactions but also enhances the Li$^+$ and electron transfer kinetics at the interface of current collector. This study offers an idea of the interfacial modification for the fast-charging ASSLIBs in all-climate environments.

8.2 Experimental section

Preparation of current collectors, cathodes, and solid-state electrolytes:

The synthesis process of bare and graphene like carbon (GLC) coated Al foils was reported in our previous studies and US patents.[13a, 19] The commercial LiCoO$_2$ (LCO) is obtained from Sigma-Aldrich (99.8%). The ALD LiNbO$_x$ coated LCO was fabricated in a Savannah 100 ALD system (Ultratech/Cambridge Nanotech., USA) by using

$(CH_3)_3COLi$, $Nb(OCH_2CH_3)_5$, and water as precursors. The deposition temperature was 235 °C. For the preparation of solid-state electrolytes (SSEs), Li_3InCl_6 (LIC) was synthesized by a water removal route. LiCl and $InCl_3$ were dissolved in deionized water with the stoichiometric molar ratio. The solution was dried under vacuum at both 100 and 200 °C. Li_6PS_5Cl (LPSCl) was synthesized following the mechanical milling and annealing process. Li_2S, P_2S_5, and LiCl were mixed with the stoichiometric molar ratio and milled at 550 rpm. After that, the mixture was sealed in a quartz tube and annealed at 550 °C for 5h.

Assembly of the model cells and electrochemical testing:

In order to investigate the electrochemical performance, different types of model cells were fabricated. In the Al//LIC model cells, 60 mg LIC was pressed at 3 tons with 10 mm diameter to form a pellet, and then a piece of as-prepared Al foil with the same 10mm diameter was put onto one side of LIC pellet and pressed at 0.5 tons of pressure. In the Al//LIC//LPSCl//In-Li cells, 60 mg LIC was first pressed at 1 ton, and then 30 mg LPSCl was spread onto on side of LIC and pressed at 3 ton. After that, the as-prepared Al foils were put onto the other side of LIC pellet and pressed at 0.5 tons. Finally, In and Li foils was put onto the surface of LPSCl and pressed at 0.5 tons. In the Al//LCO-LIC//LIC//LPSCl//In-Li cells, the difference is 3.5 mg LCO power was mixed well with 1.5 mg LPSCl, and then uniformly spread onto the surface of LIC layer and pressed under 3 tons of pressure. Other parts are same as the process of Al//LIC//LPSCl//In-Li cells. All the processes were performed in an argon-filled glove box.

The galvanostatic charge-discharge characteristics were tested in the range of 2.1-3.6 V vs. Li^+/Li-In, corresponding to 2.7-4.2 V vs. Li^+/Li by using a multichannel battery tester (LAND CT-2001A, Wuhan Rambo Testing Equipment Co., Ltd., China). Cyclic voltammograms (CV) were collected on a versatile multichannel potentiostat 3/Z (VMP3) using a scan rate of 0.1 mV s^{-1}. Electrochemical impedance spectroscopy (EIS) was also performed on the versatile multichannel potentiostat 3/Z (VMP3) by applying an AC voltage of 10 mV amplitude in the 7000 kHz to 1000 mHz frequency range. For galvanostatic intermittent titration technique (GITT) measurements, the cells were

charged and discharged with 0.1C for 10 min and rest for 1h. According to the GITT theoretical analysis, Li$^+$ diffusion coefficient can be calculated by following equation:

$$D_{Li} = \frac{4}{\pi\tau}\left(\frac{m_B V_m}{M_B S}\right)^2 \left(\frac{\Delta E_s}{\Delta E_\tau}\right)^2 \ (\tau \ll L^2/D) \ (1)$$

Where D is chemical diffusion coefficient; S is interfacial contact area between LCO and LIC SSEs in our case, the specific area of LCO is 0.5 m^2 g^{-1}; τ is pulse duration (600 s in our case), ΔEs is the steady-state voltage change; ΔEt is the transient voltage change; m$_B$ is the mass of the LCO in the cathode composite (3.5 mg); M$_B$ is the molecular weight of LCO (97.87 g. mol^{-1}); V$_m$ is the molar volume of LCO (19.56 cm^3 mol^{-1}).
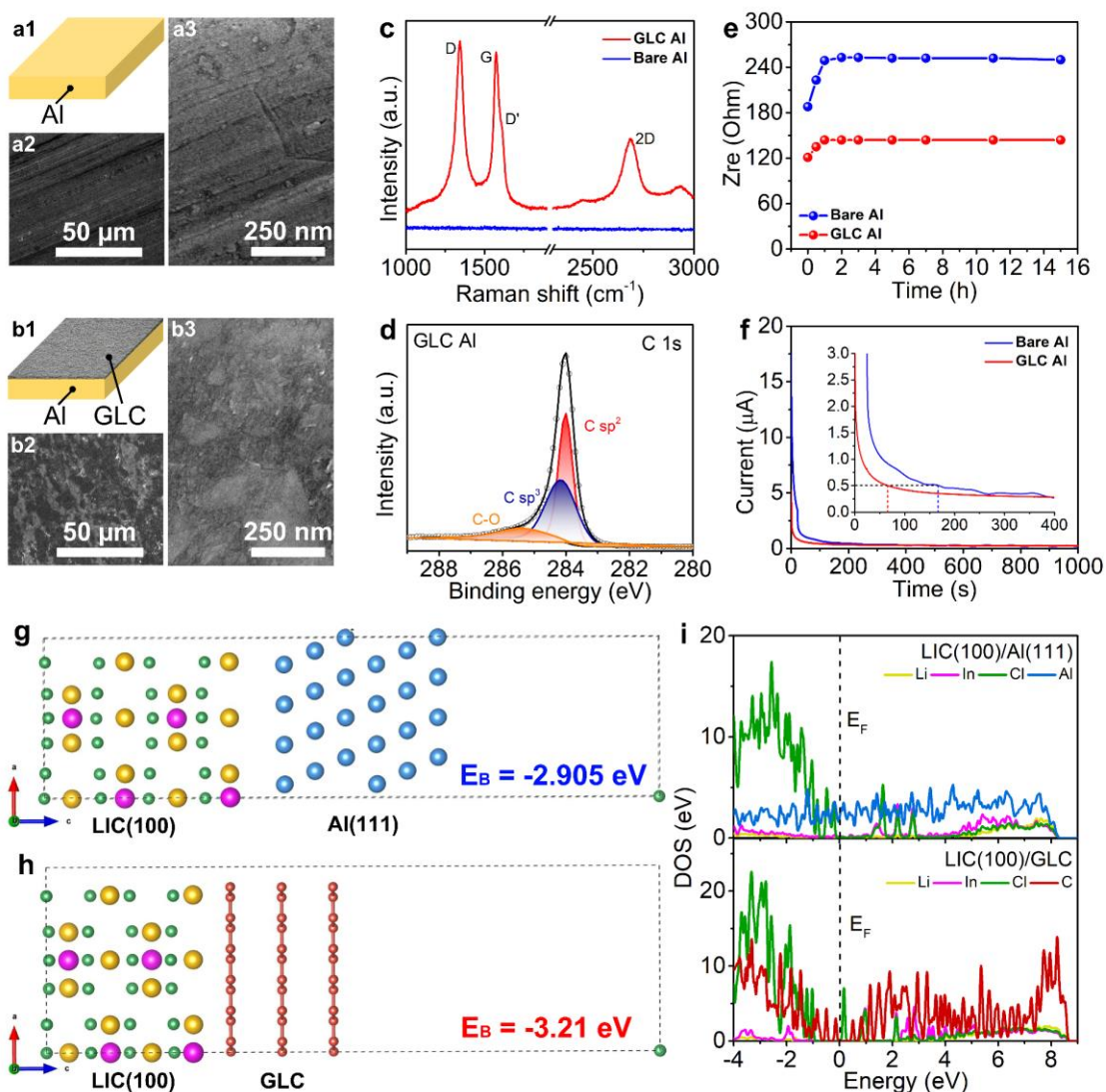
Characterizations:

The morphology and microstructure of the pristine and treated NMC811 were characterized using field emission scanning electron microscopy (FESEM, Hitachi S4800). The LiNbO$_x$ coating layer on the surface of LCO was observed by a high-resolution transmission electron microscopy (HRTEM, JEOL 2010F). Raman scattering spectra were carried out by a HORIBA Scientific LabRAM HR Raman spectrometer system. X-ray photoelectron spectroscopy (XPS) testing were measured with a monochromatic Al Kα source (1486.6 eV) in a Kratos AXIS Nova Spectrometer. The Ar filled glovebox was connected with the XPS machine to avoid the exposure of air. In the time-of-flight (ToF-SIMS) measurements, the action of the primary ion beam bombardment on the sample surface induces the emission of negative secondary ions. Sputtering with a Cs$^+$ ion beam (3 keV) was used for depth profiling analysis.

DFT calculation:

All calculations were carried out within the DFT framework as implemented in Vienna Ab Initio Simulation Package (VASP). The projector augmented-wave pseudopotentials were used to describe the interaction between ions and electrons, and the exchange-correlation effects were treated using the Perdew-Burke-Ernzerhof (PBE) functional under the generalized gradient approximation (GGA).[20] The electronic configurations

were $1s^22s^1$ for Li, $2s^22p^2$ for C, $3s^23p^5$ for Cl and $5s^25p^1$ for In. The lattice parameters of Al and LIC were optimized using a Monkhorst-Pack grid k-points of 4×4×4, and the kinetic energy cutoffs 520 eV was used. The VESTA package was used to visualize the various bulk, surface and interface structures.[21] For surface calculations, the van der Waals (vdW) correction function proposed by Grimme was adopted, which can well describe the long-range vdW interaction.[22] The vacuum space in the z direction was about 15 Å to avoid the interaction between neighboring. The k-point mesh was set to be 4×2×1 for hybrid heterostructures. All the atoms were optimized until the total energies converged to below 10-4 eV and the forces acting on atoms were less than 10-2 eV/Å. Furthermore, the binding energy was determined using the expression, $E_{Binding}=E_{A/LIC}-(E_A+E_{LIC})$, where E_A/LIC, E_A, and E_{LIC} represent the total energy of the graphene/LIC(100) (Al(111)/LIC(100)) interface, graphene (Al(111) surface) and LIC(100) surfaces slabs.

8.3   Results and discussion

Figure 8.1 Characterizations and simulation for the interface of current collectors. Schematic illustration and FE-SEM images of (a) bare Al and (b) GLC Al, (c) Raman spectra of the bare and GLC Al, (d) C 1s XPS spectrum of GLC Al. (e) Interfacial resistances of different rest time and (f) chronoamperograms profiles at 4.2 V vs Li$^+$/Li of the bare and GLC Al cells. Schematic view of (g) LIC(100)/Al(111) and (h) LIC(100)/GLC interfaces, along with their corresponding binding energy, (i) the corresponding density of states and the fermi level is set to be 0 eV.

To investigate the interfacial evolution of the current collector, the bare and GLC Al foils were applied in this study. The morphologies of the as-prepared Al foils are shown in Figure 8.1a-b. Compared to the bare Al foil, GLC Al foil demonstrates enhanced surface roughness. From the enlarged scanning electron microscope (SEM) image of the GLC Al foil (Figure 8.1b3), the irregularly layered graphene sheets are uniformly coating on the surface of Al foil. The physical properties of the GLC coating layer are investigated by Raman and X-ray photoelectron spectroscopic (XPS) characterizations, respectively. As shown in Figure 8.1c, the Raman spectrum of GLC Al foil shows the characteristic peaks of graphene (D′ and 2D bands).[12] Meanwhile, the intensity ratio of 2D/G peaks indicates the multilayered character of GLC on the surface of Al foil.[13] C 1s XPS spectrum shown in Figure 8.1d indicates that the GLC coating layer has the nature of sp2 carbon. Moreover, the emerged C-O band suggests the strong bonding between GLC layer and native oxide layer on the Al foil, which is helpful for the effective adhesion and great electron transfer at the interface between the Al foil and GLC coating layer.[14]

In addition to the physical characterizations, electrochemical analyses are also conducted to investigate the interfacial stability between the as-prepared Al foils and LIC SSEs. First of all, the chemical stability is studied and the configuration of the designed model cell is shown in Figure S1a. Electrochemical impedance spectroscopy (EIS) plots of the bare Al and GLC Al cells measured at various resting times are shown in Figure S2. The obviously increased interfacial resistance can be observed in the bare Al cell at the initial 2 h (Figure 8.1e). Although the interfacial resistance of bare Al cell is finally stable after 15 h, the large resistance of 250 Ω is still higher than that of the GLC Al cell. This result suggests that the interface between the bare Al foil and LIC is not stable even without electrochemical process. To evaluate the electrochemical stability between Al foil and LIC, the configuration of a model cell is designed (Figure S1b) and the chronoamperogram profiles of the bare and GLC Al cells are shown in Figure 8.1f. The polarization voltage of the as-prepared cells was set at 4.2 V vs Li^+/Li and held for 1 h. Interestingly, the initial current of the bare Al cell increased to 17.57 μA sharply and gradually decreased to 0.5 μA after 167 s. In contrast, the initial current maximum of the GLC Al cell is only 5.24 μA and the current quickly drops to 0.5 μA after 66 s.

Furthermore, the cyclic voltammogram (CV) profiles of the bare and GLC Al cells are shown in Figure S3. Although the oxidation current of GLC Al cell is higher than that of the bare Al cell at 4.2 V because of the higher contact area in GLC Al cell, the interfacial resistance between Al foil and LIC is suppressed by the modification of GLC coating after the CV cycling (Figure S4). Moreover, the change in contact resistance after CV testing indicates that the electronic conductivity at the interface between Al foil and LIC is improved by the GLC coating. Both the chronoamperogram and CV results suggest that the side reactions are actively occurring at the interface between bare Al foil and LIC during the electrochemical process. Impressively, GLC coating layer helps to stabilize the interface between Al foil and LIC SSE.

DFT calculations were conducted to obtain fundamental insights regarding the interfaces of LIC/Al and LIC/GLC, including their stability and electronic properties. The relaxed atomic structures of GLC, Al, and LIC are shown in Figure S5 with optimized lattice parameters summarized in Table S1. The previous DFT simulations have demonstrated that Al(111) and LIC(100) are the most stable surfaces for Al foil and LIC structures, respectively (Figure S6).[15] Therefore, LIC(100)/Al(111) and LIC(100)/GLC surfaces were energetically optimized to explore their stability and the optimized lattice parameters and binding energies are shown in Figure 8.1g-h. At the interface between GLC and LIC, the higher binding energy of -3.21 eV/atom indicates that the LIC(100)/GLC is energetically favored to form a more stable interface than the LIC(100)/Al(111). The Bader charge analysis for these two hybrid heterostructures was also performed.[16] As shown in Table S2, Li and In atoms lose electrons and the Cl atom gains electrons. Interestingly, Cl atoms gain electrons with partial transfer of 15.613 |e| at the LIC(100)/GLC interface, which is higher than that of the LIC(100)/Al(111) interface with partial transfer of 15.613 |e|. When Cl atoms gain more electrons, stronger interactions between Cl atoms and other elements could be achieved. This result indicates that there are more significant charge transfer interactions at the LIC/GLC interface than that of the LIC/Al interface, proving that GLC has better contact with composite cathodes. Furthermore, Figure 8.1i shows the density of state (DOS) of both the LIC(100)/Al(111) and LIC(100)/GLC interfaces. Because of the absence of energy gap at

the Fermi level, both LIC(100)/Al(111) and LIC(100)/GLC interfaces show a metallic character and are able to maintain a high electronic conductivity at the interface of current collector.
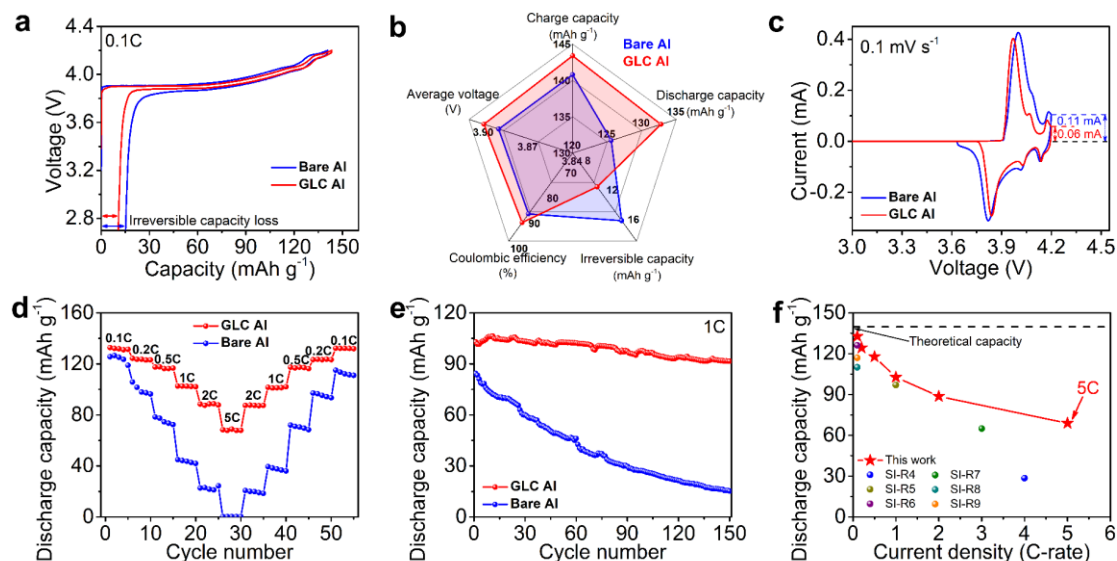

Figure 8.2 Electrochemical performance of the bare and GLC Al SSBs at room temperature. (a) Charge-discharge curves of the first cycle at 0.1C, (b) the corresponding performance parameters collected from charge-discharge curves, (c) CV profiles at 0.1 mV s^{-1}, (d) rate capability, and (e) cycling stability at 1C. (f) Comparison of rate capability between this work and other halide-based ASSLIBs from literatures.

The electrochemical performance of the bare and GLC Al ASSLIBs at room temperature (25 ^{o}C) is comprehensively studied (Figure 8.2). LCO and LIC are mixed as the composite cathode combined with LIC as the electrolyte layer and In-Li foils as the anode (Figure S1c). To exclude the effect of other interfaces on the performance of the as-prepared ASSLIBs, 5 nm LiNbO$_x$ coated LCO fabricated by atomic layer deposition (ALD) is adopted as shown in Figure S7 and a thin Li6PS5Cl (LPSCl) layer was set between LIC and In-Li anode. Figure 8.2a compares the initial charge-discharge curves between the bare and GLC Al ASSLIBs at 0.1C. An initial discharge capacity of 132.8 mAh g^{-1} and a high initial Coulombic efficiency of 92.6% are achieved by the ASSLIB with GLC Al. In contrast, the bare Al ASSLIB delivers a lower initial discharge capacity

of 125.6 mAh g^{-1} with a larger irreversible capacity loss. Notably, at the beginning of discharge, the more obvious voltage plateaus derived from the phase transition of LCO can be observed in the GLC Al ASSLIB. This phenomenon suggests faster Li$^+$ and electron transfer at the interface between GLC Al and composite cathode, resulting in higher average discharge voltage (3.91 V vs. 3.89 V) than that of the bare Al ASSLIB as shown in Figure 8.2b. From the CV profiles in Figure 8.2c, the GLC Al ASSLIB demonstrates smaller voltage intervals between the pairs of anodic-cathodic peaks and higher peak intensities than that of the bare Al ASSLIB, indicating enhanced electrochemical reaction activity with lower resistance at the interface between GLC Al and composite cathode. Furthermore, the GLC Al ASSLIB also shows the half of the current compared to the bare Al ASSLIB at the cut-off voltage (4.2 V), suggesting the suppressed side reactions at the interface between GLC Al and cathode compsites. The lithium-ion diffusion kinetics of the bare and GLC Al ASSLIBs are investigated by the galvanostatic intermittent titration technique (GITT). The corresponding polarization plots and lithium-ion diffusion coefficients (D_{Li}) during the initial charge-discharge process are demonstrated in Figure S8. The GLC Al ASSLIB shows higher D_{Li} at the end of the charge process and during the entire discharge process than that of the bare Al ASSLIB. This result indicates that Li$^+$ and electron transfer at the interface between GLC Al and composite cathode is higher than that of the bare ASSLIB.

Figure 8.2d compares the rate capability of the bare and GLC Al ASSLIBs at variable charge-discharge current densities ranging from 0.1C to 5C. The discharge capacities of the bare Al ASSLIB dramatically decay with an increase of current density. The capacities drop to zero when the current density increased to 5C. In contrast, the GLC Al ASSLIB demonstrates improved rate capacities at each current density. The discharge capacities of over 103 and 69 mAh g^{-1} are achieved at 1C and 5C, respectively. Furthermore, the capacity retention of over 99% is achieved after 55 cycles in the GLC Al ASSLIB when the current density switchs back to 0.1C, which is much higher than the capacity retention of 89% in the bare Al ASSLIB. The long cycling stability of the bare and GLC Al ASSLIBs at 1C is also demonstrated in Figure 8.2e. The GLC Al ASSLIB delivers an initial discharge capacity of 102.9 mAh g^{-1} with a capacity retention of 89.1%

after 150 cycles. In contrast, the bare Al ASSLIB shows a low initial discharge capacity of 84.4 mAh g^{-1} with a poor capacity retention of 15.2% after 150 cycles. Moreover, the corresponding Coulombic efficiency and average discharge voltage during the cycling are shown in Figure S9 and S10, respectively. The GLC Al ASSLIB shows both improved Coulombic efficiency and average discharge voltage, thus obtaining an energy density greater than that of the bare ASSLIB. Furthermore, as shown in Figure S11, the GLC Al ASSLIB shows a smaller interfacial resistance after 150 cycles than that of the bare Al ASSLIB, demonstrating that the interface between Al foil and composite cathode could be stabilized by the modification of GLC coating during the cycling. The aforementioned electrochemical performance demonstrated in LIC-based ASSLIBs suggests that the GLC modified Al foil not only suppresses the side reactions but also helps to achieve the enhanced Li$^+$ and electron transfer at the interface between current collector and cathode. The improved performance of GLC Al ASSLIB is undoubtedly competitive when compared to other halide-based ASSLIBs (Figure 8.2f and Table S3).
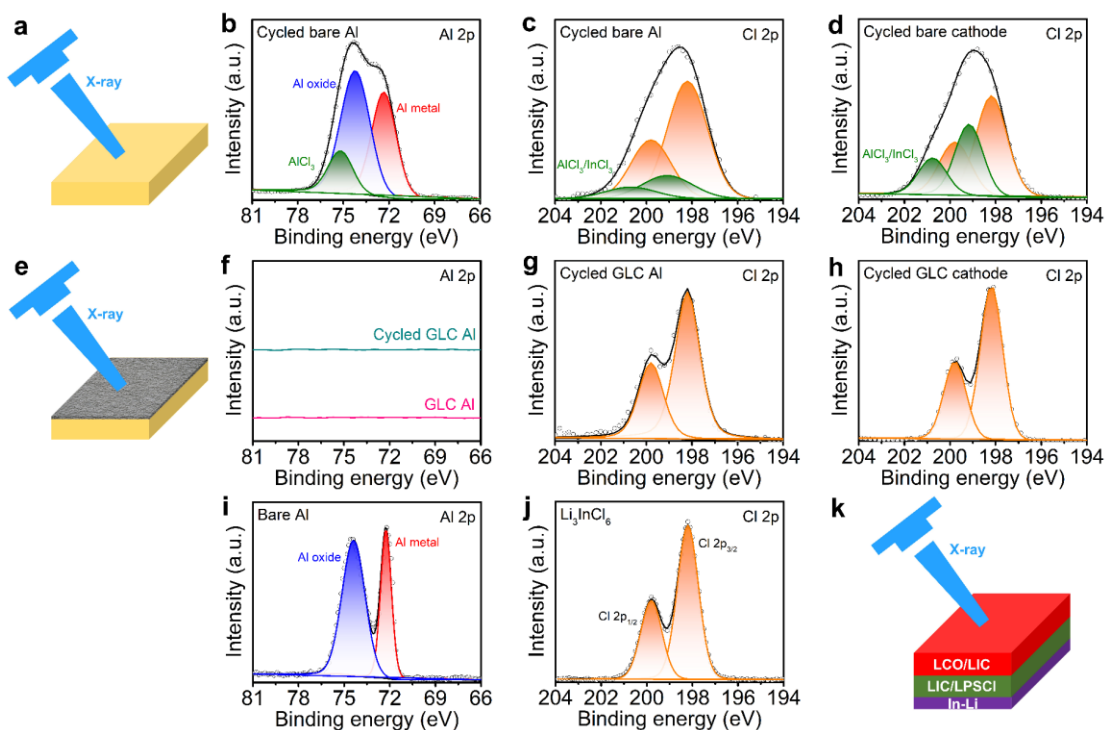
Figure 8.3 XPS characterizations of the cycled bare and GLC Al current collectors and cathodes. (a) Schematic illustration of X-ray beam on the surface of the cycled bare

Al, (b) Al 2p and (c) Cl 2p XPS spectra of the cycled bare Al, (d) Cl 2p XPS spectrum of the cycled bare cathode. (e) Schematic illustration of X-ray beam on the surface of the cycled GLC Al, (f) Al 2p and (g) Cl 2p XPS spectra of the cycled GLC Al, (h) Cl 2p XPS spectrum of the cycled GLC cathode. (i) Al 2p spectrum of the bare Al. (j) Cl 2p spectrum of Li_3InCl_6. (k) Schematic illustration of X-ray beam on the surface of the cycled composite cathode.

To investigate the interfacial evolution between the as-prepared Al foils and composite cathode during the electrochemical process, XPS measurements were performed. The cycled ASSLIBs were disassembled and both the surface of Al foils and composite cathodes were tested as shown in the schemetic diagrams of Figure 8.3a, 8.3e, and 8.3k, respectively. Compared to the Al 2p spectrum of the bare Al before cycling (Figure 8.3i), the obvious increased peak intensity of Al oxide is observed in the cycled bare Al. Interestingly, a new peak at 75.1 eV is emerged in the cycled bare Al, suggesting the formation of $AlCl_3$ or Al-O-Cl species after cycling (Figure 8.3b).[17] In contrast, there is no Al signal in the cycled GLC Al (Figure 8.3f), indicating that GLC coating layer maintained the integrity on the surface of Al foil even after cycling. Meanwhile, C 1s XPS spectrum shown in Figure S12 demonstrates that the composition of the GLC layer was not changed after the cycling. Figure 8.3c, 8.3g, and 8.3j show the Cl 2p XPS spectra collected from the cycled bare Al, cycled GLC Al, and the pristine LIC, respectively. In the cycled bare Al, the emergent peak at 199.1 eV ($2p_{3/2}$) indicates the formation of Cl species (such as $AlCl_3$, $InCl_3$, and In-O-Cl).[18] This result suggests the severe corrosion of Al foil and/or the decomposition of LIC after cycling. Although the Cl 2p XPS signal is also detected in the cycled GLC Al, no obvious change in the Cl chemistry is observed when compared to the Cl 2p XPS spectrum of the pristine LIC. This result demonstrates that LIC just adhered on the surface of GLC layer rather than reacted with GLC layer during cycling.

In addition to the XPS analysis for the cycled current collectors, the XPS characterizations of the cycled bare and GLC composite cathodes are also performed as shown in Figure 8.3d and 8.3h, respectively. Consistant with the results of the cycled Al

foils, the peak of $AlCl_3$ and/or $InCl_3$ is also observed in the Cl 2p XPS spectrum of the cycled bare cathode. In contrast, the well maintained Cl chemistry is shown in the cycled GLC cathode. Although there is no change of the In 3d XPS spectra in both the cycled bare Al and GLC cathodes (Figure S13), the evolution of Cl 2p XPS spectra is enough to demonstrate the side reactions between bare Al and LIC during the cycling. Furthermore, the unchanged Co 2p XPS spectra shown in Figure S14 indicate the ALD $LiNbO_x$ coated LCO is stable with both LIC and Al foil during the cycling.
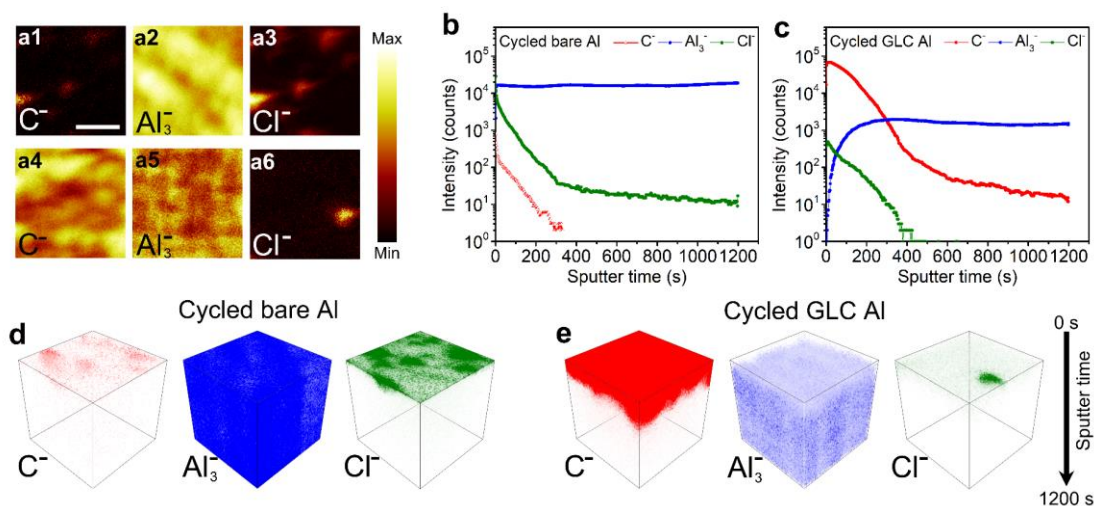
Figure 8.4 ToF-SIMS characterizations of the cycled bare and GLC Al current collectors. (a) Secondary ion images of C^-, Al_3^-, and Cl^- species after Cs^+ consecutive sputtering of 1200 s for (a1-a3) cycled bare Al and (a4-a6) cycled GLC Al (the length of scale bar is 20 μm), (b-c) the corresponding depth profile of various secondary ion species obtained by sputtering, and 3D view images of the sputtered volume corresponding to the depth profiles of (d) cycled bare Al and (e) cycled GLC Al.

Time-of-flight secondary ion mass spectrometry (ToF-SIMS) was further performed to identify the appearance and depth information at the interface between Al foil and composite cathode after the cycling. With the Cs^+ ion beam etching, the secondary ions of C^- and Al_3^- are measured in the GLC Al foil, indicating the GLC coating on the surface of Al foil with the thickness of 0.5 µm (Figure S15). From the chemical ion images (Figure 8.4a), obvious Cl^- species are observed in the cycled bare Al, which is barely

detected in the cycled GLC Al. In Figure 8.4b, the Cl⁻ signal is very strong at the beginning of sputtering in the cycled bare Al. Although decreasing quickly, Cl⁻ signal still can be detected after 300s, indicating the severe side reactions between bare Al foil and LIC after cycling. In contrast, Cl⁻ signal dropped dramatically and disappeared after 400 s in the cycled GLC Al because of the protection of GLC coating layer (Figure 8.4c). The distributions of C⁻, Al$_3$⁻, and Cl⁻ species are also clearly presented in Figure 8.4d. The obvious Cl⁻ signal is observed on the surface of bare Al, which is suppressed in the cycled GLC Al. The aforementioned XPS and ToF-SIMS results indicate that the bare Al foil reacted with LIC during the cycling, resulting in the corrosion of Al foil and decomposition of LIC. However, the application of GLC Al avoids the direct contact between Al foil and LIC, therefore circumventing the side reactions at the interface between current collector and cathode.
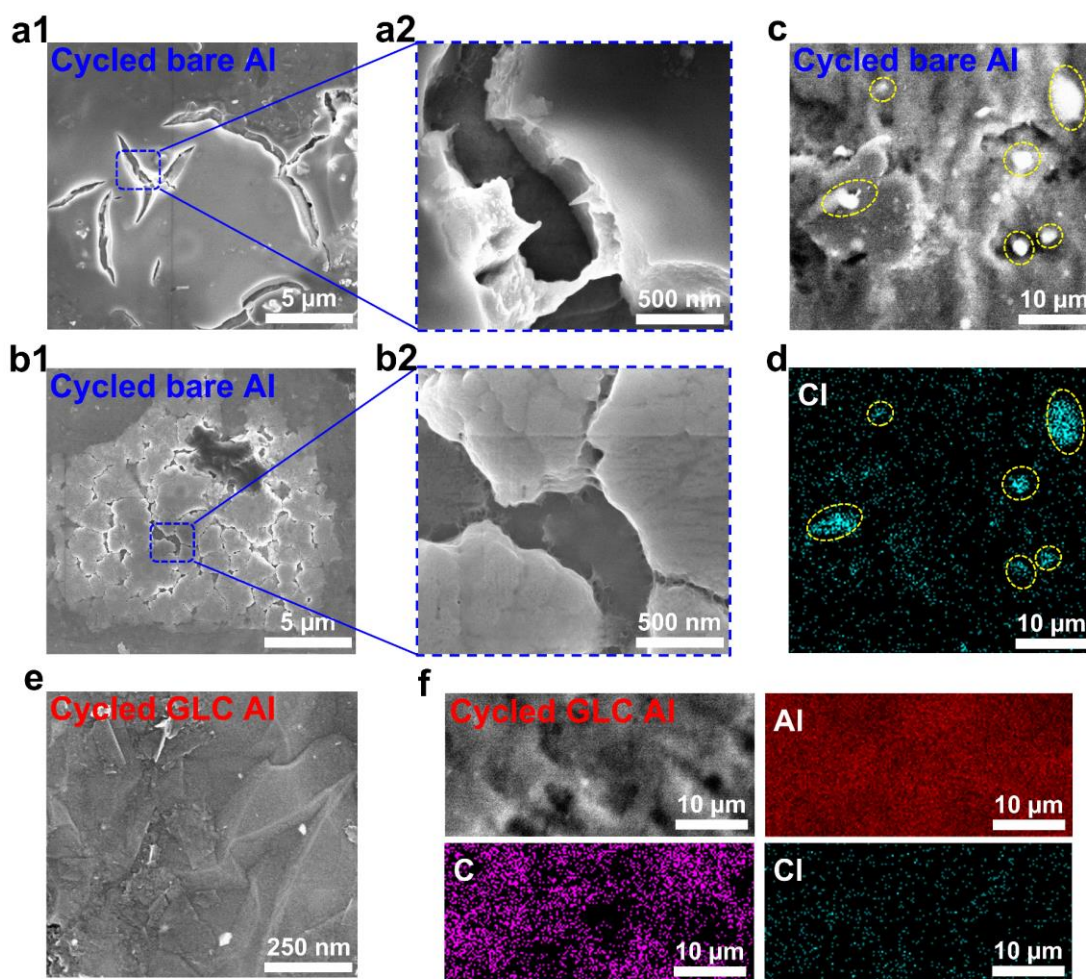
Figure 8.5 Morphology evolutions of the cycled bare and GLC Al current collectors. (a-c) SEM images and (d) EDS mapping of Cl element of the cycled bare Al. (e) SEM image and (f) EDS mapping of Al, C, and Cl elements of the GLC Al.

The surfacial morphology evolutions of the bare and GLC Al after cycling are evaluated by the SEM characterization. Figure 8.5a-b show the SEM images of the top view of the cycled bare Al. The severe cracks can be observed and extend to the deep inside of the Al foil after cycling (Figure 8.5a). Meanwhile, the by-products deposited on the surface of Al foil also can be observed because of the side reactions between bare Al and LIC during the cycling (Figure 8.5b). Energy-dispersive X-ray spectroscopy (EDS) mapping of the cycled bare Al confirms that the by-products enriched on the surface of Al, indicating the interfacial deterioration between Al foil and LIC after cycling (Figure 8.5c-

d). In contrast, from the SEM image of the cycled GLC Al as shown in Figure 8.5e, the morphology of the GLC coating layer mantains well after cycling. Meanwhile, there is no Cl signal on the surface of the cycled GLC Al (Figure 8.5f), indicating that GLC coating layer is beneficial towards the stability of the interface between current collector and cathode.
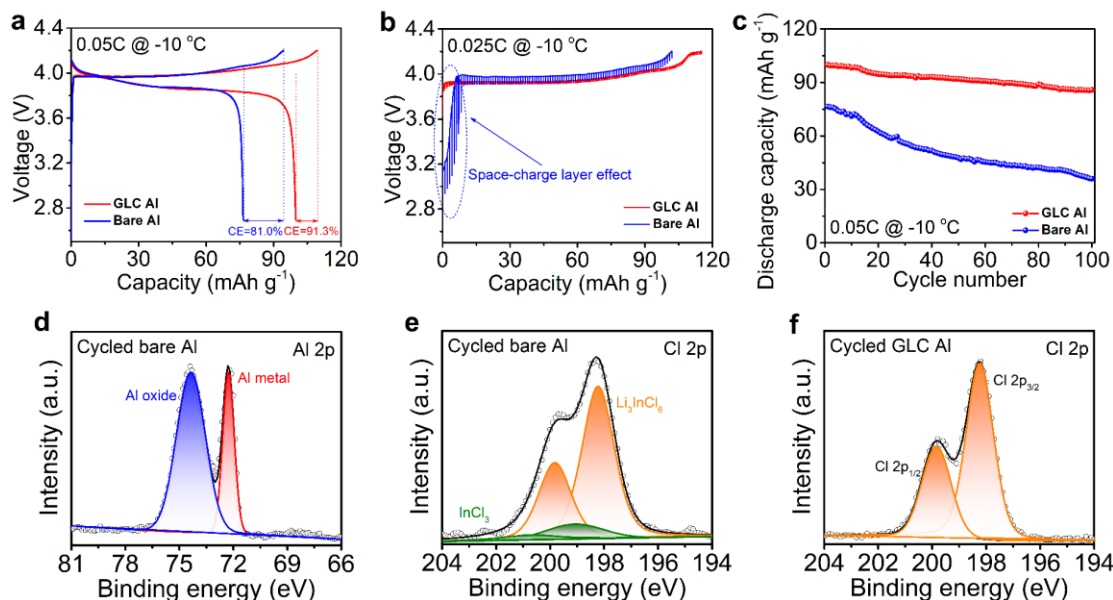
Figure 8.6 Electrochemical and XPS characterization of the bare and GLC Al at low temperature. (a) Charge-discharge curves of the first cycle at 0.05C, (b) GITT curves at 0.025C, and (c) cycling stability at 0.05C of the bare and GLC Al ASSLIBs. (d) Al 2p and (e) Cl 2p XPS spectra of the cycled bare Al. (f) Cl 2p XPS spectrum of the cycled GLC Al.

The interfacial evolution of current collector is also investigated at low temperature (-10 ^{o}C). At the low temperature, the Li$^+$ and electron transfer kinetics at the cathode interface are critical towards achieving good electrochemical performance. Figure 8.6a shows the initial charge-discharge curves of the bare and GLC Al ASSLIBs at -10 ^{o}C under the current density of 0.05C. The reduced capacity in the as-prepared ASSLIBs is achieved as expectation compared to the counterparts at 25 ^{o}C. The decreased ionic conductivity of SSEs at low temperature is the main reason that leading to the slow Li$^+$ and electron transfer kinetics. The ionic conductivity of SSEs at -10 ^{o}C is only one-tenth of that at 25

°C (Figure S16). In addition to the limitated ionic conductivity of SSEs, the interface of current collector is of crucial importance for the kinetics at the external interfaces of composite cathode. The GLC Al ASSLIB shows an initial discharge capacity of 99.9 mAh g^{-1} with the Coulombic efficiency of 91.3%. However, the bare Al ASSLIB only delivers a discharge capacity of 76.5 mAh g^{-1} with a lower Coulombic efficiency of 81.0%. Figure 8.6b shows the GITT curves of the bare and GLC Al ASSLIBs during the charging process. An obvious space-charge-layer effect is observed at the beginning of charging in the bare Al ASSLIB, indicating the inhomogeneous charge distribution at the interface of current collector. During the entire charing process, the bare Al ASSLIB demonstrates severe polarizaiton voltage, which is 2.5 times higher than that of the GLC Al ASSLIB (Figure S17a). Moreover, the D_{Li} in the bare Al ASSLIB is limited by the reduced Li$^+$ transfer kinetics, which can be enhanced by the GLC modification (Figure S17b). The cycling stability of the bare and GLC Al ASSLIBs are shown in Figure 8.6c. The capacity retention of GLC Al ASSLIB is 85.9% after 100 cycles, which is much higher than the capacity retention of 47.1% in the bare Al ASSLIB. Furthermore, the GLC Al ASSLIB also demonstrates the improved Coulombic efficiency with higher average discharge voltage and reduced interfacial resistance (Figure S18 and S19).

The XPS characterization was conducted to study the interfacial stability between Al foil and LIC SSE at low temperature. Figure 8.6d shows the Al 2p XPS spectrum of the cycled bare Al. There is no AlCl$_3$ signal indicating that the corrosion of Al foil is suppressed at low temperature. Interestingly, the signal of InCl$_3$ is observed in the Cl 2p XPS spectrum of the cycled bare Al as shown in Figure 8.6e, suggesting the decomposition of LIC still occurs at low temperature. In contrast, both the Al 2p and Cl 2p XPS spectra of the cycled GLC Al indicate that the interface between Al foil and LIC SSE is stablized by GLC coating (Figure 8.6f and S20-21). Furthermore, the composition of GLC coating layer was also not changed after cycling at low temperature, which is confirmed by the C 1s XPS spectrum (Figure S22). SEM images of the cycled bare and GLC Al foils are shown in Figure S23. The defects on the surface of the bare Al is obviously suppressed at low temperature compared to the situation at room temperature. The aforementioned results indicate that the performance of ASSLIBs at low temperature

is limited by the Li^+ and electron transfer kinetics along with the side reactions at the interface between current collector and composite cathode.

8.4 Conclusion

In conclusion, the interfacial stability between the current collector and composite cathode in inorganic ASSLIBs is investigated at both 25 ^{o}C and -10 ^{o}C by the comprehensive electrochemical, DFT, XPS, ToF-SIMS, and SEM characterizations. At room temperature, the side reactions at the interface between Al foil and LIC SSE are the main challenge that deteriorate the electrochemical performance. The modification of Al by GLC coating avoids the direct contact between Al foil and LIC SSE, therefore circumventing both the corrosion of Al foil and decomposition of LIC SSE. As a result, the notably improved electrochemical performance is achieved, including higher capacity, reduced voltage polarization, and better cycling stability. More importantly, the high-rate capability is significantly improved by the GLC modification. The discharge capacity of 69 mAh g^{-1} is achieved in the GLC ASSLIB at 5C, which surpasses the USABC target for fast-charging batteries. At low temperature, in addition to side reactions, the low Li^+ and electron transfer kinetics limit the electrochemical performance of inorganic ASSLIBs. GLC coating layer is beneficial towards the Li^+ and electron transfer at the interface between current collector and composite cathode, resulting in the improved capacity with the enhanced cycling stability. The results collected in this research indicate that current collector as the external interface in cathode is of critical importance for the performance of inorganic ASSLIBs. Both the interfacial reactions and kinetics should be considered when designing fast-charging ASSLIBs under the all-climate environments.

8.5 Acknowledgments

8.6 References

[1] a) J. C. Bachman, S. Muy, A. Grimaud, H.-H. Chang, N. Pour, S. F. Lux, O. Paschos, F. Maglia, S. Lupart, P. Lamp, L. Giordano, Y. Shao-Horn, *Chem. Rev.* **2016**, 116, 140; b) R. Chen, Q. Li, X. Yu, L. Chen, H. Li, *Chem. Rev.* **2019**, 120, 6820.

[2] a) N. Kamaya, K. Homma, Y. Yamakawa, M. Hirayama, R. Kanno, M. Yonemura, T. Kamiyama, Y. Kato, S. Hama, K. Kawamoto, A. Mitsui, *Nat. Mater.* **2011**, 10, 682; b) Y. Kato, S. Hori, T. Saito, K. Suzuki, M. Hirayama, A. Mitsui, M. Yonemura, H. Iba, R. Kanno, *Nat. Energy* **2016**, 1, 1.

[3] a) X. Li, J. Liang, J. Luo, M. Norouzi Banis, C. Wang, W. Li, S. Deng, C. Yu, F. Zhao, Y. Hu, T.-K. Sham, L. Zhang, S. Zhao, S. Lu, H. Huang, R. Li, K. R. Adair, X. Sun, *Energy Environ. Sci.* **2019**, 12, 2665; b) K.-H. Park, K. Kaup, A. Assoud, Q. Zhang, X. Wu, L. F. Nazar, *ACS Energy Lett.* **2020**, 5, 533.

[4] a) L. Peng, H. Ren, J. Zhang, S. Chen, C. Yu, X. Miao, Z. Zhang, Z. He, M. Yu, L. Zhang, *Energy Stor. Mater.* **2021**, 43, 53; b) L. Zhou, C. Y. Kwok, A. Shyamsunder, Q. Zhang, X. Wu, L. F. Nazar, *Energy Environ. Sci.* **2020**, 13, 2056.

[5] D. Cao, Y. Zhang, A. M. Nolan, X. Sun, C. Liu, J. Sheng, Y. Mo, Y. Wang, H. Zhu, *Nano Lett.* **2020**, 20, 1483.

[6] G. L. Zhu, C. Z. Zhao, J. Q. Huang, C. He, J. Zhang, S. Chen, L. Xu, H. Yuan, Q. Zhang, *Small* **2019**, 15, 1805389.

[7] a) S. Randau, D. A. Weber, O. Kötz, R. Koerver, P. Braun, A. Weber, E. Ivers-Tiffée, T. Adermann, J. Kulisch, W. G. Zeier, F. H. Richter, J. Janek, *Nat. Energy* **2020**, 5, 259; b) S. Deng, X. Li, Z. Ren, W. Li, J. Luo, J. Liang, J. Liang, M. N. Banis, M. Li,

Y. Zhao, *Energy Stor. Mater.* **2020**, 27, 117; c) H.-T. Ren, Z.-Q. Zhang, J.-Z. Zhang, L.-F. Peng, Z.-Y. He, M. Yu, C. Yu, L. Zhang, J. Xie, S.-J. Cheng, *Rare Metals* **2021**, 1.

[8]   a) K. H. Park, D. Y. Oh, Y. E. Choi, Y. J. Nam, L. Han, J. Y. Kim, H. Xin, F. Lin, S. M. Oh, Y. S. Jung, *Adv. Mater.* **2016**, 28, 1874; b) C. Wang, J. Liang, M. Jiang, X. Li, S. Mukherjee, K. Adair, M. Zheng, Y. Zhao, F. Zhao, S. Zhang, *Nano Energy* **2020**, 76, 105015.

[9]   a) S. W. Park, G. Oh, J. W. Park, Y. C. Ha, S. M. Lee, S. Y. Yoon, B. G. Kim, *Small* **2019**, 15, 1900235; b) F. Walther, S. Randau, Y. Schneider, J. Sann, M. Rohnke, F. H. Richter, W. G. Zeier, J. r. Janek, *Chem. Mater.* **2020**, 32, 6123.

[10]   S. Deng, Y. Sun, X. Li, Z. Ren, J. Liang, K. Doyle-Davis, J. Liang, W. Li, M. Norouzi Banis, Q. Sun, R. Li, Y. Hu, H. Huang, L. Zhang, S. Lu, J. Luo, X. Sun, *ACS Energy Letters* **2020**, 5, 1243.

[11]   A. Neumann, S. Randau, K. Becker-Steinberger, T. Danner, S. Hein, Z. Ning, J. Marrow, F. H. Richter, J. r. Janek, A. Latz, *ACS Appl. Mater. Interfaces* **2020**, 12, 9277.

[12]   a) M. Pimenta, G. Dresselhaus, M. S. Dresselhaus, L. Cancado, A. Jorio, R. Saito, *Phys. Chem. Chem. Phys.* **2007**, 9, 1276; b) L. M. Malard, M. A. Pimenta, G. Dresselhaus, M. S. Dresselhaus, *Phys. Rep.* **2009**, 473, 51.

[13]   a) X. Li, S. Deng, M. N. Banis, K. Doyle-Davis, D. Zhang, T. Zhang, J. Yang, R. Divigalpitiya, F. Brandys, R. Li, X. Sun, *ACS Appl. Mater. Interfaces* **2019**, 11, 32826; b) A. C. Ferrari, J. Meyer, V. Scardaci, C. Casiraghi, M. Lazzeri, F. Mauri, S. Piscanec, D. Jiang, K. Novoselov, S. Roth, *Phys. Rev. Lett.* **2006**, 97, 187401; c) C. Wu, S. Deng, H. Wang, Y. Sun, J. Liu, H. Yan, *ACS Appl. Mater. Interfaces* **2014**, 6, 1106.

[14]   a) M. Wang, M. Tang, S. Chen, H. Ci, K. Wang, L. Shi, L. Lin, H. Ren, J. Shan, P. Gao, *Adv. Mater.* **2017**, 29, 1703882; b) M. Wang, H. Yang, K. Wang, S. Chen, H. Ci, L. Shi, J. Shan, S. Xu, Q. Wu, C. Wang, *Nano Lett.* **2020**, 20, 2175.

[15]   a) Y. Liu, Y. Huang, Z. Xiao, X. Reng, *Metals* **2017**, 7, 21; b) X. Yang, M. Jiang, X. Gao, D. Bao, Q. Sun, N. Holmes, H. Duan, S. Mukherjee, K. Adair, C. Zhao, *Energy Environ. Sci.* **2020**, 13, 1318.

[16]   G. Henkelman, A. Arnaldsson, H. Jónsson, *Comput. Mater. Sci.* **2006**, 36, 354.

[17]   G. McGuire, G. K. Schweitzer, T. A. Carlson, *Inorg. Chem.* **1973**, 12, 2450.

[18]   B. H. Freeland, J. J. Habeeb, D. G. Tuck, *Can. J. Chem.* **1977**, 55, 1527.

[19]   a) R. Divigalpitiya, S. Ezugwu, G. Fanchini, Google Patents, 2018; b) R. Divigalpitiya, M. I. Buckett, Google Patents, 2015.

[20]   J. P. Perdew, K. Burke, M. Ernzerhof, *Phys. Rev. Lett.* **1996**, 77, 3865.

[21]   K. Momma, F. Izumi, *J. Appl. Crystallogr.* **2008**, 41, 653.

[22]   S. Grimme, *J. Comput. Chem.* **2006**, 27, 1787.

8.7 Supporting information
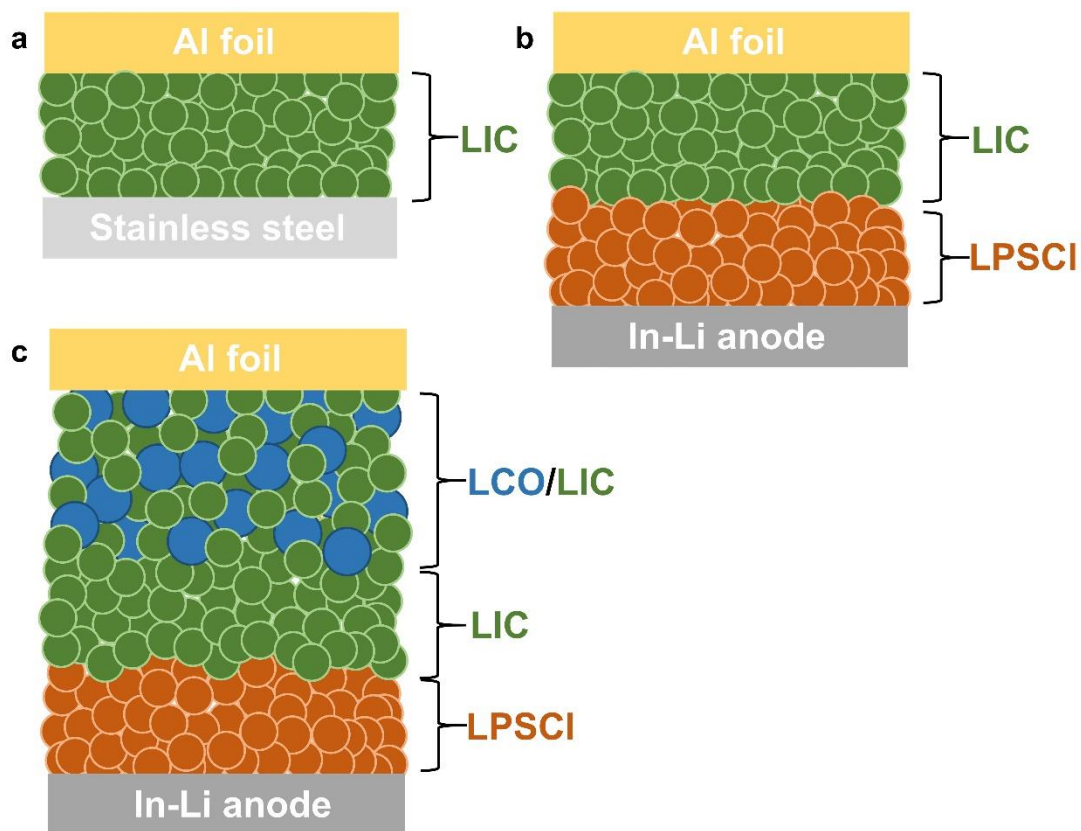
Figure S1. Schematic figures of the different model cells for electrochemical testing. (a) Al//LIC cell, (b) Al//LIC//LPSCl//In-Li cell, and (c) Al//LCO-LIC//LIC//LPSCl//In-Li cell.
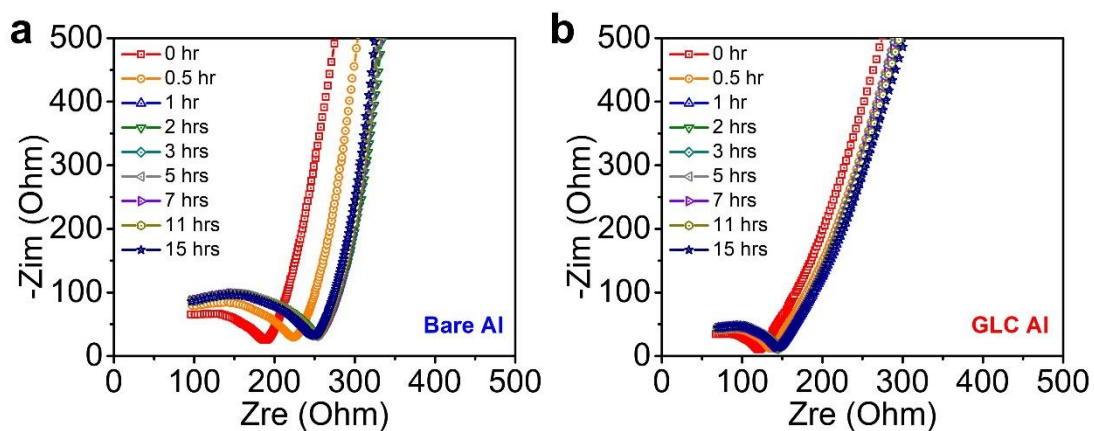
Figure S2. EIS plots of the (a) bare Al//LIC and (b) GLC Al//LIC cells measured at a various resting time.
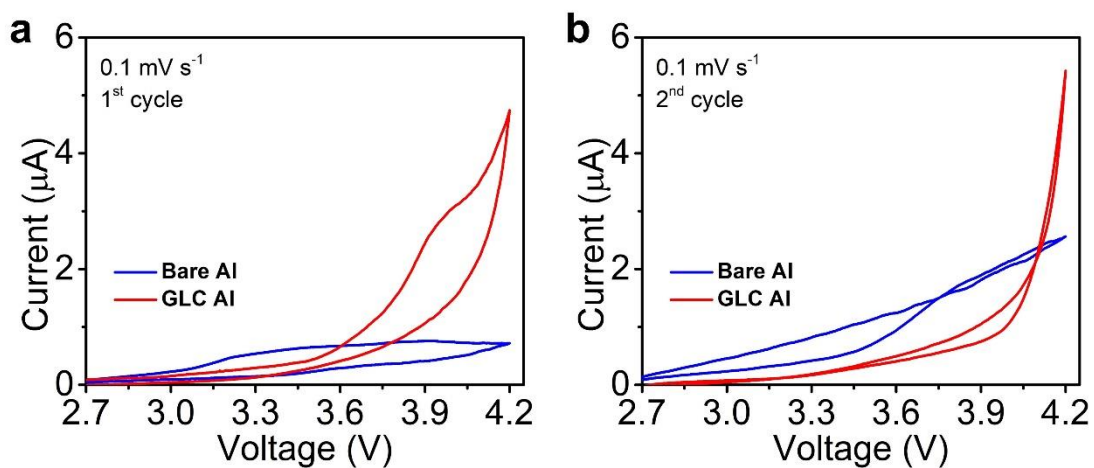
Figure S3. CV profiles of the bare Al//LIC//LPSCl//In-Li and GLC Al//LIC//LPSCl//In-Li cells. (a) 1st cycle and (b) 2nd cycle.
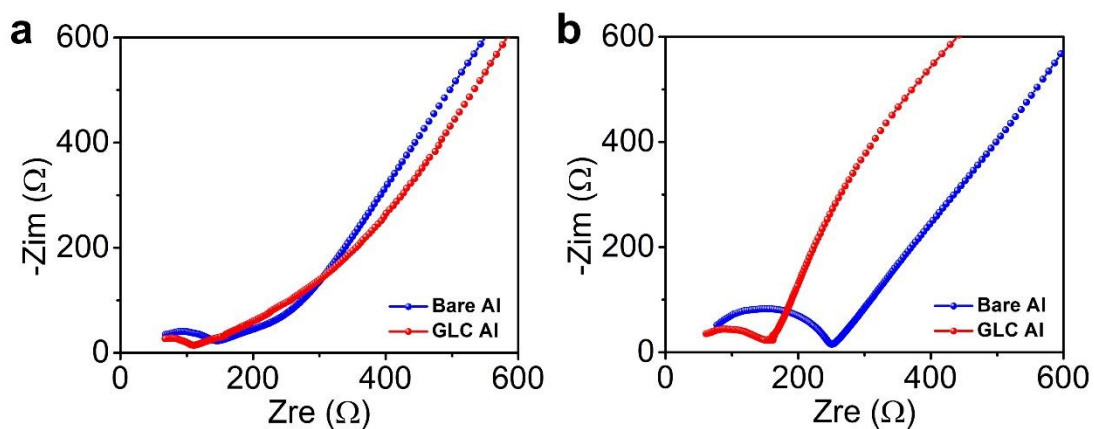
Figure S4. EIS plots of the bare Al//LIC//LPSCl//In-Li and GLC Al//LIC//LPSCl//In-Li cells (a) before and (b) after CV cycling.
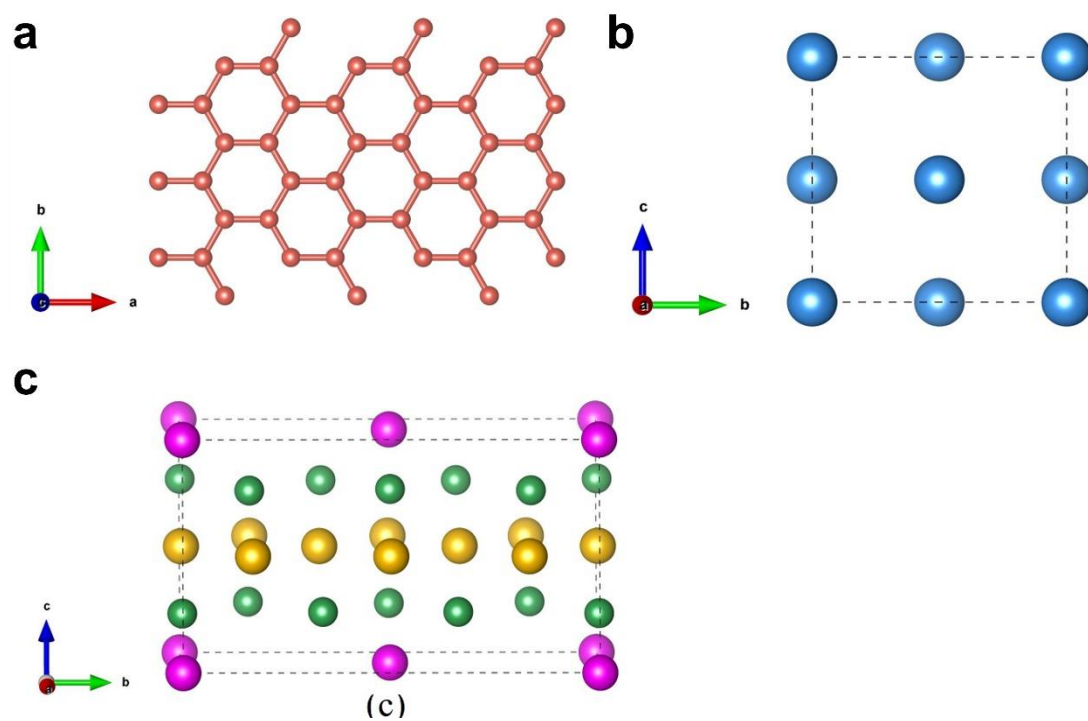
Figure S5. Schematic view of (a) GLC, (b) Al, and (c) LIC. Blue, red, yellow, green and pink spheres represent the Al, C, Li, Cl, and In atoms, respectively.
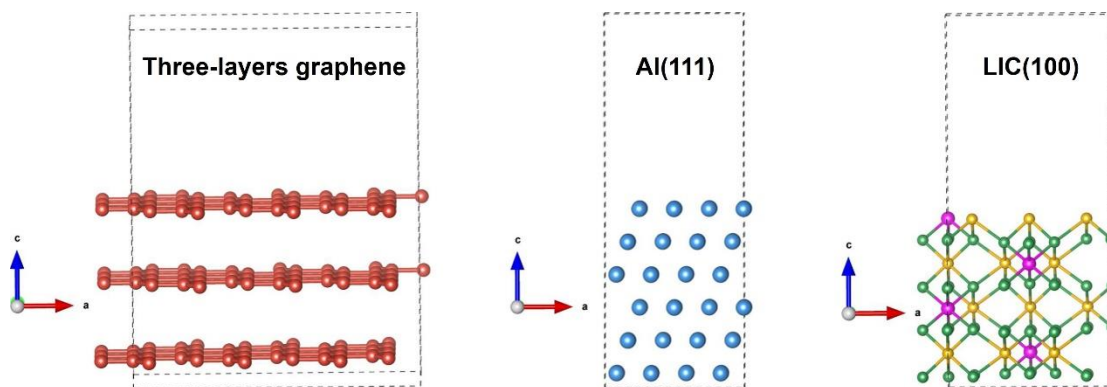
Figure S6. Schematic view of (a) three-layers graphene, (b) Al(111) surface, and (c) LIC(100) surface.
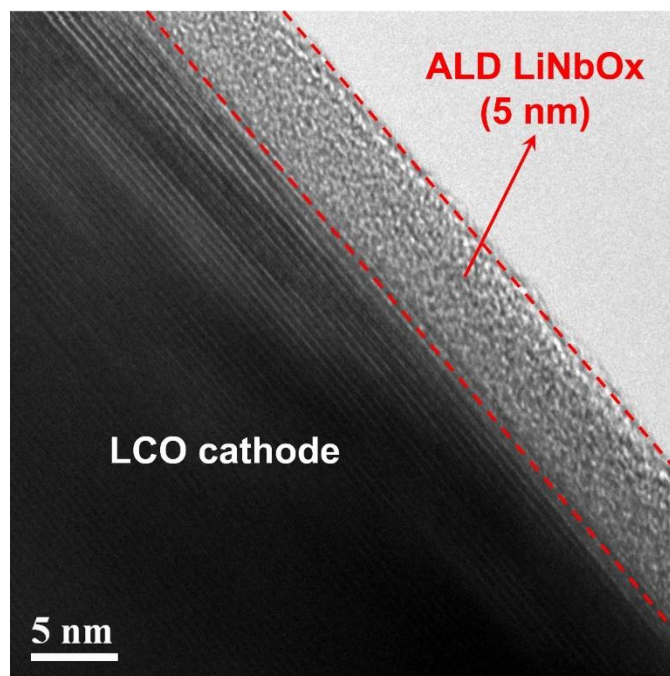
Figure S7. HR-TEM image of 5nm LiNbO$_x$ coated on the surface LCO cathode particle by ALD.
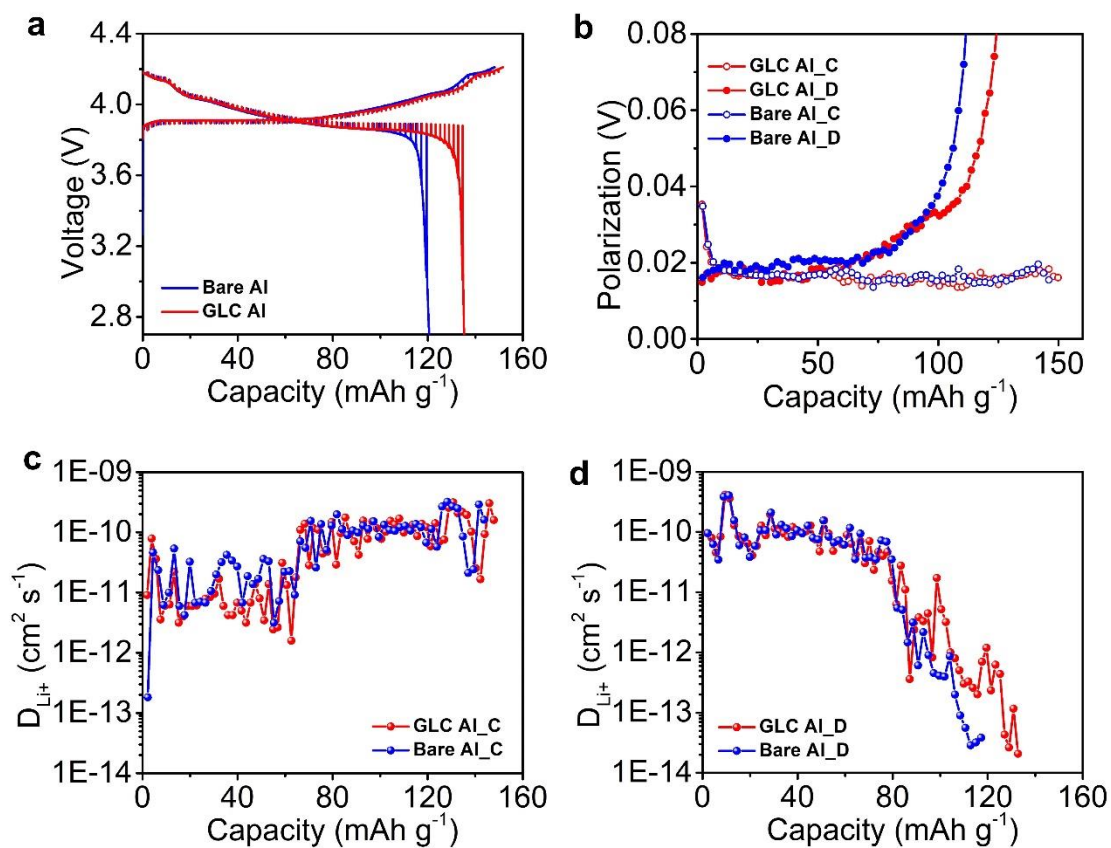
Figure S8. GITT testing of the bare and GLC Al ASSLIBs at 25 °C. (a) Charge-discharge curves, (b) the corresponding polarization plots, and lithium-ion diffusion coefficients during (c) charge and (d) discharge process.
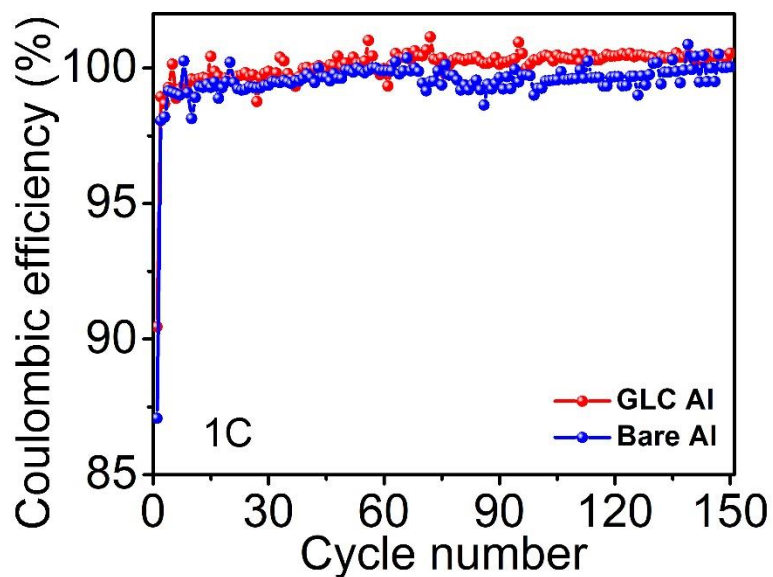
Figure S9. The corresponding Coulombic efficiency of the bare and GLC Al ASSLIBs during cycling under the current density of 1C at 25 ºC.
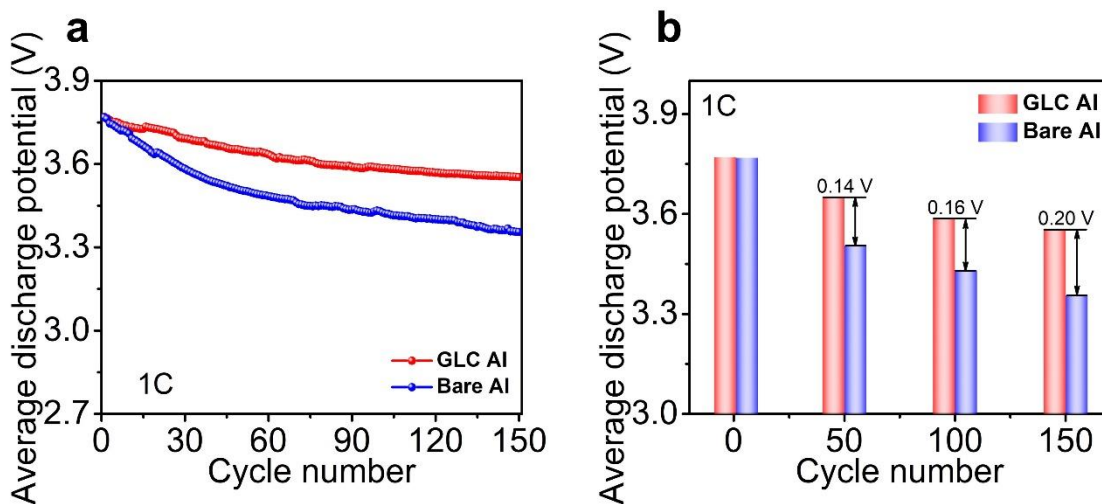
Figure S10. The corresponding average discharge voltage of the bare and GLC Al ASSLIBs during cycling under the current density of 1C at 25 ºC.
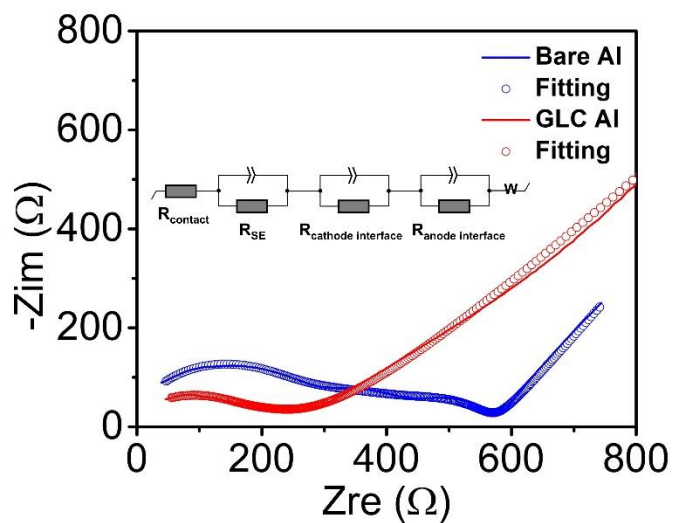
Figure S11. EIS plots of the bare and GLC Al ASSLIBs measured after cycling at 25 °C.
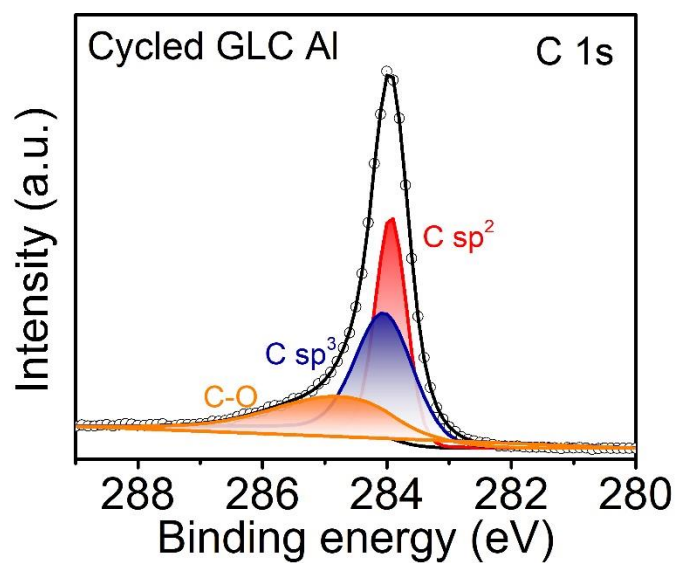
Figure S12. C 1s XPS spectrum of cycling GLC Al foil 25 °C.
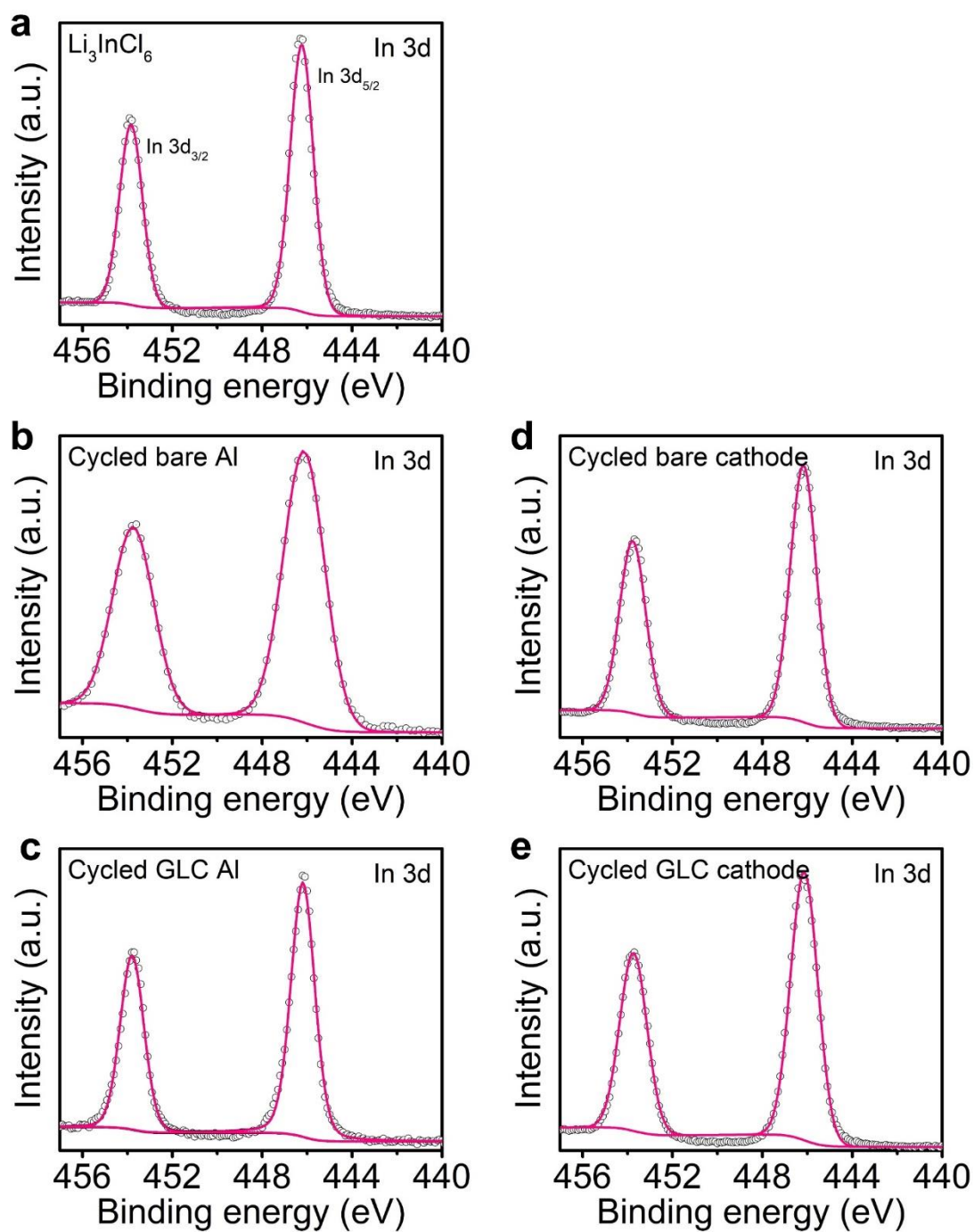
Figure S13. In 3d XPS spectra. (a) Li_3InCl_6, (b) cycled bare Al, (c) cycled GLC Al, (d) cycled bare cathode, and (e) cycled GLC cathode 25 ºC.
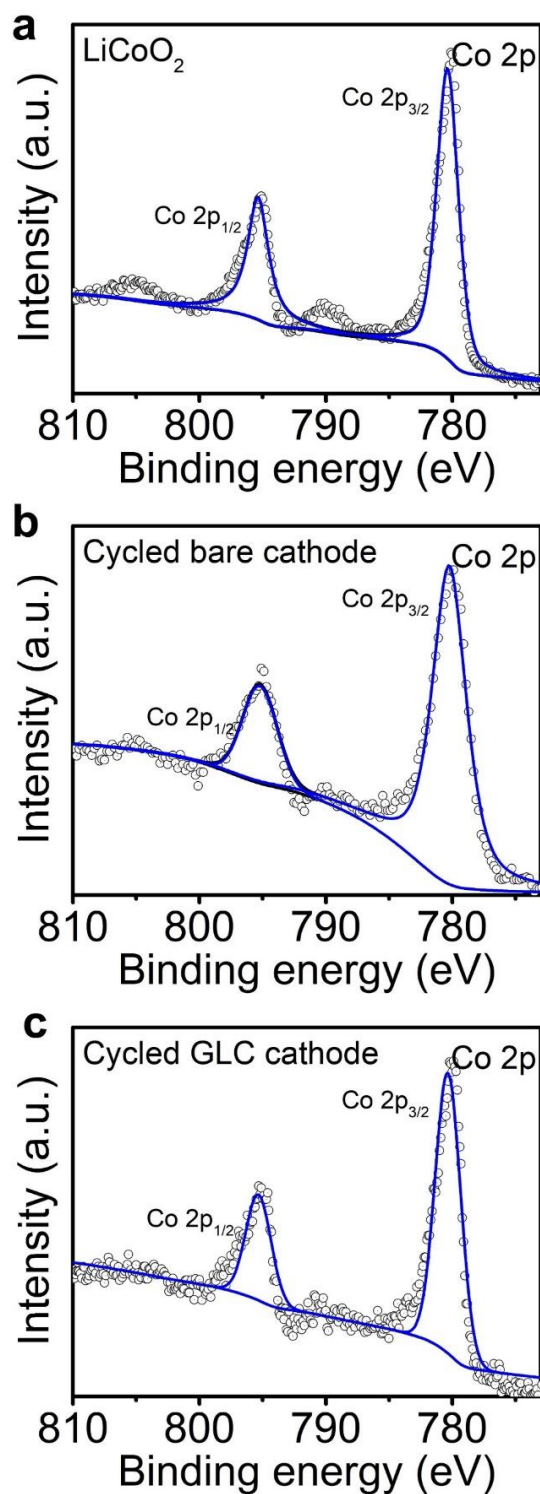
Figure S14. Co 2p XPS spectra. (a) $LiCoO_2$, (b) cycled bare cathode, and (c) cycled GLC cathode 25 °C.
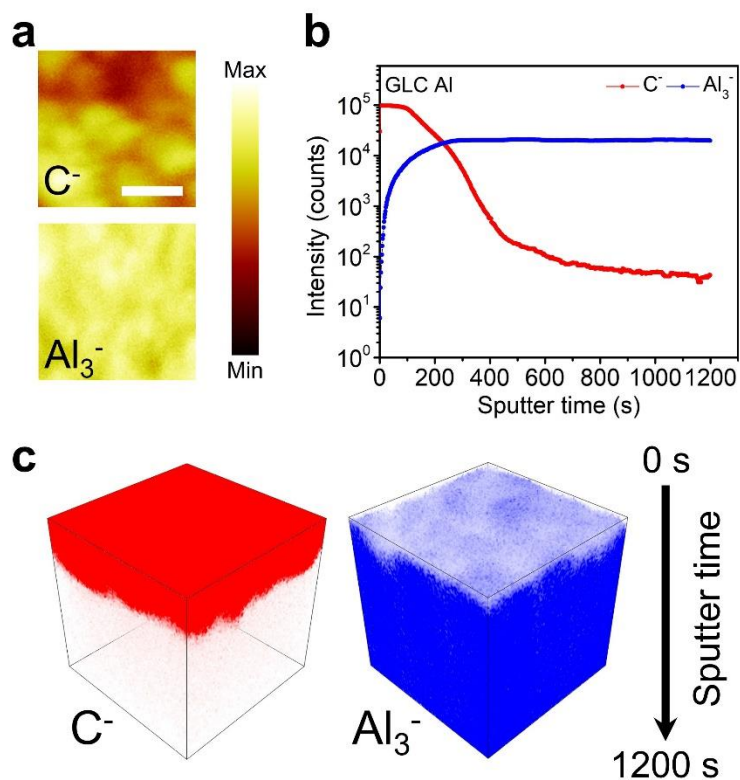
Figure S15. ToF-SIMS characterizations of GLC Al foil. (a) Secondary ion images of C^- and Al^{3-} species after Cs^+ consecutive sputtering of 1200 s (the length of scale bar is 20 μm), (b) the corresponding depth profile of various secondary ion species obtained by sputtering, and (c) 3D view images of the sputtered volume corresponding to the depth profiles.
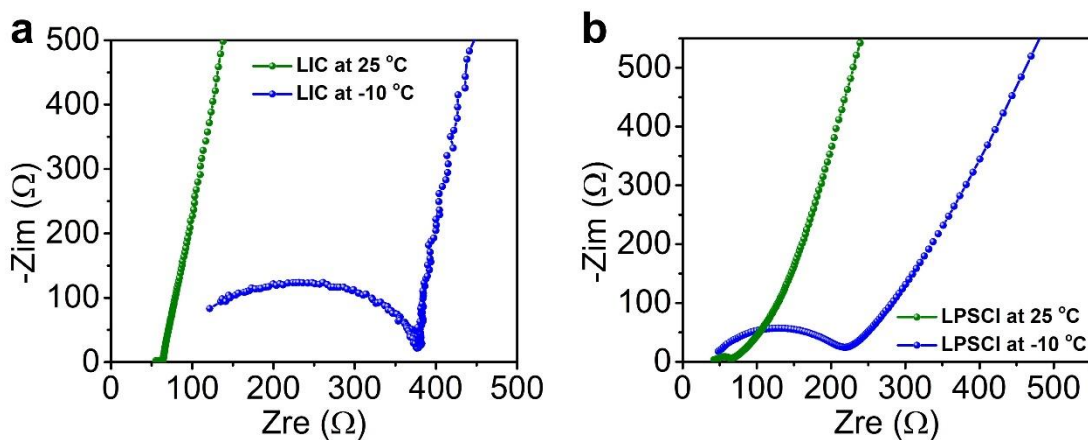
Figure S16. EIS plots of (a) LIC and (b) LPSCl SSEs measured after at 25 °C and -10 °C, respectively.
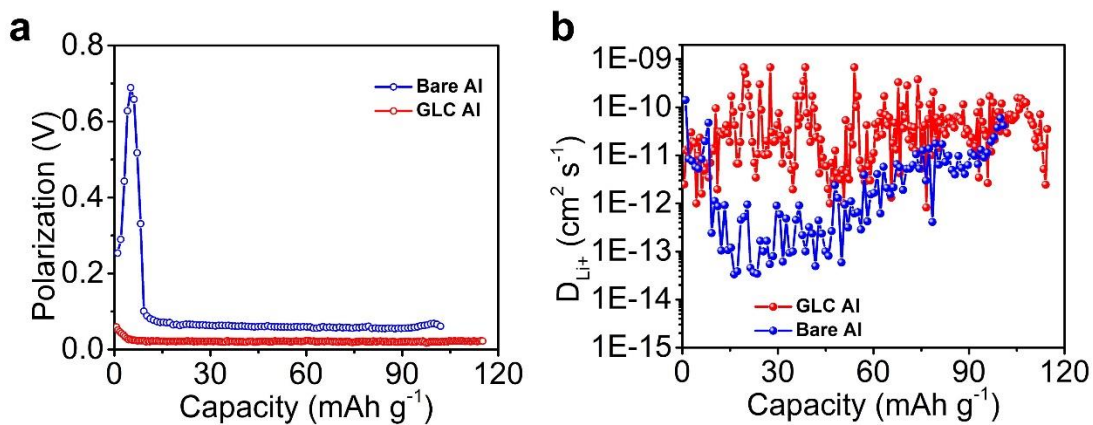
Figure S17. (a) Polarization plots and (b) lithium-ion diffusion coefficients during the charge process in the GITT testing of the bare and GLC Al ASSLIBs at -10 °C.
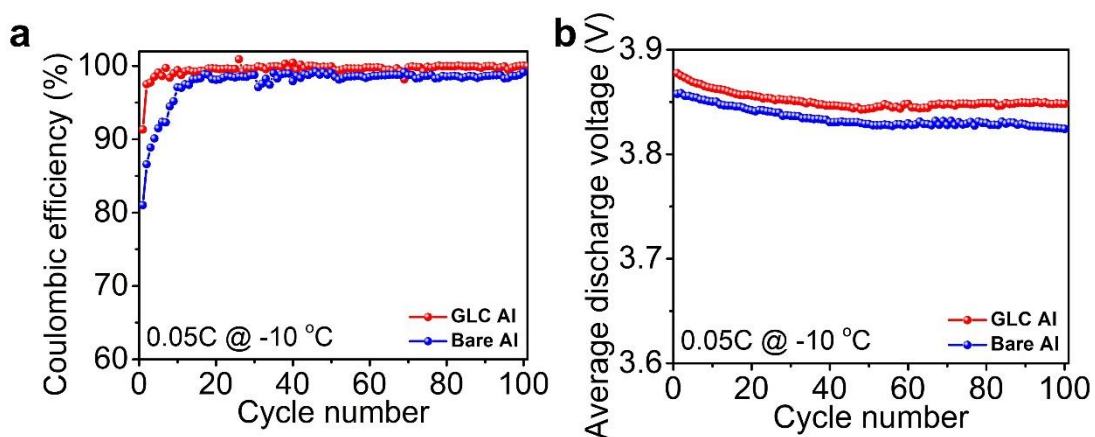
Figure S18. The corresponding (a) Coulombic efficiency and (b) average discharge voltage of the bare and GLC Al ASSLIBs during cycling under the current density of 0.05C at -10 ºC.
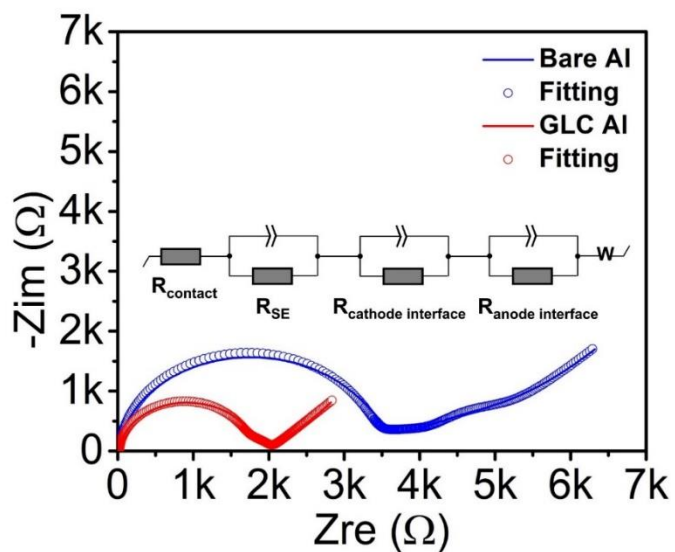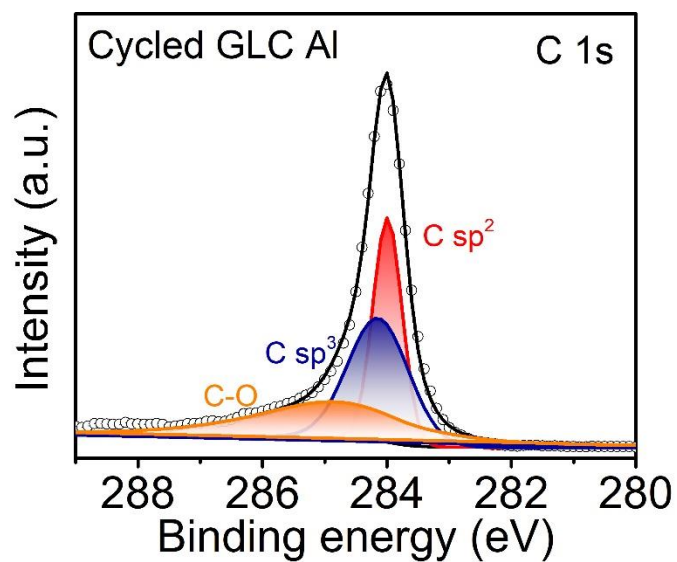

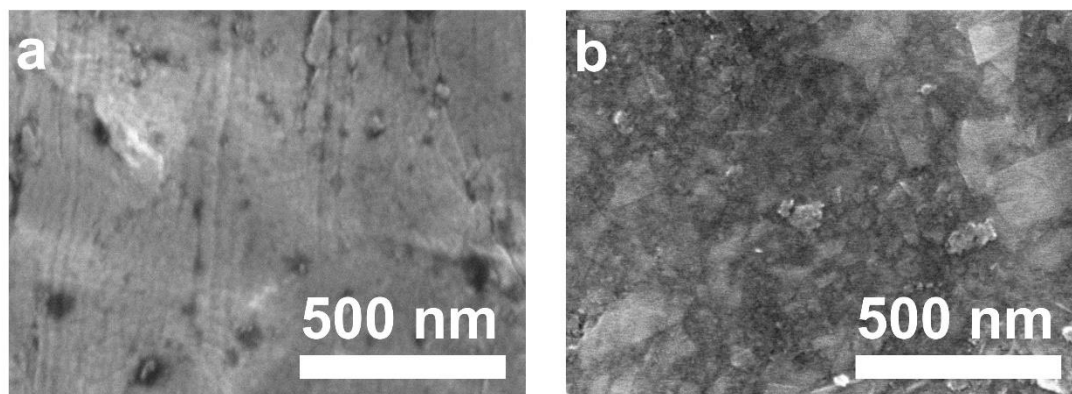**Figure S19.** EIS plots of the bare and GLC Al SSBs measured after cycling at -10 ºC.
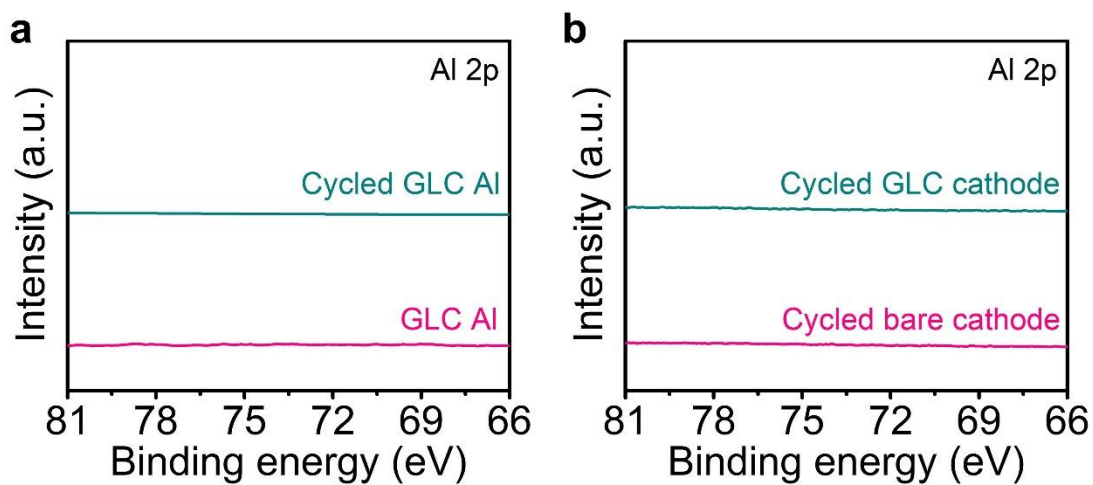
Figure S20. Al 2p spectra of the cycled (a) Al foil and (b) cathode at -10 °C.
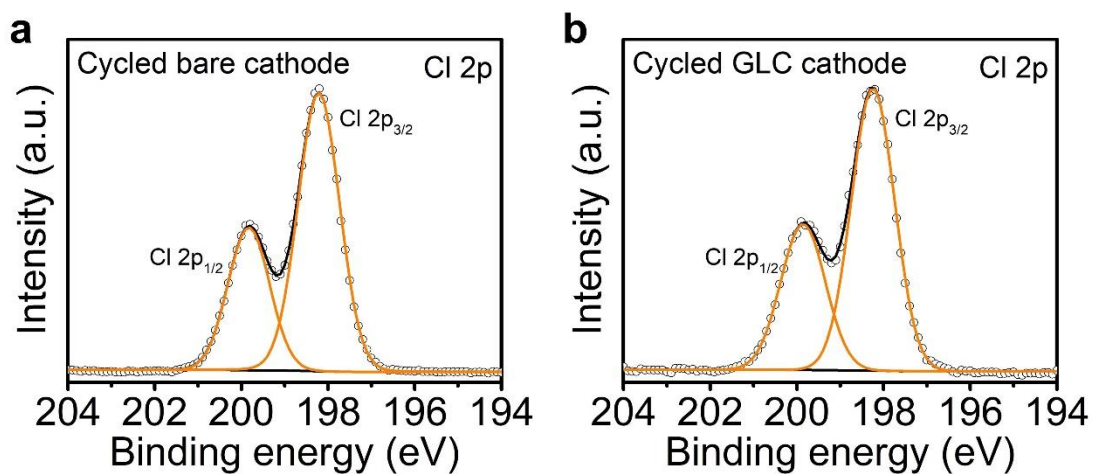
Figure S21. Cl 2p spectra of the cycled (a) Al foil and (b) cathode at -10 °C.

Figure S22. C 1s XPS spectrum of cycling GLC Al foil at -10 °C.

Figure S23. SEM images of bare and GLC Al foils after cycling at -10 °C.

Table S1. The lattice parameters of Al and Li_3InCl_6. The available results are summarized for comparison.

		a (Å)	b (Å)	c (Å)
Al	Our Cal.	4.04	-	-
	Other Cal.[1]	4.02	-	-
Li_3InCl_6	Our Cal.	6.64	11.37	6.47
	Other Cal.[2]	6.56	11.27	6.56
	Other Cal.[3]	6.43	11.09	6.39

Table S2. Partial charge at the LIC(100)/Al(111) and LIC(100)/GLC interfaces.

	Li (|e|)	In (|e|)	Cl (|e|)	Al (|e|)	C (|e|)
LIC(100)/Al(111)	10.459	4.95	-15.372	0.021	-
LIC(100)/GLC	10.579	5.046	-15.613	-	-0.011

Table S3. Summary of rate capability in the reported LCO in halide-based ASSLIBs.

	Cathode layer	Solid-state electrolytes layer	Anode	Voltage range (V vs. Li$^+$/Li)	Current density (C-rate)	Discharge capacity (mAh g^{-1})
Our work	LiNbO$_x$ coated LCO/Li$_3$InCl$_6$	Li$_3$InCl$_6$/Li$_6$PS$_5$Cl	Li-In	2.7-4.2	**5C**	**69**
Ref. [4]	Li$_3$InCl$_6$ coated LCO	Li$_3$InCl$_6$/Li$_{10}$GeP$_2$S$_{12}$	Li-In	3.1-4.2	4C	28.5
Ref. [5]	LCO/Li$_3$InCl$_6$	Li$_3$InCl$_6$/Li$_{10}$GeP$_2$S$_{12}$	In	2.5-4.2	1C	97
Ref. [6]	LCO/Li$_3$ScCl$_6$	Li$_3$ScCl$_6$	In	2.5-4.2	0.1C	126.2
Ref. [7]	LCO/Li$_2$Sc$_{2/3}$Cl$_4$	Li$_2$Sc$_{2/3}$Cl$_4$/Li$_{6.7}$Si$_{0.7}$Sb$_{0.3}$S$_5$I	Li-In	3.0-4.3	3C	65
Ref. [8]	LCO/Li$_{2.633}$Er$_{0.633}$Zr$_{0.367}$Cl$_6$	Li$_3$PS$_4$	Li$_{11}$Sn$_6$	3.0-4.3	0.1C	110
Ref. [9]	LCO/Li$_3$YCl$_6$	Li$_3$YCl$_6$	Li-In	2.5-4.2	0.1C	117

References

[1]   Y. Liu, Y. Huang, Z. Xiao, X. Reng, *Metals* 2017, 7, 21.

[2]   M. O. Schmidt, M. S. Wickleder, G. Meyer, *Zeitschrift für anorganische und allgemeine Chemie* 1999, 625, 539.

[3]   A. Zevgolis, A. Hall, T. Alvez, Z. Mehmedovic, P. Shea, J. Varley, B. Wood, N. Adelstein, Lawrence Livermore National Lab.(LLNL), Livermore, CA (United States), 2017.

[4]   C. Wang, J. Liang, M. Jiang, X. Li, S. Mukherjee, K. Adair, M. Zheng, Y. Zhao, F. Zhao, S. Zhang, *Nano Energy* 2020, 76, 105015.

[5]   X. Li, J. Liang, J. Luo, M. N. Banis, C. Wang, W. Li, S. Deng, C. Yu, F. Zhao, Y. Hu, *Energy Environ. Sci.* 2019, 12, 2665.

[6]   J. Liang, X. Li, S. Wang, K. R. Adair, W. Li, Y. Zhao, C. Wang, Y. Hu, L. Zhang, S. Zhao, *J. Am. Chem. Soc.* 2020, 142, 7012.

[7]   L. Nazar, L. Zhou, C. Y. Kwok, A. Shyamsunder, Q. Zhang, X. Wu, *Energy Environ. Sci.* 2020.

[8]   K.-H. Park, K. Kaup, A. Assoud, Q. Zhang, X. Wu, L. F. Nazar, *ACS Energy Lett.* 2020, 5, 533.

[9] T. Asano, A. Sakai, S. Ouchi, M. Sakaida, A. Miyazaki, S. Hasegawa, *Adv. Mater.* 2018, 30, 1803075.

Chapter 9

9   Conclusion and Future Perspectives

This chapter summarizes results, conclusions, and contributions of this thesis. Then, the perspectives and suggestions for the future development of next-generation high-energy cathodes and their application in high-performance ASSLIBs are discussed in detail.

9.1 Conclusion

Lithium-ion batteries (LIBs), as the most promising sustainable energy devices, are critical for the development of electric vehicles (EVs) because of their higher operating voltages compared to other energy storage technologies. However, the start-of-the-art LIBs still face the challenge of limited energy density. Therefore, development of next-generation cathode materials holds the key to realizing energy density target. Among the developed cathodes, high voltage cathode materials are promising to meet the requirement of high energy density. However, the high operating voltage challenges the stability of interface between cathodes and liquid electrolytes, leading to undesired side-reactions and safety issues. Compared to the conventional liquid LIBs, inorganic all-solid-state lithium-ion batteries (ASSLIBs) have been received significant attention due to the intrinsic safety characteristics and the potential to achieve high energy density. However, the unstable cathode interfaces are the tremendous obstacle to fulfill the advantages of ASSLIBs. In sulfide-based ASSLIBs, incompatible cathode interface leads to severe side-reactions between cathode materials and sulfide electrolytes. The anisotropic volume changes of high-energy Ni-rich layered oxide cathodes induce microstructural cracks and contact loss with sulfide electrolytes, resulting in the block of Li^+ diffusion at the cathode interface. Furthermore, sulfide-based ASSLIBs suffer from poor rate capability due to the challenge of using carbon additives in composite cathode. In halide-based ASSLIBs, the interfacial stability and Li^+/electron transfer at current collector interface are lack of understanding.

In this thesis, the main objectives aim to develop novel strategies to address the interfacial challenges of high-energy cathodes in both liquid-based LIBs and inorganic ASSLIBs. The first objective in chapter 4 is the study of high-voltage $LiNi_{0.5}Mn_{1.5}O_4$ (LNMO) cathode and investigate how to manipulate the interfacial lithium-ion and electronic conductivities by ALD. From chapter 5 to chapter 8, the studies focus on the different cathode interfaces in inorganic ASSLIBs, including cathode/solid-state electrolyte (SE) interface, cathode/carbon/SE interface, and current collector interface. Novel interfacial modifications are also developed to address the specific issues at the

different cathode interfaces and the underlying degradation mechanisms are unveiled by the multiscale characterizations.

Firstly, in the liquid LIBs, a controllable Li_3PO_4-TiO_2 hybrid interface material is employed as a coating layer for high voltage LNMO cathode with the use of ALD. Various coating materials (hybrid vs. single) and structure (hybrid vs. layer-by-layer) are optimized, which improve cycling and rate performance. Hybrid Li_3PO_4-TiO_2 coating layer effectively suppresses the polarization as well as facilitates Li-ion migration because of its capability to construct a stable interface to avoid side-reactions and also improve the interfacial ionic and electronic conductivity. Hybrid Li_3PO_4-TiO_2 coated LNMO shows much improved cycling stability at different current densities. Within 300 charge/discharge cycles at 0.5 C, the capacity decay is only 0.075 mAh g^{-1} per cycle. On the contrary, the capacity decay of bare LNMO is 0.204 mAh g^{-1} per cycle, which is 2.72 times compared to hybrid Li_3PO_4-TiO_2 coated LNMO. Even at 1 C, hybrid Li_3PO_4-TiO_2 coated LNMO still demonstrates very stable and high cycling capacity, which the capacity retention is 84.7% after 300 cycles. Synchrotron based XANES and TEM are carried out to understand the modification effect of Li_3PO_4-TiO_2 coating layer. Mn L-edge XANES demonstrates that hybrid Li_3PO_4-TiO_2 coating layer effectively suppresses dissolution of Mn and maintains the integral structure of LNMO. Ti L-edge and P K-edge XANES as well as TEM further investigate the structure and chemical stability of hybrid LPO-TiO coating layer during cycling.

To overcome the challenges in Ni-rich NMC cathodes and their interface with sulfide-based ASSLIBs, a hierarchical Li_3PO_4 (LPO) modification is developed for $LiNi_{0.8}Mn_{0.1}Co_{0.1}O_2$ Ni-rich layered oxide cathodes (NMC811) in $Li_{10}GeP_2S_{12}$-based ASSLIBs. The primary LPO coating layer with 10 nm thickness is infused into the grain boundaries of NMC811 secondary particles, which is proposed to alleviate the propagation of the microstructural cracks. A secondary coating layer with an optimized thickness is deposited to shield the NMC811 surface from the side-reactions with sulfide electrolyte. The detailed electrochemical characterizations combined with structural and interfacial chemical evaluations demonstrate that the hierarchical design of LPO not only

alleviates the severe side-reactions with sulfide electrolyte at high voltages but also suppresses the microstructural cracks of cathodes during cycling, significantly improves the ultra-long cycling life of Ni-rich layered oxide cathodes in sulfide-based ASSLIBs. The modified cathode demonstrates a significantly improved initial capacity of 170.6 mAh g^{-1} at 0.1C, better rate capability, and reduced polarization compared to the bare NMC811 cathode. More importantly, a stable and ultra-long battery life over 300 cycles is achieved with a low capacity degradation rate of 0.22 mAh g^{-1} at 0.2C.

A comprehensive X-ray analysis combined with detailed electrochemical characterizations is adopted to investigate the origin of degradation at cathode interface in sulfide-based ASSLIBs. The results reveal that the surface residual lithium compounds rather than $LiNi_{0.8}Mn_{0.1}Co_{0.1}O_2$ (NMC811) particles themselves cause the oxidation of sulfide SSEs, therefore leading to the severe side-reactions and structural evolution of NMC811. Promisingly, removal of the residual lithium compounds on the surface of NMC811 effectively alleviates the side-reactions at cathode interface, therefore suppressing the formation of an unfavorable cathode electrolyte interface (CEI) layer, resulting in clearly improved cycling stability with higher initial capacity and Columbic efficiency in both $Li_{5.5}PS_{4.5}Cl_{1.5}$ (LPSCl) and $Li_{10}GeP_2S_{12}$ (LGPS) SSEs. Without coating, the treated cathode demonstrates improved electrochemical performance in both LPSCl and LGPS SSEs. In LPSCl-based SSBs, 87.7% capacity retention is achieved in the treated NMC811 after 200 cycles at 0.2 C. In contrast, the pristine NMC811 delivers a poor capacity retention of 62.9% only after 100 cycles at the same current density. In LGPS-based SSBs, 60% capacity retention is achieved in the treated NMC811 after 219 cycles at 0.2 C, which is much higher than that of the pristine NMC811, which had a 60% capacity retention after only 98 cycles.

To overcome the challenges of using carbon additives at cathode composites in sulfide-based ASSLIBs, in this study, a semi-conductive polymer thin film, poly(3,4-ethylenedioxythiophene) (PEDOT), is constructed for sulfide-based ASSLIBs to realize the superior electrochemical performance with high-rate capacity. The detailed electrochemical characterizations combined with interfacial chemical evaluations

demonstrate that the high electronic conductivity of carbon nanotubes (CNTs) accelerates the decomposition of sulfide electrolyte and side-reactions in the cathode, therefore leading to the fast capacity degradation especially at high current densities. Promisingly, the PEDOT modification realizes the application of semi-conductive additives to modify conductive additives in the cathode composites, therefore effectively enhancing the interfacial stability between CNTs and LGPS, resulting in the obvious improved rate capability and enhanced cycling stability.

The performance of current collector are of critical importance for the high-rate performance of inorganic ASSLIBs. In this part, the interface evolution of Al foil current collector is comprehensively studied in the halide-based Li_3InCl_6 (LIC) ASSLIBs. The detailed electrochemical testing and characterizations combined with DFT results indicate that the degradation mechanism at the interface of current collector is highly related to the operating temperature of ASSLIBs. At room temperature, the side reactions between Al foil and LIC are the main challenge that deteriorate the electrochemical performance. At low temperature, in addition to side reactions, the low Li^+/electron transfer kinetics limit the electrochemical performance of inorganic ASSLIBs. Promisingly, a design of graphene like carbon (GLC) coating for the modification of Al is beneficial towards both the stability and Li^+/electron transfer at the interface of current collector. At 25 ^{o}C, the GLC Al ASSLIB demonstrates the obviously improved high-rate capability. A discharge capacity of 69 mAh g^{-1} is achieved at a high current density of 5C in the $LiCoO_2$ (LCO) based ASSLIBs, which is the first halide-based ASSLIB operating at 5C. At -10 ^{o}C, the GLC Al ASSLIB shows an initial discharge capacity of 99.9 mAh g^{-1} with a capacity retention of 85.9% after 100 cycles. However, the bare Al ASSLIB only delivers a discharge capacity of 76.5 mAh g^{-1} with a much reduced capacity retention of 47.1%.

9.2   Contribution of this thesis

1. Development of advanced nano-coatings for high-voltage lithium-ion cathodes

Developing multi-functional coatings is critical towards stabilizing the interface of high-voltage cathode materials in liquid-based LIBs. In my previous studies and this thesis, the

advanced coating materials, $AlPO_4$ (*Nano Energy 2017, 38, 19*) and Li_3PO_4-TiO_2 (*Nano Energy 2019, 65, 103988*), were developed by a controllable nanoscale thin film technique, atomic layer deposition (ALD), to suppress the side-reactions between high-voltage cathode materials and liquid electrolytes. With the protection of the coating layer, the as-prepared LIBs demonstrated significantly improved performance. Moreover, the comprehensive characterizations indicated that the coatings effectively suppressed the side-reactions at cathode interface and alleviated the structural degradation of cathode materials. These two works are funded by General Motors (GM) for the application in electric vehicles (EVs) and collaborated with Canadian Light Source (CLS) and Argonne National Laboratory (ANL) for advanced characterizations. These two studies were published on Nano Energy (IF: 17.88), the top journal in the field of nanomaterials and energy science. The novel coating materials we developed addressed long-time concerned interfacial issues of high-voltage cathodes in liquid-based LIBs.

2. Interfacial design of high-performance inorganic all-solid-state lithium-ion batteries

To address the challenges of cathode interfaces in inorganic ASSLIBs, we developed multiple strategies in this thesis. In sulfide-based ASSLIBs, a dual-functional hierarchical Li_3PO_4 modification via ALD was first designed to stabilize the interface between cathode materials and sulfide SSEs (*Energy Storage Materials 2020, 27, 117, IF: 17.79*). Our design shed lights on simultaneously solving the two key challenges including side-reactions and microstructural cracks of cathodes at SSE/cathode interface and was readily applicable to other solid-state battery systems. Furthermore, in collaboration with CLS, my second work applied synchrotron X-ray techniques to investigate the underlying degradation mechanisms at the SSE/cathode interface in sulfide-based ASSLIBs. The comprehensive synchrotron characterizations helped to deeply understand the interfacial reactions during the battery testing, providing valuable guidance for the future interface design (*Energy Storage Materials 2021, 35, 661, IF: 17.79*). In addition to the SSE/cathode interface, our interfacial design was also used to address the challenges in the SSE/carbon interface. For the first time, the semi-conductive additive was successfully applied in the sulfide-based ASSLIBs by the modification of advanced MLD (*ACS Energy Letters 2020, 5, 1243, IF: 23.10*). This study overcame long-term

challenges in the application of carbon in sulfide-based ASSBs. Because of the breakthrough in both performance and mechanisms, the aforementioned three works were published in top journals in the field of energy and reported by the internet media, such as "InfoMat", "Nanoer", and "V-suan". In addition, the current collector interface in halide-based ASSLIBs was also comprehensively studied in this thesis. For the first time, the different degradation mechanisms between halide SSE and Al foil current collector were unveiled at the different ambient temperatures in this study by the multi characterizations. More importantly, an interfacial strategy was developed to realize the excellent fast-charging performance. This work has been accepted by Advanced Functional Materials.

9.3 Perspectives

In the recent five years, ASSLIBs developed rapidly and many significant challenges have been addressed well. However, there are still some obstacles that hindering the realization of the target for high-energy, low-cost, and safe ASSLIBs. Hence, we propose six directions based on our experiences that may be beneficial for the next-generation high-performance ASSLIBs.

1. Development of high-energy, low-cost low-Co/Co-free cathode materials: The start-of-the-art cathode materials face two main challenges, limited capacity and high price of raw materials. Therefore, development of next-generation cathode materials holds the key to realizing the high energy density and low cost target. $LiNiO_2$-based low-cobalt and cobalt-free (LC/CF Ni-rich) cathodes are considered as one of the most promising candidates. On the one hand, an improved discharge capacity above 220 mAh g^{-1} is easily achieved with the high Ni content of over 90% in Ni-rich cathodes. On the other hand, the Co content can be greatly reduced by increasing the content of Ni in the layered structure, which greatly reduces the cathode material cost. However, the structural and interfacial stability of LC/CF Ni-rich cathodes still need to be further improved by the development of novel synthesis and interface strategies. Furthermore, the thermal stability of LC/CF Ni-rich cathodes also has space to be improved when applied in liquid LIBs.

2. Development of superior solid-state electrolytes: Although some reported inorganic SEs have shown the excellent performance, it still has a very long way to realize the practical application in EVs. The next-generation inorganic SEs should have the following properties: (1) higher ionic conductivity surpassing the liquid electrolytes; (2) good compatibility with electrode materials. Although halide-based SEs show excellent stability with most cathode materials, their high-voltage stability and unstable anode interface are the big obstacles for the practical application; (3) excellent air-stability which are suitable for use in the dry-room manufacturing; and (4) low price and easy for scale-up.

3. Development of advanced characterizations: With the development of new SEs, application of advanced characterization techniques in mechanism study is critical to unveil battery materials' working/failure mechanisms and therefore give valuable guidance to the design of high-performance ASSLIBs. For example, synchrotron X-ray has the capacities of in situ/operando and high temporal resolution, which is a powerful tool to study and monitor the electrochemical, physical, and chemical processes of SSEs and reveal the origin of phase evolution in ASSLIBs. Therefore, the structural evolution of SEs and electrode materials during the electrochemical process and environmental stability of SEs are very suitable to be studied by the X-ray characterizations. Furthermore, scanning/transmission electron microscopies (S/TEM) with a high spatial resolution are very suitable for observing the interfacial information and distinguishing local atomic structure changes during the battery operation that would otherwise not be possible. Unfortunately, application of TEM in ASSLIBs still faces big challenges. For example, air-sensitive SEs are difficult to be tested if there is no specific equipment to protect them. Building the in-situ experiments with suitable in-situ cell needs more efforts. Beam-damage for SE sample may need cryo-TEM help.

4. Development of novel interfacial materials: it is very necessary to develop multi-functional interfacial materials for both cathodes and anodes. At cathode side, the interfacial materials should have (1) wide electrochemical window, (2) high ionic conductivity, (3) excellent thermal stability, (4) good mechanical properties, and (5)

excellent interfacial compatibility with both cathode materials and SEs. At the anode side, how to stabilize anode interface and suppress the dendrite growth of Li metal is a big challenge. Furthermore, the mechanical properties of interfacial material is very important when alloy anodes, such as Si and Sn, are applied in ASSLIBs.

5. Development of all-climate solid-state batteries: The study about all-climate SSBs is still at the early stage, the degradation mechanisms are not very clear. For example, at high temperature, if the cathode interface is still stable when couple with halide-based SSBs and how to suppress the side reactions at both cathode and anode interfaces in sulfide-based SSBs. At low temperature, low ionic conductivity of SEs is a significant challenge. Furthermore, the interfacial evolution at both the cathode and anode needs to be deep investigated.

6. Development of high-performance pouch cell for practical application: Developing ASSLIBs from model cell to pouch cell need great effort. At the electrode level, the challenges include how to increase the compatibility between SEs, solvents, and binders in sheet-type electrode; how to increase mass-loading of cathode; and how to fabricate the ultra-thin SE layer. At the battery level, how to keep a constant pressure is a big challenge. Therefore, developing novel electrode engineer is critical to realize the practical application of ASSLIBs.

Appendices

Appendix A: Permission from Elsevier for Published Article on *Nano Energy*

Published paper:

Sixu Deng, Biqiong Wang, Yifei Yuan, Xia Li, Qian Sun, Kieran Doyle-Davis, Mohammad Norouzi Banis, Jianneng Liang, Yang Zhao, Junjie Li, Ruying Li, Tsun-Kong Sham, Reza Shahbazian-Yassar, Hao Wang, Mei Cai, Jun Lu, Xueliang Sun, Manipulation of an ionic and electronic conductive interface for highly-stable high-voltage cathodes, *Nano Energy*, 2019, 65, 103988.

Appendix B: Permission from Elsevier for Published Article on *Energy Storage Materials*

Published paper:

Sixu Deng, Xia Li, Zhouhong Ren, Weihan Li, Jing Luo, Jianwen Liang, Jianneng Liang, Mohammad Norouzi Banis, Minsi Li, Yang Zhao, Xiaona Li, Changhong Wang, Yipeng Sun, Qian Sun, Ruying Li , Yongfeng Hu, Huan Huang, Li Zhang, Shigang Lu, Jun Luo, Xueliang Sun, Dual-functional interfaces for highly stable Ni-rich layered cathodes in sulfide all-solid-state batteries, ***Energy Storage Materials***, 2020, 27, 117.

Appendix C: Permission from Elsevier for Published Article on *Energy Storage Materials*

Sixu Deng, Qian Sun, Minsi Li, Keegan Adair, Chuang Yu, Junjie Li, Weihan Li, Jiamin Fu, Xia Li, Ruying Li, Yongfeng Hu, Ning Chen, Huan Huang, Li Zhang, Shangqian Zhao, Shigang Lu, Xueliang Sun, Insight into cathode surface to boost the performance of solid-state batteries, *Energy Storage Materials*. 2021, 35, 661.

Appendix D: Permission from American Chemical Society (ACS) for Published Article on *ACS Energy Letters*

Sixu Deng, Yipeng Sun, Xia Li, Zhouhong Ren, Jianwen Liang, Kieran Doyle-Davis, Jianneng Liang, Weihan Li, Mohammad Norouzi Banis, Qian Sun, Ruying Li, Yongfeng Hu, Huan Huang, Li Zhang, Shigang Lu, Jun Luo, Xueliang Sun, Eliminating the Detrimental Effects of Conductive Agents in Sulfide-Based Solid-State Batteries, *ACS Energy Letters*. 2020, 5, 1243.

Appendix E: Permission from John Wiley and Sons for Published Article on *Advanced Functional Materials*

Sixu Deng, Ming Jiang, Adwitiya Rao, Xiaoting Lin, Kieran Doyle-Davis, Jianwen Liang, Chuang Yu, Ruying Li, Shangqian Zhao, Li Zhang, Huan Huang, Jiantao Wang, Chandra Veer Singh, Xueliang Sun, Fast-Charging Halide-Based All-Solid-State Batteries by Manipulation of Current Collector Interface, ***Advanced Functional Materials***. 2022, 2200767.

Curriculum Vitae

Name: Sixu Deng

Post-secondary   Beijing University of Technology
Education and   Beijing, China
Degrees: 2007-2011 B.Eng.

                             Beijing University of Technology
                             Beijing, China
                             2012-2018 Ph.D.

                             The University of Western Ontario
                             London, Ontario, Canada
                             2018-2022 Ph.D.

Honours and   Canada Graduate Scholarships-Doctor
Awards: 2020-2023

                             Best Graduate Student Presentation-Seminar Series
                             2021

                             Queen Elizabeth II Graduate Scholarships
                             2020

                             Ontario Graduate Scholarships
                             2019-2020

                             MITACS Accelerate Fellowship
                             2019

                             Beijing Distinguished Graduates (Doctor and Bachelor)
                             2018, 2011

                             Doctoral Thesis Awards
                             2018

                             President Scholarship
                             2018

                             National Scholarship-Doctor
                             2017

                             Chinese Government Scholarship for Studying Abroad
                             2015-2016

National Scholarship-Master
2013

Related Work   Teaching Assistant
Experience   The University of Western Ontario
2018

Publications:

1. **<u>Deng, S.</u>**; Jiang, M.; Rao, A; Lin, X.; Doyle-Davis, K.; Liang, J.; Yu, C.; Li, R.; Zhao, S.; Zhang, L.; Huang, H.; Wang, J.; Singh, C. V.; Sun, X. Fast-charging halide-based all-solid-state batteries by manipulation of current collector interface. *Advanced Functional Materials*. 2022, 2200767.

2. **<u>Deng, S.</u>**; Sun, Q.; Li, M.; Adair, K.; Yu, C.; Li, J.; Li, W.; Fu, J.; Li, X.; Li, R.; Hu, Y.; Chen, N.; Huang, H.; Zhang, L.; Zhao, S.; Lu, S.; Sun, X. Insight into cathode surface to boost the performance of solid-state batteries. *Energy Storage Materials*. 2021, 35, 661.

3. **<u>Deng, S.</u>**; Sun, Y.; Li, X.; Ren, Z.; Liang, J.; Doyle-Davis, K.; Liang, J.; Li, W.; Banis, M. N.; Sun, Q.; Li, R.; Hu, Y.; Huang, H.; Zhang, L.; Lu, S.; Luo, J.; Sun, X. Eliminating the detrimental effects of conductive agents in sulfide-based solid-state batteries. *ACS Energy Letters*. 2020, 5, 1243.

4. **<u>Deng, S.</u>**; Li, X.; Ren, Z.; Li, W.; Luo, J.; Liang, J.; Liang, J.; Banis, M. N.; Li, M.; Zhao, Y.; Li, X.; Wang, C.; Sun, Y.; Sun, Q.; Li, R.; Hu, Y.; Huang, H.; Zhang, L.; Lu, S.; Luo, J.; Sun, X. Dual-functional interfaces for highly stable Ni-rich layered cathodes in sulfide all-solid-state batteries. *Energy Storage Materials*. 2020, 27, 117.

5. **<u>Deng, S.</u>**; Wang, B.; Yuan, Y.; Li, X.; Sun, Q.; Doyle-Davis, K.; Banis, M. N.; Liang, J.; Zhao, Y.; Li, J.; Li, R.; Sham, T.-K.; Shahbazian-Yassar, R.; Wang, H.; Cai, M.; Lu, J.; Sun, X. Manipulation of an ionic and electronic conductive interface for highly-stable high-voltage cathodes. *Nano Energy*. 2019, 65, 103988.

6. **<u>Deng, S.</u>**; Xiao, B.; Wang, B.; Li, X.; Kaliyappan, K.; Zhao, Y.; Lushington, A.; Li, R.; Sham, T.-K.; Wang, H.; Sun, X. New insight into atomic-scale engineering of electrode surface for long-life and safe high voltage lithium ion cathodes. *Nano Energy*. 2017, 38, 19.

7. **<u>Deng, S.</u>**; Mao, D.; Wang, H.; Wang, B.; Liu, J.; Ma, Y.; Yan, H. Preparation and electrochemical properties of double-shell $LiNi_{0.5}Mn_{1.5}O_4$ hollow microspheres as cathode materials for Li-ion batteries. *RSC Advances*. 2016, 6, 45369.

8. **<u>Deng, S.</u>**; Wang, H.; Liu, H.; Liu, J.; Yan, H. Research progress in improving the rate performance of $LiFePO_4$ cathode materials. *Nano-Micro Letters*. 2014, 6, 209.

9. **<u>Deng, S.</u>**; Li, J.; Sun, S.; Wang, H.; Liu, J.; Yan, H. Synthesis and electrochemical properties of $Li_4Ti_5O_{12}$ spheres and its application for hybrid supercapacitors. *Electrochimica Acta*. 2014, 146, 37.

10. **<u>Deng, S.</u>**; Sun, D.; Wu, C.; Wang, H.; Liu, J.; Sun, Y.; Yan, H. Synthesis and electrochemical properties of MnO_2 nanorods/graphene composites for supercapacitor applications. *Electrochimica Acta*. 2013, 111, 707.

11. Zhao, F.; **<u>Deng, S.</u>**; Wang, C.; Sun, X. Excellent cathode interfaces achieved by atomic/molecualr layer depositions for sulfide-based all-solid-state batteries. *ECS Meeting Abstracts*. 2021, 29, 886.

12. Zheng, M.; Gao, X.; Sun, Y.; Adair, K.; Li, M.; Liang, J.; Li, X.; Liang, J.; **<u>Deng, S.</u>**; Yang, X.; Sun, Q.; Hu, Y.; Xiao, Q.; Li, R.; Sun, X. Realizing high-performance Li-S batteries through additive manufactured and chemically enhanced cathodes. *Small Methods*. 2021, 5, 2100176.

13. Zhao, C.; Sun, Q.; Luo, J.; Liang, J.; Liu, Y.; Zhang, L.; Wang, J.; **<u>Deng, S.</u>**; Lin, X.; Yang, X.; Huang, H.; Zhao, S.; Zhang, L.; Lu, S.; Sun, X. 3D porous garnet/gel polymer hybrid electrolyte for safe solid-state $Li-O_2$ batteries with long lifetimes. *Chemistry of Materials*. 2020, 32, 10113.

14. Yu, C.; Li, Y.; Adair, K.; Li, W.; Goubitz, K.; Zhao, Y.; Willans, M.; Thijs, M.; Wang, C.; Zhao, F.; Sun, Q.; **Deng, S.**; Liang, J.; Li, X.; Li, R.; Sham, T.; Huang, H.; Lu, S.; Zhao, S.; Zhang, L.; Eijck, L.; Huang, Y.; Sun, X. Tuning ionic conductivity and electrode compatibility of Li$_3$YBr$_6$ for high-performance all solid-state Li batteries. *Nano Energy*. 2020, 77, 105097.

15. Yu, C.; Li, Y.; Li, W.; Adair, K.; Zhao, F.; Willans, M.; Liang, J.; Zhao, Y.; Wang, C.; **Deng, S.**; Li, R.; Huang, H.; Lu, S.; Sham, T.; Huang, Y.; Sun, X. Enabling ultrafast ionic conductivity in Br-based lithium argyrodite electrolytes for solid-state batteries with different anodes. *Energy Storage Materials*. 2020, 30, 238.

16. Wang, C.; Liang, J.; Hwang, S.; Li, X.; Zhao, Y.; Adair, K.; Zhao, C.; Li, X.; **Deng, S.**; Lin, X.; Yang, X.; Li, R. Huang, H.; Zhang, L., Lu, S.; Su, D.; Sun, X. Unveiling the critical role of interfacial ionic conductivity in all-solid-state lithium batteries. *Nano Energy*, 2020, 72, 104686

17. Zhao, F.; Liang, J.; Yu, C.; Sun, Q.; Li, X.; Adair, K.; Wang, C.; Zhao, Y.; Zhang, S.; Li, W.; **Deng, S.**; Li, R.; Huang, Y.; Huang, H.; Zhang, L.; Zhao, S.; Lu, S.; Sun, X. A versatile Sn-substituted argyrodite sulfide electrolyte for all-solid-state Li metal batteries. *Advanced Energy Materials*. 2020, 10, 1903422.

18. Huo, H.; Li, X.; Chen, Y.; Liang, J.; **Deng, S.**; Gao, X.; Doyle-Davis, K.; Li, R.; Guo, X.; Shen, Y.; Nan, C.; Sun, X. Bifunctional composite separator with a solid-state-battery strategy for dendrite-free lithium metal batteries. *Energy Storage Materials*. 2020, 29, 361.

19. Yu, C.; Li, Y.; Willans, M.; Zhao, Y.; Adair, K.; Zhao, F.; Li, W.; **Deng, S.**; Liang, J.; Banis, M.; Li, R.; Huang, H.; Zhang, L.; Yang, R.; Lu, S.; Huang, Y.; Sun, X. Superionic conductivity in lithium argyrodite solid-state electrolyte by controlled Cl-doping. *Nano Energy*, 2020, 69, 104396.

20. Li, X.; **Deng, S.**; Banis, M. N.; Doyle-Davis, K.; Zhang, D.; Zhang, T.; Yang, J.; Divigalpitiya, R.; Brandys, F.; Li, R.; Sun, X. Suppressing corrosion of aluminum foils

via highly conductive graphene-like carbon coating in high-performance lithium-based batteries. *ACS Applied Materials & Interfaces*. 2019, 11, 32826.

21. Li, X.; Ren, Z.; Banis, M. N.; **Deng, S.**; Zhao, Y.; Sun, Q.; Wang, C.; Yang X.; Li, W.; Liang, J.; Li X.; Sun, Y.; Adair, K.; Li, R.; Hu, Y.; Sham, T.-K.; Huang, H.; Zhang, L.; Lu S.; Luo, J.; Sun, X. Unravelling the chemistry and microstructure evolution of a cathodic interface in sulfide-based all-solid-state Li-ion batteries. *ACS Energy Letters*. 2019, 4, 2480.

22. Dong, H.; Liu, G.; Li, S.; **Deng, S.**; Cui, Y.; Liu, H.; Liu, H.; Sun X. Design of a 3D-porous structure with residual carbon for high-performance Ni-rich cathode materials. *ACS Applied Materials & Interfaces*. 2019, 11, 2500.

23. Li, X.; Liang, J.; Luo, J.; Banis, M. N.; Wang, C.; Li, W.; **Deng, S.**; Yu, C.; Zhao, F.; Hu, Y.; Sham, T.-K.; Zhang, L.; Zhao, S.; Lu, S.; Huang, H.; Li, R.; Adair, K.; Sun, X. Air-stable Li_3InCl_6 electrolyte with high voltage compatibility for all-solid-state batteries. *Energy & Environmental Science*. 2019, 12, 2665.

24. Li, X.; Liu, W.; Kou, H.; Sari, H.; Song, X.; Li, J.; Dou, S.; Liu, X.; **Deng, S.**; Li, D.; Sun, X. ALD derived Fe^{3+}-doping toward high performance P2-$Na_{0.75}Ni_{0.2}Co_{0.2}Mn_{0.6}O_2$ cathode material for sodium ion batteries. *Materials Today Energy*. 2019, 14, 100353.

25. Wang, C.; Li, X.; Zhao, Y.; Banis, M.; Liang, J.; Li, X.; Sun, Y.; Adair, K.; Sun, Q.; Liu, Y.; Zhao, F.; **Deng, S.**; Lin, X.; Li, R.; Hu, Y.; Sham, T.; Huang, H.; Zhang, L.; Yang, R.; Lu, S.; Sun X. Manipulating interfacial nanostructure to achieve high-performance all-solid-state lithium-ion batteries. *Small Methods*. 2019, 10, 1900261.

26. Hao, Z.; Xu, X.; **Deng, S.**; Wang, H.; Liu, J.; Yan H.; In situ growth of Co_3O_4 coating layer derived from MOFs on $LiNi_{0.8}Co_{0.15}Al_{0.05}O_2$ cathode materials. *Ionics*. 2019, 25, 2469

27. Zhang, T.; Li, X.; Asher, E.; **Deng, S.**; Sun, X.; Yang, J. Paper with power: engraving 2D materials on 3D structures for printed, high-performance, binder-free, and all-solid-state supercapacitors. *Advanced Functional Materials*. 2018, 28, 1803600.

28. Dong, H.; Liu, G.; Li, S.; **Deng, S.**; Cui, Y.; Liu, H.; Liu, H.; Sun, X. Design of a 3D-porous structure with residual carbon for high-performance Ni-rich cathode materials. *ACS Applied Materials & Interfaces*. 2018, 11, 2500.

29. Xu, X.; **Deng, S.**; Wang, H.; Liu, J.; Yan, H.; Research progress in improving the cycling stability of high voltage $LiNi_{0.5}Mn_{1.5}O_4$ cathode in lithium-ion battery. *Nano-Micro Letters*. 2017, 7, 22.

30. Wu, C.; **Deng, S.**; Wang, H.; Sun, Y.; Liu, J.; Yan, H. Preparation of novel three-dimensional NiO/ultrathin derived graphene hybrid for supercapacitor applications. *ACS Applied Materials & Interfaces*. 2014, 6, 1106.

31. Wu, C.; Shen, Q.; Mi, R.; **Deng, S.**; Shu, Y.; Wang, H.; Liu, J.; Yan, H. Three-dimensional Co_3O_4/flocculent graphene hybrid on Ni foam for supercapacitor applications. *Journal of Materials Chemistry A*. 2014, 2, 15987.

32. Wang, Y.; Xie, S.; Deng, J.; **Deng, S.**; Wang, H.; Yan, H.; Dai, H. Morphologically controlled synthesis of porous spherical and cubic $LaMnO_3$ with high activity for the catalytic removal of toluene. *ACS Applied Materials & Interfaces*. 2014, 6, 17394.

33. Xie, M.; Zhang, X.; Wang, Y.; **Deng, S.**; Wang, H.; Liu, J.; Yan, H.; Laakso, J.; Levänen E. A template-free method to prepare porous $LiFePO_4$ via supercritical carbon dioxide. *Electrochimica Acta*. 2013, 94, 16.

34. Wang, Q.; **Deng, S.**; Wang, H.; Xie, M.; Liu, J.; Yan, H. Hydrothermal synthesis of hierarchical $LiFePO_4$ microspheres for lithium ion battery. *Journal of Alloys and Compounds*. 2013, 553, 69.

35. Wang, Y.; Shao, X.; Xu, H.; Xie, M.; **Deng, S.**; Wang, H.; Liu, J.; Yan, H.; *Journal of Power Sources*. 2013, 226, 140.

36. Wang, Y.; Shao, X.; Xie, M.; **Deng, S.**; Wang, H.; Liu, J.; Yan, H. Porous $LiMn_2O_4$ spheres synthesized by topochemical route using the porous Mn_2O_3 as precursor. *Applied Mechanics and Materials*. 2013, 291, 708.

37. Xie, M.; Zhang, X.; **Deng, S.**; Wang, Y.; Wang, H.; Liu, J.; Yan, H.; Laakso, j.; Levänen, E. The effects of supercritical carbon dioxide treatment on the morphology and electrochemical performance of $LiFePO_4$ cathode materials. *RSC Advances.* 2013, 3, 12786.

Conference presentations:

Talks:

1. **Deng, S.**; Wang, C.; Sun, X. *Materials Research Society Fall Meeting & Exhibit*, Boston,   Massachusetts, 2021

2. **Deng, S.**; Wang, C.; Sun, X. *Canadian Chemical Engineering Conference*, Montreal, Quebec, 2021 (**Invited talk**)

3. **Deng, S.**; Li, X.; Wang, C.; Sun, X. *ACS Spring*, 2021 (Online)

4. **Deng, S.**; Li, X.; Liang, J.; Sun, X. *EnviroCon-2021*, London, Ontario, 2021 (Online)

5. **Deng, S.**; Sun, X. *Western Graduate Seminar*, London, Ontario, 2021 (**Best presentation, CAD$ 100**)

6. **Deng, S.**; Sun, X. *ECS Canadian Section-Fall Symposium*, Simon Fraser University, Burnaby, British Columbia, 2020 (Online)

7. **Deng, S.**; Sun, X. *Fourth Annual ECS Student Virtual Symposium*, 2020 (Online)

8. **Deng, S.**; Sun, X. *International Forum on Functional Materials of China, America and Canada,* 2020 (Online) (**Invited talk**)

9. **Deng, S.**; Sun, X. *Canadian Society for Mechanical Engineering and CFD Society of Canada Congress*, London, Ontario, 2019

Posters:

1. **Deng, S.**; Li, X.; Wang, C.; Sun, X. *ACS Spring*, 2021 (Online) (**Student Poster Award, USD$ 400**)

2. **Deng, S.**; Sun, X. *CAMBR Day Events*, Western University, London, Ontario, 2021 (Online) (**Invited poster**)

3. **Deng, S.**; Sun, X. *Annual Users' Meeting and CLS 2.0 event*, Saskatoon, Saskatchewan, 2020 (Online)